

**Studies for a Linear Collider Drift Chamber
and
Search for Heavy Stable Charged Particles in
 e^+e^- Collisions up to $\sqrt{s} = 209$ GeV**

Dissertation

**zur Erlangung des Doktorgrades
des Fachbereichs Physik
der Universität Hamburg**

vorgelegt von

Markus Hamann

aus Gifhorn

**Hamburg
2003**

Gutachter der Dissertation : Prof. Dr. R.-D. Heuer
Prof. Dr. B. Naroska

Gutachter der Disputation : Prof. Dr. R.-D. Heuer
Prof. Dr. P. Schleper

Datum der Disputation : 4.12.2003

Vorsitzender des Prüfungsausschusses : Prof. Dr. G. Heinzelmann

Vorsitzender des Promotionsausschusses : Prof. Dr. R. Wiesendanger

Dekan des Fachbereichs Physik : Prof. Dr. G. Huber

Kurzfassung

Im ersten Teil dieser Arbeit werden Studien für eine TPC (“Time Projection Chamber”) vorgestellt, die als Hauptspurkammer für den Detektor des zukünftigen e^+e^- Linearbeschleuniger TESLA geplant ist. Anstelle der konventionellen Auslese, basierend auf Drahtkammern, wurde ein Auslesesystem mit GEMs (“Gas Electron Multipliers”) entwickelt. Erste Messungen mit kosmischen Myonen mit einer Doppel-GEM-Struktur werden vorgestellt. Die Einzelpunktauflösung wird für verschiedene Auslese-Pad-Geometrien bestimmt und mit Simulationen verglichen.

Im zweiten Teil wird eine Suche nach schweren stabilen geladenen Teilchen (Masse > 45 GeV, Lebensdauer $\geq 10^{-6}$ s) vorgestellt. Die zugrundeliegenden Daten wurden in e^+e^- Kollisionen bei Schwerpunktenergien von (131 – 209) GeV mit dem OPAL Detektor am LEP Speicherring aufgezeichnet. Die Datenselektion basiert auf der Forderung von mindestens einer Spur mit anomalem spezifischen Energieverlust, so daß viele verschiedene Signaltopologien berücksichtigt werden, z.B. Kaskadenzerfälle von paar-produzierten Teilchen in schwere stabile geladene Teilchen. Im untersuchten Datensatz, der einer integrierten Luminosität von 632.1 pb^{-1} entspricht, wird kein Ereignis selektiert, während das Standard-Modell 0.795 ± 0.394 Ereignisse vorhersagt. Hieraus ergeben sich obere Grenzen für den Wirkungsquerschnitt für die direkte und indirekte Produktion schwerer stabiler geladener Teilchen, die im Rahmen supersymmetrischer Modelle, speziell GMSB (“Gauge Mediated Supersymmetric Breaking”), interpretiert werden.

Abstract

In the first part of this thesis studies for a TPC (Time Projection Chamber) are presented which is planned to constitute the main tracking device of the detector at the future linear e^+e^- collider TESLA. Instead of conventional readout based on wire chambers a gas amplification system using GEMs (Gas Electron Multipliers) was developed. First basic studies with a TPC prototype equipped with a double GEM structure using cosmic muons are presented. The single point resolution is determined with different readout pad geometries, and the results are compared with simulations.

In the second part a search for heavy stable charged particles (mass > 45 GeV, lifetime $\geq 10^{-6}$ s) in e^+e^- collisions is presented. The analysed data were recorded with the OPAL detector at LEP at centre-of-mass energies of (131 – 209) GeV. As the data selection is based only on the requirement of at least one track per event with an anomalous specific energy loss, many different signal event topologies are covered, e.g. cascade decays of pair-produced particles into heavy stable charged particles. In the analysed data corresponding to an integrated luminosity of 632.1 pb^{-1} no data event is selected while 0.795 ± 0.394 events are expected from the Standard Model. Upper cross-section limits are derived for the direct and indirect production of heavy stable charged particles, which are interpreted within supersymmetric models, especially focussing on GMSB (Gauge Mediated Supersymmetric Breaking).

Contents

Preface	1
I Studies for the Readout of a Linear Collider TPC	3
1 Basic Principles of Gaseous Particle Detectors	5
1.1 Operational Modes	5
1.2 Detector Gas	6
1.3 Diffusion	6
1.4 Signal Generation	7
1.5 Drift Chambers	7
1.5.1 Time Projection Chambers	9
1.5.2 Jet Chambers	13
1.5.3 Discussion	15
1.6 Measurement of the Specific Energy Loss dE/dx	15
2 The Linear Collider Project	21
2.1 The Accelerator	21
2.2 Detector Requirements and Concept	22
2.3 The Linear Collider TPC	24
2.3.1 GEM Readout	26
2.3.2 Alternative Readout Technologies	29
3 TPC R&D	31
3.1 Experimental Setup	31
3.1.1 Field Cage and Gas	32
3.1.2 GEM Readout Module and Endplate	32
3.1.3 Trigger	37
3.1.4 Readout Electronics and Data Acquisition	37
3.2 Data Set	37
3.3 Basic Performance Studies	37
3.3.1 Pulse Finding	38
3.3.2 Signal to Noise Ratio	39
3.3.3 Drift Velocity and Pulse Shape	40
3.3.4 Gas Amplification	41
3.3.5 Pad Efficiency	45

3.4	Resolution	46
3.4.1	Cosmic Muon Data	46
3.4.2	Simulation	50
3.4.3	Discussion	53
3.5	Outlook	56
II	Search for Heavy Stable Charged Particles at LEP	59
4	Theoretical Context	61
4.1	Decay Rate and Lifetime	61
4.2	The Standard Model	62
4.3	Supersymmetric Extensions of the Standard Model	64
4.3.1	Shortcomings of the Standard Model	64
4.3.2	Basic Ideas of a Supersymmetric Extension	65
4.3.3	Supersymmetry Breaking	67
4.4	Production, Decay and Lifetime of Supersymmetric Particles	68
4.4.1	Gauge Mediated Supersymmetry Breaking	71
4.4.2	Gravity and Anomaly Mediated Supersymmetry Breaking	74
4.4.3	General Searches for Supersymmetric Particles with Lifetime	74
5	Experimental Approach	77
5.1	The LEP Collider	77
5.2	The OPAL Detector	77
5.2.1	Coordinate System and Track Parameters	78
5.2.2	General Design	79
5.2.3	Event Reconstruction	80
5.3	The OPAL Jet Chamber	80
5.3.1	Design	80
5.3.2	Performance	81
5.3.3	Signal Separation using the dE/dx Measurement	81
5.3.4	Particles with low $\beta\gamma$	83
5.4	The OPAL Trigger	83
5.4.1	Track Trigger	86
5.4.2	Monopole or High dE/dx Trigger	86
5.4.3	Particles with low $\beta\gamma$	87
5.4.4	Trigger Simulation	88
6	Data Set and Simulation	91
6.1	e^+e^- Data Set	91
6.2	Monte Carlo Simulation	91
6.2.1	Physics Processes	93
6.2.2	Background Event Simulation	95
6.2.3	Signal Event Simulation	95
6.2.4	Detector Simulation	96
6.2.5	Event Reconstruction	97

7 Data Selection and Signal Efficiency	99
7.1 Selection Concept	99
7.2 Selection Cuts	99
7.2.1 Preselection	99
7.2.2 Reduction of non-simulated Background	100
7.2.3 Main Selection	100
7.3 Result	108
7.4 Determination of the Selection Efficiency	108
7.5 Systematic Uncertainties	116
7.5.1 Systematic Uncertainties of the Data Selection	116
7.5.2 Systematic Uncertainties of the Efficiency	121
7.6 Summary	122
8 Interpretation	127
8.1 Limit Calculation	127
8.2 Cross-Section Limits	128
8.2.1 Pair-Production of Heavy Stable Charged Particles	128
8.2.2 Indirect Production of Heavy Stable Charged Particles	129
8.3 Interpretation within the Framework of GMSB Models	132
8.3.1 The GMSB Parameter Space	133
8.3.2 Mass Limits	136
8.3.3 Exclusions in the GMSB Parameter Space	138
8.3.4 Constraints on the SUSY Particle Mass Scale Λ	140
9 Summary and Conclusion	143
A Technical Sketch of Endplate 2	147
B The Signal Monte Carlo Grid used in the Search	149
C Interpretation of the Search Result in the MSSM with small $\Delta m_{\tilde{\chi}_1}$	151
Danksagung	163

Preface

Physics aims for the formulation of a theory of matter and its interactions. Inspired by the Greek natural philosophy, the hypothesis that matter consists of small indivisible particles has become accepted.

Elementary Particle Physics investigates the smallest subatomic structures. According to the so-called *Standard Model* (SM) matter is made out of very small constituents ($< 10^{-18}$ m), the elementary particles. Two different classes are known, the *leptons* whose most prominent representative is the electron e^- and the *hadrons*. The most important hadrons are the up-quark u and the down-quark d . For all particles there are anti-particles with the opposite charge (and the other additive quantum numbers) but with the same mass. The anti-particle of the electron for example is the *positron* e^+ , and the anti-particle of a quark q is denoted with \bar{q} .

The constituents of matter interact via different forces, which can lead to bound states like protons, neutrons (three quark bound states) and atoms. Today three forces are known: the *strong interaction* which acts between quarks, the *electroweak interaction* which describes phenomena like the radioactive decay and is responsible for all interactions between electrically charged particles and the *gravitation*. The gravitational interaction is the weakest of all and is negligible in the world of elementary particles at energies reachable today. The interactions between the matter particles are described by the exchange of force carrier particles.

The Standard Model has been very successful in explaining all phenomena of elementary particle physics, investigated in many laboratories where the collisions of very high energetic particles, produced for example in a particle accelerator, are used to study the laws of Nature at the smallest distances. However the Standard Model is unsatisfactory in the sense of a simple and consistent description of particles and their interactions. It contains for example 18 free parameters without providing guidelines in choosing the values, and the unification of the electroweak and the strong interaction, similar to the successful unification of the electromagnetic and weak phenomena to the electroweak interaction, is impossible.

Extensions of the Standard Model which account for these shortcomings are being extensively discussed. One very attractive option is *Supersymmetry* (SUSY) which introduces supersymmetric partner particles for every SM particle.

Hence a tremendous effort is being carried out in order to measure a deviation from Standard Model predictions or to directly detect new phenomena like SUSY particles.

The present thesis is divided into two parts both of which are motivated by these tasks: in Part I studies for a gas filled drift chamber are presented which is planned to

constitute the main device for the detection of charged particles at a future linear electron positron collider. The drift chamber must fulfil special requirements determined by the expected physics processes and the accelerator where e^+e^- collisions will be studied up to a centre-of-mass energy of the order of 1 TeV. A series of precision measurements and searches for new phenomena are planned which will provide new insights into the world of elementary particles.

Until now the highest energy reached in e^+e^- collisions was 209 GeV at the LEP (Large Electron Positron) collider at the CERN laboratory. In Part II a search for heavy stable charged particles in e^+e^- collisions recorded with the OPAL (Omni Purpose Apparatus at LEP) detector at LEP is presented. The existence of elementary stable charged particles with mass larger than the mass of the proton would be evidence for phenomena beyond the Standard Model. The search is sensitive to a large variety of production mechanisms: apart from pair-produced stable particles, heavy stable charged particles produced for example as decay products of previously produced particles are searched for, too.

The thesis is structured as follows: Part I starts with a chapter containing a general introduction into the principles of gaseous particle detectors because they play a crucial role in both parts of the thesis. In Chapter 2 the linear collider project TESLA (Tera Electronvolt Energy Superconducting Linear Accelerator) is introduced for which the detector studies described in Chapter 3 are carried out.

In Chapter 4, the first chapter of Part II, a general introduction to particle lifetime is given and the Standard Model is explained in more detail; Supersymmetry is introduced which under certain assumptions predicts the existence of heavy stable charged particles. The experimental approach is explained in detail in Chapter 5 under the special consideration of the role of the drift chamber. The simulation of the physics processes, which is indispensable for the understanding of the measurements, is discussed in Chapter 6. Then in Chapter 7 the strategy of the search including the data selection is explained. In addition this chapter contains the determination of the selection efficiency and the search result. Finally in Chapter 8 an interpretation of the result is given within the framework of supersymmetric models.

Part I

Studies for the Readout of a Linear Collider TPC

Chapter 1

Basic Principles of Gaseous Particle Detectors

The use of gaseous detectors has spread to many fields of applications and research apart from high energy particle physics, e.g. astrophysics, nuclear medicine, X-ray imaging and protein crystallography [1, 2]. The basic working principles of gaseous particle detectors and the operation of drift chambers are overviewed in this chapter. More details on this topic can be found for example in [3–6].

1.1 Operational Modes

Gaseous particle detectors exploit the electromagnetic interaction, i.e. ionisation, of charged particles along their flight path. The energy E of a charged particle required to ionise gas molecules along the distance x is called specific energy loss and is usually expressed as the differential quantity dE/dx . In high energy physics the specific energy loss is in general small ($\mathcal{O}(\text{keV/cm})$) compared to the kinetic energy of the particle ($E_{\text{kin}} > 1 \text{ GeV}$).

The amount of charge collected at the readout depends on the intensity of the applied electric field inside the chamber. At some low voltage the recombination of electrons and ions is overcome, but no gas amplification occurs; a detector in this mode is called an *ionisation chamber*. As the voltage is increased the primary ionisation electrons cause *electron avalanches*: the accelerating electric field is high enough to impart to the primary electrons an energy higher than the first ionisation potential of the gas. These electrons then produce electron-ion pairs while continuing along their path; the secondary electrons may, in turn, form further pairs. This phenomenon is called *gas multiplication*. If space charge (owing to the longer-lived positive ions) remains negligible and the accumulated charge is proportional to the energy loss of the particle, the chamber is said to operate in *proportional mode*. At higher voltages the accumulated space charge may change the effective electric field in a way that the signal is no longer strictly proportional to the initial ionisation, this region is called *limited proportionality*. Further increase of the electric field leads finally to electric breakdown of the gas. This takes place when the space charge inside the avalanche is strong enough to shield the external field. A recombination of ions then occurs, which results in photon emission and thus secondary ionisation with new avalanches. If this process propagates, a chamber is said to work in the *Geiger-Müller mode*.

Avalanche electron multiplication is essential in all gaseous detectors, in order to produce an electrical signal of sufficient amplitude to be further processed by the readout electronics. In conventional chambers working in proportional mode, the corresponding high electric field is produced near a thin *sense wire* which has a high voltage applied to it and at the same time is used to read out the accumulated charge.

1.2 Detector Gas

In principle all gases can be used for generating electron avalanches if the electric field in the amplification region of the detector is strong enough. However, depending on the mode of operation and the intended use of the chambers, specific requirements towards, e.g. signal proportionality, high gain, or good drift properties limit the choice of gases or gas mixtures.

Multiplication occurs in noble gases at lower fields than in gases with complex molecules; the addition of other components increases the threshold voltage. This suggests the use of a noble gas as the main component of a chamber gas. However, noble gases do not allow operation at high enough gas gain without entering into permanent discharged operation: the atoms excited during the avalanche process return to the ground state emitting photons at high enough energies to initiate a new avalanche in the gas. This problem is solved by adding a *quenching gas* which absorbs energetic photons. Often organic gases are used, like isobutane (CH_3CHCH_3). Most organic compounds and alcohol families are efficient in absorbing photons in the relevant energy ranges. The molecules dissipate the excess of energy either by elastic collisions, vibration and rotation or by dissociation into simpler radicals. A small amount of polyatomic quencher added to a noble gas changes completely the operational characteristics of a chamber and may allow gas amplification up to 10^6 before discharge. A classical gas mixture for a proportional counter is P10 (90% Ar, 10% CH_4).

Special requirements apply to chambers with long drift distances (see next chapter); they include particularly good drift properties. Among them are a high gas purity, and a high drift velocity, if the chamber is to operate at high counting rates. For better spatial resolution, however, drift velocities should be lower in order to minimise the influence of timing errors on position resolution. Characteristic for this category of quenching gases is CO_2 with a relative low drift velocity.

In addition to the gases foreseen for a chamber, there will always be some contamination by impurities from outgassing structural materials or from the outside atmosphere through leaks. Even a minor contamination may have a large effect on the operation of the chamber. It can change the drift velocity, or drifting electrons can be lost due to attachment to oxygen molecules [7]; finally, the process of chamber ageing, i.e. deterioration of the chamber performance due to radiation [3,8], can be accelerated.

1.3 Diffusion

Diffusion occurs because drifting electrons or ions experience a thermal zitterbewegung and are scattered on the gas molecules. Hence, their drift direction deviates from the

average owing to the random nature of collisions. In the simplest case the deviation is the same in all directions, and a point-like cloud of electrons, e.g. electrons from primary ionisation, assumes, after having drifted some time, a Gaussian density distribution. It can be shown [3] that in the absence of a magnetic field the diffusion width σ of a charged cloud after travelling the distance L in an electric field \vec{E} is given by

$$\sigma^2 = \frac{2DL}{\mu|\vec{E}|}, \quad (1.1)$$

where D is the diffusion coefficient and μ the mobility of the charge carriers. In the case of electrons it is $\mu = \frac{e}{m}\tau$ with e and m being the charge and mass of the electron and τ the mean time between two collisions of the electron with a gas molecule.

In the case of the presence of a magnetic field \vec{B} , the longitudinal diffusion is given by Eq. 1.1, while the transverse diffusion is affected by the field, since \vec{B} forces the electrons to follow the arc of a circle. The corresponding transverse diffusion coefficient is given by

$$D_T(B) = \frac{D_0}{1 + \omega^2\tau^2}. \quad (1.2)$$

Here D_0 is the diffusion coefficient in the absence of a magnetic field, and ω denotes the cyclotron frequency with $\vec{\omega} = e\vec{B}/m$. Hence a large magnetic field can reduce the transverse diffusion by orders of magnitude owing to a large value of $\omega\tau$.

1.4 Signal Generation

Given the simple case of a proportional counter which consists of an anode wire (radius $\approx 10\ \mu\text{m}$) surrounded by a cathode cylinder (radius = several mm), the process of electron multiplication starts typically at less than $50\ \mu\text{m}$ from the anode surface. It appears that the whole process of multiplication takes place in less than 1 ns. In this time the electrons have been collected on the anode and the positive ions start to drift along a distance of $\mathcal{O}(\text{cm})$ towards the cathode. The detected signal, negative on the anode and positive on the cathode, is the consequence of the change in energy of the system owing to the movement of charges. Therefore the electron contribution to the total signal is very small (about 1%) while positive ions generate most of the signal.

The drift velocity of ions is, however, much smaller ($\approx 10\ \text{mm}/\text{ms}$) than the electron drift ($\approx 50\ \text{mm}/\mu\text{s}$), such that all ions are collected at the cathode after several $100\ \mu\text{s}$. The time growth of the signal is very fast at the beginning, as shown in Fig. 1.1. About half of the signal is developed after one thousandth of the total time. It is therefore usual to terminate anode and cathode with a resistor R such that the signal is differentiated with a time constant $\tau = RC$ with C being the capacitance of the counter. The figure shows additionally two examples of pulse shapes obtained by differentiation [6].

1.5 Drift Chambers

A drift chamber is an apparatus for measuring the space coordinates of the trajectory of a charged particle. In common for all drift chambers is that the drift of the ionisation

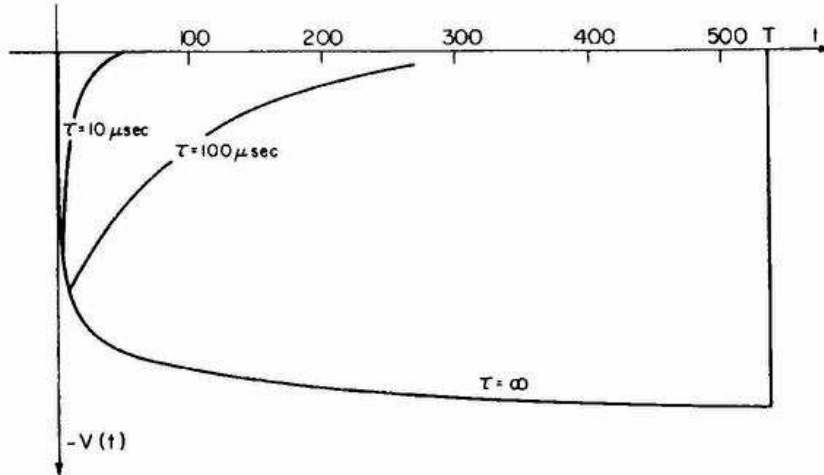


Figure 1.1: Time development of the pulse, $V(t)$, in a proportional counter; T is the total drift time (in μs) of positive ions from anode to cathode. The pulse shape obtained with several differentiation time constants is also shown. The plot is taken from [6].

electrons in the gas is used for a coordinate determination by measurement of the drift time.

The simplest drift chamber is ideally a sensitive volume placed across the path of a particle in order to measure the coordinates of the point of penetration. It was developed from the *Multi-Wire Proportional Chamber*, MWPC [9], basically a hodoscope of parallel wires working in proportional mode. By equipping the anode sense wires with electronics to measure the time of the avalanche pulse with respect to the time of incidence of the ionising particle (and hence the drift time of the electrons), the coordinate is measured. A schematic view of a simple drift chamber is shown in Fig. 1.2. Additional field-shaping wires, called *field wires*, are used to produce the desired shape for the electric field, e.g. a uniform drift field or a simple relation between drift time and distance.

Special drift chambers have been developed for colliding beam experiments: cylindrical geometry (with the axis along the beam pipe) enables a high angular coverage, such that a large fraction of the scattered particles traverses the sensitive volume. The additional presence of a magnetic field (parallel to the cylindrical axis) allows to measure the particle momentum, which is inversely proportional to the track curvature. Given enough ionisation measurement samples along the track, it is possible to determine the ionisation density ($= dE/dx$) to a degree useful for particle identification as will be described in Section 1.6.

Two prominent representatives of collider drift chambers are the *Time Projection Chamber* (TPC) and the *jet chamber*. Since studies for the TPC readout are presented in Section 3, and the analysis presented in Part II is based on jet chamber measurements, in the following, both drift chamber types are described.

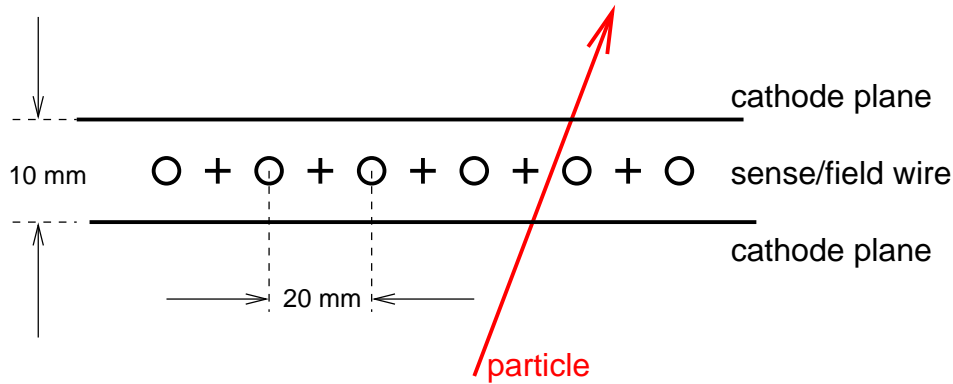


Figure 1.2: Disposition of the electrodes in the chamber [10].

1.5.1 Time Projection Chambers

A time projection chamber, first proposed by Nygren [11], consists of a large volume filled with the detector gas, which is enclosed by a field cage which creates the electric drift field, which should be as homogeneous as possible. The walls parallel to the direction of the drift are equipped with electrodes connected to a resistor chain creating a linearly degraded electric potential. Figure 1.4 shows a schematic side view of (one half of) a conventional TPC.

The drift volume is terminated on one side by a high voltage plane (cathode) and on the other side by the readout plane, which conventionally consists of a MWPC and readout pads connected to preamplifiers. This part of the TPC is usually called the *endplate*. The $x - y$ (or $r - \phi$ in cylindrical coordinates) plane of the coordinate system which is introduced normally, is parallel to while the z axis is orthogonal to the endplate. In the case of colliding beam experiments, the high voltage cathode is often located in the symmetry plane of the detector at the interaction point, orthogonal to the beam axis. The pads close the drift volume on both sides. Charged particles traverse the drift volume and create tracks of ionisation. Under the influence of the electric field the electrons drift towards the endplate. An electron avalanche is created close to the sense wires of the MWPC. Charges are induced on several adjacent readout pads which are each connected to a preamplifier. This induced charge distribution is called *pad response function*, PRF. The width of the PRF is one of the important parameters of a TPC since it is a direct measure of the power to distinguish between two close-by coordinates in the $r - \phi$ plane and therefore determines the *two-track resolution*. Figure 1.3 shows the PRFs for various pad sizes, denoted with Δ and a gap between pad plane and sense wires of $G = 4$ mm. Typical TPC two-track resolutions in $r - \phi$ are $0.5 - 1$ cm. The signal created on the wire can be used too, e.g. for the measurement of the specific energy loss.

Apart from the field and sense wires, the MWPC consists of two more wire grids above them: the *potential grid* serves to close the proportional cell and to separate it from the drift volume. This grid is held at the same potential as the pad plane and closes the volume of the proportional region. The function of the *gating grid*, located above the cathode grid, is as follows. The uniformity of the electric field is of prime importance in a TPC. Even if the field cage creates a homogeneous field, it can be destroyed by the

presence of space charge in the form of ions in the drift volume. The positive ions created together with the electrons in the primary ionisation process drift towards the high voltage electrode. These are generally not a concern as they represent only a small amount of charge. In contrast, the amount of positive ions created in the avalanche process at the sense wires is more important (the usual gas gain is in the order of $10^3 - 10^4$) and cannot be neglected. A large fraction of it is neutralised at the pad plane, the field wires and the cathode grid, but a part reaches the drift volume. Owing to their low drift velocity which is more than three orders of magnitude smaller than the velocity of electrons, the ions travel only slowly towards the high voltage plane. They could produce considerable space charge if entering the drift volume, and thus destroy the uniformity of the electric field. This so-called *ion feedback* can be reduced strongly by the gating grid which in its closed state prevents electric charges from traversing the grid. The gating grid consists of a layer of wires which are alternatively connected together. Figure 1.5 shows the electric field for the two states of the gating grid. For the “gate open” state the grid is at a potential given by its location, in order to not disturb the original drift field. For the “gate closed” state a potential difference between the two semi-grids is applied such that a dipole field is created which stops the ions of the avalanche process from travelling back into the drift volume.

The gating grid can be used in different modes: in the *asynchronous mode* counters outside the TPC select the wanted event and open the gate. Depending on the time delay between the moment of the event and the moment the gate has been opened, sensitivity is lost as the electrons drift toward the MWPC during this delay. The *synchronous mode* can avoid this loss, if there is a regular time pattern when the events occur, e.g. at a collider the gate is triggered “open” a few μs before every particle bunch crossing. When there is no event, the gate is switched back to “closed”, otherwise the gate stays open long enough to read the event.

Coordinate Reconstruction

In Fig. 1.3 it is clearly seen that for $\Delta \gg G$ (Δ = pad size, G = gap size) the charge is collected mainly by a single pad, which leads to a PRF with a wide flat maximum and Gaussian wings. In this case no precise single coordinate reconstruction is possible. For $\Delta \approx G$ the PRF becomes Gaussian in good approximation and the charge is spread over two or three adjacent pads. This allows to determine the centre of the distribution with a much better resolution than the pad width. A minimum pad size, however, is necessary to collect a sufficiently strong signal.

At the TPC of the ALEPH experiment [14] the PRF was found to be Gaussian in good approximation [15], the amplitude of the i th pad was assumed to be $P_i = A \exp[(x - x_i)^2/2\sigma_{\text{PRF}}]$. Then the ratio of the amplitudes P_i and P_{i+1} from a pair of adjacent pads was used to provide a coordinate

$$x = x_0 + \sigma_{\text{PRF}}^2 / [\Delta \times \ln(P_i/P_{i+1})] \quad (1.3)$$

in the range $x = x_0 \pm \Delta/2$ with x_0 being the mid-point of two adjacent pads. With growing number of involved pads, more sophisticated algorithms were used.

Apart from the PRF the $r - \phi$ single coordinate resolution is governed by

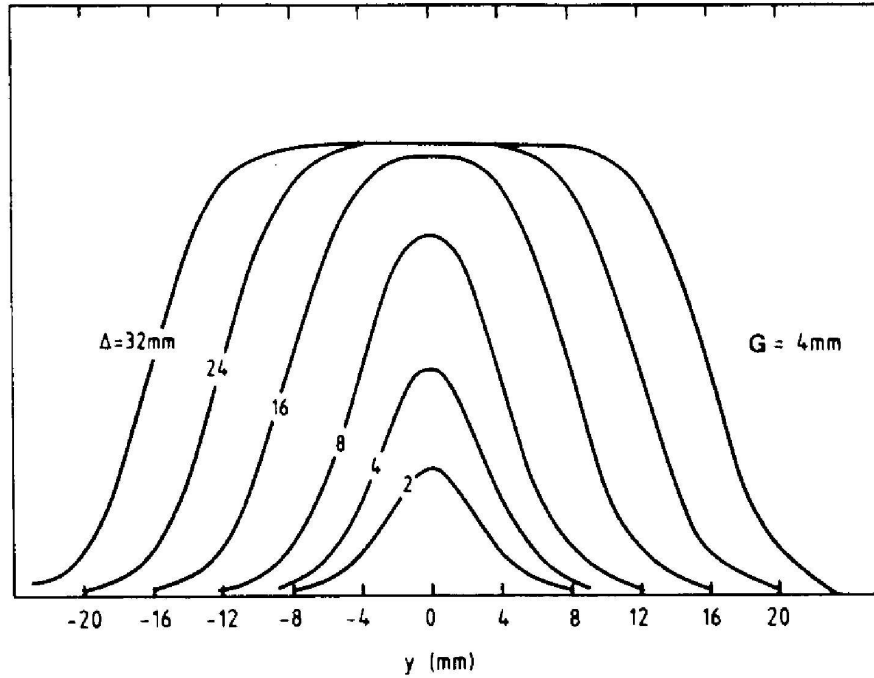


Figure 1.3: Shape of the charge distribution (in arbitrary units) along pad rows (y direction) for various pad sizes (called “ Δ ” in the figure). The distance between the sense wire plane and the pad plane is $G = 4$ mm [12].

- the transverse diffusion,
- the angle under which the tracks cross the wire and the pads, (*angular wire and angular pad effect*),
- the $\vec{E} \times \vec{B}$ effect: close to the wires the electric field is no longer parallel to the magnetic field, and electrons drifting in this region experience a significant transverse movement. This can result in a broadening of the electron cloud.

Typical TPC $r - \phi$ resolutions are $\sigma_{r-\phi} \approx (200 - 400) \mu\text{m}$ (ALEPH TPC [16]).

The z coordinate is determined by measuring the drift time of the primary electrons. Apart from the fluctuations in the primary ionisation, the z single point resolution depends mainly on

- the longitudinal diffusion and
- the sampling rate, i.e. the number of recorded “pictures” per time unit, which determines the width of a so-called *time slice*.

Typical TPC z resolutions are $\sigma_z \approx (0.7 - 1.7) \text{ mm}$ (ALEPH TPC [16]).

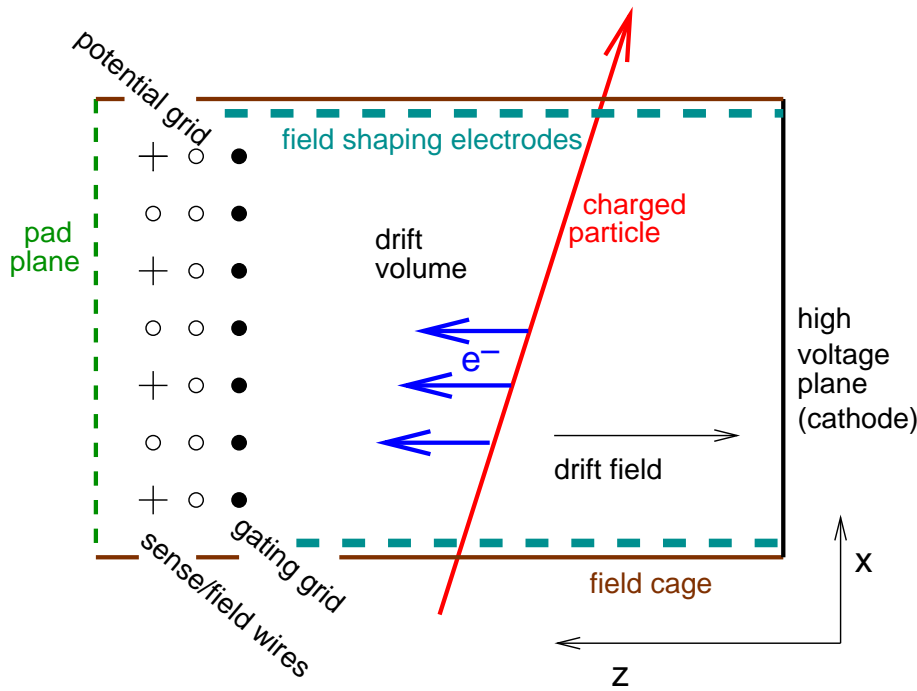


Figure 1.4: Schematic side view of a time projection chamber (TPC).

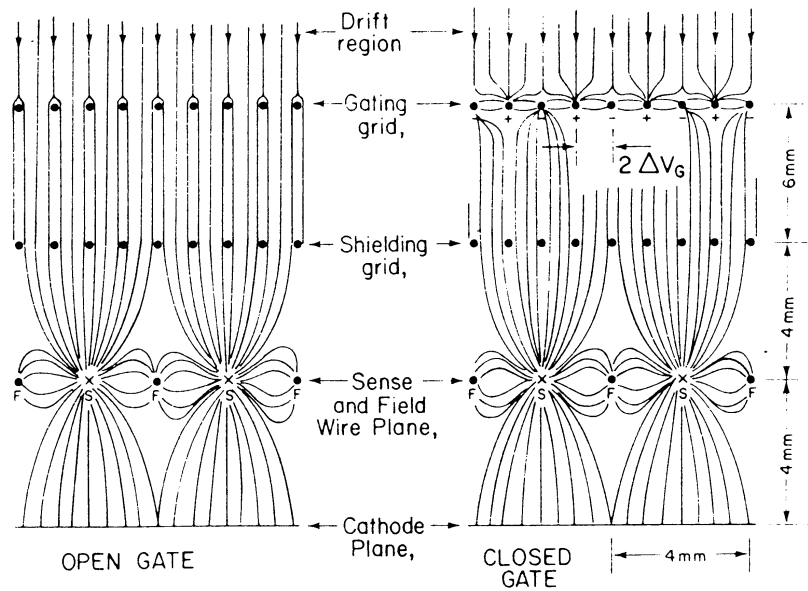


Figure 1.5: Electric field lines with the gate in “open state” and in “close state” [13].

1.5.2 Jet Chambers

In jet chambers, the cylindrical volume consists of multiple independent cells or sectors, each with a single sense wire plane. Figure 1.6 shows a schematic picture of a jet chamber including the usual choice of the coordinate system; one sector containing both sense and field shaping wires is displayed in more detail. Often the drift on both sides of the wire is used. Measuring the drift time leads therefore to a left-right ambiguity of the coordinate, which can be resolved by staggering the wires so that wrongly assigned hits will not result in a smooth track during the reconstruction of particle paths. The drift direction in a jet chamber is roughly perpendicular to the wire plane. Figure 1.7 contains a schematic view of a single jet chamber sector including drift trajectories, lines of equal drift time (isochrones) and the staggered position of the sense wires.

Owing to their two-track resolution capability (1 mm – 3 mm) jet chambers are especially suited to reconstruct *particle jets*, i.e. particles produced in highly collimated form.

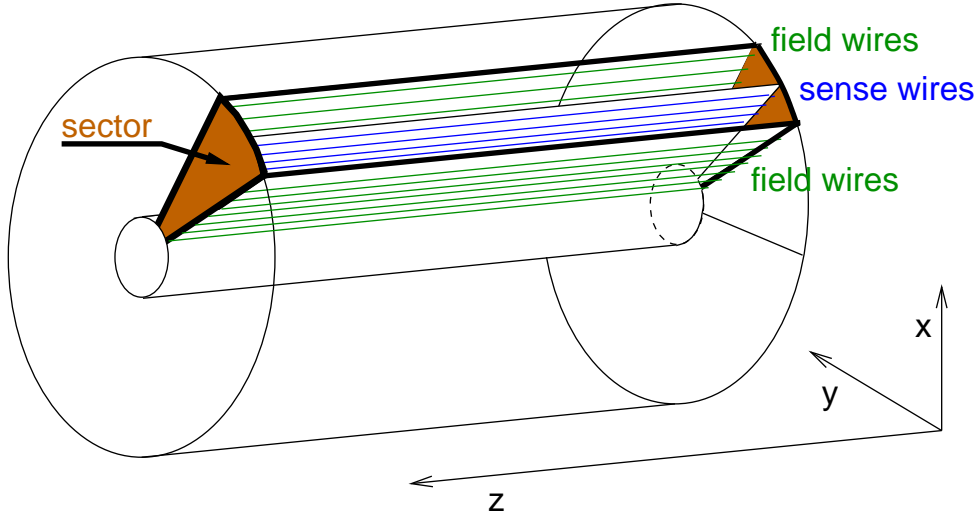


Figure 1.6: Schematic picture of a jet chamber.

Coordinate Reconstruction

In the $r - \phi$ plane, space points can be calculated in a sector reference frame (which differs in general from the coordinate system of the entire chamber) with the \tilde{x} axis along the sense wire plane according to [18]

$$\begin{aligned}\tilde{x} &= \tilde{x}_w - v_D \cdot \sin \alpha_L \cdot t + \text{corrections}, \\ \tilde{y} &= v_D \cdot \cos \alpha_L \cdot t + \text{corrections}.\end{aligned}\tag{1.4}$$

Here \tilde{x}_w denotes the \tilde{x} coordinate of the anode wire, and t the measured drift time. A homogeneous drift field, and a constant drift velocity v_D is assumed over the whole sector (except near the anode wires). The Lorentz angle α_L is the angle by which the electrons moving in the electric field are deflected due to the effect of the magnetic field. (for

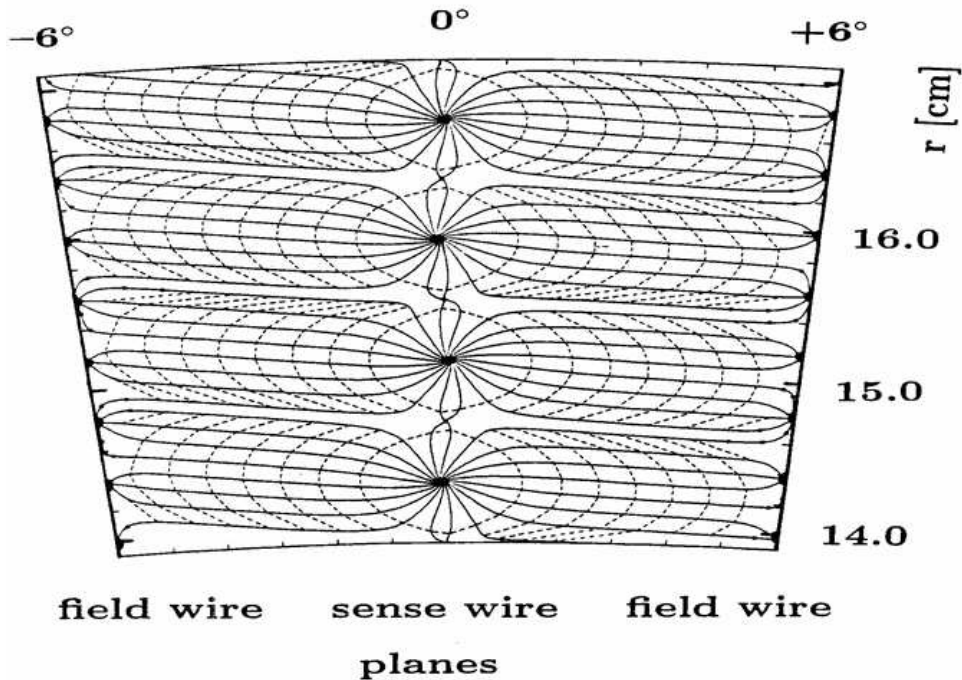


Figure 1.7: Drift lines in a sector of the Crystal Barrel jet chamber [17]. The drift isochrones (dashed lines) are equally spaced at time intervals of 0.2 ms.

the OPAL jet chamber [18]: $\alpha_L \approx 20^\circ$). Corrections are applied in order to account for various sources affecting the coordinate information, e.g. distortions of the electric field and sagging of the wires owing to gravitation. Apart from gas properties like diffusion, the $r - \phi$ point resolution depends on

- the good knowledge of the Lorentz angle and
- the exact considerations of the corrections.

At the OPAL jet chamber for example, a single $r - \phi$ point resolution of $\sigma_{r-\phi} = 135 \mu\text{m}$ was found averaging over all drift distances.

A frequently used method to measure the z coordinate in a jet chamber is *charge division* (or *charge sharing*): from the charges Q_L and Q_R of the two pulses arriving at the amplifiers at both ends of each wire, the z coordinate is given by [18]

$$z = \frac{l_{\text{eff}}}{2} \frac{g_Q Q_L - Q_R}{g_Q Q_L + Q_R}. \quad (1.5)$$

Here l_{eff} is the effective wire length including both the anode wire resistance (for OPAL: $175 \Omega/\text{m}$) and the input impedance of the amplifiers, and g_Q is the relative gain given by the ratio of the amplification of the amplifiers on each side.

Typically, z resolutions of jet chambers are much worse than in $r - \phi$. At OPAL σ_z was found to be $(4.5 - 6.0) \text{ cm}$.

1.5.3 Discussion

Compared to other competing detector technologies used for tracking in high energy physics, e.g. different kinds of silicon detectors, drift chambers offer a variety of advantages. Some of them are the large number of measured space points per track, i.e. $\mathcal{O}(100)$, which yields efficiencies up to 99% in pattern recognition and track finding, very low material budget reducing multiple scattering, and good multi track capability. In addition, particle identification by measuring the specific energy loss of charged particles can be carried out. Section 1.6 is dedicated to this topic.

Depending on the specific application, these advantages outweigh the moderate two-track capability and the relatively poor single hit resolution of gaseous drift chambers compared to silicon detectors. This holds true particularly due to the fact that at modern particle detectors, tracking is performed including information of additional devices, such as silicon layers close to the interaction point (microvertex detector), which provide the necessary accuracy in point resolution (Section 5.3).

Compared to a jet chamber, a TPC offers the big advantage, that it provides high quality three dimensional space points with no ambiguities, whereas the poor z resolution of a jet chamber requires in general additional devices providing better z information in order to perform robust three dimensional tracking. However, because of the long drift distance, the applied drift voltages are high (several 10 kV), and the field must be very homogeneous.

1.6 Measurement of the Specific Energy Loss dE/dx

In TPCs and jet chambers the measurement of the specific energy loss is often used for particle identification [3, 4, 19]. The average specific energy loss dE/dx can be described by the *Bethe-Bloch equation*:

$$-dE/dx = K z^2 \frac{Z}{A} \frac{1}{\beta^2} \left(\frac{1}{2} \ln \frac{2m_e c^2 \beta^2 \gamma^2 T_{\max}}{I^2} - \beta^2 - \frac{\delta}{2} \right), \quad (1.6)$$

with

$$T_{\max} = \frac{2m_e c^2 \beta^2 \gamma^2}{1 + 2\gamma m_e/M + (m_e/M)^2}.$$

The variables are:

E	= energy of the ionising particle,	Z	= atomic number of the gas,
x	= path length,	A	= atomic weight of the gas,
c	= speed of light,	I	= mean excitation energy,
β	= v/c = velocity of the particle,	δ	= density correction,
z	= charge of the ionising particle,	m_e	= electron mass,
M	= mass of the ionising particle,	γ	= $\sqrt{1 - \beta^2}$.

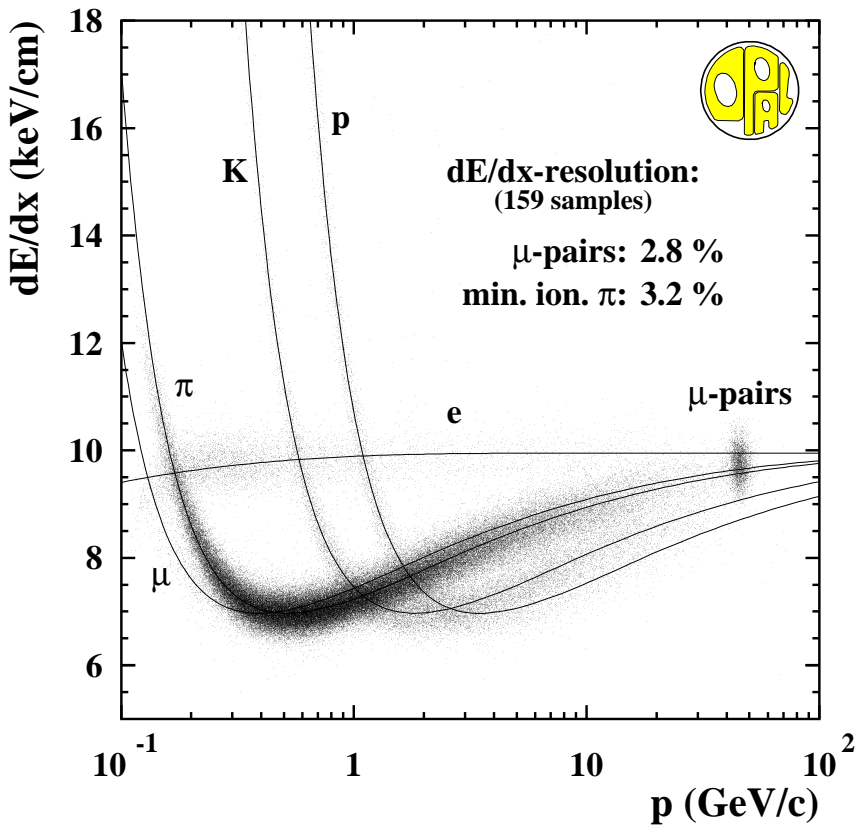


Figure 1.8: This scatter plot shows the measured dE/dx for multihadronic tracks and muon pairs together with the expected functional from. The dE/dx resolution for minimum ionising pions within multihadrons and muon pairs with 159 hits used for dE/dx measurement is also indicated.

The energy loss as a function of $\beta\gamma$ shows a characteristic decrease with $1/\beta^2$, reaches a minimum around $\beta\gamma = 3$, and continues with a logarithmic rise, until reaching the *Fermi plateau*. Figure 1.8 shows the measured and expected specific energy loss recorded with the OPAL detector at the LEP e^+e^- storage ring. The Bethe-Bloch equation is a universal function of $\beta\gamma = p/m$ (p = particle momentum, m = particle mass) for all particles except electrons. For different particle masses the energy loss function separates as a function of the particle momentum $dE/dx(p)$.

Measurement method

A charge measurement on a sense wire provides a sample for the determination of the specific energy loss. Generally a charged particle produces many samples along its ionisation path. As can be seen in Fig. 1.9, these samples are Landau distributed: the peak is caused by *soft collisions* of the particle with the (gas) molecule as a whole and with low energy transfer while the long tail, the *Landau tail*, is due to hard collisions or creation of delta electrons with large energy transfer [20, 21].

A significant fraction of the highest measured energy loss samples are rejected (at

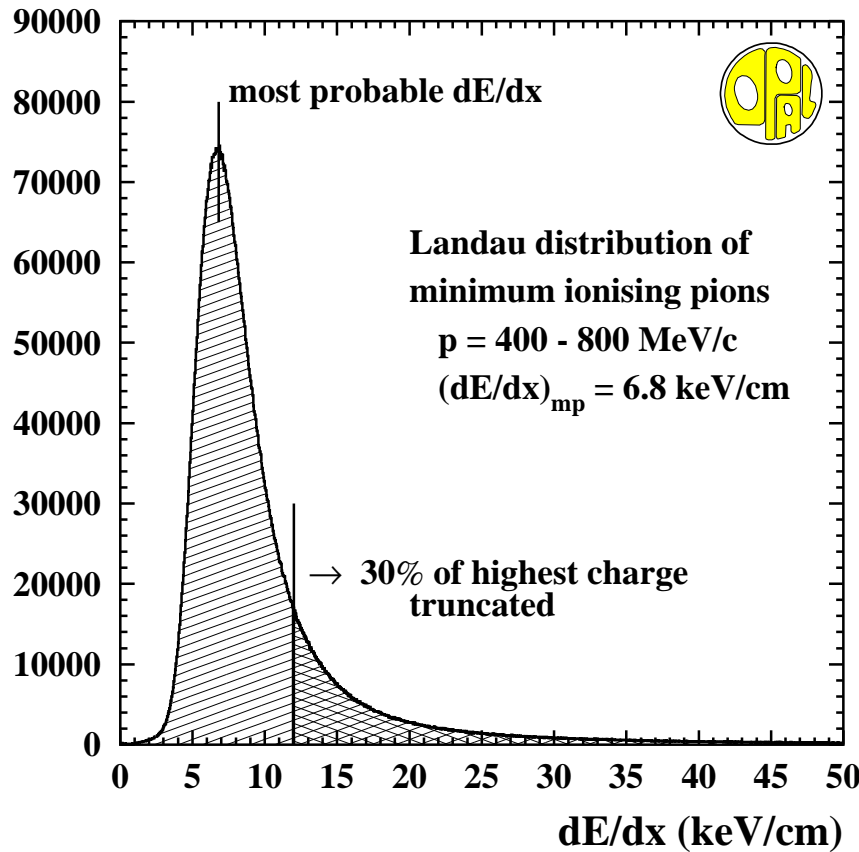


Figure 1.9: Landau distribution for minimum ionising pions. The most probable value is about 6.8 keV/cm. In order to determine the average energy loss from a couple of dE/dx samples the method of truncated mean is used (see text). At OPAL, the 30% highest energy loss samples are rejected and not used to calculate the average energy loss.

the OPAL jet chamber: 30%) and the mean energy loss dE/dx is then calculated as the mean of the remaining energy fraction of the samples. Using this method, called *truncated mean*, the Gaussian-like peak originating from soft collisions is essentially taken for the dE/dx measurement. However, for very few samples the presence of the Landau tail cannot be completely suppressed and becomes visible more and more. Figure 1.10 shows the measured dE/dx distribution, recorded with the OPAL jet chamber, for 2, 10, 20 and 40 dE/dx measurement samples along a track, respectively, together with a Gaussian fit. Both for 2 and 10 measurements the Landau tail is prominent making any particle identification probability based on Gaussian distributed measurements unreliable. At 20 and 40 samples the Landau tail starts to disappear and the distributions are more Gaussian-like leading to more reliable particle identification.

dE/dx resolution and separation power

The dE/dx resolution depends mainly on three quantities [20, 21]:

- number of samples N ,

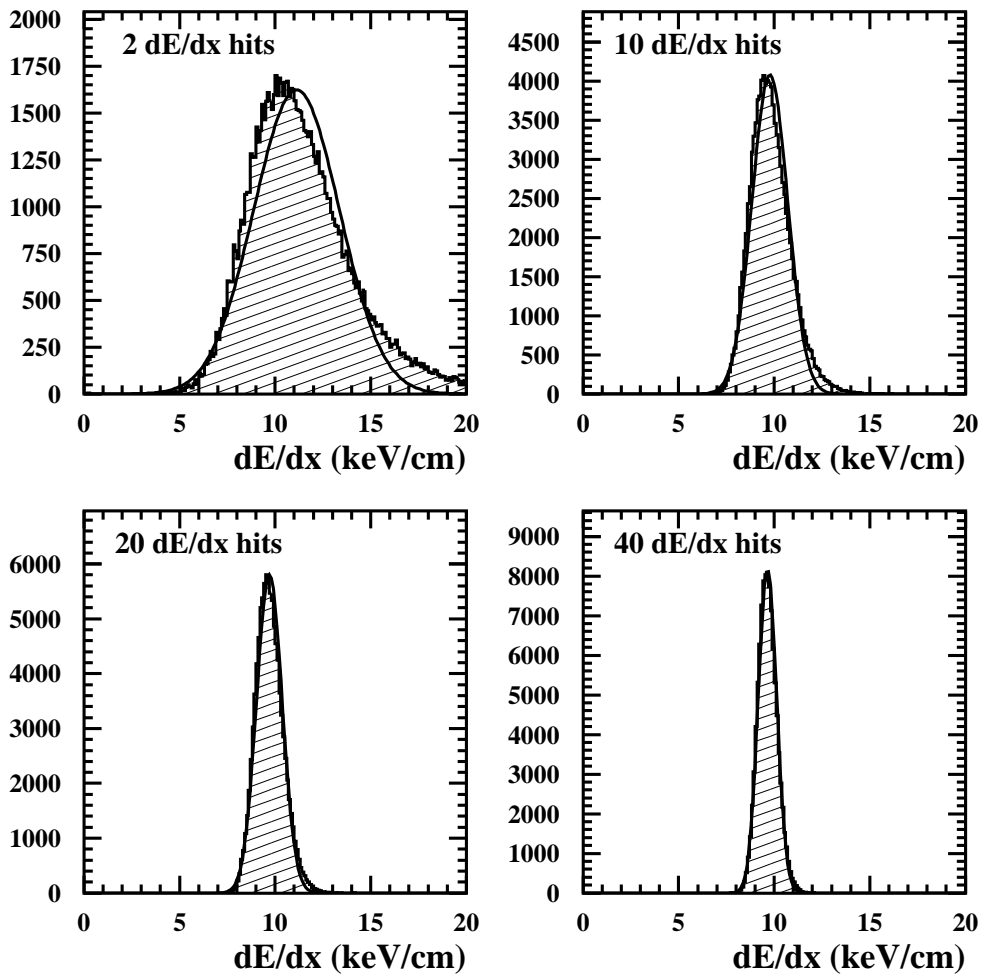


Figure 1.10: Measured dE/dx distribution (truncated mean, see text) for 2, 10, 20, and 40 dE/dx measurements per track, respectively, together with a Gaussian fit. The plots are taken from [21].

- effective sampling length l (thickness \times pressure),
- gas mixture.

For a given gas mixture a better resolution might be obtained by increasing the pressure. The figure of merit which has to be optimised, however, is not the resolution but the particle separation power between two particle species A and B defined as:

$$\text{separation power} = \frac{\text{separation}}{\text{resolution}} = \frac{dE/dx(A) - dE/dx(B)}{\sigma(dE/dx)_{A,B}}. \quad (1.7)$$

Here $\sigma(dE/dx)_{A,B}$ is the average dE/dx resolution for the two particle species. For commonly used drift chamber gases, the optimum value for the separation power was found to be at a pressure of two to four bar [22, 23].

The momentum dependence of the separation power depends on various gas and detector parameters. The typical separation power is of the order of only a few σ for momenta

above 2 GeV, which inhibits an identification of particles on an individual track by track basis and statistical methods have to be used.

Both at the ALEPH and OPAL experiments a separation power for $e - \pi$ separation of more than 2σ up to ≈ 14 GeV was achieved for tracks in multihadronic events. At OPAL the $2\sigma \pi - K$ separation reaches 21 GeV in multihadrons and 40 GeV for single isolated tracks. The $K - p$ separation does not achieve the 2σ level (for OPAL: $\approx 1.5\sigma$ and for ALEPH: $\approx 1\sigma$). Nevertheless, some enrichment of signal events and reduction of background is possible if the systematics of the energy loss measurement is kept under control.

Some major applications of the measurement of the specific energy loss are

- exclusive reconstruction of mesons and baryons,
- differential cross-section measurements for different hadron species,
- flavour tagging of heavy quarks,
- search for exotic particles with anomalous energy loss (Part II of this thesis).

Chapter 2

The Linear Collider Project

The studies presented in this part of the thesis are carried out for the planned linear e^+e^- collider TESLA, which is being developed by an international collaboration. A detailed description of TESLA can be found in [24–27]. The collider is planned to run at centre-of-mass energies of up to 800 GeV. Apart from TESLA, there are the linear collider projects NLC (Next Linear Collider) [28] and JLC (Japan Linear Collider) [29], which have a similar goal with a different accelerator technology.

2.1 The Accelerator

At the planned energies the accelerated electrons cannot be stored like in a storage ring, because the energy loss owing to synchrotron radiation would exceed any reasonable amount. One of the main challenges for linear collider projects is to provide anyhow a sufficient high luminosity while operating at centre-of-mass energies ranging from the Z pole, i.e. 91 GeV, up to $\mathcal{O}(1 \text{ TeV})$. Figure 2.1 shows a schematic picture of the planned TESLA linear collider layout. The overall length is 33 km. A second interaction region, possibly for $\gamma\gamma$ collisions, is planned in addition.

In contrast to the other linear collider projects, TESLA is based on superconducting accelerator structures (cavities). This has the advantage of very small power loss, and it allows to operate the accelerator at a rather moderate frequency of $f = 1.3 \text{ GHz}$. (NLC and JLC operate at $f \approx 11 \text{ GHz}$ with room temperature cavities). Higher operating frequencies lead in general to smaller cavities with larger accelerating gradients. However, smaller cavities require tighter alignment tolerances and cause strong *wakefields*. This term refers to electromagnetic fields induced by the accelerated charges, which act back on the electron beam and can spoil its quality by increasing the energy spread and the beam size. As these effects decrease strongly with increasing distance between the beam and the surrounding cavity walls, wakefields are much weaker in larger cavities working at lower frequencies.

The superconducting cavities allow for rather long pulses, i.e. 1 ms, with a relatively large space between two electron bunches, i.e. 337 ns. A total of 2820 bunches are combined in one so-called *bunch train*, and the train repetition rate is 5 Hz at TESLA. The beam dimensions at the interaction point (IP) are $(500 \times 5) \text{ nm}$, which allows a luminosity of $\mathcal{L} = 3 \cdot 10^{34} \text{ cm}^{-2} \text{s}^{-1}$. A summary of some technical parameters can be found in Ta-

ble 2.1 including a comparison with the parameters of the LEP storage ring. More details concerning the TESLA accelerator technology can be found in [25].

In parallel to the TESLA linear collider an X-ray free electron laser laboratory has been developed based on the same accelerator technology.

	TESLA	LEP	
\sqrt{s}	500	208	GeV
\mathcal{L}	$3 \cdot 10^{34}$	$1 \cdot 10^{31}$	$\text{cm}^{-2}\text{s}^{-1}$
IP beam sizes (x,y)	553, 5	200 000, 2 500	nm
bunch spacing	337	22 000	ns
bunch charge	$2.0 \cdot 10^{10}$	$3.0 \cdot 10^{11}$	$1/e$

Table 2.1: Comparison of TESLA and LEP machine parameters.

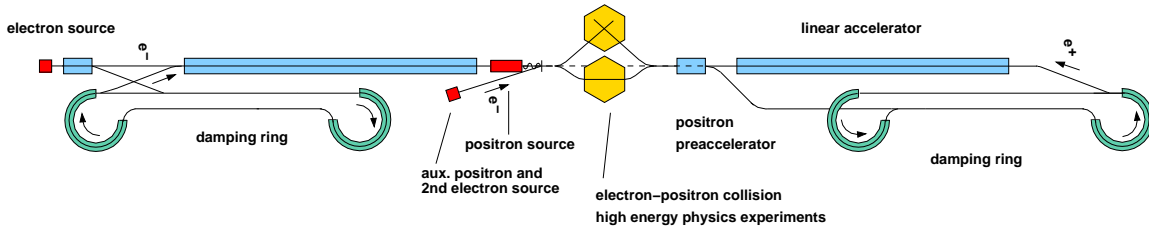


Figure 2.1: Schematic of the overall layout of the TESLA linear collider.

2.2 Detector Requirements and Concept

The general goal of a particle detector in a collider experiment is the reconstruction of all particles produced in the particle interaction. In order to meet this task, the detector has to fulfil several requirements: coverage of as much as possible of the complete solid angle (hermeticity), identification of charged particles via their momentum, charge and specific energy loss and tagging of particles produced in the close neighbourhood of the primary interaction point, i.e. at a *secondary vertex*. Additional information provided by the calorimeters, the electromagnetic and hadronic energy, supports particle identification, and can be used in the so-called *energy flow*. This technique combines the information from tracking and calorimetry to obtain an optimal estimate of the flow of particles and of the original parton four-momenta. Further subdetectors outside of the calorimeters are dedicated to identify muons exploiting their minimum ionising character. The measurement of the absolute luminosity is carried out via a well known reference process, e.g. Bhabha scattering. Additional devices are used to measure the beam energy and the beam polarisation.

The physics programme at a linear collider, in particular, mandates a detector capable of precision measurements, in order to fully exploit the discovery potential, where new

physics can be detected either directly or by measuring deviations from the Standard Model prediction. The vertex detector is primarily optimised to reconstruct secondary vertices in b - and c -decays. An optimal resolution requires to build the first layer of the detector as close as possible to the interaction point. A high track finding efficiency is required for the main tracker as well as the capability to reconstruct non-standard physics events like charged particles with an intermediate lifetime causing so-called *kinked tracks* and heavy stable charged particles (see part II of this thesis). In order to reconstruct the Z line shape with its natural width, the resolution of the transverse momentum, p_t , of the whole tracking system must be $dp_t/p_t^2 \leq 6 \times 10^{-5} \text{ GeV}^{-1}$ (at OPAL: $dp_t/p_t^2 \approx 1.3 \times 10^{-3} \text{ GeV}^{-1}$, at ALEPH: $dp_t/p_t^2 \approx 0.6 \times 10^{-3} \text{ GeV}^{-1}$).

Both tracking and calorimetric systems have to fulfil high requirements since a precise measurement of energy flow objects is crucial for the reconstruction of complex final states. The subdetectors must have high 3-D granularity to enable an energy flow algorithm which

- resolves energy depositions of almost overlapping objects, e.g. jets,
- combines redundant measurements properly, e.g. electrons measured in the tracking device and in the electromagnetic calorimeter,
- resolves photon conversions in the tracker volume
- reconstructs non-standard physics events, e.g. *non-pointing photons*, i.e. photons not originating from the primary vertex.

The TESLA detector [27] is designed in order to meet these requirements. A schematic view of one of its quadrants is shown in Fig. 2.2. Starting at the e^+e^- interaction point the TESLA detector consists of

- **the tracking system.** It comprises several devices: the vertex detector (VTX) is located close to the beam pipe. Several technologies are being discussed, i.e. CCD, CMOS, DEPFET and hybrid pixels. A TPC forms the main tracking device. It will be described in detail in Section 2.3. Two additional layers of silicon between vertex detector and TPC are planned in order to improve the momentum resolution: the silicon intermediate tracker, SIT. On both ends of the TPC straw tubes serve as forward chambers, FCH. With an additional precise measurement at this position, the FCH will compensate the degrading track reconstruction performance at low scattering angles and addresses the problem of material in the endcap. The tracking system is surrounded by
- **the calorimeter system.** It consists of the electromagnetic and hadronic calorimeter, ECAL and HCAL. Both feature high granularity suited to efficiently separate the contributions of different particles. Their performance is not degraded by a huge amount of dead material because
- **the magnet** is located outside the calorimeters. It provides a magnetic field of 4 T;
- **the muon system** is the outermost part of the detector. Apart from muon identification, it serves as return yoke for the magnetic flux.

For a full coverage down to very small angles, additional detectors are located in

- **the forward region.** Its main constituents are the low angle tagger, LAT, which covers angles down to approximately 28 mrad, and, mainly for luminosity measurements, the luminosity calorimeter, LCAL, which is sensitive down to angles of roughly 5 mrad. One on hand, both detectors are designed for particle detection, on the other hand, they serve as particle shields against the special beam-induced background environment at TESLA [25].

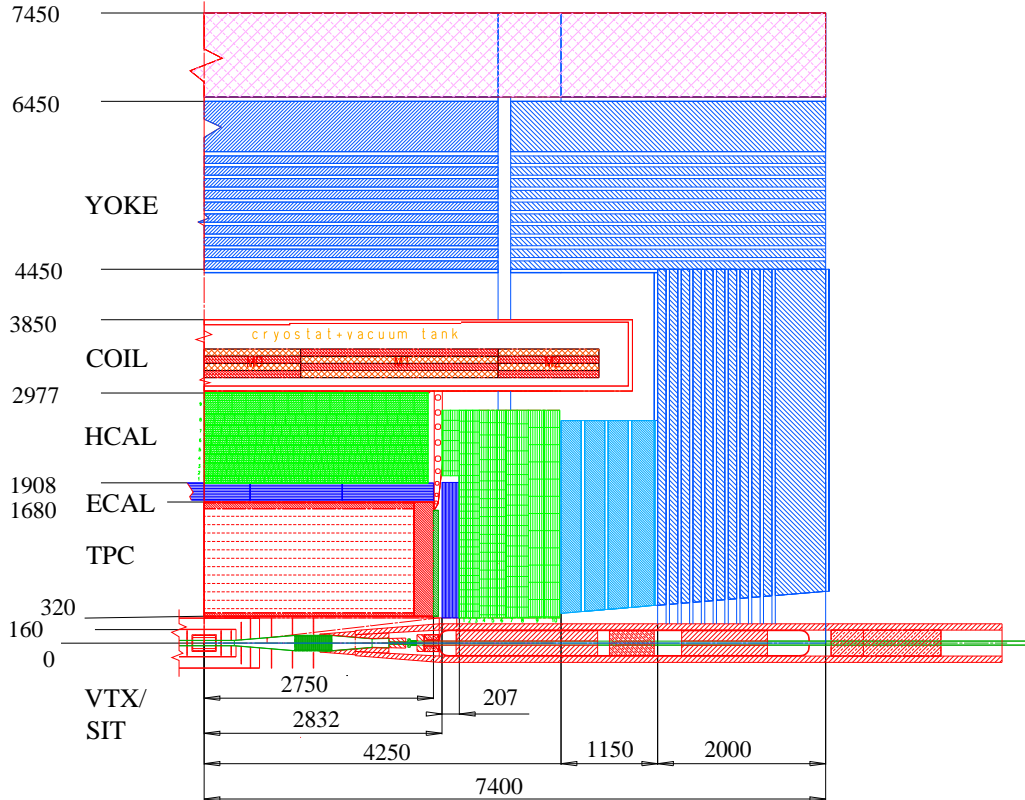


Figure 2.2: Schematic picture of a quadrant of the TESLA detector as proposed in [27]. Dimensions are in mm.

2.3 The Linear Collider TPC

The TPC is chosen as the central tracking device because it has a number of advantages to other options, as described in Section 1.5.3. Especially the large number of unambiguous three dimensional space points along a track is crucial. It has to be taken into account that events from many bunch crossings are superimposed while the whole drift volume is read out. In the case of the TESLA bunch structure the timing information from the TPC will be sufficiently precise to disentangle events from different bunch crossings.

The overall layout of the TESLA TPC including the other central tracking devices is shown in Fig. 2.3. The inner (outer) radii of 32 cm (170 cm) are given by geometrical constraints (beam focusing magnets, shielding system against beam-induced background, calorimeters), and the requirement that the desired momentum resolution of $\delta p_t/p_t^2 < 2 \cdot 10^{-4} \text{ GeV}^{-1}$ (TPC only) and a dE/dx resolution of better than 5% can be reached. The TPC will be divided into two separate drift regions which share one cathode, the central membrane. Endplates will be mounted on both sides at a distance of roughly 250 cm from the interaction point. Assuming a readout pad size of $2 \times 6 \text{ mm}^2$ each endplate will be equipped with approximately 600 000 readout channels. The main mechanical parameters of the proposed TPC are listed in Table 2.2.

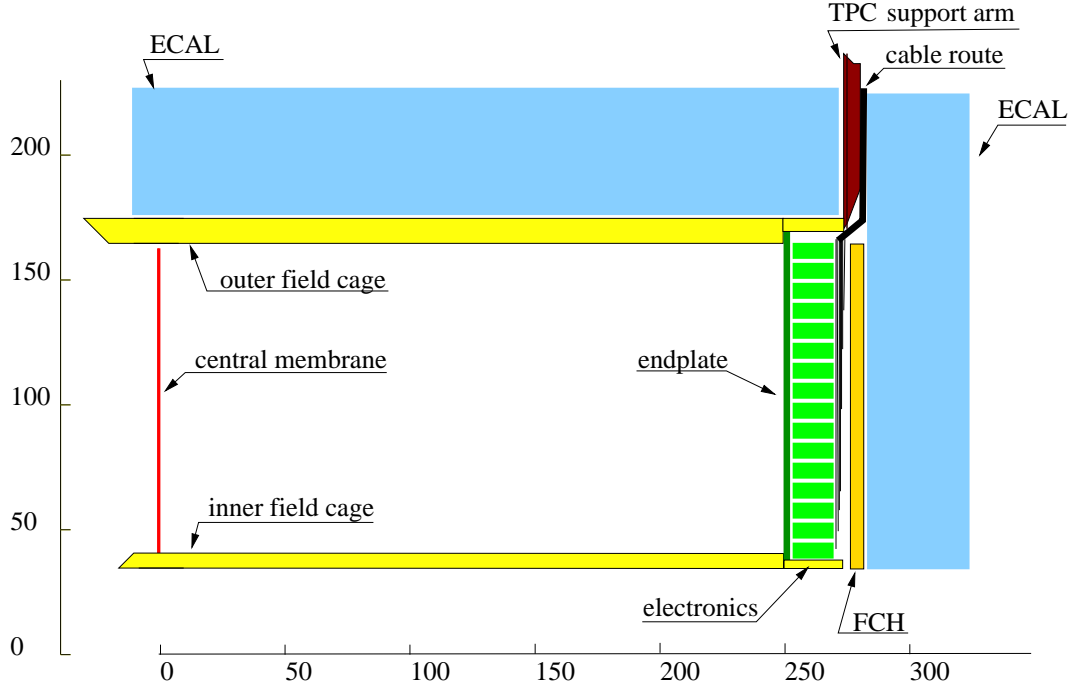


Figure 2.3: General layout of one quarter of the central tracking devices. The displayed dimensions are in cm.

mechanical radii	320 mm inner, 1700 mm outer
overall length	$2 \times 2730 \text{ mm}$
radii of sensitive volume	362 mm inner, 1618 mm outer
length of sensitive volume	$2 \times 2500 \text{ mm}$
weight	$\approx 4 \text{ t}$
gas volume	38 m^3
radiation length	$\approx 0.03 X_0$ to outer field cage

Table 2.2: List of main mechanical parameters of the TPC.

The drift gas which is considered to be a good candidate for the TESLA TPC is a three component mixture of Ar-CO₂-CH₄ (93 : 2 : 5)%. It is a promising candidate owing to the sum of its properties: this mixture has an acceptable drift field of 230 V/cm for a reasonable drift velocity (4.6 cm/μs), thus limiting the total voltage at the cathode to around 60 kV, while the time to completely empty the drift volume is around 55 μs, or 160 bunch crossings in TESLA. The diffusion coefficient for this mixture is $D_{L(T)} = 300(70) \mu\text{m}/\sqrt{\text{cm}}$ at a magnetic field of 4 T. The neutron cross-section is smaller relative to the gases of the LEP tracking chambers due to the reduced amount of hydrocarbon as quencher, thus reducing the number of spurious hits in the TPC from beam-induced neutron background [30]. Finally the aging properties for gases with small hydrocarbon concentrations are also better than for those with large ones, though at the levels of backgrounds expected at TESLA this is not expected to be of major concern. However other gases are under investigation as well, such as Ar-CH₄ and Ar-CF₄.

The TPC has been simulated using the BRAHMS programme [31, 32] based on the simulation tool GEANT [33] to evaluate its performance. Important numbers are the single point resolution in $r - \phi$ ranging from 70 μm at 10 cm drift distance up to 190 μm at 200 cm drift distance. The corresponding z resolution ranges from 0.6 mm to 1 mm. The achievable dE/dx resolution is 4.3% for 200 pad rows and the $\pi - K$ separation is larger than 2σ for momenta between 2 GeV and 20 GeV. All main results of the simulation are summarised in Table 2.3.

	Drift distance	
	10 cm	200 cm
$r - \phi$ resolution	70 μm	190 μm
z resolution	0.6 mm	1 mm
double pulse resolution in $r - \phi$		≤ 2.3 mm
double pulse resolution in z		≤ 10 mm
dE/dx resolution	4.3% for 200 pad rows	
$\pi - K$ separation		> 2σ between 2 and 20 GeV
momentum resolution ($ \cos \theta < 0.75$)	$1.4 \times 10^{-4} \text{ GeV}^{-1}$	
momentum resolution ($ \cos \theta \approx 0.90$)	$3.2 \times 10^{-4} \text{ GeV}^{-1}$	

Table 2.3: Summary of key performance figures of the central tracker from a full simulation.

2.3.1 GEM Readout

In conventional TPCs avalanche electron multiplication is caused by high electric fields generated near thin wires of a MWPC, and the signals are read out with a system of pads (see Section 1.5.1). This technology is accompanied by several shortcomings like a non negligible $\vec{E} \times \vec{B}$ effect and the angular wire effect (i.e. the dependence of the resolution on the projected angle between track and wires) as well as significant ion feedback without gating.

An attractive alternative to a wire chamber readout is based on *Micro Pattern Gas Detectors*, MPGDs, such as *Gas Electron Multipliers*, GEMs [34, 35].

A GEM consists of a thin polymer foil, metal coated on both sides, and perforated by a high density of small holes, typically $\mathcal{O}(100\text{ }\mu\text{m})$ apart. An electron microscope view of the GEM surface is displayed in Fig. 2.4. An appropriate potential difference between the two conducting sides generates a strong field, typically 80 kV/cm , in the small holes where avalanche amplification of the drifting electrons occurs. A large fraction of the electrons drifting to the GEM from the TPC volume are tunnelled into these holes, amplified and transferred by the electric field to the readout electrodes. A schematic view of a GEM and how it could be used in a TPC is shown in Fig. 2.5. Often two or three GEMs are used in cascade in order to increase the total gain while operating at moderate voltages and hence reducing the probability of electric discharges (sparks). The gas gain of a multi GEM structure is close to the product of the gas gain of each individual GEM [35]. The charge produced in the avalanche in the GEMs is collected by readout pads located typically $(1 - 5)\text{ mm}$ behind the last GEM.

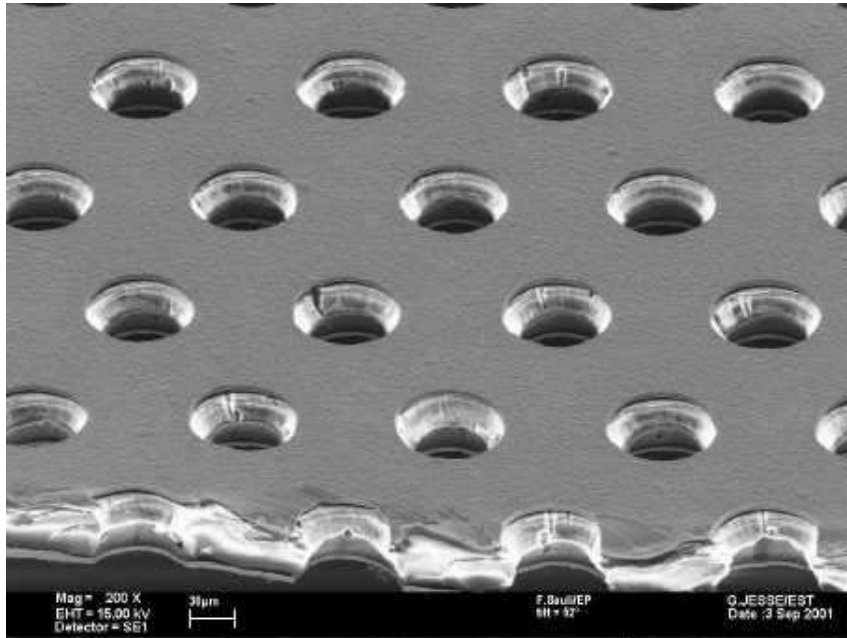


Figure 2.4: Electron microscope view of a GEM foil [36].

As the signal is created mainly by electrons rather than by slow ions the intrinsic time resolution of a GEM equipped TPC is orders of magnitudes better than in the case of wire chamber readout. In addition, the narrow electron charge cloud allows in principle a more precise determination of the position of the primary charge. But, as the total number of readout channels is limited, which leads to the proposed pad size of $2 \times 6\text{ mm}^2$, it may happen, that the charge after amplification is collected on a single pad as demonstrated in Fig. 2.6, left side. In this case the expected point resolution is around $2\text{ mm}/\sqrt{12}$. The induced signals on neighbouring pads are very small compared to wire chamber based readout systems, where the induced charge can be used to significantly improve the resolution by averaging the signals, as illustrated the right picture of the figure.

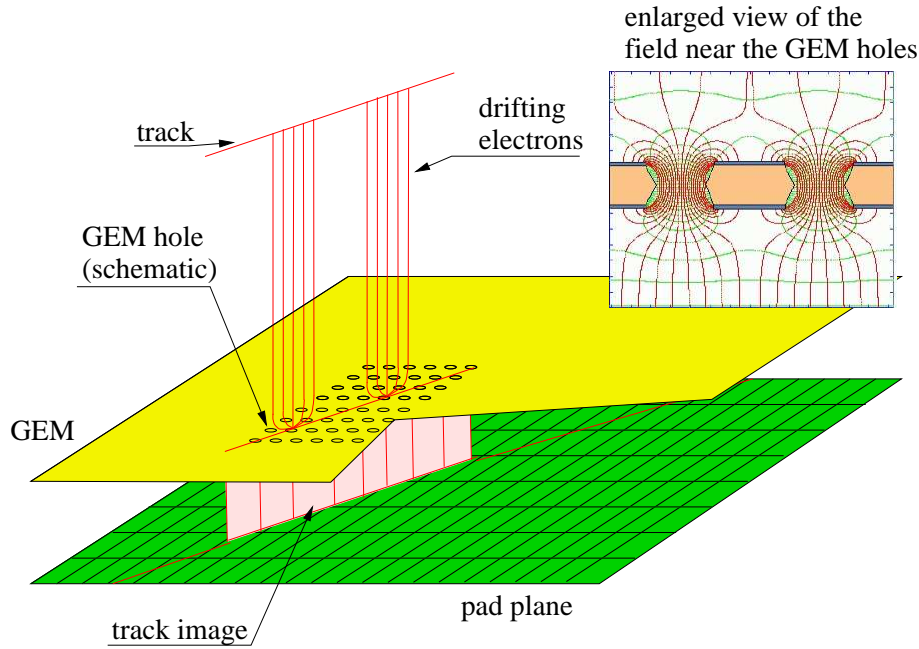


Figure 2.5: Sketch of the GEM principle (not to scale: distance between holes: $\mathcal{O}(0.1\text{ mm})$, pad size: $\mathcal{O}(\text{mm})$). The picture is taken from [27]. In addition, the electric field map near the GEM holes is shown [37].

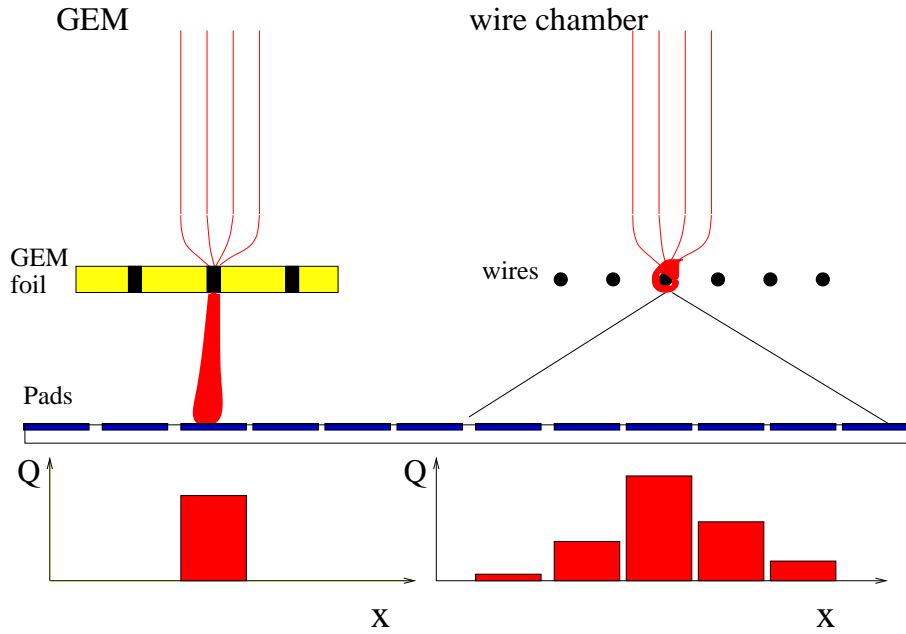


Figure 2.6: Spread of the charge in case of GEM (left) and wire chamber (right) readout: with GEMs the fast and narrow electron signal is collected, leading to a high intrinsic resolution capability. Using readout pad dimensions of $\mathcal{O}(\text{mm})$, however, the charge may be collected on a single pad only. The (positive) charge is spread over several pads in the case of wire chamber readout which can be used to significantly improve the resolution by averaging the signals.

An approach to compensate the absence of a sizable induction signal is the use of specially shaped pads, e.g. the so-called *chevrons*. Figure 2.7 shows schematic of a chevron pad array with a superimposed track and the arriving charge clouds. Owing to the “zigzag” shape significant charge sharing between neighbouring pads is achieved if the extension of the charge cloud is of similar size as the pad dimension.

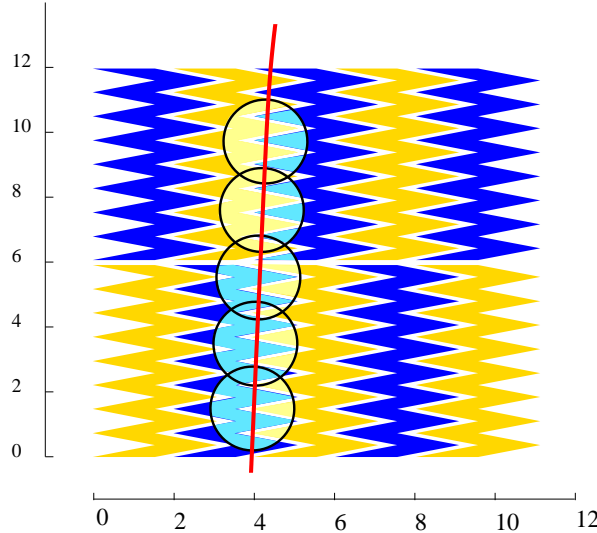


Figure 2.7: Layout of chevron pads, with a track superimposed to illustrate the sharing of charge between different pads. The circles indicate a typical size of the charge cloud arriving on the pads. Dimensions are in mm. The picture is taken from [27].

Apart from the high intrinsic resolution capability, GEM based readout systems offer several further advantages: as GEM holes are only of the order of $100\ \mu\text{m}$ apart, the $\vec{E} \times \vec{B}$ effect is limited to $\mathcal{O}(50\mu\text{m})$. Also GEMs do not have a preferred direction, such that the resolution and double hit separation is expected to be more uniform as in the case of wire chamber readout. Additionally GEMs show an intrinsic suppression of ion feedback [38]. However, a gating system might still be employed to further reduce ions moving towards the drift field. Finally, no strong supporting structure is needed for the assembly of GEMs. This is a further advantage compared to conventional TPC readout, where a significant material budget is necessary for the structure which holds the mechanical wire tension.

2.3.2 Alternative Readout Technologies

An alternative MPGD readout to GEMs is that of *Micro Mesh Gaseous Structures*, Micromegas [39], which is shown schematically in Fig. 2.8. A uniform high field is produced between a thin metallic mesh stretched at a distance of $(50 - 100)\ \mu\text{m}$ above the readout pad plane and held by dielectric supports. With a very high field across the gap, typically $30\ \text{kV}/\text{cm}$, electrons arriving from the TPC drift volume are collected, multiplied in the gap and readout at the pad plane. A Micromegas has also no preferred direction (i.e. two dimensional geometry) and similar operating properties as a GEM like the absence of a sizable ion signal and the intrinsic reduction of ion feedback.

Since GEM and Micromegas are new technologies which have not yet been thoroughly tested for the TPC application, as a fall-back solution a wire chamber readout is being retained.

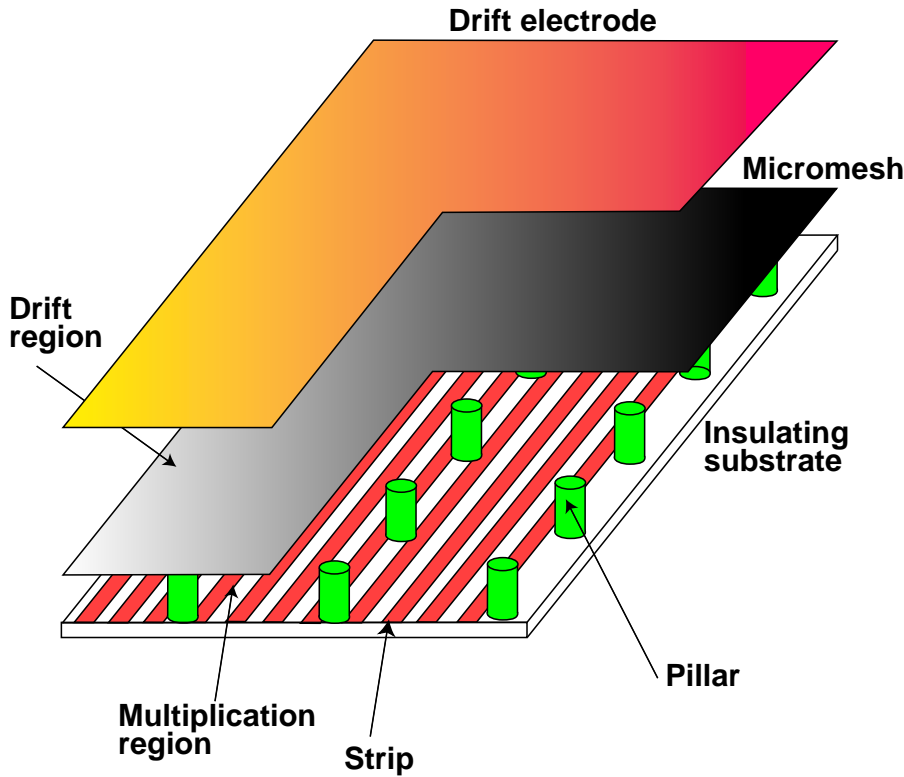


Figure 2.8: Schematic layout of a Micromegas. The picture is taken from [27].

Chapter 3

TPC R&D

In this chapter the TPC prototype used for R&D (Research and Development) on the readout system is introduced and several measurements are presented. The determination of the single point resolution is accompanied by simulations. In all measurements no magnetic field was applied.

3.1 Experimental Setup

In the following the different parts of the TPC test setup are introduced. A schematic view of the prototype is shown in Fig. 3.1.

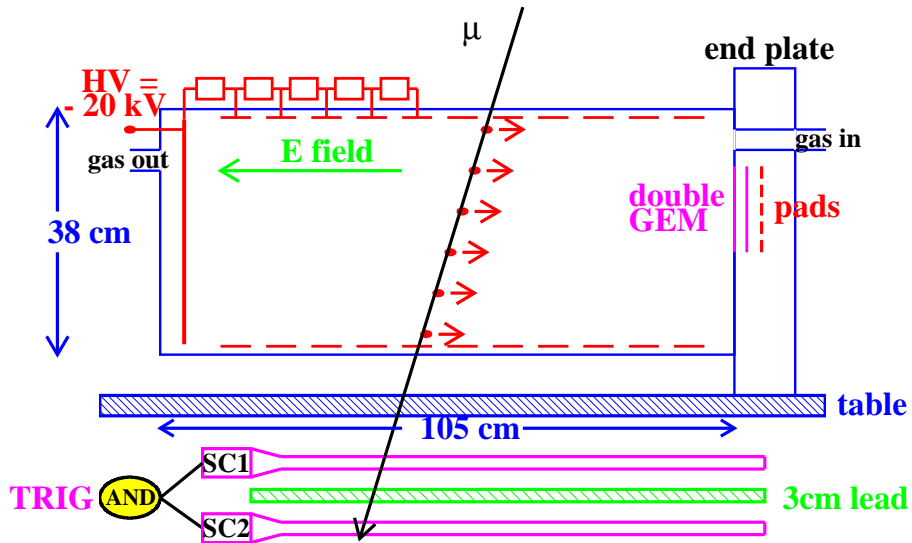


Figure 3.1: Schematic picture of the setup.

3.1.1 Field Cage and Gas

The field cage has a length of 105 cm, an inner diameter of 38 cm and it is made out of Rohacell® surrounded by a copper layer which is grounded. The homogeneous drift field is produced by 100 equipotential rings realized by copper strips of a width of 0.8 cm. The rings are connected in series via $1\text{ M}\Omega$ resistor. The high voltage (HV) applied to the field cage can be adjusted up to 22 kV.

The volume of the field cage is filled with the drift gas proposed in [27], which is a mixture of 93% argon, 2% carbon dioxide and 5% methane.

3.1.2 GEM Readout Module and Endplate

The GEM module, shown in Fig. 3.2, contains two “standard” GEMs [35]. This term refers to a GEM of $10 \times 10\text{ cm}^2$, with holes of a double conical shape of inner (outer) diameter: 55 (70) μm , and a pitch of 140 μm . The two GEMs are mounted in cascade with a gap of (1.5 – 2.0) mm between the GEMs (transfer gap) and between the lower GEM and the array of readout pads, respectively (induction gap). The corresponding fields are $E_{\text{induction}} \approx E_{\text{transfer}} = \mathcal{O}(\text{kV/cm})$.

In addition to the geometrical alignment Fig. 3.2 shows two possible circuits which provide the desired voltages. The GEM closest to the readout pads is denoted GEM 1 and the other one GEM 2. The protection resistances in front of each GEM electrode are $1\text{ M}\Omega$, the other resistors are adjusted according to the desired voltages and electric fields, in the present setup they are all of $\mathcal{O}(10\text{ M}\Omega)$. In case (a) both GEMs are connected to the high voltage ($\text{HV} \approx 2000\text{ V}$) via a single voltage divider. Here, an occasional discharge and thus a breakdown of the voltage in one of the GEMs, say GEM 1, leads to an increased voltage on GEM 2. This might, in turn, cause a discharge in GEM 2. Hence, an oscillating system of discharges might occur which eventually can destroy the GEMs. To prevent this, the improved circuit (b) is introduced: each GEM is connected separately to the high voltage power supply. A discharge in one of the GEMs does not influence the voltage of the other one. For most measurements presented circuit (b) is used.

The measurements were performed with two different endplates: one endplate, called *endplate 1*, is equipped with eight fixed readout strips of 5 mm thickness mounted among one another. Thus only two-dimensional track information is available. A schematic picture is shown in Fig. 3.3. The pads are connected to ground potential via the preamplifiers. In order to reduce drift field distortions caused by the different potentials on the upper side of GEM 2 ($\approx 2000\text{ V}$) and the potential defined by the field cage ($\approx 0\text{ V}$) an aluminium foil is installed surrounding the GEM, which is put on the same potential as the upper side of GEM 2. A photographic view of endplate 1 is shown in Fig. 3.4.

A more elegant way to reduce drift field distortions in the region of the readout module is provided by the second endplate, which was developed especially for the present R&D studies. It is shown schematically in Fig. 3.5, a technical sketch can be found in Appendix A. This endplate, called *endplate 2*, is made out of glass fibre reinforced plastic coated with a copper layer on the side which points towards the drift region. The other side of the endplate is closed by an aluminium cap which serves at the same time as shield against electromagnetic pick-up. The endplate contains a separate GEM module which can be equipped with different kinds of readout pads. The upper side of GEM 2 is on the

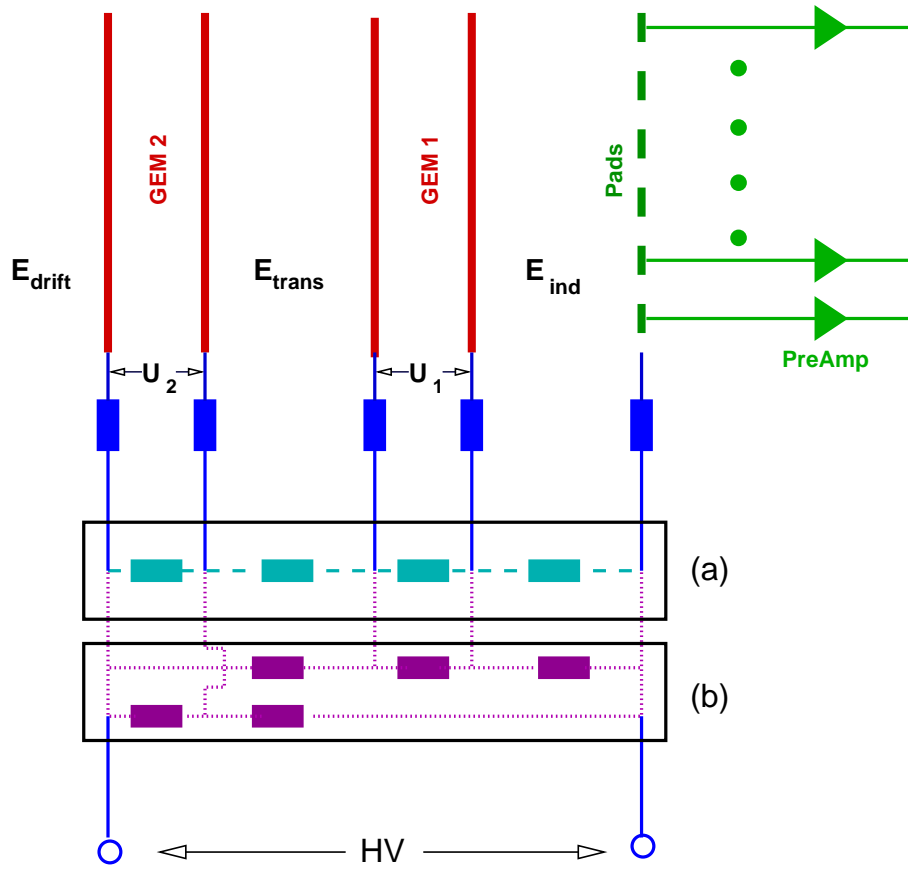


Figure 3.2: Schematic of the GEM readout module. Two possible circuits for providing the voltages are displayed: in case (a) both GEMs are connected to one single voltage divider, in case (b) each GEM is connected separately to the high voltage power supply. The pads can either be connected to ground, or to positive high voltage. In the latter case, the surface of GEM 2 which points to the drift volume can be grounded, but an additional capacitor between pads and preamplifier is needed. The high voltage is $HV \approx 2000$ V, the protection resistors are each $R = 1 \text{ M}\Omega$, and the voltage dividers contain resistors of $\mathcal{O}(10 \text{ M}\Omega)$.

same geometrical level as the end of the field cage. Both surfaces are grounded. Hence the readout pads must be connected to positive high voltage of $\mathcal{O}(1000)$ V in order to maintain the potential gradient. A capacitor must be connected between each pad and preamplifier. However, this setup has the disadvantage that the capacitors store additional electrical energy, which, in case of propagating discharges, can destroy one of the GEMs. A capacitance of $C = 1.5 \text{ nF}$ per readout channel as used in the presented measurements turns out to be very critical and may reduce the average GEM survival time to $\mathcal{O}(\text{days})$ when operating at GEM voltages of $U \lesssim 400$ V in the proposed gas mixture. In order to operate the pads on ground level without causing major drift field distortions the voltage divider of the field cage can be modified slightly such that the field cage ends at the negative potential of the upper side of GEM 2 rather than on ground potential. A photographic view of the endplate is shown in Fig. 3.6.

Apart from rectangular readout pads of the size proposed in [27] ($2 \times 6 \text{ mm}^2$), more

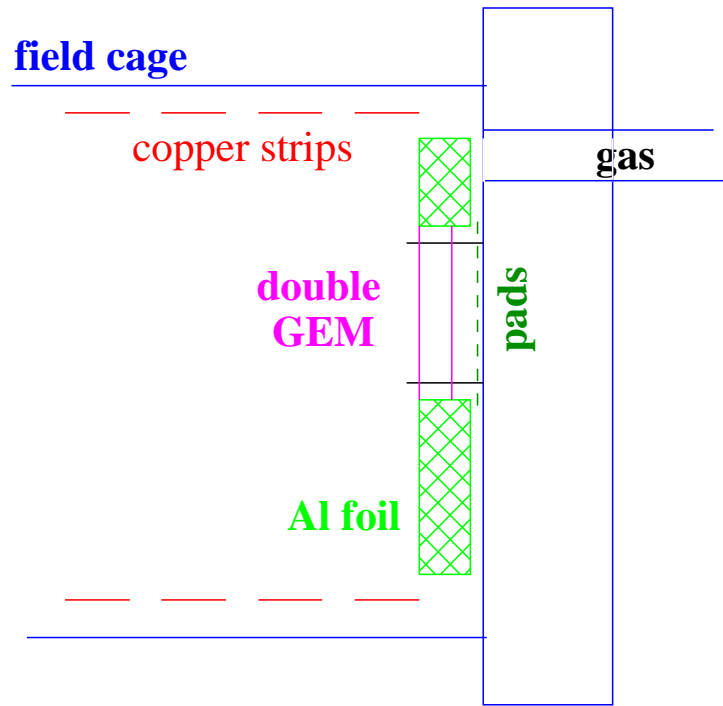


Figure 3.3: Schematic of endplate 1, equipped with a fixed GEM module. The aluminium foil reduces drift field distortions, see text.

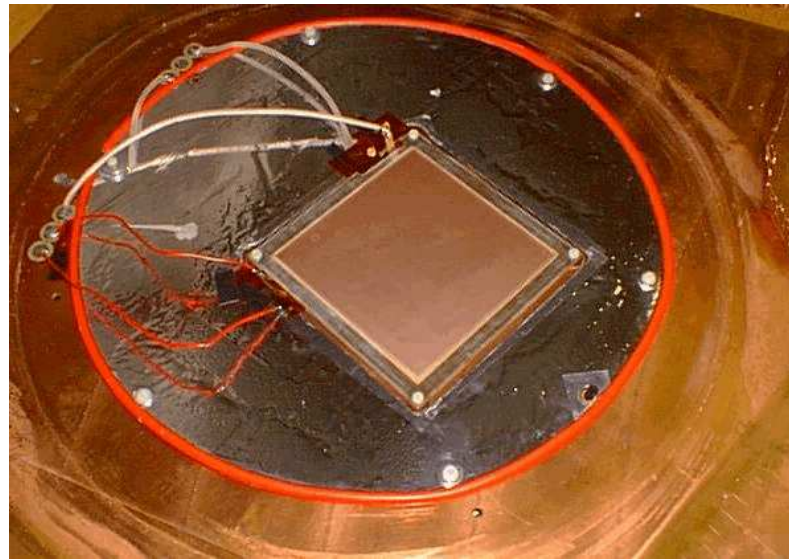


Figure 3.4: Photographic view of endplate 1 with fixed GEM readout module. The side which points towards the drift volume is shown.

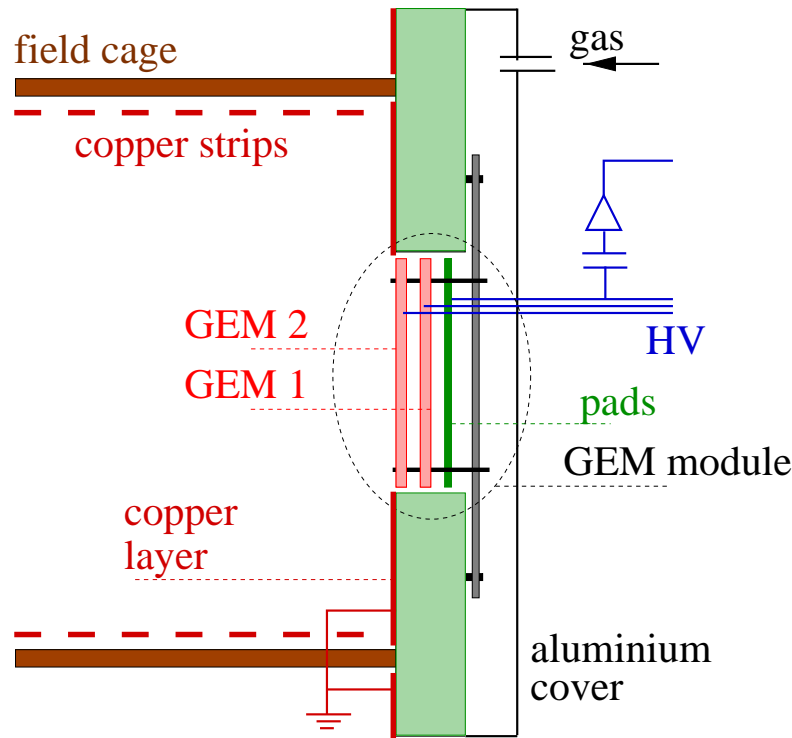


Figure 3.5: Schematic of endplate 2. It was developed especially for the presented resolution studies. The separate GEM module can be equipped with different kinds of readout pads.

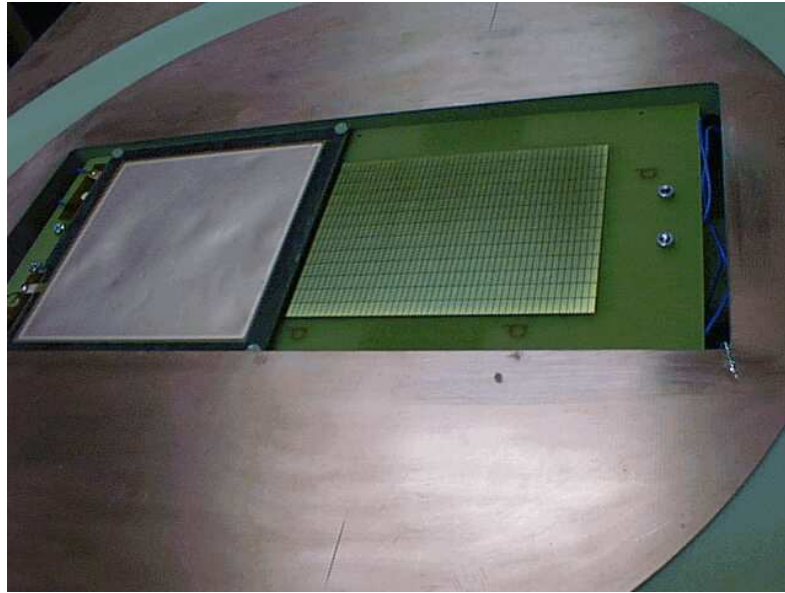


Figure 3.6: Photographic view of endplate 2. The side which points towards the drift volume is shown. The installed GEM module contains rectangular readout pads of the size proposed in [27], i.e. $2 \times 6 \text{ mm}^2$. On the picture only one half of the pads is covered by a double GEM structure. 64 pads are connected to preamplifiers while the others are connected to ground potential.

sophisticated pad geometries, i.e. chevrons, are studied as well. They may lead to a better point resolution due to larger charge sharing [40].

However, as in the presented setup no magnetic field was applied, the diffusion of the electron charge cloud was much larger than expected for TESLA conditions ($B_{\text{TESLA}} = 4 \text{ T}$). Computer simulations using the MAGBOLTZ programme [41] show that for the diffusion coefficient

$$D(B = 0 \text{ T}) \approx 6.5 \cdot D(B_{\text{TESLA}} = 4 \text{ T}) \quad (3.1)$$

applies in the drift volume. In the test setup with small pads the resolution is expected to be dominated completely by the shape of the charge cloud rather than by pad geometry effects. In order to measure effects of the pad shape anyhow the pad size was scaled in x . Thus the ratio of pad dimension and extension of the charge expected at TESLA could be maintained: rectangular pads were developed with an extension in x of $d = 14 \text{ mm}$ as well as the corresponding chevron pads with four “zigzags” and an equal sized sensitive area, leading to an overall extension in x of $d = 28 \text{ mm}$. Both geometries are shown in Fig. 3.7. All used pads and the parameters concerning geometry and alignment are summarised in Table 3.1.

end plate	pad shape	pad size: $x \times y$ (mm 2)	space betw. pads (mm)	numb. of channels	geometr. alignm. of active pads: $x \times y$
1	strips	50×5	≈ 1	8	1×8
2	rectangles	2×6	0.1	64	13×5
2	rectangles	14×14	0.2	35	5×7
2	chevrons	28×14	0.2	42	6×7

Table 3.1: Different pad types used in this thesis and the corresponding parameters concerning geometry and alignment (in case of small rectangular pads (size = $2 \times 6 \text{ mm}^2$) the fifth pad row contains only 12 pads).

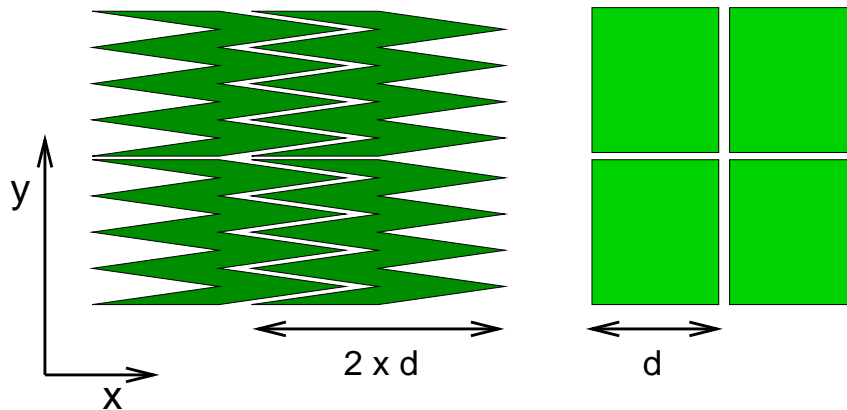


Figure 3.7: Pad geometries: chevron pads (left) and corresponding rectangular pads (right).

3.1.3 Trigger

The readout of the TPC data is started by a coincidence signal of two scintillators caused by high energetic muons from cosmic radiation opening a readout time interval of $50\,\mu\text{s}$. The scintillators have each a size of $20\,\text{cm} \times 80\,\text{cm}$ and are located below the TPC, separated by a lead filter to stop low energetic muons ($E \lesssim 100\,\text{MeV}$). Owing to the alignment, in the case of a trigger a high energetic muon produces with high probability a signal on the pads of the TPC (Fig. 3.1).

3.1.4 Readout Electronics and Data Acquisition

The first element of the electronics chain is the ALEPH TPC preamplifier for wire chambers with 16 channels [42]. The input part is a charge-integrating circuit with a decay-time constant of $2\,\mu\text{s}$. The charge sensitivity is determined by the feedback capacitor ($C_F = 1\,\text{pF}$) to $1\,\text{V}/\text{pC}$. A signal of a minimally ionising particle yields two output pulses of $\mathcal{O}(\pm 10\,\text{mV})$. The noise of the preamplifier, equivalent to 600 electrons, would produce an r.m.s. (root mean square) fluctuation of $\sigma = 100\,\mu\text{V}$. The linear range of the amplifier is more than $1.0\,\text{V}$. The r.m.s. deviation from the nominal values of gain is $\leq 1.5\%$.

The preamplified signal is fed into an ADC (analogue to digital converter) module realised as the F6831 Time Projection Digitiser (TPD). Each TPD module includes analogue shaping amplifiers and Flash ADCs (FADCs). A minimally ionising particle would produce a signal of $\approx 0.5\,\text{V}$ at the output of the shaper. The resultant intrinsic gain fluctuations are $\pm 3\%$.

The output signal from the shaper is connected to the input of the 8-bit FADC (Thomson TS 8328P) which, under control of the external clock, digitises the information (dynamic range: $2^8 = 256$ counts).

Since the memory capacity is limited to 512 time samples, the maximum readout time for an event is $512 \times 88\,\text{ns} \approx 45\,\mu\text{s}$. The TPD module is connected to a Macintosh II computer and the data is stored using a LabView® programme (including routines from the ALEPH TPC data acquisition). The readout system is driven by fastbus technology.

3.2 Data Set

Cosmic muon events were recorded with the four pad types described above and GEM voltages varying between $350\,\text{V}$ and $450\,\text{V}$. The trigger rate was approximately $10\,\text{Hz}$. Depending on the number of connected readout channels the rate of data acquisition was between $\approx 3.5\,\text{Hz}$ for eight and $\approx 1.0\,\text{Hz}$ for 64 channels. Several thousand events were recorded per run. The typical run duration was between one day and one week.

3.3 Basic Performance Studies

In this section, measurements concerning basic GEM operation in a TPC are presented. In all measurements the drift field is $E_{\text{drift}} = 0.2\,\text{kV}/\text{cm}$.

Figure 3.8 shows an analogue signal from a cosmic muon event recorded with an oscilloscope at the output of one preamplifier channel. Both negative (1) and positive (2) outputs are shown as well as the difference (M).



Figure 3.8: Analogue signal from a cosmic muon event recorded with an oscilloscope at the output of one preamplifier channel [43]. The negative (1) and the positive (2) outputs are shown as well as the difference (M).

3.3.1 Pulse Finding

A digitised pulse is recorded if it fulfils basic requirements:

- $\#FADC$ counts/time slice $>$ pulse threshold T_P ,
- pulse length ≥ 2 time slices.

The threshold T_P is varied individually from run to run in order to account for the noise caused by external fields ($T_P = 5, \dots, 30$ FADC counts). In general this electromagnetic pick-up was found to be smaller for endplate 1 owing to its simpler and more compact construction. Using endplate 2, larger pads are found to pick up more noise than smaller ones.

3.3.2 Signal to Noise Ratio

The presented measurements of the signal to noise ratio were performed with endplate 2 and small pads ($2 \times 6 \text{ mm}^2$). The applied voltages and fields were: $U_1 = U_2 = 400 \text{ V}$, $E_{\text{ind}} = E_{\text{trans}} = 1.5 \text{ kV/cm}$.

The noise (N) is determined by the charge collected per pad and time slice recorded in a run which was triggered externally by a pulse generator. The left histogram of Fig. 3.9 shows the corresponding distribution. The mean value of 4.8 FADC counts represents the mean pedestal level averaged over 64 channels. The r.m.s. of the Gaussian fit yields the averaged noise, i.e. $\sigma \approx 1$ FADC count. The right histogram of the figure shows the signal distribution extracted from a “normal” run triggered by cosmic muons. The peak at 255 counts is owing to the limited dynamic range of the FADCs. In this run, a minimum of twelve FADC counts per time slice was required for a pulse to be recorded (pulse threshold). This threshold was applied in order to reduce noise caused by external interfering fields which is not considered in the determination of the signal to noise ratio. Depending on the specific run, however, for large pads pulse thresholds up to 30 FADC counts had to be applied where necessary for a reasonable suppression of noise events.

After subtracting the mean pedestal value from the mean signal charge per pad and time slice, the signal to noise ratio can be estimated to be $S/N \approx 48$.

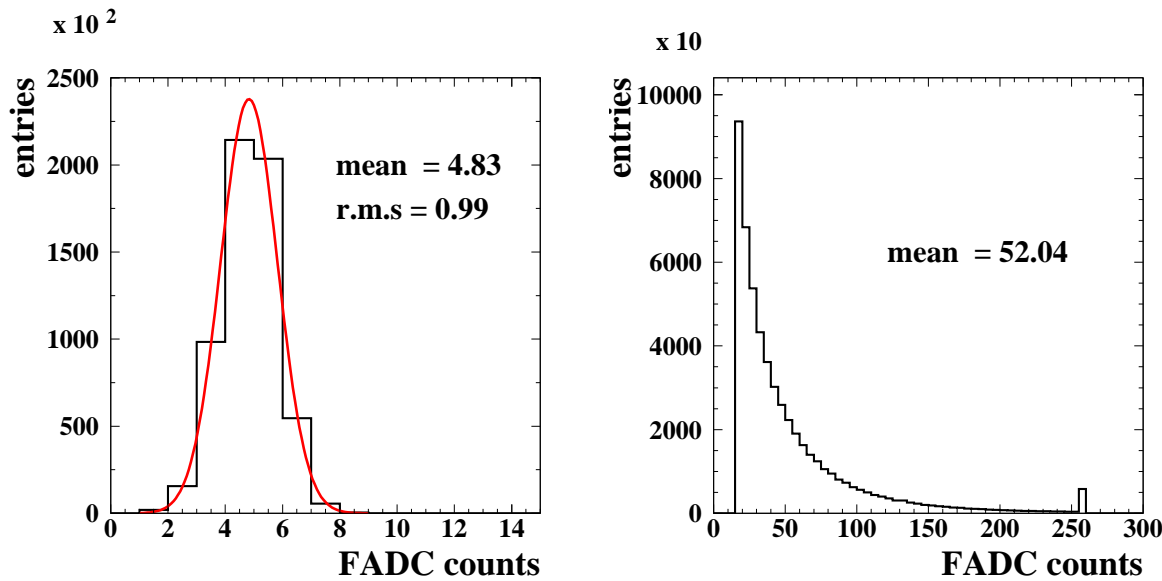


Figure 3.9: Charge collected per pad and time slice: left: noise (N), the mean value represents the mean pedestal level, the r.m.s. of the Gaussian fit yields the averaged noise; right: signal (S), the peak at 255 counts is owing to the limited range of the FADCs. After subtracting the mean pedestal value from the mean signal charge, the signal to noise ratio can be estimated to be $S/N \approx 48$.

3.3.3 Drift Velocity and Pulse Shape

Data for the drift velocity and the pulse shape measurements were recorded using end-plate 2.

The electron drift velocity, v_{drift} , can be estimated from the time distribution of arriving signals with respect to the trigger. Only tracks of cosmic muons with vertical incident, i.e. $|\theta| < 20^\circ$, are taken into account (the track fit is explained later in Section 3.4.1). The largest measured drift times correspond to the maximum drift length, i.e. 1 m. The relative flat distribution of the drift time t_{drift} shown in Fig. 3.10 decreases dramatically at $t_{\text{drift}} = 25 \mu\text{s}$. In order to account for the shape of the drop, the maximum drift time is estimated to $t_{\text{drift,max}} = (26 \pm 2) \mu\text{s}$, which yields $v_{\text{drift}} = (3.8 \pm 3) \text{ cm}/\mu\text{s}$. The drift velocity obtained by a computer simulation [44] with MAGBOLTZ is $v_{\text{drift}} = 4.3 \text{ cm}/\mu\text{s}$ for the same gas mixture and a drift field of 0.2 kV/cm. The small difference between both values is probably due to gas impurities of the drift gas, particularly water, which has a large impact on the drift velocity.

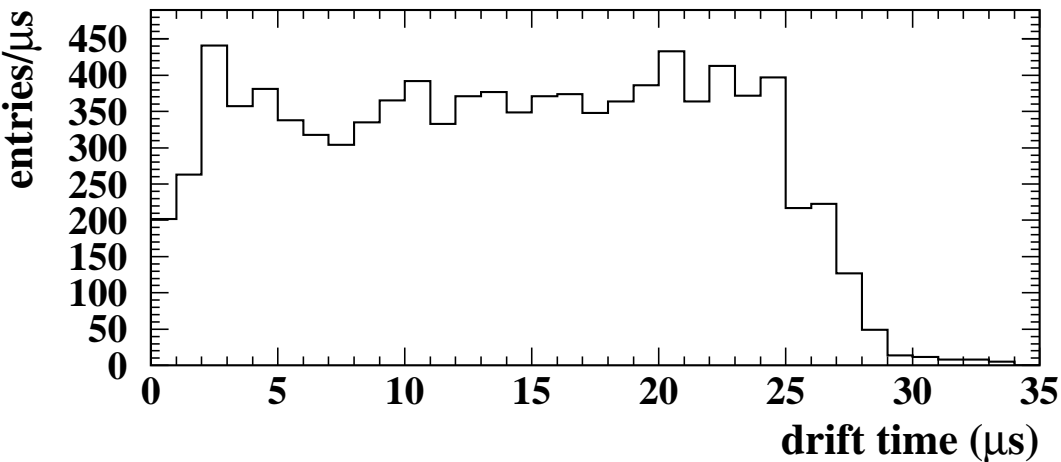


Figure 3.10: Time distribution of arriving signals with respect to the trigger of one data taking period. Only tracks of cosmic muons with vertical incident, i.e. $|\theta| < 20^\circ$, are taken into account. The largest measured drift time estimated to $t_{\text{drift,max}} = (26 \pm 2) \mu\text{s}$ corresponds to the maximum drift length, i.e. 1 m which yields $v_{\text{drift}} = (3.8 \pm 3) \text{ cm}/\mu\text{s}$. Entries at $t_{\text{drift,max}} \gtrsim 29 \mu\text{s}$ are due to muon coincidences where the detected primary ionisation originated from another muon than the muon which triggered the data acquisition.

Figure 3.11 shows averaged pulse shapes after digitisation for different pad sizes and applied voltages of $U_{\text{GEM}} = U_{1,2} = 400 \text{ V}$ ($E_{\text{ind}} = E_{\text{trans}} = 1.5 \text{ kV}/\text{cm}$) and $U_{1,2} = 370 \text{ V}$ ($E_{\text{ind}} = E_{\text{trans}} = 1.4 \text{ kV}/\text{cm}$). In order to reduce noise caused by external fields, a minimum charge per time slice was required for a pulse to be recorded (pulse threshold): twelve FADC counts in case of small ($2 \times 6 \text{ mm}^2$) and 30 FADC counts in case of large rectangular pads ($14 \times 14 \text{ mm}^2$). For a given voltage, roughly five times more charge was

recorded in the case of large pads compared to the small ones. The overall average pulse lengths do not exceed seven time slices ($= 616$ ns); due to longitudinal diffusion the pulse shapes at small drift times (left plot) are sharper than the average shapes for long drift times (right plot). In each case the averaging is performed with more than 10000 samples.

Note that, assuming normal incident of the cosmic muons, the average charge collected depends much stronger on the vertical than on the horizontal pad size.

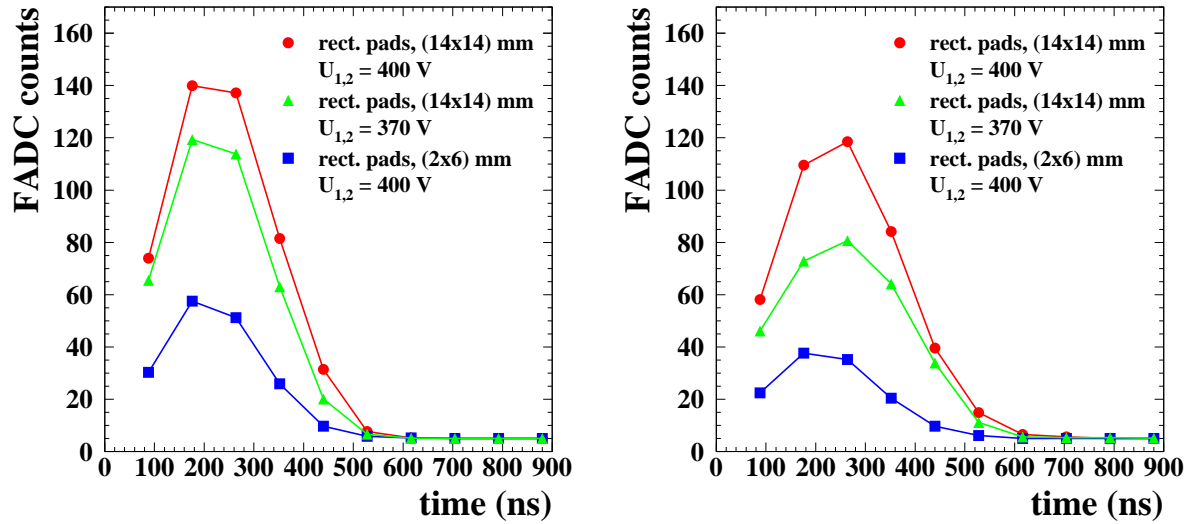


Figure 3.11: Average pulse shape (averaged over > 10000 samples) after digitisation measured with small rectangular pads at $U_{\text{GEM}} = U_{1,2} = 400$ V and large rectangular pads at $U_{1,2} = 400$ V and $U_{1,2} = 370$ V ($E_{\text{ind}} = E_{\text{trans}} = 1.5$ kV/cm). The large pads collect significantly more charge compared to the small pads. Left: drift time $< 4.4 \mu\text{s}$; right: drift time $> 26.4 \mu\text{s}$. The broadening of the pulse shapes is due to longitudinal diffusion.

3.3.4 Gas Amplification

Unless specified otherwise, the following measurements for the determination of the gas amplification (or gas gain) were performed with endplate 1.

Effective gain

The quantity for the characterisation of the gas amplification which can be extracted from the presented measurements is the so-called *effective* gain, G_{eff} [35]. It can be expressed as the product of the *real* gain G_{real} , which is the intrinsic gain of the GEMs, and a field and geometry dependent factor, the transparency T_{GEM} , describing charge losses owing for example to charge following field lines which end on the GEM surface rather than on the readout pads:

$$G_{\text{eff}} = T_{\text{GEM}} \times G_{\text{real}}. \quad (3.2)$$

With the number of electrons N_{prim} released by a minimally ionising particle traversing the distance s , the effective gain is given by

$$G_{\text{eff}} = \frac{q}{(N/s) \times T_{\text{tot}} \times (d_y / \cos \phi)} . \quad (3.3)$$

q denotes the charge collected on a pad, d_y is the vertical pad size, and ϕ denotes the angle of incidence in the $x - y$ plane; T_{tot} is the overall transparency of the system (from the point of primary ionisation to the pads). It describes charge losses mainly owing to electron attachment in the drift gas (oxygen molecules) and diffusion. Finally, feeding well defined charge pulses (from a pulse generator) into the preamplifier yields the FADC calibration

$$\#\text{FADC counts} = 1.1 \times 10^{-2} q . \quad (3.4)$$

This calibration does not take into account fluctuations of the amplification of individual channels.

The number of released electrons per path length by a minimally ionising particle in the used gas mixture is $N_{\text{prim}}/s \approx 100/\text{cm}$ [6]. The overall transparency is difficult to determine because it depends strongly on gas impurities like oxygen which could not be measured with the setup. Therefore, T_{tot} is estimated as the charge loss along the drift, displayed in Fig. 3.12: in the first bin significantly more charge is collected ($Q_1 = 5100$ units) than in the bins corresponding to drift times $> 5\mu\text{s}$ (average value: $Q_{2-6} \approx 4300$ units). The ratio $Q_{2-6}/Q_1 \approx 0.8$ gives an estimate of the average charge loss in the drift volume which will be used in the following. A systematic error of 0.2 is assumed.

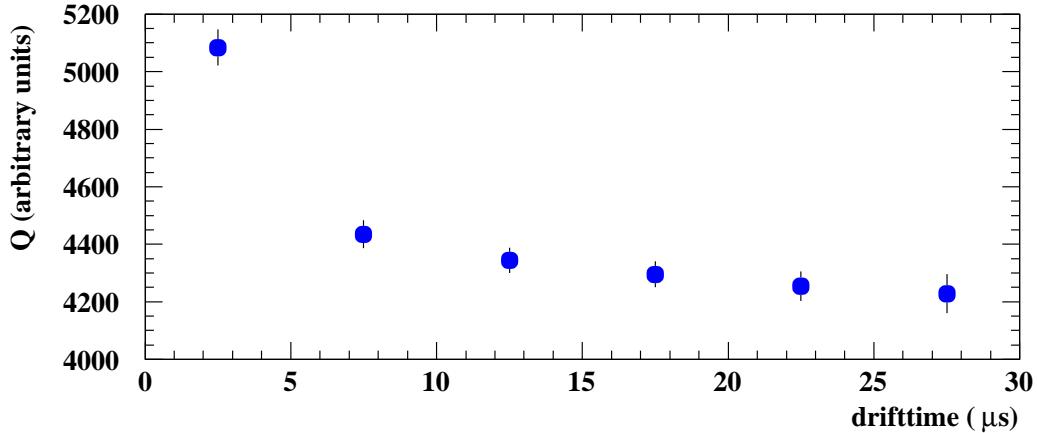


Figure 3.12: Total charge collected (Q in arbitrary units) as a function of the drift time.

Using pads with a vertical size of $d_y = 0.5\text{ cm}$, furthermore assuming normal incidence of the muons ($\cos \phi = 1$ is a good approximation due to the alignment of the trigger scintillators) the effective gain is

$$G_{\text{eff}} = (0.23 \pm 0.06) \times (\#\text{FADC counts}) . \quad (3.5)$$

The systematic error is determined by the assumed uncertainty on the overall transparency. In the results presented, however, this systematic uncertainty is not shown because the quantity is the same for all individual measurements.

Gain dependence on applied electric fields

In order to investigate the gain dependence fields three different series of measurements are performed: gain as a function of the GEM voltages, gain as a function of the induction and transfer field respectively, and gain dependence on the drift field.

Figure 3.13 shows the effective gain vs. the sum of the voltages of the two GEMs. For each measurement series the voltage of one GEM is constant. The gain shows an exponential behaviour, which is in agreement with other measurements [45]. For higher voltages the overall gain is in good approximation independent of the division of the gain between the two GEMs. At values $U_1 + U_2 > 850$ V the region of saturation of the FADCs is entered, i.e. in some time slices the amount of charge collected exceeds the dynamic range of the FADCs.

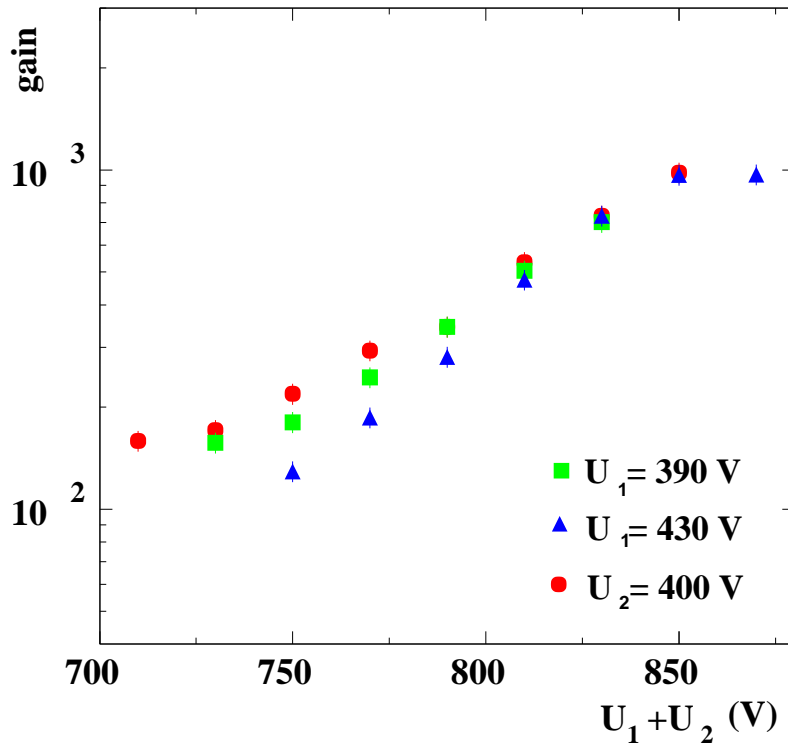


Figure 3.13: Effective gain vs. GEM voltages. For $U_1 + U_2 > 850$ V saturation effects owing to the limited dynamic range of the FADCs become relevant. Statistical errors are shown.

The gain dependence on the induction and the transfer field is shown in Fig. 3.14. The GEM voltages are $U_1 = 430$ V and $U_2 = 420$ V, respectively. In the case of variable induction field the transfer field is fixed to $U_{\text{trans}} = 1.09$ kV/cm, in the second case, i.e. variable transfer field, the induction field is adjusted to $U_{\text{ind}} = 1.25$ kV/cm. In both cases a rise of the gain with increasing field strength can be seen. The dependence is moderate and reflects the enhancement of the electrical energy as the field strengths increase. Only at higher transfer fields (and low induction field) the gain decreases slightly. The configuration of the transfer and induction field has obviously a large impact on the parameter T in a way that the charge collection efficiency and the electrical transparency

of the GEM foils are influenced. Due to a high transfer field for example a significant fraction of the field lines may not be tunnelled into the GEM hole but end on the GEM surface. Hence the electrons following these lines are lost. Therefore the transfer field should not exceed 2 kV/cm at GEM voltages of ≈ 420 V. For a deeper understanding of the charge transfer in GEM structures, however, simulations of the microscopic processes are necessary, see for example [46].

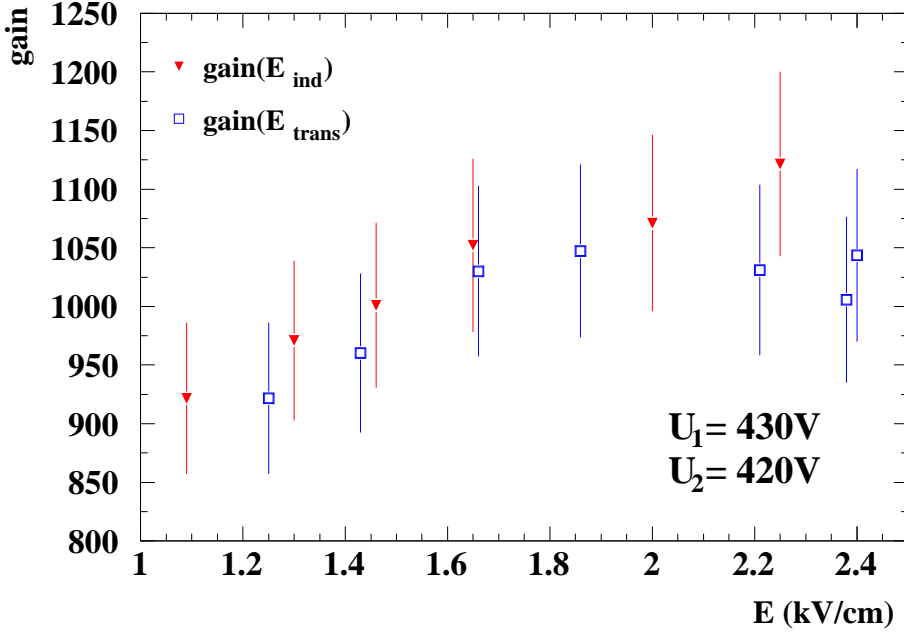


Figure 3.14: Effective gain vs. induction and transfer field. The errors take into account statistics and uncertainties in the applied GEM voltage of ± 1 V.

GEM gas amplification and charge transfer processes have been extensively studied by other groups, e.g. [35], which yield similar results. In different gas mixtures however, e.g. Ar-CO₂-CO₂(70 : 30)% higher gains can be achieved without significant electric discharges (sparks). In single GEMs gas amplifications of a few times 10³ have been measured.

Uniformity

Several factors may degrade the gain uniformity. Among them are: the deviation from the nominal gain of each preamplifier and shaper (r.m.s. deviation < 3%); owing to small inaccuracies in the GEM manufacturing, the GEM thickness is a function of the coordinates, such that the electric field inside the GEM holes may differ slightly from one hole to another. Furthermore, the distance between the two GEMs as well as GEM 1 and readout pads may vary at $\mathcal{O}(0.1)$ mm resulting in slightly different field configurations. Finally, gain variations may occur owing to a bad quality of cabling of individual channels.

The resulting behaviour of the relative gain, recorded using endplate 2, is shown in Fig. 3.15 as a function of the vertical (y) coordinate (normalised to the second bin). Each displayed point corresponds to one pad (14×14 mm²). Without calibration of the

individual channels the r.m.s. variation of the measured relative gain is $\approx 3\%$ which is a very good result taking into account the above mentioned sources of uncertainties.

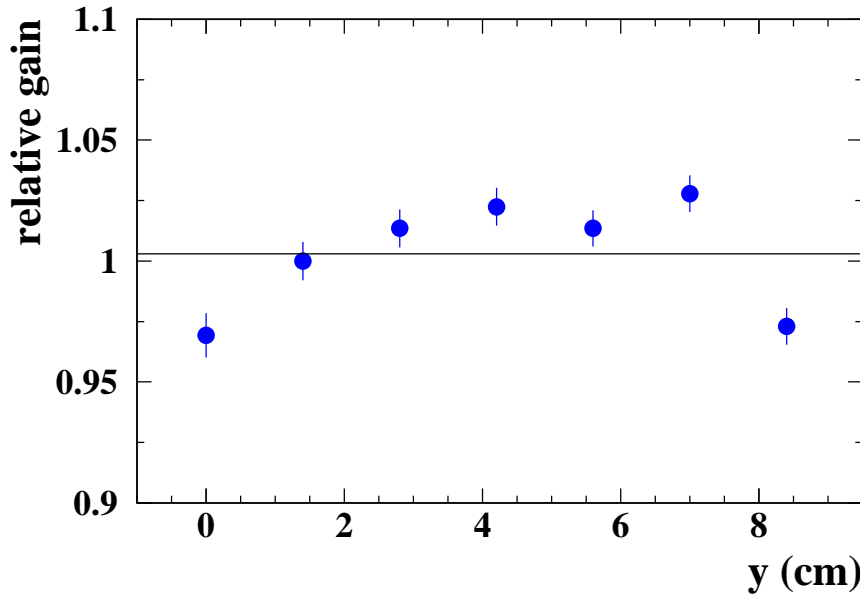


Figure 3.15: Gain uniformity vs. (vertical) distance on the pads. Each measurement point corresponds to one channel. The values are normalised to the second bin; the vertical line denotes the mean value. Without calibration of the individual channels the r.m.s. variation of the relative gain is $\approx 3\%$.

3.3.5 Pad Efficiency

The efficiency of a pad is determined as the efficiency to measure a signal on the pad, if pulses are simultaneously recorded on all other pads, providing a “pad trigger” signal. This measurement was carried out using the pad row consisting of eight pads of the size $5 \times 50 \text{ mm}^2$ mounted below one another (endplate 1). In order to make sure the produced primary charge lies in the geometrical acceptance of the investigated pad the topmost and the lowest pads are omitted in the determination.

The mean efficiencies of the remaining six pads as a function of the sum of the applied GEM voltages are displayed in Fig. 3.16. Two cases are considered: first the pulse threshold is set to 10 FADC counts for all pads; in the second case, the signal on the investigated pad was required to have at least 15 FADC counts per time slice, whereas the threshold of the “trigger pads” is still at 10 counts. In both cases a saturation of the efficiency close to 100% can be observed for $U_1 + U_2 > 800 \text{ V}$. With decreasing GEM voltage the efficiency drops down until it reaches $\epsilon = 62\%$ (threshold = 10 counts) and $\epsilon = 38\%$ (threshold = 15 counts) at $U_1 + U_2 = 710 \text{ V}$.

Taking into account reasonable values for the pulse threshold the GEM voltage should obviously not fall below a certain value ($U_1 + U_2 \approx 800 \text{ V}$) in order to maintain an individual pad efficiency close to 100%. At lower GEM voltages the minimum charge

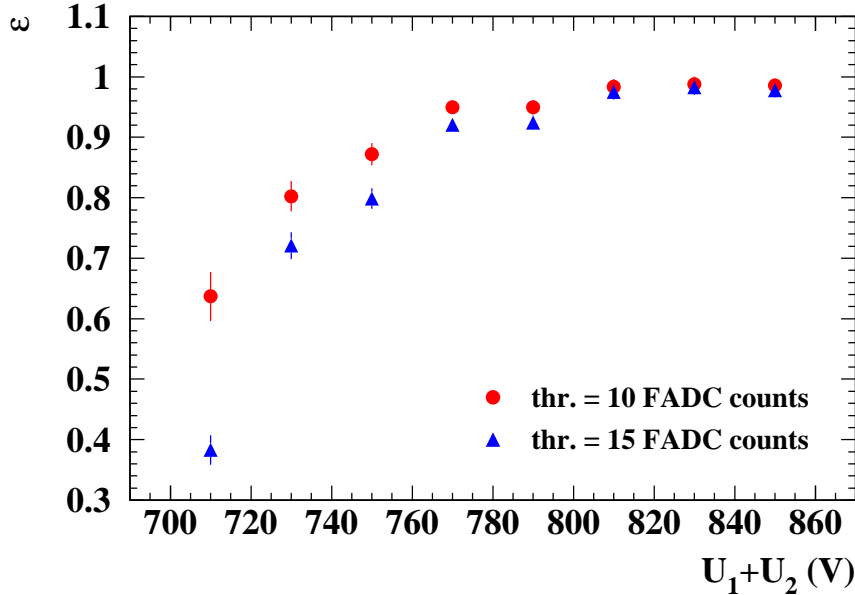


Figure 3.16: Efficiency ϵ of a single pad ($50 \times 5 \text{ mm}^2$) as a function of the GEM voltage if a pulse is simultaneously measured on all other pads. Dots: pulse threshold = 10 FADC counts for all pads; rectangles: pulse threshold = 15 FADC counts for the investigated pad and pulse threshold = 10 counts for all other pads. The error bars indicate statistical errors.

required per pulse can reduce the efficiency dramatically. Note that the measured efficiencies depend strongly on the vertical pad size (5 mm), which determines the average amount of charge collected.

3.4 Resolution

The single point resolution in x (parallel to the endplate) and z (along the drift direction) is determined using cosmic muons. The x resolution studies are carried out with different pad geometries and accompanied by computer simulations. The measurements are carried out using endplate 2.

3.4.1 Cosmic Muon Data

The data used to extract the point resolution were recorded at $U_{1,2} = 400 \text{ V}$ and $E_{\text{ind}} = E_{\text{trans}} = 1.5 \text{ kV/cm}$ for small pads ($2 \times 6 \text{ mm}^2$) and at $U_{1,2} = 370 \text{ V}$ and $E_{\text{ind}} = E_{\text{trans}} = 1.4 \text{ kV/cm}$ for large rectangular and chevron pads. The pulse threshold was set to 12 FADCs for small pads and to 30 FADC counts for both kinds of large pads.

Method

In each recorded event one charge cluster is searched for in each $x - z$ plane. The most simple charge cluster is an isolated pulse according to the definition of Section 3.3.1. Pulses from several pads in x belong to one cluster if the corresponding pads are direct neighbours and the individual pulses have an overlap in z of at least one time slice. The maximum allowed length for one cluster in z is 12 time slices; in x no restriction is made. Figure 3.17 shows two examples of hypothetical clusters in the $x - z$ plane.

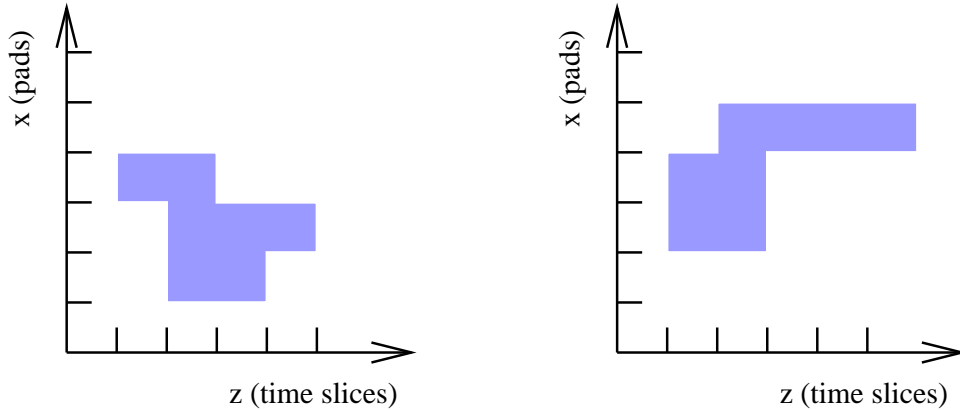


Figure 3.17: Two hypothetical charge clusters in the $x - z$ plane.

The centre of a cluster is determined as the charge centre of gravity in x and z . A χ^2 -straight-line-fit is performed in the $x - y$ and $y - z$ plane if

- in at least four different $x - z$ planes a cluster is found, and if
- at least one of the found clusters extends over more than one pad.

Otherwise the event is rejected.

Figure 3.18 shows two projections of a cosmic muon event, recorded with small rectangular pads ($= 2 \times 6 \text{ mm}^2$). The amount of charge accumulated on the pads is represented by the displayed box sizes. The filled squares indicate the charge centre of gravity (left plot only), and the lines show the reconstructed muon track.

Then the residual between the reconstructed coordinate and the coordinate of the charge centre of gravity of the cluster is determined. The point resolution is determined as the width of a Gaussian fitted to the distribution of the residuals. Figure 3.19 shows the distribution of residuals in x (left) and z (right) for a drift length of 40 cm.

Results

First the distortions of the drift field which may degrade the measured single point resolution are investigated. In the presented setup distortions were caused for example by the insulating material of the readout module or by slight misalignment of the GEMs. Figure 3.20 shows the mean differences between the coordinates obtained from the track fit and the charge centre of gravity of the cluster when that specific cluster is omitted

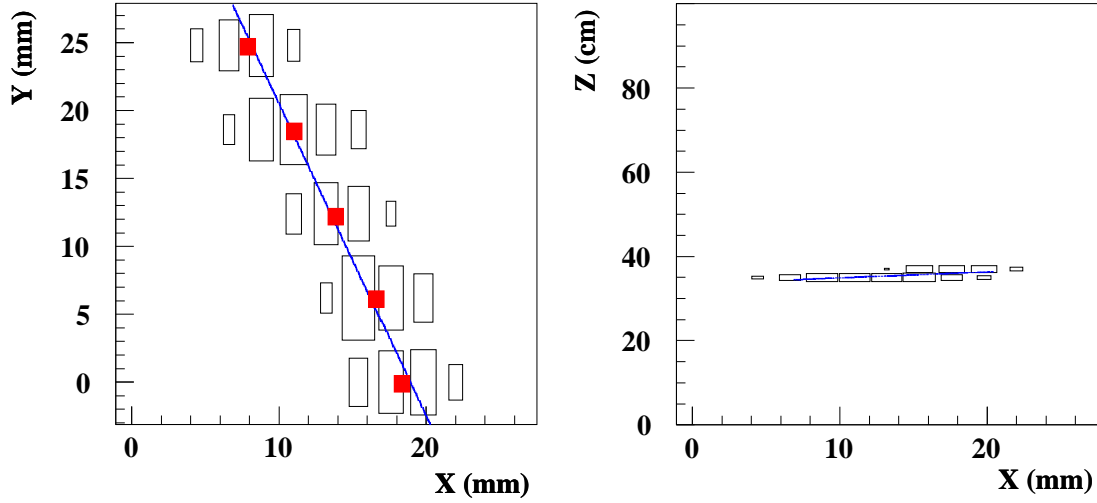


Figure 3.18: Cosmic muon event recorded with small pads ($2 \times 6 \text{ mm}^2$) and $U_{1,2} = 400 \text{ V}$. The projection on the $x - y$ plane (left) and on the $x - z$ plane (right) is shown. The amount of charge accumulated on the pads is represented by the displayed box sizes. The rectangles indicate the charge centre of gravity (left plot only), and the lines show the reconstructed muon track.

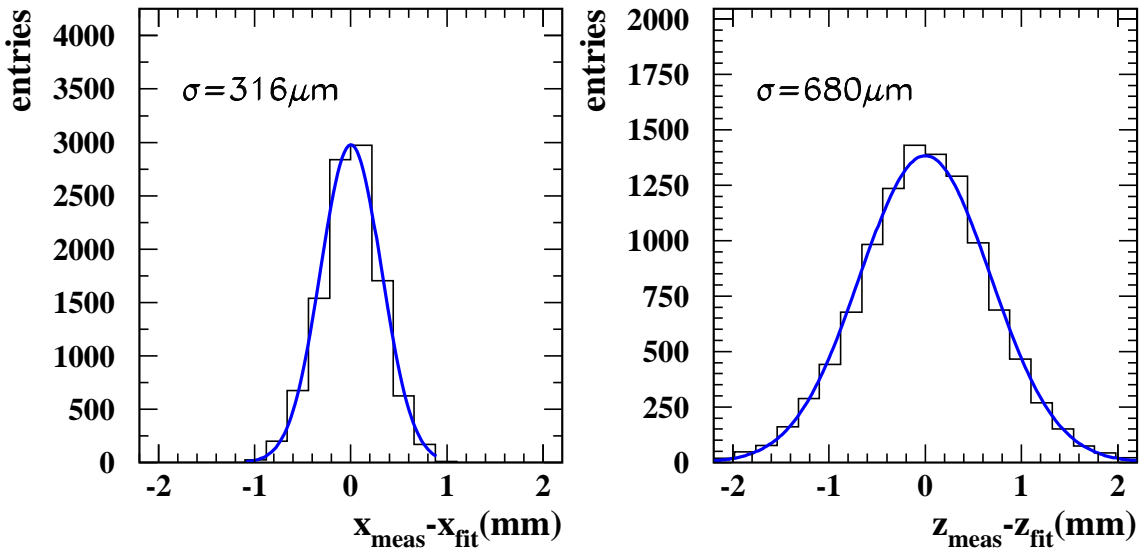


Figure 3.19: Residuals: distributions of the difference between measured (index “meas”) and fitted coordinate (index “fit”) in x (left) and z (right) at a drift length of 40 cm, recorded with small rectangular pads ($2 \times 6 \text{ mm}^2$).

in the fit procedure. Apart from small deviations within the statistical error, in x (left plot) no significant field distortions can be observed. However, in the direction along the drift field (z) there are systematic coordinate deviations of $\mathcal{O}(\text{mm})$. Therefore the determination of the z resolution is carried out using only the restricted region in the centre of the sensitive area ($30 \text{ mm} < y < 70 \text{ mm}$) where the systematic deviations below 0.15 mm.

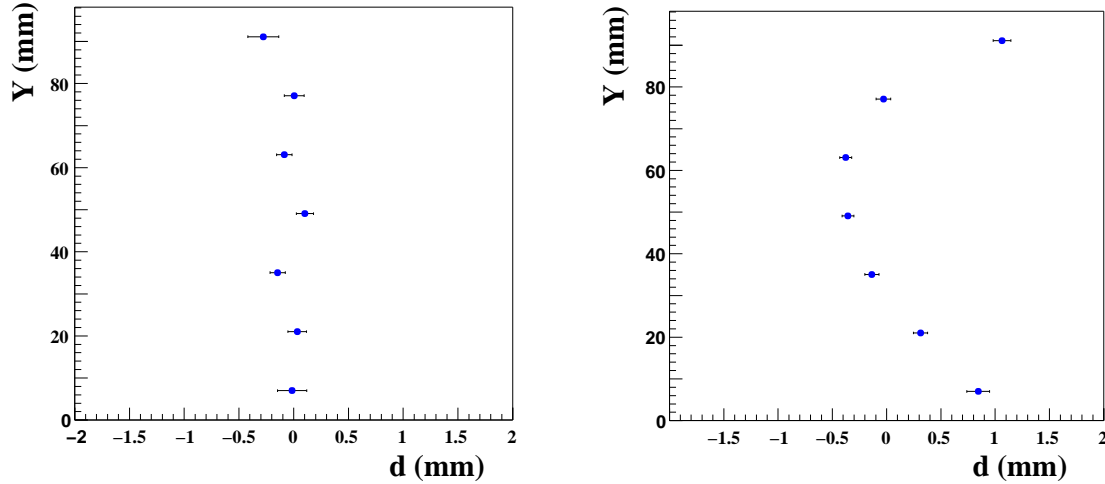


Figure 3.20: Drift field distortion: the mean differences (denoted with d) between the coordinates obtained from the track fit and the charge centre of gravity of the cluster are shown when that specific cluster is omitted in the fit procedure. Apart from small deviations within the statistical error, in x (left plot) no significant field distortions can be observed, but along z (right plot), there are systematic coordinate deviations of $\mathcal{O}(\text{mm})$. The uncertainties are given by the errors of the Gaussian fitted to the distribution of residuals.

The x single point resolution σ_x obtained with rectangular pads of the size of $2 \times 6 \text{ mm}^2$ is shown Fig. 3.21. Owing to the absence of a magnetic field the resolution is dominated entirely by the diffusion of the charge cloud. For all measurable drift distances the extension of the charge cloud is significantly larger than the pad size. The left plot of the figure shows the resolution as a function of the drift length. σ_x starts at $\approx 200 \mu\text{m}$ for very short drift distances and increases up to $\approx 370 \mu\text{m}$ for $l_{\text{drift}} = 90 \text{ cm}$ showing a behaviour proportional to $\sqrt{l_{\text{drift}}}$.

The right plot contains the resolution as a function of the azimuthal angle of incidence ϕ . With increasing angle the projection of the charge cloud on the x coordinate becomes larger, too, which leads to a degradation of the resolution performance. Owing to the asymmetric alignment of the scintillators, where cosmic muons were not in the acceptance for $|\phi| > 20^\circ$, not enough statistics is available in this angular region. Hence the corresponding values are not displayed.

Figure 3.22 shows σ_x obtained with large rectangular pads ($14 \times 14 \text{ mm}^2$) and the corresponding chevron pads. Due to the large pad size, the resolution is no longer

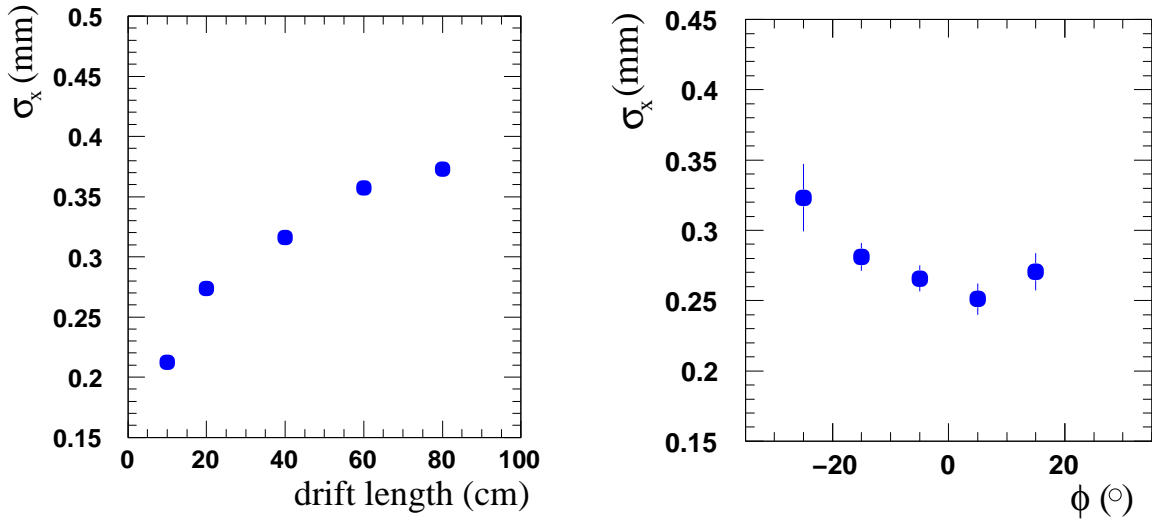


Figure 3.21: Residual point resolution in x . Left plot: resolution as a function of the drift length l_{drift} . Right plot: resolution as a function of the azimuthal angle of incidence ϕ ; owing to the asymmetric alignment of the scintillators, where cosmic muons were not in the acceptance for $|\phi| > 20^\circ$, not enough statistics is available. The uncertainties are given by the errors of the Gaussian fitted to the distribution of residuals.

determined exclusively by the diffusion. As described above, pad geometry effects become visible. A relative uniform resolution of ≈ 1 mm for all drift distances is obtained with chevron pads. A slight degradation of the resolution is noticeable with increasing drift distance. The rectangles show, however, a significantly worse performance for $l_{\text{drift}} \lesssim 60$ cm. It reaches values up to $\sigma_x = 2.5$ mm for $l_{\text{drift}} = 5$ cm. This is due to the fact that the charge cloud is often collected on one single pad.

Figure 3.23 shows the z single point resolution σ_z , measured with small rectangular pads. The left plot displays the dependence on the drift length. The resolution yields values from 0.5 mm at $l_{\text{drift}} = 10$ cm up to 0.9 mm at $l_{\text{drift}} = 90$ cm. The right plot shows the dependence on the polar angle of incidence θ . Integrated over all drift times the z point resolution is determined to ≈ 0.5 mm for vertical tracks. With increasing θ the resolution degrades and reaches values around 0.7 mm.

3.4.2 Simulation

Method

The simulation was based on the method described in [40]. The simulation programme was upgraded in order to achieve an improved description of the primary ionisation, gas properties and gas gain fluctuations. The steps described below were carried out. An example of a simulated track is shown in Fig. 3.24.

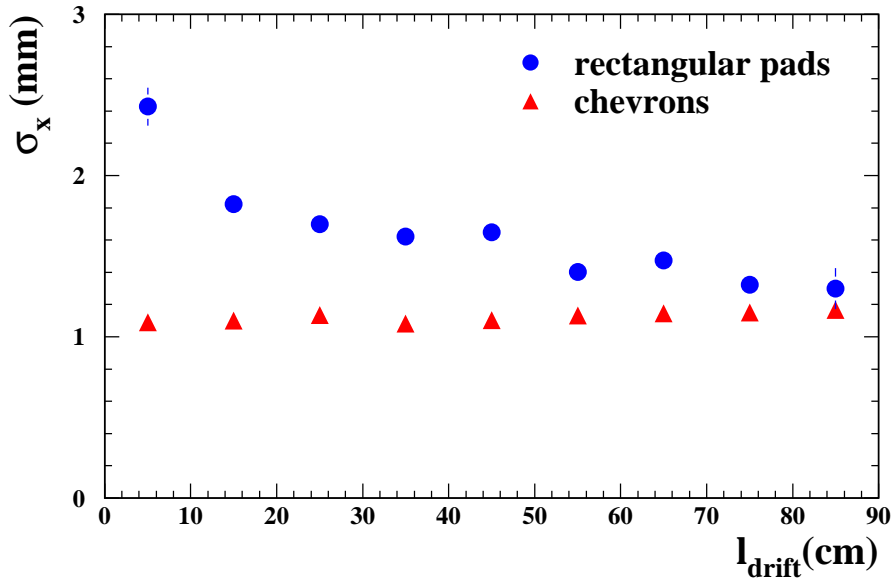


Figure 3.22: Residual resolution obtained with large rectangular pads ($14 \times 14 \text{ mm}^2$) and the corresponding chevron pads. Due to the large pad size the resolution is dominated by the pad geometry rather than by diffusion. Chevrons feature a relative uniform resolution of 1 mm for all measured drift distances. Rectangular pads show, however, a significantly worse performance for $l_{\text{drift}} \lesssim 60 \text{ cm}$. The uncertainties are given by the errors of the Gaussian fitted to the distribution of residuals.

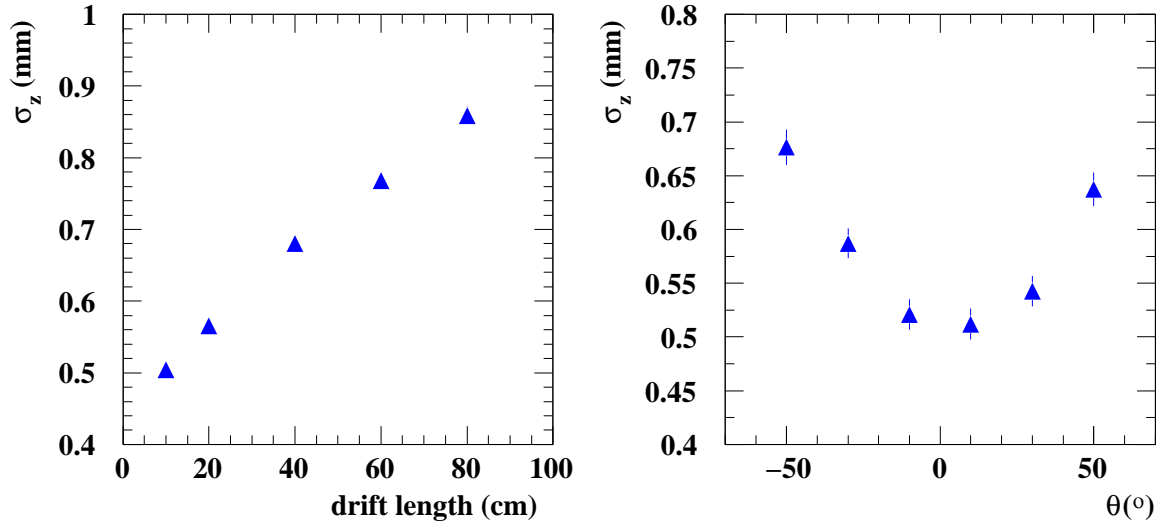


Figure 3.23: Residual resolution in z as a function of the drift length (left plot) and as a function of the polar angle of incidence θ (right plot), measured with small rectangular pads. The uncertainties are given by the errors of the Gaussian fitted to the distribution of residuals.

- Starting at the centre of one pad the x coordinate of the track was increased in 1000 steps until it reached the centre of the neighbouring pad. This was repeated with different z coordinates. All tracks were produced at normal incidence. 21 rows of rectangular rectangular pads of size $2 \times 6 \text{ mm}^2$ and the corresponding chevrons with four “zigzags” were simulated.
- The primary ionisation was simulated with the HEED programme [47]. The primary charge produced by one minimum ionising particle including a “delta electron” is shown in the left plot of Fig. 3.24.
- Gas properties were simulated with the MAGBOLTZ programme [41]. In the presented simulation the proposed three component mixture of Ar-CO₂-CH₄ (93 : 2 : 5)% was used, and a magnetic field of $B = 4 \text{ T}$ was applied. The drift field was set to $E_{\text{drift}} = 230 \text{ V/cm}$. The second plot of Fig. 3.24 shows, how diffusion lead to a spread of the primary charge cloud.
- The drifted electrons were moved to the nearest hole in the first GEM foil. Amplification of one GEM was simulated with an average (effective) gain of 31.62 ($= \sqrt{1000}$) with the fluctuations of the gain following a polya distribution. After passing the transfer region with $E_{\text{trans}} = 2 \text{ kV/cm}$ the second GEM was treated in the same way as the first one. Finally, all secondary charges were moved to the pad plane via the induction gap ($E_{\text{ind}} = 2 \text{ kV/cm}$), see right plot of Fig. 3.24. In the presented simulation different induction gap sizes were studied, and the induction field was set to $E_{\text{ind}} = 2 \text{ kV/cm}$.
- The position of each avalanche electron on the readout pad structure was finally calculated, and if it hit a readout pad, the charge was accumulated. Readout pads with charge above zero were then used to calculate the reconstructed x position by taking the charge centre of gravity. No cluster finding algorithm was applied, since only single tracks were simulated.

Results

At each pad the residual between reconstructed and true x coordinate is determined. The point resolution is defined as the width σ of the Gaussian fitted to the distribution of the residuals. The dependence of the point resolution on the drift length for rectangular pads ($2 \times 6 \text{ mm}^2$) and the corresponding chevron pads is shown in Fig. 3.25.

In addition, different induction gap sizes are studied because in general, fields in the order of the induction field strength, i.e. $\mathcal{O}(\text{kV/cm})$, yield higher diffusion than fields in the order of the drift field strength, i.e. $\approx 0.2 \text{ kV/cm}$ (a factor of 5.7 is found for the simulated parameters). Hence a sufficiently large induction gap can be used as a “diffusion gap” which produces the desired charge spread. Figure 3.26 shows the development of the r.m.s. extension of a charge cloud σ_{cloud} on the pad plane as a function of the induction gap, assuming 10 cm (solid line) and 70 cm (dashed line) drift distance.

For conventional gap sizes ($\mathcal{O}(\text{mm})$), a significant dependence of the resolution on the drift length can be observed, because charge cloud diffusion takes place mainly in the

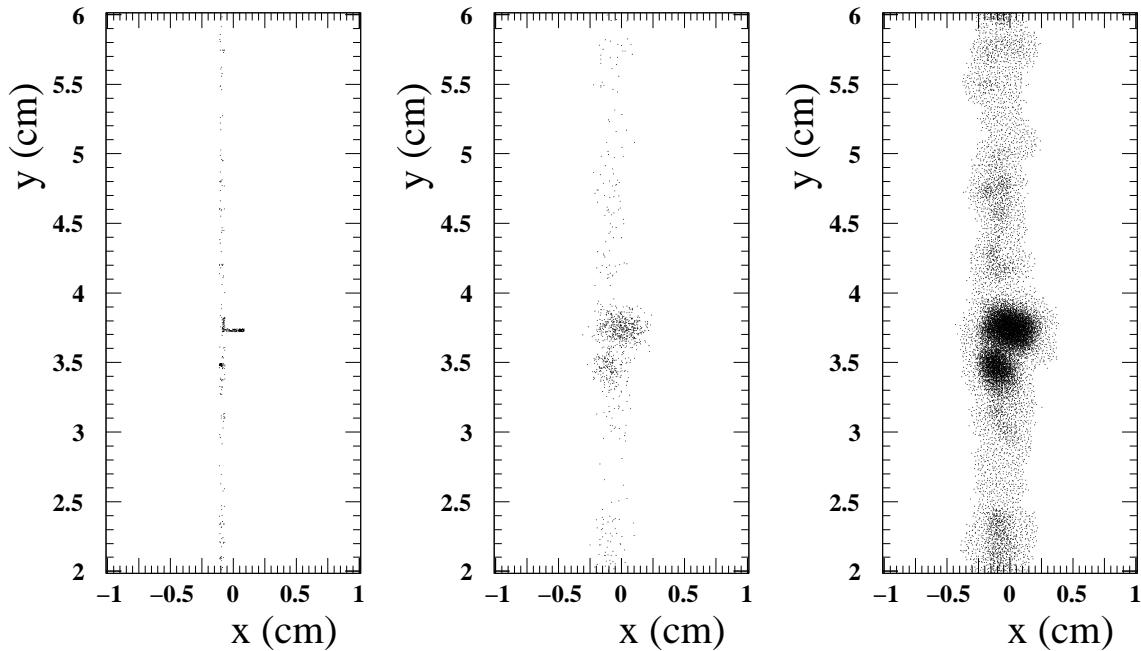


Figure 3.24: Simulated development of the charge cloud produced by a minimally ionising particle. Left: primary ionisation including a “delta electron”; centre: primary charge on the surface of the first GEM; right: secondary charge after the amplification process on the pad plane.

drift region. For short drift distances ($l_{\text{drift}} \lesssim 50 \text{ cm}$) the resolution is dominated by the pad geometry. Using the charge centre of gravity method the marginal charge spread over the rectangular pads leads to a relatively poor point resolution of $\sigma > 350 \mu\text{m}$ for $l_{\text{drift}} < 25 \text{ cm}$, while chevron pads yield $\sigma \approx 100 \mu\text{m}$ up to very close to the endplate. At $l_{\text{drift}} > 100 \text{ cm}$ both pad geometries perform equally well and yield $\sigma \approx 200 \mu\text{m}$ up to drift distances of $l_{\text{drift}} = 250 \text{ cm}$. If the induction gap is increased, diffusion and hence the spread of the charge cloud over the pads increases equally for all drift lengths. The discrepancy between the performance of both geometries almost vanishes, and a resolution at short drift distances of $\sigma \approx 50 \mu\text{m}$ is obtained for an induction gap of 4 cm.

3.4.3 Discussion

The x single point resolution for rectangles and chevrons obtained in simulation and measurements show qualitatively the same behaviour (compare upper plot of Fig. 3.25 and Fig. 3.22). For a quantitative comparision the measured resolution must be scaled down by a factor of ≈ 6.5 according to Eq. 3.1. This yields $\sigma_{x,\text{scaled}} \approx 150 \mu\text{m}$ for chevrons and $\sigma_{x,\text{scaled}} \approx 380, \dots, 150 \mu\text{m}$ for rectangles. Except for very small drift distances ($\lesssim 20 \text{ cm}$)

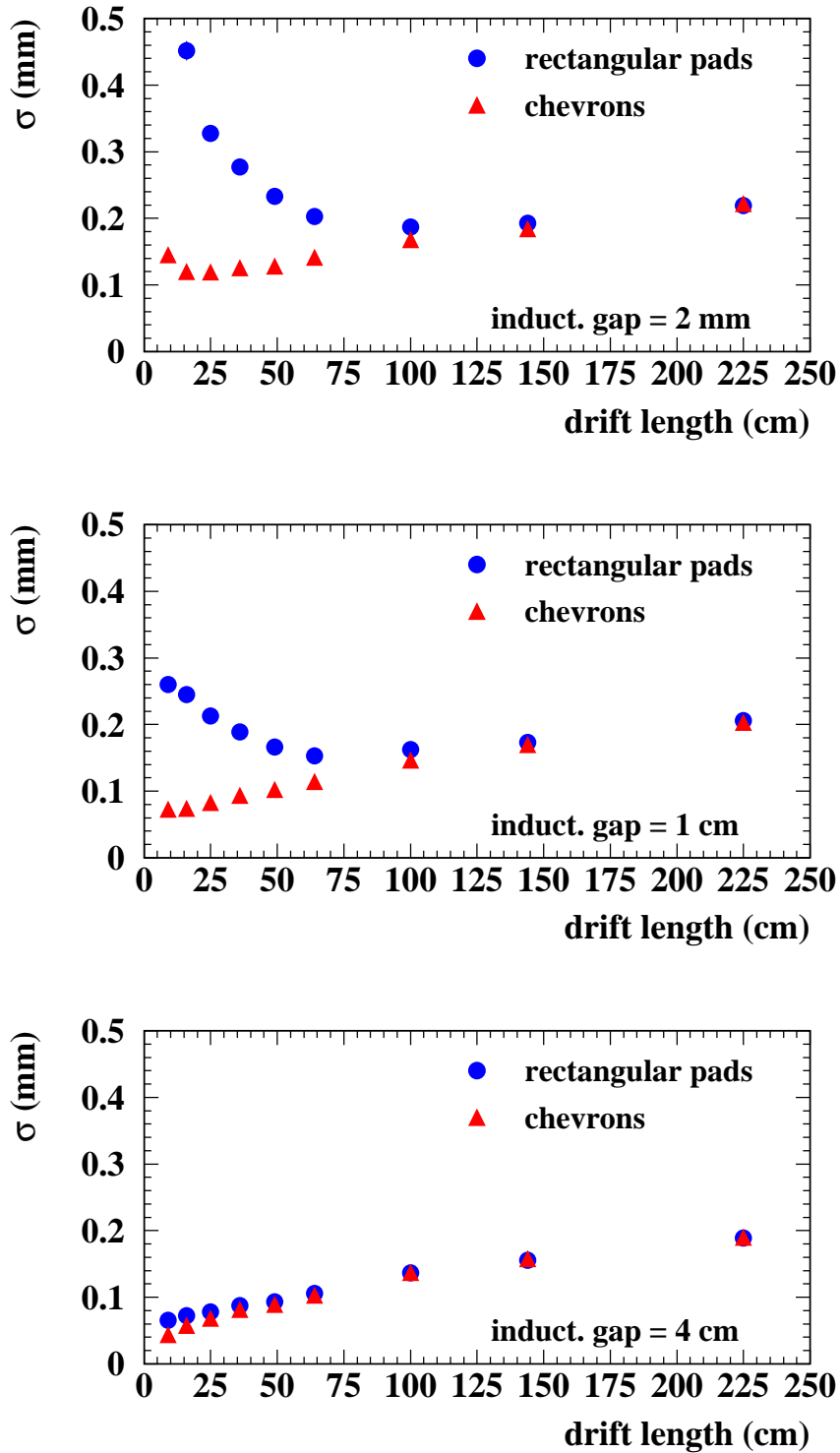


Figure 3.25: Single point resolution vs. drift length (simulation). At each pad the residual between reconstructed and true x coordinate is determined. The point resolution is defined as the width σ of the Gaussian fitted to the distribution of the residuals. Results are shown for both rectangular pads of $2 \times 6 \text{ mm}^2$ (dots) and the corresponding chevron pads (rectangles) for different sizes of the induction gap.

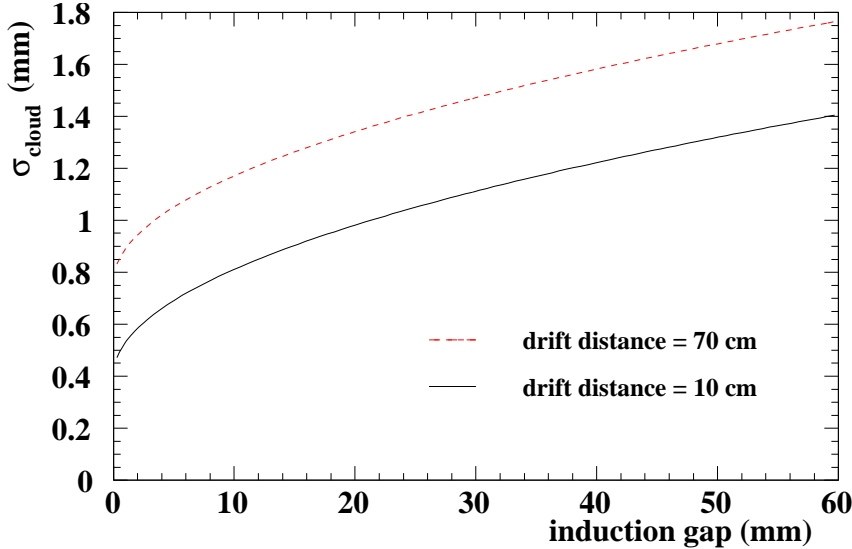


Figure 3.26: Simulated development of the transverse r.m.s. extension of the charge cloud σ_{cloud} on the pad plane as a function of the induction gap (transfer gap = 2 mm), simulated with $E_{\text{ind}} = E_{\text{trans}} = 2.0 \text{ kV/cm}$, $E_{\text{drift}} = 0.23 \text{ kV/cm}$, $B = 4 \text{ T}$ in a gas mixture of Ar-CO₂-CH₄(93 : 2 : 5)% at a drift distance of 10 cm (solid line) and 70 cm (dashed line).

the scaled measurements and the simulation for an induction gap size of 2 mm agree within 20%.

Possible reasons for this discrepancy are drift field distortions, gas impurities, which may change gas diffusion properties, slightly different geometries in simulation (induction gap: 2.0 mm) and measurements (induction gap: 1.5 mm), as well as the fact that for cosmic muon data a threshold for each charge pulse of 30 FADC counts was required while in the simulation no threshold was applied. Furthermore only tracks with normal incident were simulated and the individual channel pedestals (Section 3.3.2) are neglected in the measurements.

The results of the single point resolution studies are summarised in Table 3.2. Some concluding remarks are given below.

- In order to run the GEM module with an induction gap of several centimetres, however, the induction voltage must be adjusted to several thousand volts, which would complicate the handling of the chamber. Other than the studied gas mixtures, e.g. Ar-CF₄, have more suitable diffusion properties, like a high electron diffusion in fields of $\mathcal{O}(\text{kV/cm})$ and low diffusion in fields of the typical drift field strength. Some of these gases are, however, toxic and cause in general fast chamber ageing.
- In order to fully exploit the resolution capability of rectangular pads, however, the simple charge centre of gravity method must be replaced by a fit which takes into account the shape of the pad response function [48].
- Another approach to broaden the electron charge cloud is the use of so-called *resistive foils* between GEM and readout pads [49].

- Alternatively, smaller pads could be used (e.g. $1 \times 6 \text{ mm}^2$) in combination with Time to Digital Converters (TDC) instead of FADCs. This solution would keep the amount of material small in the endplate and is probably within the budget because of the lower cost of TDCs. It has to be shown, however, if TDCs meet all performance requirements [50].
- Finally, a further way to increase the resolution by exploiting the small size of the electron charge cloud after amplification is the use of silicon pixel sensors instead of pads [51, 52].

event type	pad shape	B (T)	ind. gap (mm)	pad size: $x \times y (\text{mm}^2)$	σ_x (mm)	σ_x (mm) scaled to $B = 4 \text{ T}$	σ_z (mm)
muons	rect.	0	1.5	2×6	0.20 – 0.38	–	0.5 – 0.9
muons	rect.	0	1.5	14×14	1.3 – 2.5	$\approx (0.2 – 0.4)$	–
muons	chev.	0	1.5	28×14	1.1 – 1.2	≈ 0.2	–
sim.	rect.	4	2.0	2×6	0.18 – 0.45	–	–
sim.	chev.	4	2.0	2×6	0.10 – 0.20	–	–
sim.	rect.	4	40.0	2×6	0.06 – 0.20	–	–
sim.	chev.	4	40.0	2×6	0.04 – 0.20	–	–

Table 3.2: Summary of the single point resolution studies. The measurement results (muon events) and the results from simulation (sim.) are shown.

3.5 Outlook

The presented results are encouraging for the GEM application in the TPC of a future linear collider. However many more studies are necessary to investigate if all detector requirements are met, such that the advantages offered by GEM application can be fully exploited.

In order to be able to cover all important TPC related issues an international collaboration has been formed with participation of institutes from Asia, North America and Europe [53]. Further R&D issues are

- the determination and optimisation of the double track resolution,
- the operation in a multi track environment using electron/proton test beams,
- the determination and reduction of ion feedback
- TPC and MPGD performance in a magnetic field of 4 T,
- field cage studies concerning the combination of mechanical/electrical stability with low material budget,

- understanding the microscopic processes in MPGDs and
- gas studies.

Finally, the dE/dx performance of a TPC equipped with MPGDs has to be investigated. First simulation studies have already been carried out [54]. Nevertheless test measurements are essential in order investigate the dE/dx potential of GEMs and Micromegas.

Part II

Search for Heavy Stable Charged Particles at LEP

Chapter 4

Theoretical Context

The existence of long-lived or stable charged particles with masses larger than the proton mass ($m \approx 938.27$ MeV) would be evidence for the existence of new phenomena which do not fit into the Standard Model of Elementary Particle Physics, SM [55–57].

A general calculation of particle lifetime via decay rates is introduced in Section 4.1. The approach follows the description given in [58]. The ingredients of the Standard Model will be overviewed in Section 4.2. Many textbooks, for example [58–61], contain more comprehensive and pedagogically nice introductions. Among those theories which predict heavy particles with a long lifetime supersymmetric extensions of the Standard Model are very attractive. A motivation for Supersymmetry (SUSY) and a short introduction of its basic concepts is given in Section 4.3. More fundamental descriptions can be found for example in [62–66]. Then, in Section 4.4, it is explained how heavy charged particles with a long lifetime arise in specific supersymmetric models.

4.1 Decay Rate and Lifetime

For a number of particles N changing with time t , the decay rate Γ is defined via the differential equation

$$\frac{dN}{dt} = -\Gamma N(t). \quad (4.1)$$

Solving this equation yields the decay law

$$N(t) = N(0) \cdot e^{-\Gamma t}. \quad (4.2)$$

If particles decay via i different modes the total decay rate is the sum of the single rates:

$$\Gamma_{\text{tot}} = \sum_i \Gamma_i, \quad (4.3)$$

and the branching ratio, BR_i , for the decay mode i is defined by

$$\text{BR}_i = \frac{\Gamma_i}{\Gamma_{\text{tot}}}. \quad (4.4)$$

Decay rates can be calculated using *Fermi's Golden Rule*: More generally speaking, a decay can be interpreted as a transition between an initial and a final state. The two ingredients for the calculation of the transition rate are the transition amplitude from the initial to the final state and the phase space, which is available for the transition. The amplitude is given by the squared absolute value of the matrix element \mathcal{M} which can be determined using the Feynman calculus:

$$\text{transition rate} = 2\pi|\mathcal{M}|^2 \times (\text{phase space}) . \quad (4.5)$$

In the special case of one particle (with mass m) decaying into two other particles the transition rate becomes the differential decay rate $d\Gamma$; integration over all final state momenta yields the total decay rate

$$\Gamma = \frac{S|\vec{p}|}{8\pi m^2} |\mathcal{M}|^2 . \quad (4.6)$$

Here and in the following, the speed of light (c) and the the Planck constant divided by 2π (\hbar) are set to one. $|\vec{p}|$ is the momentum of any of the outgoing particles in the rest frame of the decaying particle. It depends only on the three particle masses.

The mean lifetime τ is given by the reciprocal value of the decay rate:

$$\tau = \frac{1}{\Gamma} . \quad (4.7)$$

The distance a particle of rest mass m and 3-momentum \vec{p} traverses e.g. in a detector is given by the mean decay length

$$L = \beta\gamma\tau , \quad \text{with} \quad \beta\gamma = \frac{|\vec{p}|}{m} . \quad (4.8)$$

If \sqrt{s} denotes the e^+e^- centre-of-mass energy, pair-produced heavy particles with $\sqrt{s}/2 \gtrsim m \gtrsim \sqrt{s}/4$ yield $\beta\gamma$ values between 0 and 2. If the mean lifetime of a particle is assumed to be $\tau = 10^{-6}$ s, the mean decay length becomes $L \approx 300$ m for $\beta\gamma = 1$. Then, according to Eq. 4.2, more than 99 % of the produced particles traverse the whole detector before they decay (the dimensions of the OPAL detector were roughly 12 m \times 12 m \times 12 m). In this analysis a particle is called long-lived or stable if its mean lifetime is $\tau \geq 10^{-6}$ s.

4.2 The Standard Model

In elementary particle physics, almost all experimental observations are compatible with the Standard Model at a level of very high accuracy [67]. Its fundamental principle is *gauge invariance*: the equations of motion must be invariant under transformations of fermion fields: $\psi \rightarrow S\psi$. Here S is either a phase factor for Abelian transformations or a unitary matrix for non-Abelian transformations. To guarantee the invariance of a Lagrangian density \mathcal{L} under local transformations, i.e. S depends in the space-time coordinate x , the usual space-time derivatives ∂_μ must be extended to covariant derivatives D_μ which include new vector fields V_μ^j :

$$i\partial_\mu \rightarrow iD_\mu = i\partial_\mu - g \sum_j V_\mu^j . \quad (4.9)$$

V_μ^j is interpreted as fields which mediate the interaction while g defines the gauge coupling to matter particles.

The physical contents of the Standard Model can be divided into three parts:

Leptons and quarks, both spin-1/2 fermions, which can be grouped into three families, are the constituents of

$$\text{matter (1)} \quad \left\{ \begin{array}{ll} \text{leptons} & \left(\begin{array}{c} \nu_e \\ e \end{array} \right), \left(\begin{array}{c} \nu_\mu \\ \mu \end{array} \right), \left(\begin{array}{c} \nu_\tau \\ \tau \end{array} \right) \\ \text{quarks} & \left(\begin{array}{c} u \\ d \end{array} \right), \left(\begin{array}{c} c \\ s \end{array} \right), \left(\begin{array}{c} t \\ b \end{array} \right) \end{array} \right. .$$

(Note that the notation used in the present thesis generally does not distinguish between particles and anti-particles. If not specified, either both states are represented at the same time, or, if a particle is named twice in succession, particle and anti-particle are addressed one after the other, e.g.: $ee = e^+e^-$.)

The transformation properties of leptons and quarks are described by the $SU(2)_L \otimes U(1)_Y$ group. $SU(2)_L$ is the non-Abelian weak isospin group, to which three gauge fields, W , are associated; the index L refers to the fact that only left handed fermions couple. The coupling constant is often denoted with g . $U(1)_Y$ is the Abelian hypercharge group associated with the gauge field B . The hypercharge Y is connected with the electric charge Q and the third component of the weak isospin vector by the relation $Y = 2(Q - I_3)$. The corresponding coupling constant is called g' . The photon, γ , and the W^\pm and Z bosons, i.e. the physical fields, are linear combinations of the original gauge fields B and W^j .

The quark mass eigenstates are given by a rotation of the electro-weak eigenstates represented by the Cabibbo-Kobayashi-Maskawa matrix. In addition, quarks interact strongly via colour interaction, mediated by gluons, g . Quarks are eigenstates of the group $SU(3)_C$. Thus, the Standard Model is often called the $SU(3)_C \otimes SU(2)_L \otimes U(1)_Y$ model.

The gravitational interaction is mediated by a spin-2 field, describing the graviton, G . The gravity sector is attached *ad hoc* to the Standard Model, not properly formulated yet as a quantum phenomenon. To summarise, the Standard Model interactions between the constituents of matter are mediated by the

$$\text{gauge fields (2)} \quad \gamma, W^\pm, Z, g.$$

The electromagnetic and weak fields are unified in the electro-weak theory.

A theory can be gauge invariant only if the introduced gauge fields are massless. In the case of the weak interaction this is obviously not the case ($m_{W^\pm} \approx 80$ GeV, $m_Z \approx 91$ GeV). However, the

$$\text{Higgs mechanism (3)}$$

allows to maintain the very successful principle of local gauge invariance by introducing a complex scalar field doublet of the weak isospin, $\Phi = (\Phi^+, \Phi^0)$. The following ansatz is made for the potential density V :

$$V(\Phi) = -\mu^2 |\Phi^* \Phi| + \lambda^2 |\Phi^* \Phi|^2, \quad \mu^2 > 0. \quad (4.10)$$

The ground state of Φ is given by the so called *vacuum expectation value*

$$\langle 0 | \Phi | 0 \rangle = \frac{v}{\sqrt{2}} \begin{pmatrix} 0 \\ 1 \end{pmatrix} \quad \text{with } v = \frac{\mu}{\lambda}. \quad (4.11)$$

The gauge interaction of the three massless vector bosons W^\pm and Z with the Higgs field Φ can be interpreted as the gauge boson masses. In addition, the particle spectrum contains a new boson H with mass $m_H = \sqrt{2\mu^2}$.

The fermion masses are added as *Yukawa couplings* of the fermions with the field Φ . The corresponding coupling constant is denoted with \tilde{g}_f .

The Higgs boson H is the only SM particle which has not been discovered yet.

4.3 Supersymmetric Extensions of the Standard Model

Despite the very successful description of phenomena of elementary particle physics some unsatisfying aspects of the Standard Model in terms of a consistent and simple description of matter cannot be ignored. Some of the most important aspects will be explained in Section 4.3.1. A very elegant solution to these shortcomings provided by supersymmetry, SUSY, is presented in Section 4.3.2. For a reasonable description of Nature, SUSY must be a broken symmetry. SUSY breaking is introduced in Section 4.3.3.

4.3.1 Shortcomings of the Standard Model

The Parameter Problem

The Standard Model contains 18 parameters. If the gravitational constant, the speed of light and the Planck constant are added, matter including its interactions can be described (in principle) using 21 parameters. No guidelines in choosing these values are provided.

Generations

The Standard Model gives no reason for the existence of three generations of leptons and quarks.

Gauge Unification

The success of the unification of the electric and magnetic force and later, the unification of the electromagnetic and the weak interaction, is a strong motivation to assume, that all fundamental interactions unify at a hypothetical mass scale Λ_{GUT} , the scale of a *Grand Unifying Theory* (GUT). The extrapolated $SU(3)_C$, $SU(2)_L$ and $U(1)_Y$ coupling constants do not meet in one single point (Fig. 4.2). Thus, unification of the interactions is impossible in the Standard Model.

Fine Tuning

The Higgs boson mass in the SM is theoretically bounded from above at approximately 1 TeV [67, 68]. However, m_H receives quantum corrections from fermions and bosons via virtual effects of every particle which couples directly or indirectly to the Higgs boson. Figure 4.1 shows the Feynman diagrams of first order corrections to m_H^2 ; the corresponding terms are quadratically divergent:

$$\text{fermion corrections} \quad \Delta m_{H,\text{Yukawa}}^2 \propto -\frac{\tilde{g}_f^2}{16\pi^2} \Lambda_{\text{UV}}^2, \quad (4.12)$$

$$\text{boson corrections} \quad \Delta m_{H,\text{gauge}}^2 \propto \frac{g^2}{16\pi^2} \Lambda_{\text{UV}}^2, \quad (4.13)$$

$$\text{Higgs self interaction} \quad \Delta m_{H,\text{Higgs}}^2 \propto \frac{\lambda^2}{16\pi^2} \Lambda_{\text{UV}}^2. \quad (4.14)$$

\tilde{g}_f , g and λ are the Yukawa, gauge and Higgs self couplings. Note the negative sign for the fermion contribution. The corrections are proportional to Λ_{UV} , which is an (ultraviolet) energy cut-off given by the mass at which the theory becomes invalid. It is often identified with the Planck mass¹ $M_{\text{Pl}} = 1/\sqrt{G} \approx 10^{19}$ GeV (G = gravitational constant). Then, with $m_{H,0}$ denoting the uncorrected or bare Higgs mass, the “correction” turns out to be around 30 orders of magnitude larger than the physical Higgs mass:

$$m_H^2 = m_{H,0}^2 + \Delta m_{H,\text{Yukawa}}^2 + \Delta m_{H,\text{gauge}}^2 + \Delta m_{H,\text{Higgs}}^2. \quad (4.15)$$

Although quantum corrections to fermions and bosons do not depend on Λ_{UV}^2 , the whole mass spectrum is highly sensitive to the cut-off, because all Standard Model particles gain their mass via Yukawa interaction with the Higgs field.

A cancellation of the three correction terms in Eq. 4.15 is technically possible by adjusting λ and the uncorrected mass $m_{H,0}$. However, a tuning of v by 17 orders of magnitude is needed. This is known as the *fine tuning* or *hierarchy problem*.

4.3.2 Basic Ideas of a Supersymmetric Extension

Supersymmetry [69–71] introduces new particles which lead to an unconstrained cancellation of the divergences caused by the quantum corrections to the Higgs mass: for every fermionic particle a bosonic partner is introduced and vice versa. Mathematically, this procedure is described by the complex SUSY generator Q , which carries spin-1/2 and allows transformations like

$$Q|\text{fermion}\rangle = |\text{boson}\rangle \quad \text{and} \quad Q|\text{boson}\rangle = |\text{fermion}\rangle. \quad (4.16)$$

Hence, supersymmetry eliminates the distinction between force mediating and matter particles. In the model with minimal field content, the minimal supersymmetric extension of

¹A theory which does not include gravitation must become invalid and thus be replaced by a more general theory at energies around this scale: The force between two particles at a distance r with the energy $E = M_{\text{Pl}}$ can be estimated according to the gravitational law to be $F \approx 1/r^2$ and cannot be ignored anymore in a theory of matter beyond this scale.

the Standard Model (MSSM) [63, 72], one SUSY partner for each Standard Model particle with the same quantum numbers except for the spin is introduced. In this model, SUSY is a global symmetry, i.e. SUSY transformations are constant throughout space. However, SUSY is often assumed to be a local symmetry, since then it might be possible to unify space-time symmetries of general relativity with local supersymmetric transformations. Local supersymmetry is often called supergravity or SUGRA and can be embedded in the wider framework of string theories [73].

The Standard Model particles and their supersymmetric partners are summarised in Table 4.1 (The supersymmetric partners of Standard Model fermions are called like the fermion plus an additional “s”, e.g. *selectron*, while the name of the partners of bosons is built with the ending “ino”, e.g. *zino*. Sometimes SUSY particles are also called *sparticles* without distinguishing between fermions or bosons.).

SM particle	spin	SUSY particle	spin
lepton ℓ	1/2	slepton $\tilde{\ell}$	0
neutrino ν	1/2	sneutrino $\tilde{\nu}$	0
quark q	1/2	squark \tilde{q}	0
photon γ	1	photino $\tilde{\gamma}$	1/2
W	1	wino \tilde{W}	1/2
Z	1	zino \tilde{Z}	1/2
gluon g	1	gluino \tilde{g}	1/2
Higgs boson H	0	higgsino \tilde{H}	1/2
graviton G	2	gravitino \tilde{G}	3/2

Table 4.1: Standard Model particles (left) and the corresponding supersymmetric particles (right)

The SUSY Higgs sector is slightly more complicated than in the Standard Model, because two Higgs doublets are required [62]: $H_1 = (H_1^0, H_1^-)$ and $H_2 = (H_2^+, H_2^0)$. The ratio of their vacuum expectation values v_1 and v_2 is expressed by the parameter

$$\tan \beta = \frac{v_2}{v_1}. \quad (4.17)$$

From the eight degrees of freedom of the two complex doublets, like in the Standard Model, three are identified with the longitudinal degrees of freedom of the the W and Z bosons, leaving five physical states: two CP-even neutral states h^0 and H^0 , the CP-odd neutral state A^0 and two charged states, H^\pm . H_1 and H_2 exhibit mixing which is described by the parameter μ , called *Higgs sector mixing parameter*.

The superpartners of the electroweak gauge bosons, the photino, Zino and wino, are called *gauginos* while the superpartners of the Higgs bosons are named *higgsinos*. Linear combinations of the gauginos and higgsinos yield two charged states, the charginos χ_i^\pm ($i = 1, 2$), and four neutral states, the neutralinos χ_i^0 ($i = 1, \dots, 4$). Here the smaller index denotes the lighter particle by convention.

If supersymmetry exists, the Higgs boson mass receives quantum corrections not only from Standard Model particles but also from the corresponding SUSY partners. Since there are equal numbers of fermion and boson particles with equal couplings, the contributions from the supersymmetric particles cancel those from their Standard Model partners, which means that no fine tuning is necessary anymore.

Once supersymmetric particles are introduced, even more defects of the Standard Model can be solved: a unification of the electroweak and the strong interaction becomes possible [59]: extrapolation of the the $U(1)_Y$, $SU(2)_L$, $SU(3)_C$ coupling constants to energies around 10^{16} GeV yields a common intersection point, see Fig. 4.2.

Furthermore, assuming that all supersymmetric particles decay into lighter superpartners except for the lightest supersymmetric particle (LSP), the latter, if stable, is a candidate for dark matter in the universe [74]. The condition of a stable LSP can be formulated as the requirement of conservation of R-parity. This quantum number is introduced to distinguish between SUSY and Standard Model particles and given by

$$P_R = (-1)^{3(B-L)+2s}. \quad (4.18)$$

B and L denote the baryon and lepton number, respectively, and s is the spin of the particle. Following the majority of SUSY models, in this analysis R-parity conservation is assumed.

4.3.3 Supersymmetry Breaking

Since exact supersymmetry leads to mass degeneracy of Standard Model and supersymmetric partner particles, supersymmetry must be a *broken* symmetry. Otherwise supersymmetric partner particles would have been already observed. There would exist for example a negatively charged particle with a mass of 0.511 MeV and spin 0, the selectron.

However, the exact cancellation of the quadratic divergences in the calculation of the Higgs mass is given only, if Standard Model and supersymmetric particles have exactly the same mass. Nevertheless, if the condition $|m_b^2 - m_f^2| \lesssim 1 \text{ TeV}^2$ is fulfilled for the boson and fermion masses m_b and m_f , quadratically divergent radiative corrections to the Higgs mass can still be avoided [64]. This kind of symmetry breaking is often referred to as *soft* SUSY breaking and the effective Lagrangian can be written as

$$\mathcal{L} = \mathcal{L}_{\text{SUSY}} + \mathcal{L}_{\text{soft}}. \quad (4.19)$$

Here $\mathcal{L}_{\text{SUSY}}$ preserves and $\mathcal{L}_{\text{soft}}$ violates supersymmetry invariance. The soft breaking part of the Lagrangian contains only mass terms and couplings with positive mass dimensions. It can be shown, that in this case, quantum corrections to the squared Higgs mass can only be logarithmic, i.e. they are of reasonable size compared to the physical mass [62]:

$$\Delta m_H^2 \propto m_{\text{soft}}^2 \ln \left(\frac{\Lambda_{\text{UV}}}{m_{\text{soft}}} \right); \quad (4.20)$$

m_{soft} describes the largest mass scale in $\mathcal{L}_{\text{soft}}$.

From a theoretical point of view, supersymmetry should be an exact symmetry which is spontaneously broken analogously to electroweak symmetry breaking [59] by the introduction of a field with a non-zero vacuum expectation value. However it turns out,

that this procedure is not possible without breaking additionally the $SU(3)_C$ or $U(1)_Y$ symmetry. Therefore, supersymmetry breaking is believed to happen in an additional sector of particles, the *hidden sector*, which has only small couplings to the *visible sector* of MSSM particles. According to this model, the soft breaking terms in the MSSM arise indirectly or radiatively as a result of the interaction between both particle sectors.

Depending on the messenger field which mediates this interaction, different kinds of breaking mechanisms are distinguished. Each reduces dramatically the number of model parameters: A careful counting [75] shows that the supersymmetry breaking term, $\mathcal{L}_{\text{soft}}$, introduces 105 masses, phases and mixing angles for the MSSM. This large number can be reduced to six or less if a specific SUSY breaking is assumed.

The way supersymmetry is broken influences directly the particle spectrum, and, in particular, it determines, how heavy stable charged particles can arise in e^+e^- reactions.

4.4 Production, Decay and Lifetime of Supersymmetric Particles

Assuming R-parity conservation, in e^+e^- collisions SUSY particles are pair-produced. The production proceeds via s-channel and, if allowed by conservation laws, via additional t-channel contribution. The Feynman diagram for slepton pair-production is shown in Fig. 4.3. The production of staus and smuons is model-independent, since this process is mediated only by s-channel γ, Z exchange. The e^+e^- pair-production cross-section, however, has a contribution from t channel neutralino exchange and thus depends on the neutralino mass and couplings. The diagrams for chargino and neutralino pair-production are shown in Figs. 4.4 and 4.5, respectively. For charginos, sneutrino t-channel exchange contributes to the production cross-section. For neutralinos, a selectron is exchanged in the t-channel. A complete description of all supersymmetric interactions and a computation of the Feynman rules of the MSSM can be found in [72, 76, 77].

In the following, the three most discussed SUSY breaking scenarios are surveyed including the way supersymmetric stable charged particles can be produced.

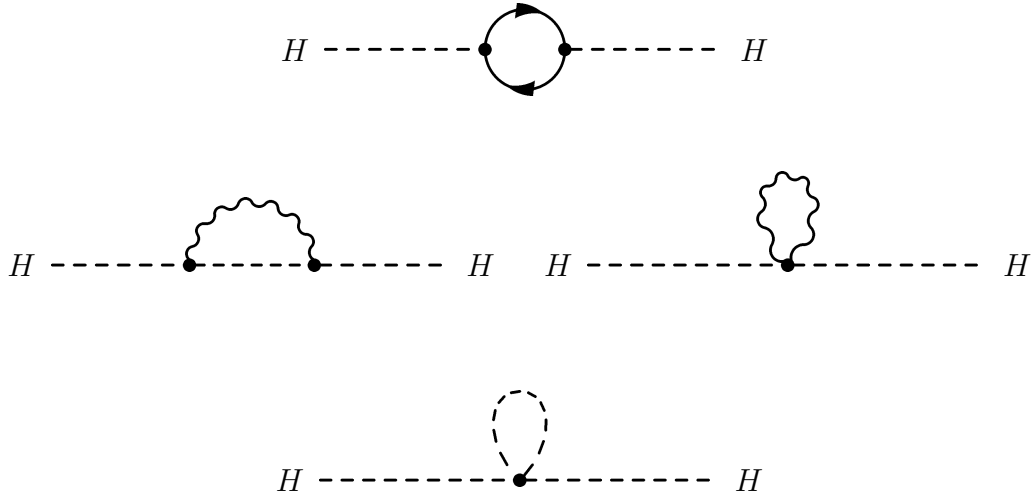


Figure 4.1: Quantum corrections to the square of the Higgs mass: upper diagram: fermion contribution, middle: boson contributions, lower diagram: Higgs self interaction.

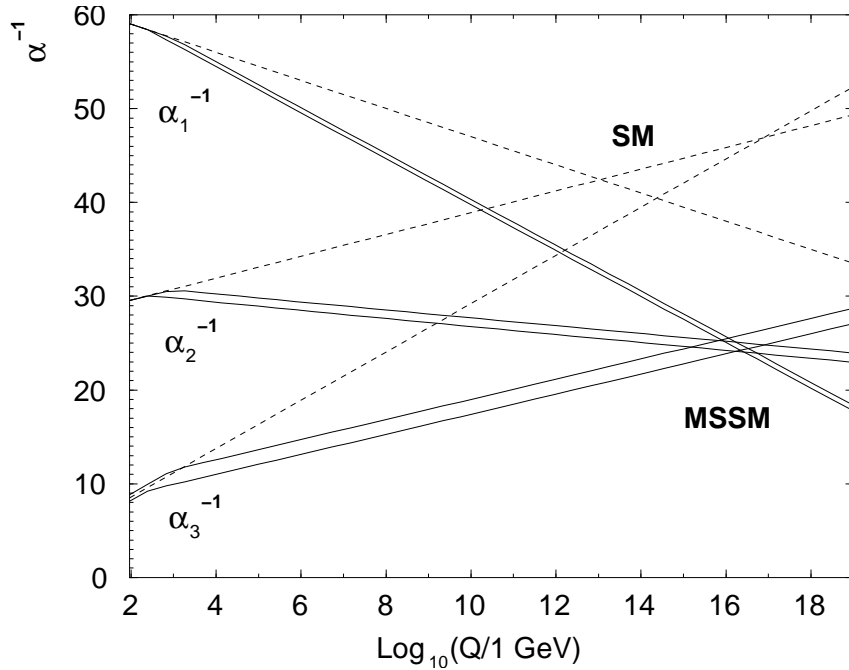


Figure 4.2: Running of the inverse of the coupling constants $\alpha_a^{-1}(Q)$ of the $U(1)_Y$, $SU(2)_L$, $SU(3)_C$ gauge groups in the Standard Model (dashed lines) and in the MSSM (solid lines; the widths represent the theoretical uncertainties). Quantum corrections up to 2 loops are included [59]. In contrast to the Standard Model, in supersymmetry a unification of the gauge constants at around 10^{16} GeV is possible.

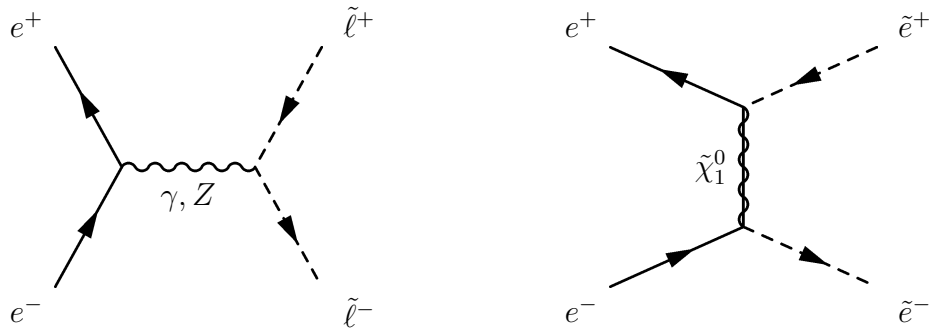


Figure 4.3: Pair-production of supersymmetric scalar leptons (sleptons) ($\tilde{\ell} = \tilde{\tau}, \tilde{\mu}, \tilde{e}$). t-channel production is possible for selectrons only, it may contribute destructively or constructively; . In the presented search, the production of the lightest sleptons are considered, i.e. $\tilde{\tau}_1$ in the stau NLSP scenario and $\tilde{\tau}_1, \tilde{\mu}_R, \tilde{e}_R$ in the slepton co-NLSP scenario.

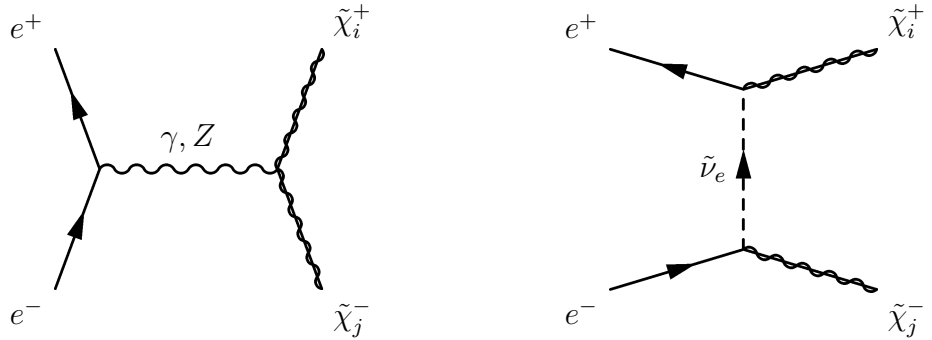


Figure 4.4: s- and t-channel production of chargino pairs; s- and t- channel interfere destructively. The shown indices can be one or two. In the presented search only $i = j = 1$ is considered.

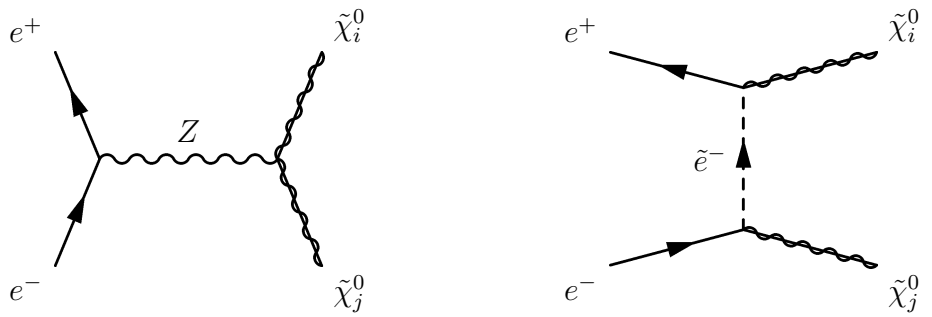


Figure 4.5: s- and t-channel production of neutralino pairs. The channels may interfere constructively or destructively. The shown indices run from one to four. In the presented search only $i = j = 1$ is considered.

4.4.1 Gauge Mediated Supersymmetry Breaking

In gauge mediated supersymmetry (GMSB) models, SUSY breaking is transmitted to the visible sector via gauge interactions [65, 66, 78]. Here the hidden sector communicates via new gauge interactions with the messenger sector, which, in turn, communicates via ordinary gauge interaction with the observable sector. In this case, the mass scale of the messenger field, M , can be anywhere between the electroweak and the Planck scale. The energy scale below which supersymmetry is broken is called the SUSY *breaking scale* and denoted with \sqrt{F} . In GMSB models, it is basically unconstrained and can be as low as 10 TeV.

Apart from M and \sqrt{F} , the GMSB framework is determined by Λ , denoting a universal mass scale of the SUSY particles, $\tan \beta$, the ratio of the vacuum expectation values of the two Higgs doublets, $\text{sign}(\mu)$, the sign of the mixing parameter of the Higgs doublet fields and N which represents the number of generations of messenger particles. Thus, six parameters are enough to constrain GMSB models.

The LSP is always the gravitino, \tilde{G} . Under the condition of vanishing cosmological constant [79], its mass is given by [78, 80]

$$m_{\tilde{G}} = \frac{F}{k\sqrt{3}M_P} \quad (4.21)$$

k is a model-dependent parameter describing how SUSY breaking is communicated to the messenger sector, with $k < 1$ and possibly $k \ll 1$. The next-to-lightest supersymmetric particle (NLSP) determines the experimental signature via its decay into the LSP plus Standard Model particles. Different NLSP scenarios are distinguished [80]: the NLSP can be the lightest neutralino, $\tilde{\chi}_1^0$, or the lightest stau, $\tilde{\tau}_1$, which constitutes, together with $\tilde{\tau}_2$, the mixed mass eigenstates of the superpartners of the left- and right-handed taus, $\tilde{\tau}_L$ and $\tilde{\tau}_R$. The scenarios are called *neutralino NLSP* and *stau NLSP scenario*, respectively. Alternatively, the $\tilde{\tau}_1$ can be almost mass degenerate with the superpartner of the right-handed electron, \tilde{e}_R , and the superpartner of the right-handed muon, $\tilde{\mu}_R$. This case is called *slepton co-NLSP scenario*.

The decay of the NLSP depends on the coupling of the gravitino, which is proportional to $1/m_{\tilde{G}}$. Hence, the NLSP decay width is

$$\Gamma_{\text{NLSP}} \propto (1/m_{\tilde{G}})^2 \propto (1/\sqrt{F})^4, \quad (4.22)$$

and a numerical value for the mean NLSP decay length can be obtained using [78, 80]:

$$L = 9.9 \times 10^{-7} \frac{1}{\kappa_\gamma} \left(\frac{100 \text{ GeV}}{m_{\text{NLSP}}} \right)^5 \left(\frac{\sqrt{F/k}}{10 \text{ TeV}} \right)^4 \left(\frac{E_{\text{NLSP}}^2}{m_{\text{NLSP}}^2} - 1 \right)^{1/2} \text{ cm}. \quad (4.23)$$

κ_γ is a factor determining the mixing of the neutralino components. For the stau and slepton-co NLSP scenario it is equal to 1; m_{NLSP} and E_{NLSP} are the mass and the energy of the NLSP. Depending on \sqrt{F} , the decay length of the NLSP can vary between microscopical and astronomical distances. Figure 4.6 shows the mean slepton decay length in the laboratory frame as a function of the gravitino mass, with different slepton masses, calculated according to Eqs. 4.21 and 4.23. In the present analysis, the stau and slepton co-NLSP scenarios are relevant, because they can give rise to a heavy stable charged particle, the charged NLSP, leaving an anomalous ionisation track in the detector. The NLSP production modes considered in the present search are the following.

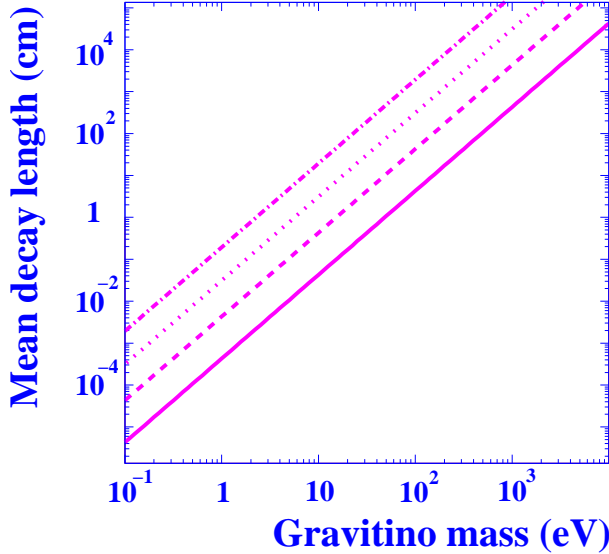


Figure 4.6: Mean slepton decay length in the laboratory frame as a function of the gravitino mass in GMSB models, for pair-produced sleptons with masses of 100 GeV (solid line), 80 GeV (dashed line), 60 GeV (dotted line), and 45 GeV (dashed-dotted line). The plot is taken from [81].

Direct NLSP production

In the simplest case the lightest slepton is pair-produced (Fig. 4.3) and decays into its corresponding lepton and a gravitino, as illustrated in Fig. 4.7. This mode is possible in the stau and slepton co-NLSP scenario. The t-channel may contribute destructively or constructively [80].

NLSP as secondary particle

In both stau and slepton co-NLSP scenarios, the stable slepton (NLSP) and a lepton may be produced as decay products of previously pair-produced SUSY particles: pair-produced charginos decay into a stable slepton and a neutrino, which carries away a significant energy fraction without being detected. The chargino decay is shown in the Feynman graph in Fig. 4.8. The NLSP production via pair-produced neutralinos (Fig. 4.9) can be an important discovery mode because s- and t-channel may interfere constructively, such that the production cross-section is larger than for direct NLSP production [80]. The neutralino decay is shown in the Feynman graph in Fig. 4.9.

NLSP as tertiary particle

In the case the pair-produced sleptons are not the NLSP (in the stau NLSP scenario), the stable particle can arise as tertiary particle via an additional intermediate state, the neutralino. The decay chain is shown in Fig. 4.10.

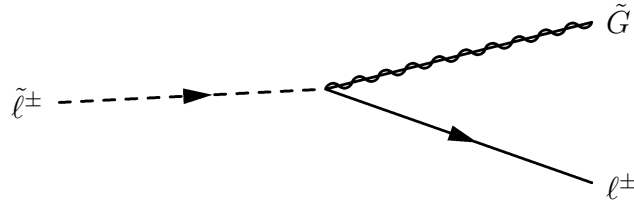


Figure 4.7: NLSP decay in the GMSB model in the stau NLSP and slepton co-NLSP scenario; $\tilde{\ell} = \tilde{e}_R, \tilde{\mu}_R, \tilde{\tau}_1$ and $\ell = e, \mu, \tau$.

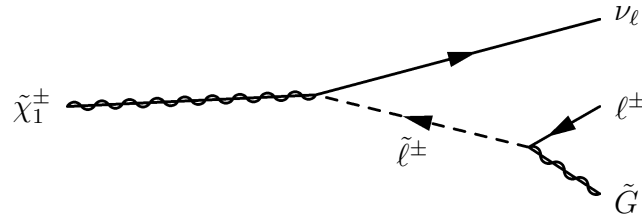


Figure 4.8: Chargino decay in the GMSB model in the stau NLSP and slepton co-NLSP scenario. The stable slepton (NLSP) appears as secondary particle in the decay chain; $\tilde{\ell} = \tilde{e}_R, \tilde{\mu}_R, \tilde{\tau}_1$; $\ell = e, \mu, \tau$.

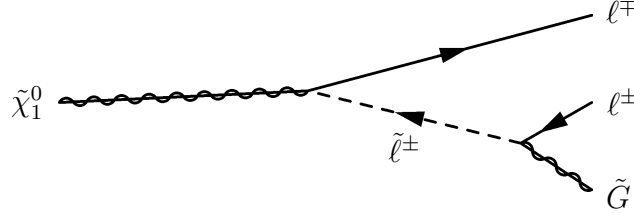


Figure 4.9: Neutralino decay in the GMSB model in the stau NLSP and slepton co-NLSP scenario. The stable slepton (NLSP) appears as secondary particle in the decay chain; $\tilde{\ell} = \tilde{e}_R, \tilde{\mu}_R, \tilde{\tau}_1$; $\ell = e, \mu, \tau$.

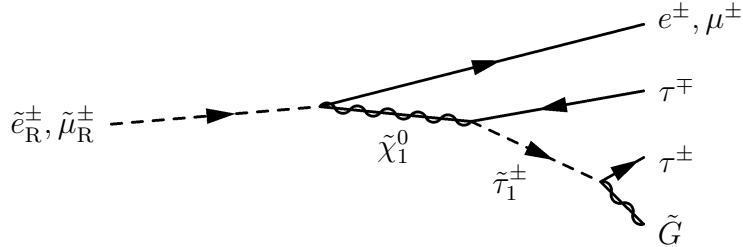


Figure 4.10: Slepton decay mode in the GMSB model in the stau NLSP scenario. The stable stau (NLSP) appears as tertiary particle in the decay chain of a previously pair produced selectron or smuon; $\tilde{\ell} = \tilde{e}_R, \tilde{\mu}_R, \tilde{\tau}_1$ and $\ell = e, \mu, \tau$

4.4.2 Gravity and Anomaly Mediated Supersymmetry Breaking

In the gravity mediated SUSY breaking scenario the hidden and visible sector interact via gravitational interactions. The mass scale of the messenger field M is required to be near the Planck scale. \sqrt{F} is in the order of 10^{11} GeV [65].

The minimal Supergravity (mSUGRA), which assumes unification of gaugino masses, Yukawa couplings and masses of scalar fermions (sfermions) at the GUT scale, is fully described by five parameters: a universal scalar mass, m_0 , the universal gaugino mass, $m_{1/2}$, a (trilinear) coupling A_0 , $\tan\beta$, and $\text{sign}(\mu)$. The LSP is either the lightest stau, $\tilde{\tau}_1$, or the lightest neutralino, $\tilde{\chi}_1^0$.

A special case of gravity mediation is the anomaly mediated supersymmetry breaking (AMSB). Here no direct tree level coupling transmits the SUSY breaking from the hidden sector to the observable one. In this case the masses of the gauginos are generated at one-loop, while those of the scalars are generated at two-loop level. The AMSB framework is described by four parameters: the scalar mass m_0 , the gravitino mass $m_{3/2}$, $\tan\beta$ and $\text{sign}(\mu)$.

The LSP is the lightest neutralino, $\tilde{\chi}_1^0$, which is almost degenerate in mass with the lightest chargino, $\tilde{\chi}_1^\pm$, the NLSP. A possible discovery channel searched for in this analysis is the pair-production of $\tilde{\chi}_1^\pm$ (Fig. 4.4). s- and t-channel interfere destructively; for electron sneutrino masses larger than $\mathcal{O}(100\text{ GeV})$ the s-channel production dominates. In mSUGRA and AMSB the NLSP lifetime depends only on the accessible phase space determined by the small mass difference $\Delta m_{\tilde{\chi}_1} = m_{\tilde{\chi}_1^\pm} - m_{\tilde{\chi}_1^0} \approx (0.1 - 2)\text{ GeV}$ [82]. For values below the pion mass, $\tilde{\chi}_1^\pm$ decays entirely into $\tilde{\chi}_1^0 + e/\mu + \nu_{e/\mu}$; values below 0.1 GeV yield long-lived or stable charginos according to the definition given above. Figure 4.11 shows the lifetime as a function of the mass difference and the corresponding branching ratios. The figure is taken from [83].

Apart from AMSB, very small mass differences between chargino and neutralino can also occur in other SUSY models [83–86].

4.4.3 General Searches for Supersymmetric Particles with Lifetime

As neither the SUSY breaking mechanism nor the values of the free parameters are known in the previously described scenarios, the lifetime of the NLSP is basically arbitrary. This implies, that apart from long NLSP lifetimes ($\tau \geq 10^{-6}\text{ s}$), shorter lifetimes down to almost promptly decaying NLSPs are possible. For this reason, a general search for SUSY particles must cover all lifetime scenarios by combining the present analysis with other searches [87,88]: For very short lifetimes ($\tau \lesssim 10^{-10}\text{ s}$) special topologies with lepton pairs are searched for, for short lifetimes ($10^{-11}\text{ s} \lesssim \tau \lesssim 10^{-9}\text{ s}$) event signatures contain tracks with displaced vertices and a medium lifetime NLSP ($10^{-9}\text{ s} \lesssim \tau \lesssim 10^{-6}\text{ s}$) produces a kinked track in the detector.

For completion, it must be mentioned that different sources of SUSY breaking may be present at once, so that the model which is realised in nature can be quite complicated.

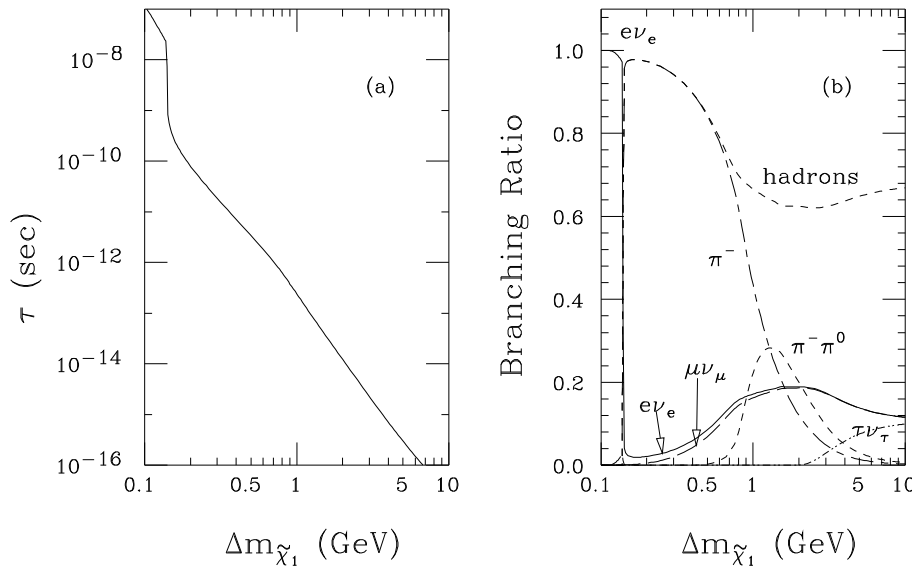


Figure 4.11: Lifetime of the lightest chargino $\tilde{\chi}_1^\pm$ as a function of $\Delta m_{\tilde{\chi}_1} = m_{\tilde{\chi}_1^\pm} - m_{\tilde{\chi}_1^0}$ (a) and the corresponding branching ratios of the $\tilde{\chi}_1^\pm$ (b); the neutralino (LSP) is not listed. For $\Delta m_{\tilde{\chi}_1} < 0.1$ GeV the chargino becomes long-lived or stable, i.e. it decays outside the detector. The figure is taken from [83].

Chapter 5

Experimental Approach

This chapter deals with the experimental apparatus, which was used to take data for the present search for heavy stable charged particles: first, the LEP collider is introduced in Section 5.1; hereafter the OPAL Detector (Section 5.2) is overviewed including the introduction of track parameters and the event reconstruction software. As the jet chamber is the most important detector part in this analysis, it is described in more detail in Section 5.3. A major part is dedicated to its application in the identification of heavy stable charged particles including a new approach for maximum ionising particles, i.e. heavy stable charged particles with low $\beta\gamma$. Finally, Section 5.4 deals with the OPAL trigger; the monopole or high dE/dx trigger will be explained in detail as well as the determination of its efficiency.

5.1 The LEP Collider

The LEP collider was built at CERN close to Geneva, Switzerland during the 1980s. A picture of the LEP site is shown in Fig. 5.1. From 1989 to 1995 LEP was operating at centre-of-mass energies around the Z resonance (LEP I period), i.e. beam energies of about 45.6 GeV, accelerating electrons and positrons in opposite direction. From 1996 onwards, the centre-of-mass energy was increased continuously up to a maximum of 209 GeV in the year 2000 (LEP II period). In the end of the year 2000 the LEP collider was shut down and dismantled.

5.2 The OPAL Detector

Four particle detectors for the investigation of e^+e^- collisions were located at the LEP storage ring: ALEPH, DELPHI, L3 and OPAL. The present analysis is based on data recorded with the OPAL detector. A schematic picture of the detector is shown in Fig. 5.2. In the following the OPAL coordinate system and the track parameters are introduced, and the design of the detector is explained briefly. Finally, the event reconstruction software is presented.

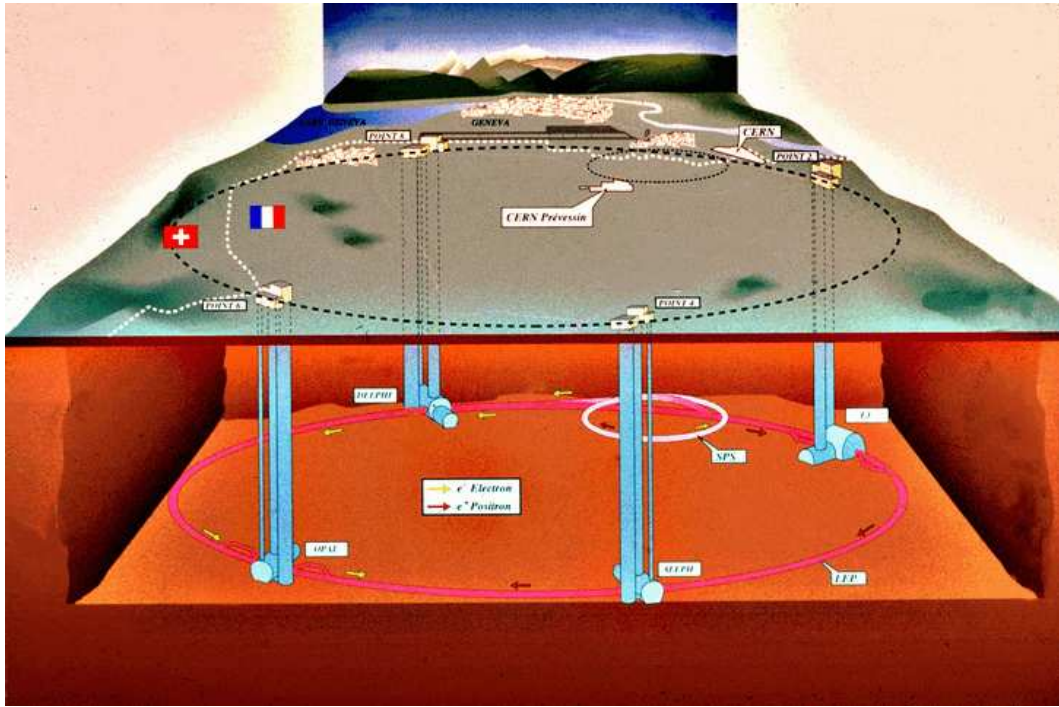


Figure 5.1: View of the LEP accelerator location at CERN

5.2.1 Coordinate System and Track Parameters

The OPAL coordinate system has its origin at the interaction point with the z axis along the electron beam direction and the x axis horizontal, directed towards the centre of LEP. The y axis is perpendicular to the $z - x$ plane. In order to meet the detector geometry, cylindrical coordinates are introduced: the radius r , the azimuthal angle ϕ , and the polar angle θ (Fig. 5.2).

In this coordinate system a helical track from a charged particle is determined by five parameters:

- κ is the curvature defined as $\kappa = q_0/2\rho$; with ρ being the radius of the track and q_0 is the charge of the particle. κ is signed such that it is clock-wise/anti clock-wise for positively/negatively charged particles;
- ϕ_0 is the azimuthal angle of the tangent to the track at the point of closest approach, PCA;
- $\tan \lambda = \cot \theta$;
- d_0 , the *impact parameter*, is the distance from the origin to the PCA in the transversal $r - \phi$ plane;
- z_0 is the z coordinate of the track at the PCA.

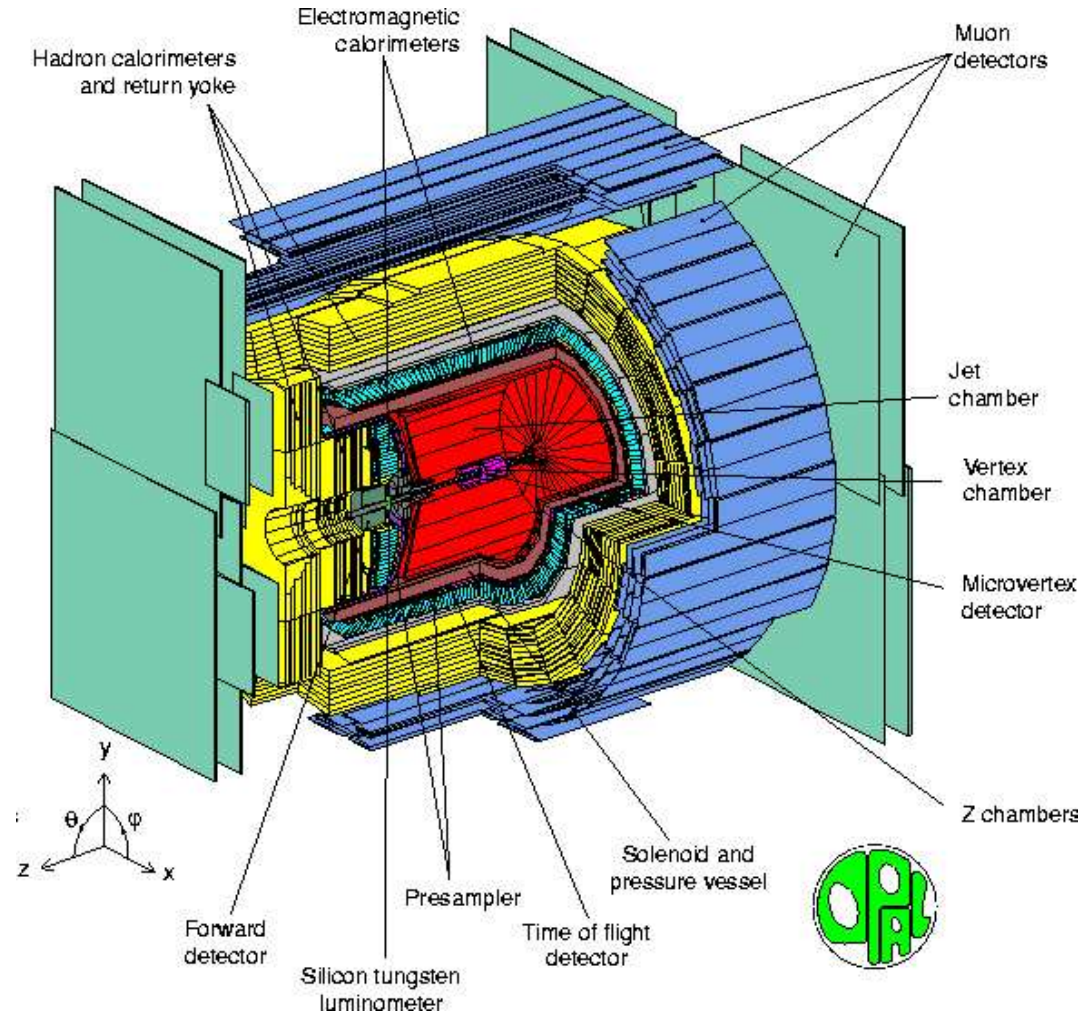


Figure 5.2: Schematic of the OPAL Detector

5.2.2 General Design

The OPAL detector, described in detail in [89], was a multipurpose particle detector with almost full solid angle coverage. Its central tracking system consisted of the silicon microvertex detector (SI), the vertex drift chamber (CV), the central jet chamber (CJ), and the z-chambers (CZ). The aim of the vertex detectors was to improve the measurement of secondary vertices of short-lived particles and to provide a precise measurement of the z coordinate near the interaction region. SI consisted of two concentric layers of silicon strip detectors with radii 6.1 and 7.5 cm, respectively. The length of the layers was 18.3 cm providing an angular acceptance of $|\cos \theta| < 0.93$ and $|\cos \theta| < 0.89$, respectively. The point resolution was measured to $\sigma_\phi = 18 \mu\text{m}$ and $\sigma_z = 24 \mu\text{m}$. CV had a length of 1 m, an inner/outer radius of 8.8/23.5 cm. It was divided into 36 sectors. The inner part (up to a radius of 17.5 cm) of each sector was called the *axial cell*. Each axial cell contained twelve staggered signal wires parallel to the beam. A spatial resolution of 55 μm in $r - \phi$ and of 4 cm in z was reached. The so-called *stereo cell* was the outer part of each sector. Here six signal wires were oriented such that the angle between them and the axial wires was 4° , improving the z resolution to 700 μm . For tracks in the barrel

region of the detector the CZ system enhanced the z resolution and the precision of the measurement of the polar angle θ . It consisted of 24 drift chambers with a thickness of 5.9 cm. Each chamber was divided into eight sectors which in turn contained six signal wires perpendicular to the beam direction. Point resolutions of 1.5 cm in $r - \phi$ and 100 – 300 μm . in z , depending on the drift distance, were achieved. The design and performance of the CJ is described separately in Section 5.3.

The central tracking system was surrounded by scintillators measuring the time-of-flight (TOF), presamplers and the electromagnetic lead glass calorimeter (ECAL). Outside the electromagnetic calorimeter was the magnet return yoke, which was instrumented with streamer tubes and served as hadronic calorimeter (HCAL). The muon chambers formed the outermost part of the detector while the silicon tungsten calorimeters (SW), the forward detectors (FD) and the gamma catcher (GC) on both sides of the interaction point were used to measure the luminosity and to increase the sensitive area of the detector close to the beam pipe, i.e. small polar angles, see next section.

5.2.3 Event Reconstruction

The reconstruction of particle reactions, the *event reconstruction*, is carried out with the computer programme ROPE [90]. It is a collection of modules designed to reconstruct events from digits produced by the OPAL detector or by the OPAL simulation (Section 6.2). Its aim is to produce the Data Summary Tapes (DST) containing all relevant information for further physics analyses such as *raw data*, i.e. event information on the level of individual hits, and *processed data*, i.e. event information such as tracks along the particle path or calorimeter clusters built from the response of the ECAL and HCAL.

In a further step, tracks and clusters are put together. In order to avoid energy double counting an energy flow algorithm (see also Section 2.2) is applied [91–93]. The algorithm tries to match reconstructed tracks and calorimeter clusters. Clusters without matching tracks, i.e. unassociated clusters, are treated as originating from neutral massless particles. In case of associated clusters the expected deposited energy is calculated from the track momenta and the tracks' polar angles. If the expected energy exceeds the measured energy in the calorimeter, the cluster is discarded and the track is treated as originating from a charged particle with the pion mass assigned to it. If the measured energy exceeds the expected energy, the energy difference is assumed to be deposited by an additional photon. From an experimental point of view the term *particle* assigns to the objects reconstructed by this procedure.

5.3 The OPAL Jet Chamber

5.3.1 Design

The CJ was a drift chamber (Section 1.5) which consisted of a 4 m long cylinder with an outer/inner radius of 1.85/0.25 m. It was divided in ϕ into 24 identical sectors, each containing a sense wire plane with 159 anode wires and two cathode wire planes which formed the boundaries between adjacent sectors. All wires were parallel to the beam direction and the wire planes are radial. The anode wires provided up to 159 measurements

per track in the region $|\cos\theta| < 0.73$. The maximum drift distance in the sectors was 25.5 cm. It operated in a gas mixture of 88.2 % argon, 9.8 % methane and 2.0 % isobutane in a pressure vessel at 4 bar.

5.3.2 Performance

Coordinate resolution and tracking

Averaging over all drift distances, the overall point resolution in the $r-\phi$ plane, determined with $Z \rightarrow \mu^+\mu^-$ events was determined to be $\sigma_{r-\phi} = 135 \mu\text{m}$. In $r - z$, the intrinsic coordinate resolution was found via charge division (Section 1.5.2) to be $\sigma_z = 4.5 \text{ cm}$. For hadronic events it is slightly worse ($\sigma_z = 6.0 \text{ cm}$). The values correspond to roughly (1–2) % of the wire length, which is typical for resolutions obtained with charge division. The point resolutions are summarised in Table 5.1 together with the single hit performance of the other OPAL tracking devices.

The momentum resolution of the CJ was $\sigma_p/p^2 = 1.410^{-3} \text{ GeV}^{-1}$. The resolution of the other track parameters was 0.32 mrad in ϕ , 13.9 mrad in θ , 88 μm for the impact parameter d_0 , and 5.3 cm for z_0 . The tracking performance, especially of the z parameters, i.e. θ and z_0 , was improved significantly by combining the information of all tracking detectors: 1.4 mrad in θ and 22 cm in z_0 were achieved. Table 5.2 summarises the CJ tracking capability and the corresponding numbers obtained by using information of all gaseous trackers together as well as all trackers including the silicon vertex detector, SI. The tracking performance was determined with data collected at the centre-of-mass energy of the Z resonance.

dE/dx performance

For at least 130 required charge samples per track, i.e. 130 measurements used to determine the specific energy loss, dE/dx resolutions of $\sigma(dE/dx)/(dE/dx) = 3.1\%$ for muons in Z decay and 3.8 % for minimum ionising pions are achieved. In the region of the relativistic rise, a separation with a probability of at least 2σ is possible up to 13 GeV between electrons and pions, and up to 20 GeV between pions and kaons or pions and protons [94].

point resolution	central jet chamber	silicon vertex detector	central vertex detector	z-chambers
$r - \phi$	135 μm	10 μm	55, μm	1.5 cm
z	(5.5 – 6.0) cm	15 μm	700 μm	300 μm

Table 5.1: Single hit performance of the central jet chamber and the other tracking subdetectors.

5.3.3 Signal Separation using the dE/dx Measurement

The measurement of the specific energy loss, dE/dx (Section 1.6), provides a powerful tool to isolate signal topologies searched for in this analysis. The dE/dx of Standard

resolution	central jet chamber	jet chamber + vertex chamber + z-chambers	all tracking devices
σ_p/p^2	$1.410^{-3} \text{ GeV}^{-1}$	$1.310^{-3} \text{ GeV}^{-1}$	$1.2510^{-3} \text{ GeV}^{-1}$
ϕ	0.32 mrad	0.29 mrad	0.275 mrad
θ	13.9 mrad	1.4 mrad	1.4 mrad
d_0	$88 \mu\text{m}$	$39 \mu\text{m}$	$16 \mu\text{m}$
z_0	5.3 cm	930 μm	22 μm

Table 5.2: Tracking performance of the central jet only chamber and combined tracking performances. The numbers were obtained mainly from 1995 data collected at the energy of the Z resonance.

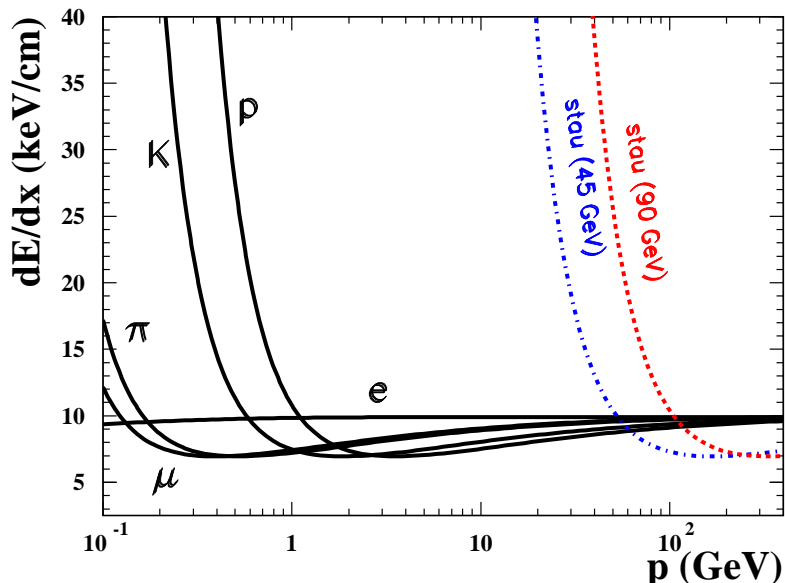


Figure 5.3: Expected distribution of the ionisation energy loss dE/dx as a function of the momentum for Standard Model particles and two heavy stable charged scalar particles ($\tilde{\tau}$) with $m = 45 \text{ GeV}$ and $m = 90 \text{ GeV}$.

Model particles and heavy stable charged particles is shown in Fig. 5.3. While Standard Model particles with $Q = \pm 1$ (e, μ, π, p, K) and momentum $> 50 \text{ GeV}$ have a specific energy loss of between 9 and 11 keV/cm, at LEP energies, heavy stable charged particles ($m \gtrsim 40 \text{ GeV}$) are expected to yield dE/dx values outside this region (except for a small kinematical region). Particles produced at the maximum kinematically accessible masses, feature low $\beta\gamma$ values ($\beta\gamma \lesssim 0.25$). They are treated in a special way as will be explained in the next section.

5.3.4 Particles with low $\beta\gamma$

Particles with $\beta\gamma \lesssim 0.25$ produced very high ionisation in the gas volume of the CJ. Once a slow heavy stable charged particle traversed a CJ sector, the dynamic range of the FADCs (Flash Analogue to Digital Converters) which were connected to both sides of the CJ wires could be exceeded, i.e. the FADCs worked in overflow. The z coordinate of a CJ hit was reconstructed using the method of charge sharing between the integrated charge on either wire ends (Section 1.5.2). If the left and/or right signal could not be fully digitised, e.g. owing to the limited dynamical range of the FADCs, the precision of the measurement of the z coordinate would degrade strongly, see Fig. 5.4. This was taken into account in the standard OPAL reconstruction code: if a hit on the CJ wire produced an FADC overflow on either side of the wire the hit was flagged to be bad. Although it still contained useful information in $r - \phi$ it was not used for track reconstruction. As a minimum of three hits was needed to reconstruct a track, this could lead to the consequence that tracks from highly ionising particles were not recognised.

To improve the detection of particles with low $\beta\gamma$, a modified track reconstruction is introduced, which takes into account all hits, including overflow hits: once an FADC overflow on either side of the CJ wire was detected, the measurement error in z of the corresponding hit is multiplied by the factor of 1000, assigning a very low weight to the hit: $\sigma_z = \mathcal{O}(m)$. Thus in the overall track reconstruction other subdetectors (CV and CZ) almost exclusively determine the track position in the z direction. The $r - \phi$ information of the jet chamber, however, is almost unchanged with respect to the standard OPAL reconstruction. Only small corrections for the variation of the wire position along the z axis due to gravity are neglected, as no z information is available.

The advantage of the modified reconstruction algorithm is demonstrated in Fig. 5.5. It contains two event displays of the OPAL tracking detectors, each showing the same simulated event: $e^+e^- \rightarrow \tilde{\tau}\tilde{\tau}\tau\tau$ at $\sqrt{s} = 206$ GeV, $m(\tilde{\tau}) = 100$ GeV (see also Section 6.2.3). thus two highly ionising tracks are expected plus two “standard” tracks from the tau decay products. Each hit in the central jet chamber is represented by a (green) dot, while the reconstructed tracks are shown as (blue) lines. In the upper display, the standard OPAL reconstruction code is used: the tracks of the tau decay products are reconstructed while the heavy staus escape detection. Most hits are reconstructed at $z \approx 0$. This is due to the fact that charge division yields no longer a reasonable result, once the maximum value of the FADCs is reached. In the lower display, the modified event reconstruction is applied. The two additional tracks from the staus can now be reconstructed.

Heavy stable charged particles produced at the kinematic limit with low $\beta\gamma$ could be produced with a larger momentum and less ionisation at an increased centre-of-mass energy. therefore the described changes in the event reconstruction are important especially for events at the highest energies achieved at LEP.

5.4 The OPAL Trigger

In order to reduce the event rate by rejecting the major fraction of background events an efficient trigger system is needed. Given a readout dead time of 20 ms per event, the trigger rate should not exceed 5 Hz in order to keep losses below 10% [95]. At LEP

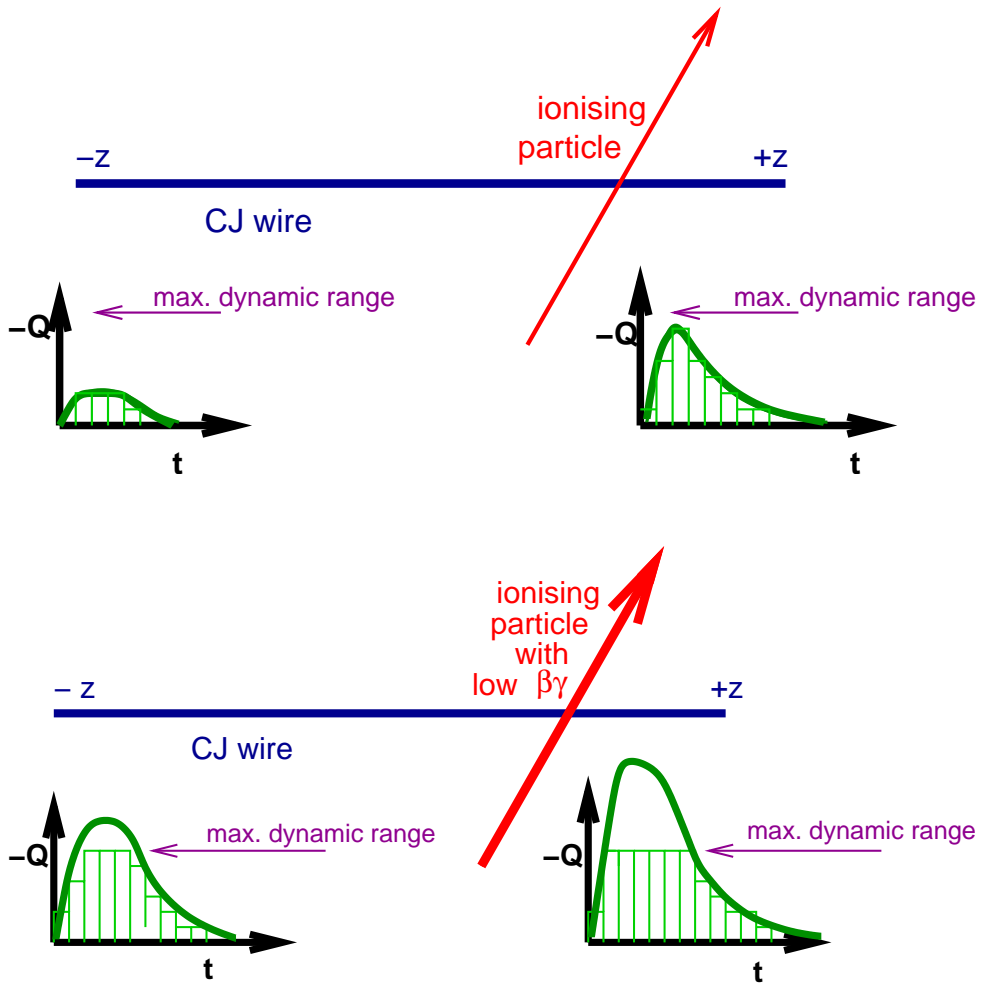


Figure 5.4: Schematic of a CJ wire and the charge collected at each wire end. The upper picture shows the case of a traversing charged Standard Model particle: on both wire ends the analogue charge signal (dark green line) can be transformed properly into a digital signal (light green squares). Charge division using the digitised signal leads to a reasonable reconstruction of the z coordinate. Lower picture: if a very highly ionising particle traverses the CJ volume the amount of charge deposited on the wires is to large to be transformed properly into a digital signal, i.e. the dynamical range of the FADC is exceeded. Charge division leads no longer to a reasonable reconstruction of the z coordinate. Nevertheless, the $r - \phi$ coordinate is almost unchanged, and the hit still contains useful information. In the standard OPAL reconstruction these overflow hits are ignored while the modified track reconstruction used in the present analysis takes them into account and thus enhances the detection efficiency for highly ionising particles.

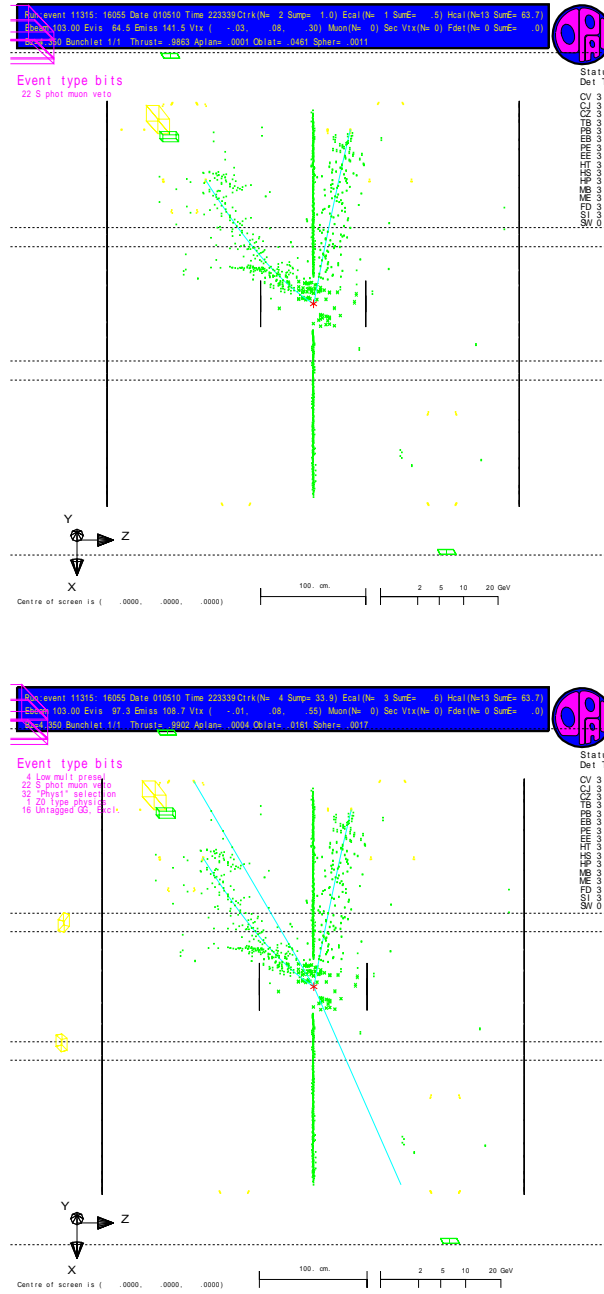


Figure 5.5: Standard and modified event reconstruction: both event displays show a side view of the OPAL tracking devices and contain the same simulated event: $e^+e^- \rightarrow \tilde{\tau}\tilde{\tau}\tau\tau$ at $\sqrt{s} = 206$ GeV, $m(\tilde{\tau}) = 100$ GeV. Thus two highly ionising tracks are expected plus two “standard” tracks from the tau decay products. Each hit in the central jet chamber is represented by a (green) dot, while the reconstructed tracks are shown as (blue) lines. In the upper picture, the standard OPAL reconstruction code is used: the tracks of the tau decay products are reconstructed while the heavy stau escapes detection. Most hits are reconstructed at $z \approx 0$. This is due to the fact that charge division yields no longer a reasonable result, once the maximum value of the FADCs is reached. In the lower picture, the modified event reconstruction is applied. Two additional tracks can be seen. They are caused by the high ionisation of the stable staus. After the modification the highly ionising tracks are reconstructed with a very low weight assigned to the individual CJ hits.

distinctive physics and background signatures allow strong discrimination at trigger level.

The OPAL trigger system was designed mainly to be sensitive to multihadronic and charged leptonic signatures, single photons ($e^+e^- \rightarrow \nu\bar{\nu}\gamma$), large angle photons ($e^+e^- \rightarrow \gamma\gamma$), possible new event signatures (like $e^+e^- \rightarrow ZH$) and energetic two-photon processes ($e^+e^- \rightarrow e^+e^-X$). In addition, it is important to trigger on small angle Bhabha scattering events for luminosity measurement.

Backgrounds to these processes are mainly due to the following sources: single beam particles interacting with residual gas or the wall of the beam pipe, synchrotron radiation as well as cosmic rays and detector noise.

The OPAL trigger decision is based on information from most of the subdetectors, comprising the track trigger, described in Section 5.4.1, the time-of-flight (TOF) trigger, electromagnetic and hadronic calorimeter triggers, muon detector and forward detector triggers. The monopole or high dE/dx trigger [96], which formed part of the track trigger, was sensitive to high energy deposition in the Jet Chamber volume. Originally installed to trigger magnetic monopoles, it plays an important role in this analysis and will be described in Section 5.4.2.

5.4.1 Track Trigger

The working principle of the track trigger is shown in Fig. 5.6. The trigger uses information from the twelve axial wires of each sector of the vertex chamber and from three groups of twelve adjacent wires at different radii of each jet chamber sector (inner ring: wires 9 to 20, central ring: wires 37 to 48, outer ring: wires 97 to 108). Charged tracks with transverse momentum of interest are essentially straight lines in the r - z plane. Therefore tracks originating from the beam-beam vertex ($z=0$) will have nearly constant values of θ at all points along the track. A histogram for z/r ($= \cot \theta$) on such a track will show a narrow peak at a well defined value, see Fig. 5.6. Due to the curvature of the tracks caused by the magnetic field, a track may be located in more than one sector. To make sure no tracks are missed, histogram contents are summed over adjacent sectors.

5.4.2 Monopole or High dE/dx Trigger

Magnetic monopoles are supposed to deposit a high amount of energy in the detector volume. Events with monopoles should contain only few tracks, such that the average occupancy of tracks per CJ sector is lower than one.

The monopole trigger is designed to be activated by a highly ionising particle traversing a CJ sector. The presence of additional conventional tracks in the event can produce a positive trigger decision of the main track trigger while the monopole bit is not set: if a conventional track is nearer to the anode plane than the monopole track, the main track trigger is satisfied and the monopole trigger is held off. If – the other way around – the monopole track is nearer to the anode plane than the conventional track, the trigger condition is satisfied.

Of the 159 sense wires per CJ sector the same three wire groups with twelve wires each are used as for the track trigger. For each trigger wire there is one electronic unit called the *Multi Hit Sampler* (MHS), which processes the analogue signal from both wire

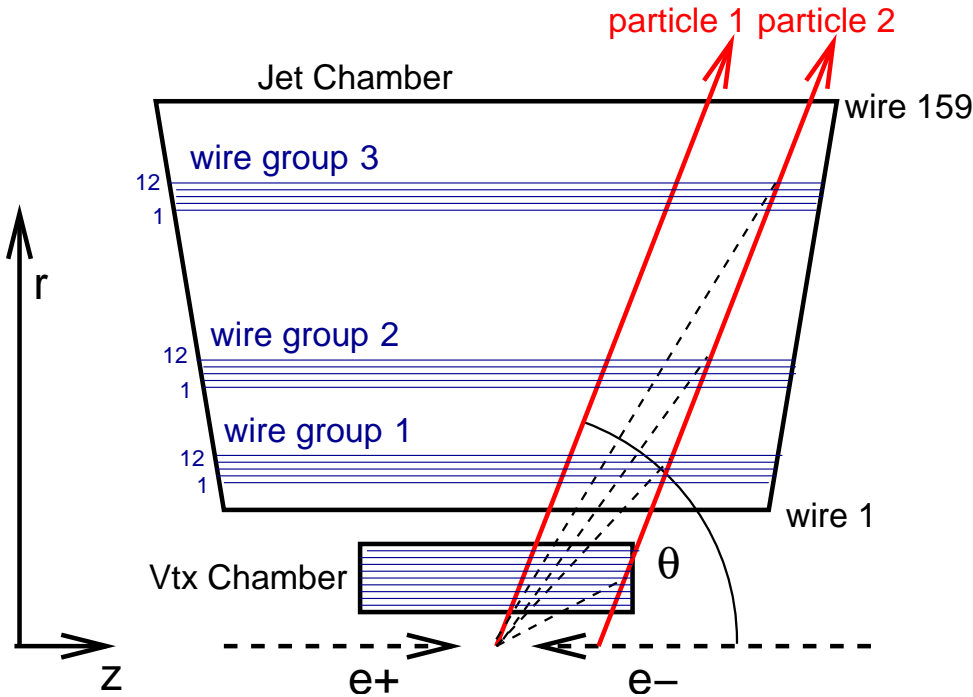


Figure 5.6: Principle of track finding in the r - z plane in the track trigger: the track trigger electronics forms histograms of the ratio of z and r for four groups of 12 wires in each sector. For tracks originating from the interaction region the z/r distribution shows a narrow peak, it is flat for other tracks.

ends. It detects hits by looking for a summed signal above a certain threshold. The total charge of the hit signal is calculated as a 6 bit word and tested against a second (high) threshold. The MHS processors of one wire group (twelve wires in a sector) are controlled by a *Twelve Wire Scanner* (TWS).

The TWS contains one flip flop for each wire. The flip flops are set when a track charge above a certain threshold T_H is registered on the condition that there is no track with charge below that threshold. If more than ten out of the twelve flip flops are set the corresponding *Group Decision Bit* (GDB) is set to one. Finally, the outputs of the three groups are connected in an analogue way to a *Sector Decision Bit* (SDB). The SDB is set if all three of the GDBs are set. If at least one of the SDBs is set then the OPAL trigger system is activated. A schematic of the decision logic is given in Fig. 5.7.

Apart from the LEP I period the monopole trigger was included into the general trigger decision logic only in the data taking of the year 2000, i.e. at highest centre-of-mass energies ($\sqrt{s} \geq 200$ GeV), where it is important for the present analysis.

5.4.3 Particles with low $\beta\gamma$

Low multiplicity events with high energy deposition may not be triggered by other parts of the track trigger but the monopole trigger because the track trigger rejects all wire pulses which exceed the threshold T_H . However, the monopole trigger recognises such

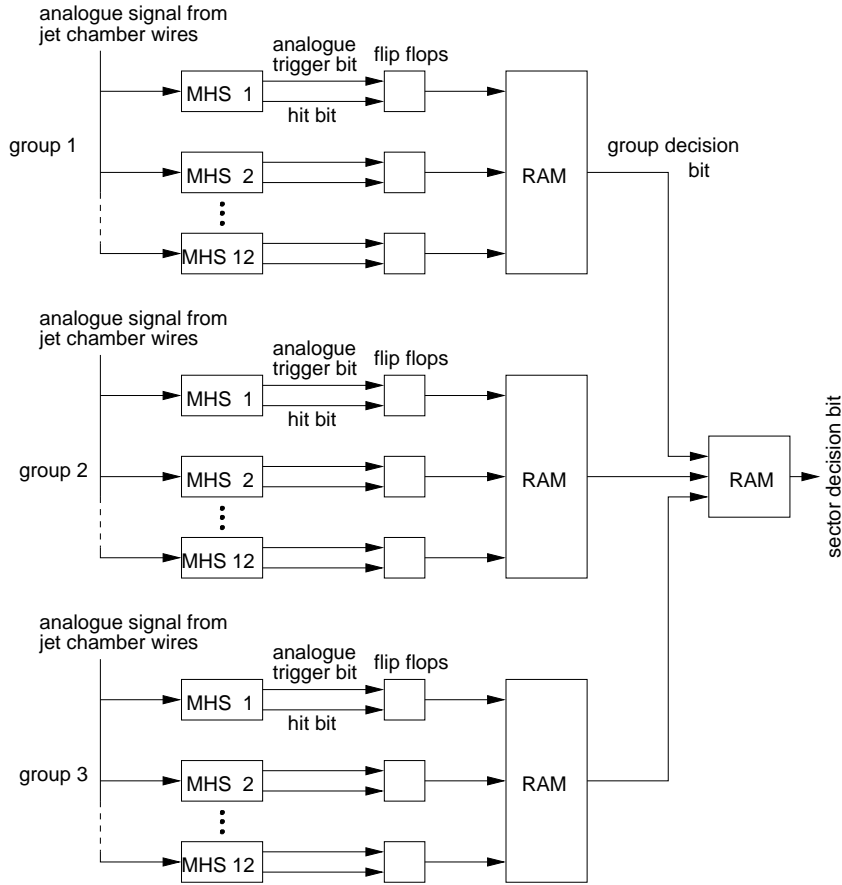


Figure 5.7: Schematic of the track trigger decision logic for one jet chamber sector (see text).

events once the condition described above is satisfied. Hence, the monopole trigger is an indispensable tool to study heavy ionising particles produced in low multiplicity events at the maximum kinematically accessible masses.

Events with higher multiplicity contain tracks caused by other particles than the highly ionising ones. These additional tracks cause usually a positive trigger decision in the remaining parts of the track trigger. In this case the monopole trigger is not needed to record the event.

5.4.4 Trigger Simulation

Except for the monopole trigger, all trigger elements are described properly in the OPAL simulation code (Section 6). Therefore in the present analysis a software emulation of the monopole trigger is performed according to the description of Section 5.4.2.

First, the threshold T_H is determined using data events: in a special selection low multiplicity events (events with less than three tracks) with monopole trigger bit are selected. Only the CJ sector with the highest overall charge deposition is considered. Each of the twelve group wires is allowed to have at most one good hit. Otherwise the event is rejected. This takes into account, that in the emulation, no conventional ionisation

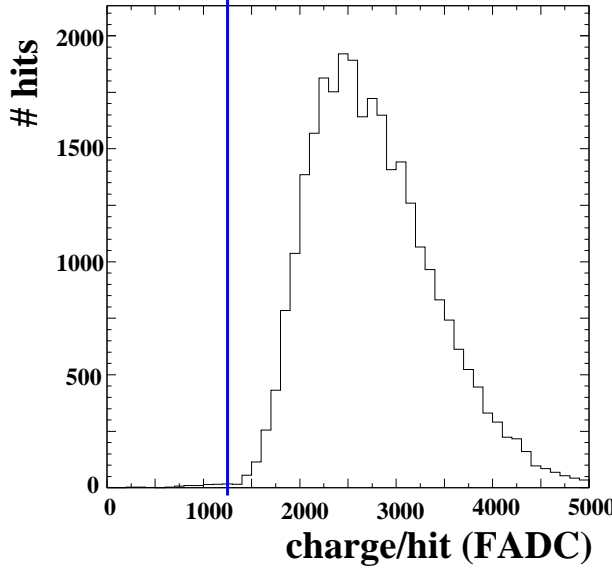


Figure 5.8: Determination of the threshold T_H (see text): the rise of the distribution indicates the position of the threshold. For the emulation of the trigger, the threshold is set to 1250 FADC counts.

(i.e. $\text{charge}/\text{hit} < T_H$) will hold off the monopole decision, like it was the case during data taking. Then, the charge of the ten wires with the highest charge within each group is filled into a histogram (see Fig. 5.8). The rise of the distribution indicates the position of the threshold T_H . For the emulation of the trigger, $T_{H,EMU}$ is set to 1250 FADC counts. However, some entries lie below this value, they are mostly caused by charge collected on one specific CJ wire. This is in agreement with the fact that some wires were treated differently during CJ data taking, but it has no relevance for the emulation.

The comparison between the OPAL monopole trigger bit and the bit constructed by software emulation can be seen in Table 5.3: low multiplicity events (number of tracks ≤ 2) of the first runs of the year 2000 are considered ($\sqrt{s} \geq 200 \text{ GeV}$), and the same selection which has been used to estimate T_H is applied. Out of roughly 300000 events, 2048 with either monopole bit or emulated bit are selected. A high agreement is achieved: in six cases events have no monopole bit but the emulated bit is set and twelve events with monopole bit are not recognised by the emulation. Thus the misidentification of the software emulation for events with ≤ 2 tracks lies below 1 %.

events with	#
monopole bit on and emulated bit on	2030
monopole bit off and emulated bit on	6
monopole bit on and emulated bit off	12
monopole bit off and emulated bit off	326098

Table 5.3: Comparison of the OPAL monopole trigger with the trigger emulation used in this analysis for low multiplicity events (≤ 2 tracks).

Chapter 6

Data Set and Simulation

This chapter is divided into two parts: First, in Section 6.1, an overview of the used OPAL data set is given. Hereafter, Section 6.2 deals with the simulation of particle reactions which is indispensable for the understanding and interpretation of the measurements.

6.1 e^+e^- Data Set

The present analysis is based on recorded e^+e^- collisions at centre-of-mass energies (\sqrt{s}) from 131 up to 209 GeV taken in the years 1996 – 2000. The growth of the integrated luminosity during the periods of data taking is shown in Fig. 6.1. A total integrated luminosity of $\mathcal{L} = 632.1 \text{ pb}^{-1}$ of data is available for which all detector components which are relevant for the present analysis were fully operational. Table 6.1 lists the chosen centre-of-mass energy bins, the luminosity weighted mean energy and the corresponding year of data taking.

The integrated luminosities are determined with the ROCROS [97] programme, which uses Bhabha events ($e^+e^- \rightarrow e^+e^-$) with low scattering angles and dominating t-channel contribution. The cross-section can be determined from quantum electrodynamics. Bhabha scattering events were recorded with the silicon tungsten calorimeters, or, in case these were not fully operational, with the forward detector (compare Section 5.2.2). The total relative uncertainty on the luminosity (including statistics and systematics) is found to be $\delta\mathcal{L}/\mathcal{L} \approx (0.2 - 0.3) \%$.

6.2 Monte Carlo Simulation

The interpretation of experimental data requires a comparison with theoretical predictions. These predictions are given by computer simulation: First, the physics processes in e^+e^- collisions are simulated using Monte Carlo (MC) event generators. These are computer programmes which produce (generate) the four-vectors (E, \vec{p}) of all participating particles of a certain physics process. Then the response of the detector components was simulated which is required to perform the same event reconstruction as applied on e^+e^- data. A possible discovery is based on the comparison of the number of simulated, i.e. expected, Standard Model background events and the number of candidates selected in

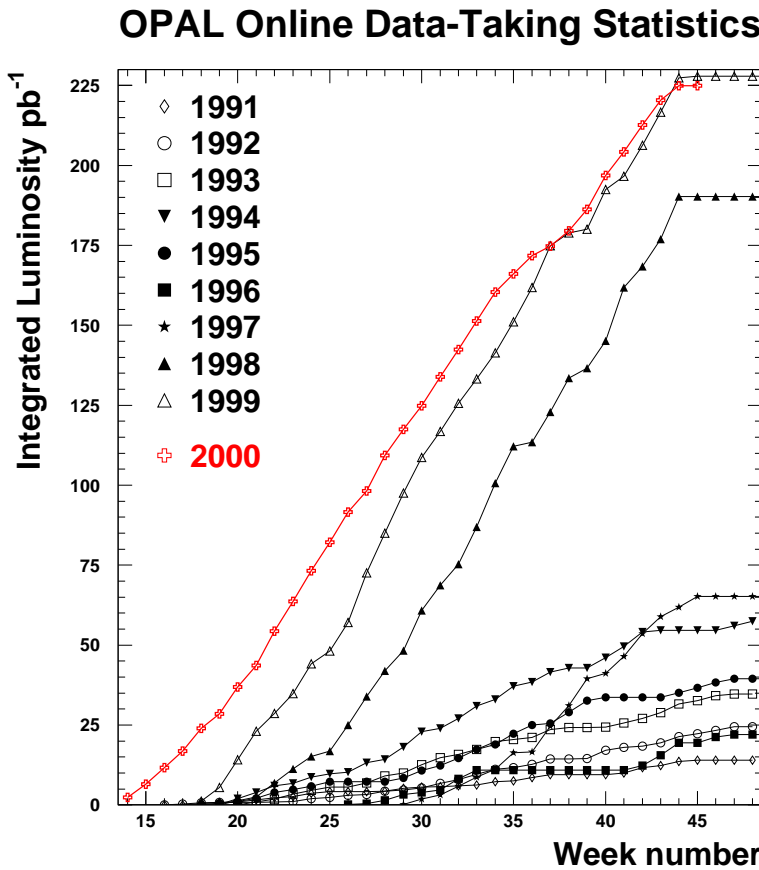


Figure 6.1: Integrated luminosity collected for all years of OPAL running.

\sqrt{s} bin range (GeV)	$(\sqrt{s})_{\text{mean}}$ (GeV)	\mathcal{L} (pb ⁻¹)	year
131.0 – 137.0	133.2	5.6	1996/1997
160.0 – 162.0	161.3	8.0	1996/1997
171.0 – 173.0	172.3	9.0	1996
180.0 – 184.0	182.7	40.1	1997
188.0 – 190.0	188.5	174.0	1998
195.0 – 197.0	195.5	70.8	1999
199.0 – 201.0	199.5	73.9	2000
201.0 – 203.5	201.6	37.8	2000
203.5 – 205.5	205.0	77.2	2000
205.5 – 207.5	206.4	127.6	2000
> 207.5	208.0	8.1	2000
131.0 – 209.0	195.8	632.1	1996 – 2000

Table 6.1: Luminosity weighted mean centre-of-mass energy, integrated luminosity \mathcal{L} and corresponding year of data taking of each energy bin.

the data sample.

In this section the most important Standard Model physics processes for this analysis are described, as well as the event generation, detector simulation and MC event reconstruction.

6.2.1 Physics Processes

At centre-of-mass energies above the Z resonance the dominating Standard Model processes in e^+e^- collisions are the following:

Two-Photon Processes

This term is used for reactions of the type $e^+e^- \rightarrow e^+e^- f\bar{f}$ which take place via the exchange of two photons. The virtuality of the photon, Q^2 , is defined as the negative squared four-momentum: $Q^2 = -q^2 = -(E^2 - \vec{p}^2)$. For small Q^2 the photon is called quasi-real. The two-photon vertex in Fig. 6.2 indicates that a more detailed event classification according to the photon structure can be chosen [98]. The two-photon cross-section rises logarithmically with the centre-of-mass energy; at $\sqrt{s} = 200$ GeV it is of $\mathcal{O}(10 \text{ nb})$.

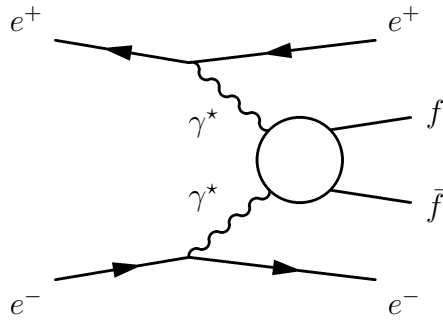


Figure 6.2: A diagram of the reaction $e^+e^- \rightarrow e^+e^- f\bar{f}$, proceeding via the exchange of two photons (see text). The virtuality of the photons is indicated by the star.

Two-Fermion Processes

The annihilation of the e^+e^- pair into a neutral gauge boson (γ, Z) and the subsequent decay into a fermion-anti-fermion pair is called two-fermion process (left diagram of Fig. 6.3). Its production cross-section reaches a maximum at the Z -pole and decreases with increasing centre-of-mass energy according to $1/s$ for $\sqrt{s} \gg M_Z$. At $\sqrt{s} = 200$ GeV the two-fermion cross-section is roughly 100 pb, excluding Bhabha scattering events. In Bhabha scattering, the t-channel (right diagram of Fig. 6.3) contributes significantly. The Bhabha cross-section depends strongly on the scattering angle. Including angles down to $\cos \theta = 0.96$, at $\sqrt{s} = 200$ GeV a cross-section of roughly 250 pb is reached [99].

Four-Fermion Processes

This term covers all electro-weak processes (excluding two-photon events) with four fermions in the final state. The most important Feynman-diagrams are shown in Fig. 6.4.

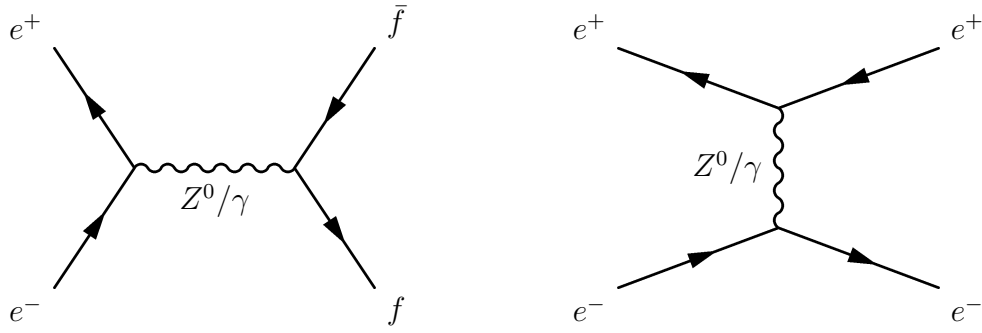


Figure 6.3: Feynman-diagrams of the s- and t-channel two fermion processes.

W and Z pair-production as well as single W and single Z production in Compton scattering of quasi-real photons contribute to the final state. The cross-sections are of the order of 50 pb at $\sqrt{s} = 200$ GeV.

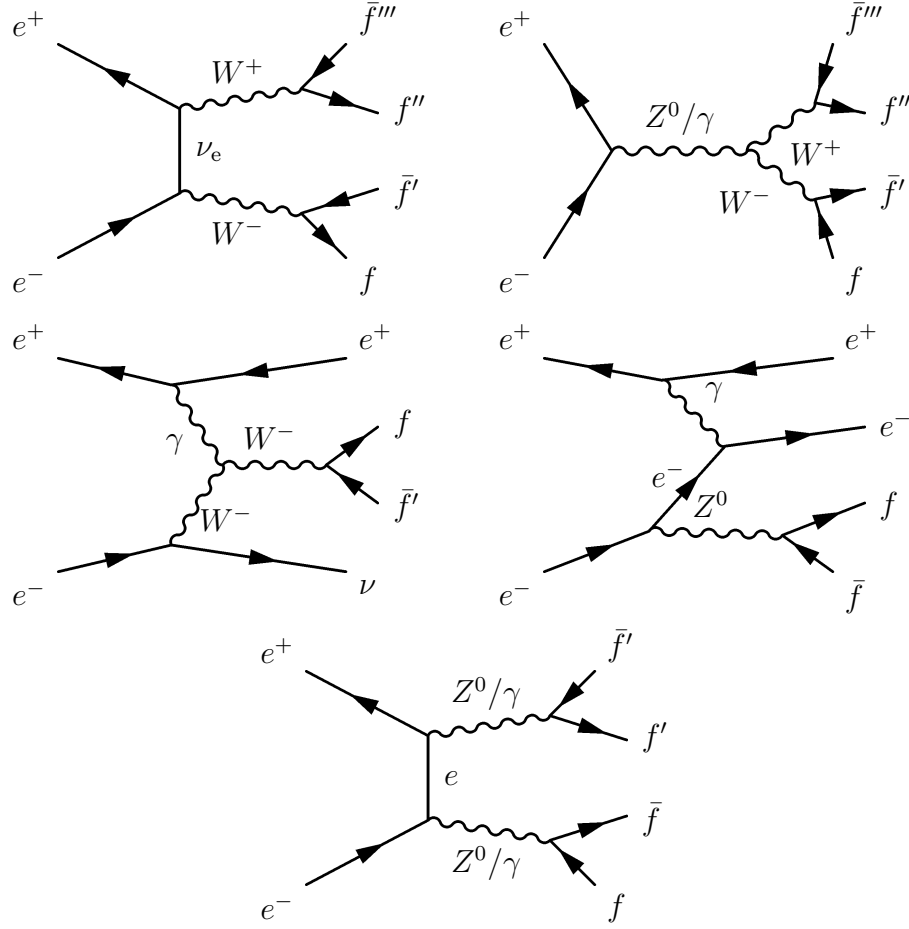


Figure 6.4: Feynman-diagrams of the most important four-fermion processes: W pair-production, single gauge boson production, pair-production of neutral gauge bosons.

Two-Photon Production

Two photons can be produced in the reaction $e^+e^- \rightarrow \gamma\gamma(\gamma)$, see Fig. 6.5. The cross-section of this process is about 20 pb at $\sqrt{s} = 200$ GeV.

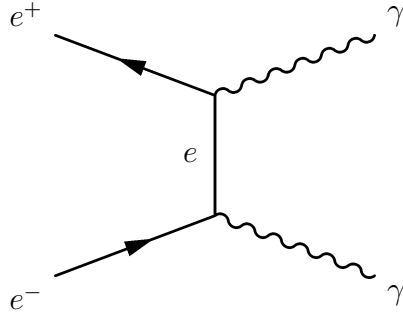


Figure 6.5: Production of two photons via e^+e^- annihilation.

6.2.2 Background Event Simulation

Leptonic two-photon processes were generated with the BDK [100–103] and Vermaeren [104] programmes, hadronic two-photon processes with PHOJET [105] and HERWIG [106] programmes. For two-fermion processes, the following generators were used: BHWIDE [107] and TEEGG [108] for Bhabha scattering processes at large and small angles, respectively; KK2F [109] was used to generate muon and tau pairs as well as multi hadron events. $\nu\nu(\gamma)$ events were generated with NUNUGPV [110]. For four-fermion processes, the KORALW [111] generator and, for final states with electron pairs, the grc4f [112] programme was used. Photon pair final states were generated with RADCOR [113]. All hadronisation processes were simulated with the PYTHIA and JETSET [114] programmes and tau decays with TAUOLA [115, 116].

6.2.3 Signal Event Simulation

For the considered GMSB topologies, signal event four-vectors at tree level were produced using the SUSYGEN [117, 118] generator. For slepton pair-production in the slepton co-NLSP scenario and neutralino pair-production version 2.2 is used, other processes were generated with the newer version 3.0. The four-vectors of pair-produced stable spin-1/2 particles were produced with the EXOTIC [119] event generator. Again, hadronisation was simulated with JETSET. The complete list of generated signal Monte Carlo events can be found in Appendix B.

Apart from four-vector production SUSYGEN can also be used for SUSY parameter scans, described later in Section 8.3.1: the programme can calculate the mass spectrum, production cross-sections and branching ratios for each parameter setting. This mode is used for the interpretation of the results within the GMSB framework in Section 8.3.

6.2.4 Detector Simulation

The modelling of the detector response, including the trigger logic, to the generated particles (four-vectors) is called detector simulation. The simulation programmes contain information about the geometry and property of the all active and passive detector components. Thus the interaction of the particles with the detector material can be calculated, e.g. ionisation loss of charged particles, shower evolution and multiple scattering processes. The programme for the simulation of the OPAL detector is called **GOPAL** [120,121]. It is based on the **GEANT 3** [33] package.

Modifications for the signal simulation

Several modifications were implemented in the **GOPAL** programme because the standard code is not suited to handle supersymmetric or exotic heavy particles with long lifetimes: they are assumed to decay promptly and are not tracked by **GEANT**. A detailed description of all modifications can be found in [81]; the main changes in **GOPAL** and **GEANT** are listed below.

- To pass SUSY (or exotic) particles to **GEANT**, the particles and their properties were first defined as heavy stable muons in a separate routine.
- The same was done for tau leptons, which, due to their short lifetime ($\approx 290 \cdot 10^{-15}$ s), are normally assumed to decay in the beam pipe. In the presented analysis, however, the tau can be a decay product of a long-lived particle, so that the tau decay within the detector volume has to be simulated.
- The flag, which indicates whether the particle has already decayed in the generator (end flag), was changed to “still alive” for supersymmetric particles and taus.
- After choosing a certain lifetime for the supersymmetric or exotic particle i.e. 10^{-6} s in this analysis, its decay length was calculated using a random number generator. The decay products of this particle, however, had to be attached to the end point of the parent particles trajectory. Therefore the decay products were first removed, i.e. their start point was set to a large number.
- After a supersymmetric or exotic particle had decayed in **GEANT**, the decay particles were moved to their parents end point. For this purpose, a new routine was written, in which the decay particles were found and their start points were set to their parents end point. This modification takes into account, that the parent particle might have lost energy due to interaction with the detector material and that the trajectory of the parent particle follows a helical path.
- Finally, the end flag was set to “still alive” for particles which had not decayed inside the detector, and the start and end point of the unused decay particles were set to the end point of the parent particle.

6.2.5 Event Reconstruction

After the complete simulation of the detector response, simulated signal and SM background events are submitted in general to the same reconstruction procedure as e^+e^- data (Section 5.2.3). The modified track reconstruction (Section 5.3.4), which is introduced for year 2000 data (i.e. $\sqrt{s} \geq 200$ GeV), however, is applied to data and simulated signal events only. The simulated Standard Model background is in contrast, reconstructed conventionally, owing to the following reason: to obtain track information from the modified reconstruction, each event must be reconstructed from hit level (raw data), while conventionally reconstructed OPAL events are already available on tape, such that a standard physics analysis can use track level data as input (processed data). Thus the application of the modified track reconstruction is roughly ten times more (CPU) time consuming than the standard reconstruction. Hence, the huge statistics needed to describe the Standard Model background properly in all centre-of-mass energy bins with $\sqrt{s} \geq 200$ GeV in combination with the presently available CPU power makes it impossible to carry out the modified event reconstruction without exceeding a reasonable time frame.

But as will be shown later, the influence on the result of using different reconstruction algorithms in simulated SM background and e^+e^- data is negligible.

Chapter 7

Data Selection and Signal Efficiency

After the discussion of the general concept behind the data selection in Section 7.1, the specific cuts which lead to a clear separation of signal topologies from Standard Model events are presented in Section 7.2. Section 7.3 contains the search result. Hereafter, the determination of the efficiency for the selection of all relevant signal topologies is explained (Section 7.4); extensive studies of the systematic uncertainties of both data selection and determination of the efficiency are described in Section 7.5. Finally, in the last section, a summary of this chapter is given.

7.1 Selection Concept

In order to perform a search for heavy stable charged particles which is as model independent as possible, a rather general data selection is chosen. Its core piece is the requirement of at least one track per event with an anomalous specific energy loss. This leads to a coverage of a large variety of different signal event topologies including the production of stable charged supersymmetric particles presented in Section 4.4.

7.2 Selection Cuts

The selection is divided into three parts. First, a preselection is performed in order to reduce the amount of data to a size which is reasonable in terms of disk space and CPU time needed for further processing. After the preselection each remaining event contains at least one track which fulfils basic dE/dx and quality criteria. The subsequent set of cuts rejects the major part of the non-simulated background and finally, the main selection separates the signal from Standard Model background.

7.2.1 Preselection

The preselection consists of the following cuts:

- In order to reduce two-photon events, which form the main background at this stage of the selection, a minimum reconstructed relativistic invariant energy per event (visible energy, E_{vis}) is required: $E_{\text{vis}} > 0.10 \sqrt{s}$.

The visible energy is calculated by summing up the deposited energy of all energy flow objects.

Note that all quantities related with the energy flow algorithm described in Section 5.2.3, e.g. visible energy, E_{vis} , and visible mass, M_{vis} , are in general unphysical for events with heavy stable charged particles, because energy flow objects are calculated under the pion mass hypothesis. However, the cuts on the concerned quantities are chosen carefully, such that the signal efficiency hardly suffers, even for largest considered masses of the stable charged particle.

- Events with more than 20 CJ tracks (with at least ten CJ hits each) are rejected.
- Events are required to have at least one track with
 - 20 or more hits used for dE/dx measurement,
 - at least one hit in CV (axial or stereo).
 - a relevant dE/dx (Fig. 5.3):
 $dE/dx > 11 \text{ keV/cm}$ or $(dE/dx < 9 \text{ keV/cm} \text{ and } p > 10 \text{ GeV})$

7.2.2 Reduction of non-simulated Background

To reduce non-simulated background, which is mainly caused by cosmic muons and the interaction of the electron and positron beams with the wall of the beam pipe and with remaining gas atoms, for at least 75% of the tracks per event one of the following criteria is required (Fig. 7.1):

- The distance between the beam axis and the track at the point of closest approach in the $r - \phi$ plane (PCA) must be smaller than 1.5 cm, and the z coordinate of the PCA must be lower than 10 cm.

or

- If there are good hits in the time-of-flight (TOF) barrel scintillators the measured time of the closest TOF barrel hit is required to differ at most 10 ns from the time expected from a physics event, i.e. the time a particle produced in the primary interaction needs to reach the barrel TOF detector.

7.2.3 Main Selection

Like the preselection, the main selection consists of cuts concerning the entire event and track requirements. The event wise cuts are:

- (1) To reduce two-photon background events, which deposit a large fraction of energy under small polar angles, i.e. close to the beam pipe, the maximum energy deposited in either side of the forward subdetectors SW, FD and GC must be

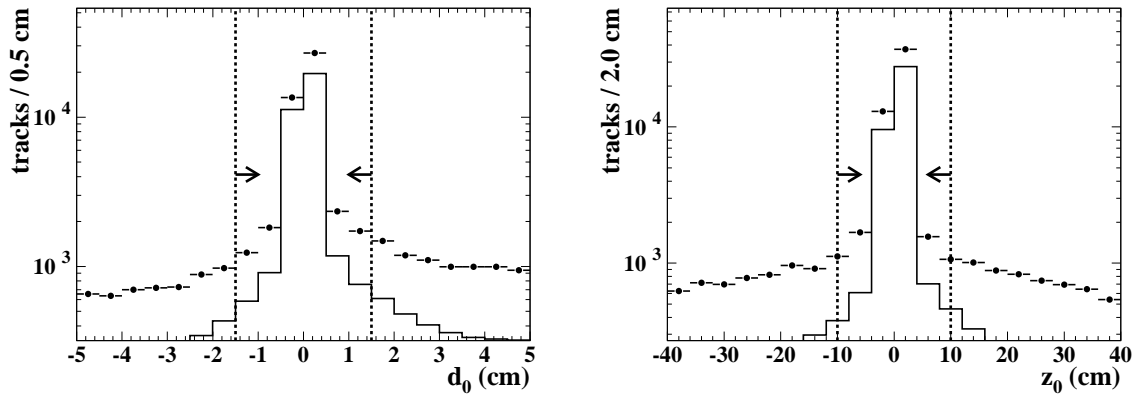


Figure 7.1: Reduction of the non-simulated background: at least 75% of the tracks must originate close to the interaction region: the distance between the beam axis and the track at the point of closest approach (PCA) must be less than 1.5 cm in $r - \phi$ (d_0). The z coordinate of the PCA (z_0) must be less than 10 cm. The data distributions are indicated by dots and the MC background by a solid line. The huge discrepancy between both distributions is due to the large fraction of non-simulated background, which is reduced to a tolerable fraction thanks to the cut indicated by the dotted thick lines. The data shown were taken in the years 1998 – 2000 with $\sqrt{s} = 189 \text{ GeV} – 209 \text{ GeV}$. The simulated background is normalised to the integrated luminosity ($\mathcal{L} = 569.4 \text{ pb}^{-1}$).

- $E_{\text{SW}} < 5 \text{ GeV}$
- $E_{\text{FD}} < 2 \text{ GeV}$
- $E_{\text{GC}} < 5 \text{ GeV}$.

Note that apart from two-photon events, energy was deposited in the forward subdetectors due to accelerator related activity, e.g. synchrotron radiation (not included in the Monte Carlo simulation). Therefore more data events are vetoed than predicted by the Monte Carlo simulations and the effective luminosity is smaller than the measured one. To account for this effect the frequency of the occurrence of such accelerator related background is estimated from a sample of so-called *random beam crossing* events, i.e. events for which the data acquisition was triggered randomly rather than by a real physics event. From this study it is found that the effective luminosity is approximately 2% smaller than the measured luminosity, which will be taken into account in the further analysis.

- (2) The total measured invariant (visible) mass must be $M_{\text{vis}} > 10 \text{ GeV}$ in order to reduce further two-photon events (Fig. 7.2).
- (3) $0.15 < E_{\text{vis}}/\sqrt{s} < 1.10$; two-photon and two-fermion events are reduced (Fig. 7.3).
- (4) The maximum electromagnetic energy is required to be $E_{\text{ECAL}}/\sqrt{s} < 0.3$. This cut is against two-fermion processes (Fig. 7.4).

(5) For events with the sum over all track momenta $P = |\vec{P}| = |\sum \vec{p}_{\text{track}}|$ being greater than 10 GeV, the z component of the momentum P_z must hold $|P_z/P| < 0.9$. This cut reduces mainly Bhabha scattering events with one electron escaping through the beam pipe carrying away a significant fraction of the total momentum of the event (Fig. 7.5).

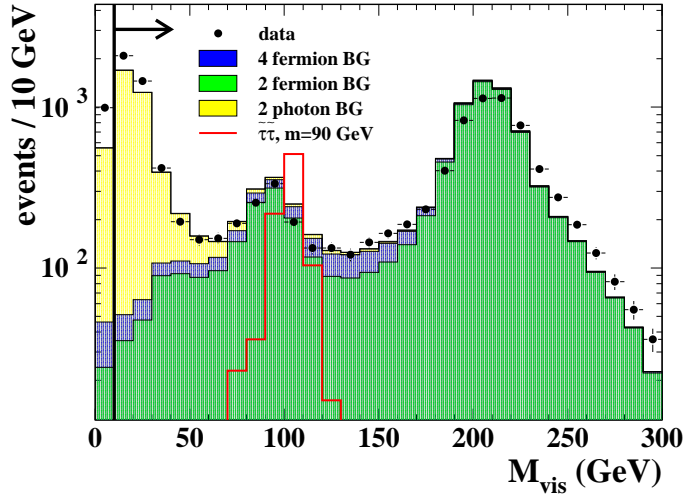


Figure 7.2: Distribution of the reconstructed invariant mass per event (visible mass) and cut 2: data and the different contributions of the expected background is shown as well as the position of the cut (thick line). The displayed data were taken in the years 1998 – 2000 with $\sqrt{s} = 189 \text{ GeV} – 209 \text{ GeV}$. The simulated background is normalised to the integrated luminosity ($\mathcal{L} = 569.4 \text{ pb}^{-1}$). The simulated distribution of the $e^+e^- \rightarrow \tilde{\tau}\tilde{\tau}$ is shown with $m_{\tilde{\tau}} = 90 \text{ GeV}$, generated at $\sqrt{s} = 208 \text{ GeV}$ (in arbitrary scale).

In addition, at least one track per event must fulfil all of the following criteria:

- (6) $e_{\text{ECAL}}/p \leq 0.15$ with e_{ECAL} denoting the energy of the ECAL cluster associated with the track. This cut reduces further Bhabha scattering events, four-fermion and two-photon background (Fig. 7.6).
- (7) At least one axial or stereo CV hit; this requirement reduces tracks produced by photon conversion.
- (8) Tightened quality criteria (Fig. 7.7): at least 40 hits used for dE/dx measurement and the error of the track momentum measurement must be smaller than 10 GeV. Again tracks from photon conversion are reduced efficiently, and the quality of momentum and dE/dx measurement is improved (see also Fig. 1.10).
- (9) $dE/dx-p$ cut (Fig. 7.8): the specific energy loss of the track must either be located in the high or low dE/dx region in the two dimensional $dE/dx-p$ plane. The regions are given by:

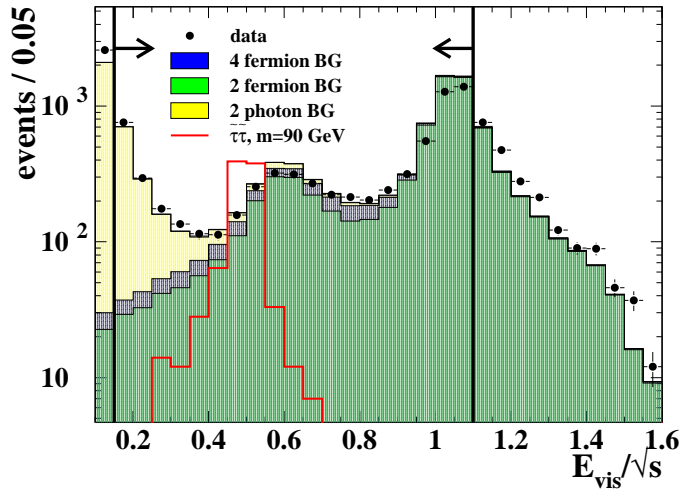


Figure 7.3: Distribution of the reconstructed energy per event (visible energy) and cut 3: data and the different contributions of the expected background is shown as well as the position of the cut (thick lines). The displayed data were taken in the years 1998 – 2000 with $\sqrt{s} = 189 \text{ GeV} – 209 \text{ GeV}$. The simulated background is normalised to the integrated luminosity ($\mathcal{L} = 569.4 \text{ pb}^{-1}$). The simulated distribution of the process $e^+e^- \rightarrow \tilde{\tau}\tilde{\tau}$ is shown with $m_{\tilde{\tau}} = 90 \text{ GeV}$, generated at $\sqrt{s} = 208 \text{ GeV}$ (in arbitrary scale).

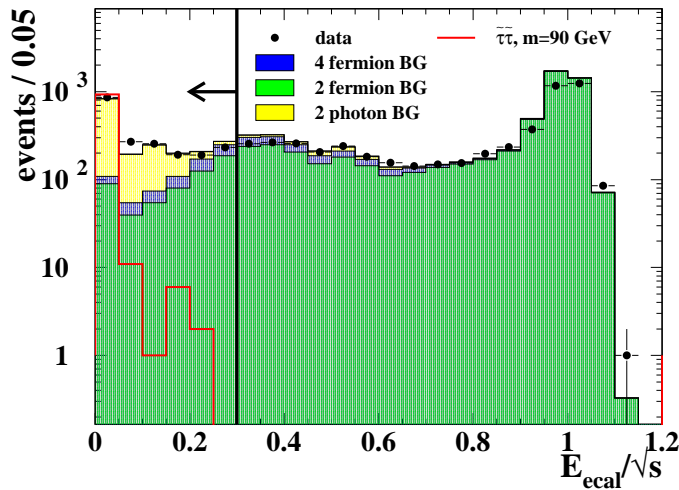


Figure 7.4: Electromagnetic energy per event and cut 4: the figure shows the sum of the energy measured in the electromagnetic calorimeter divided by the centre-of-mass energy of the event; e^+e^- data and the different contributions of the expected background is shown as well as the position of the cut (thick line). The displayed data were taken in the years 1998 – 2000 with $\sqrt{s} = 189 \text{ GeV} – 209 \text{ GeV}$. The simulated background is normalised to the integrated luminosity ($\mathcal{L} = 569.4 \text{ pb}^{-1}$). The simulated distribution of the process $e^+e^- \rightarrow \tilde{\tau}\tilde{\tau}$ is shown with $m_{\tilde{\tau}} = 90 \text{ GeV}$, generated at $\sqrt{s} = 208 \text{ GeV}$ (in arbitrary scale).

- $p > a \cdot (dE/dx - b)$ and $dE/dx > 12.0 \text{ keV/cm}$,
- $a = \frac{2}{17} \text{ cm}$, $b = 181.5 \text{ keV/cm}$, and
- $p > 52 \text{ GeV}$ and $dE/dx < 8.2 \text{ keV/cm}$

This cut separates signal topologies from Standard Model background.

(10) Isolation: in a cone of 20° no other track is allowed. Here, a final reduction of the number of expected Standard Model events is achieved by rejecting mainly four-fermion background and events with tau pairs.

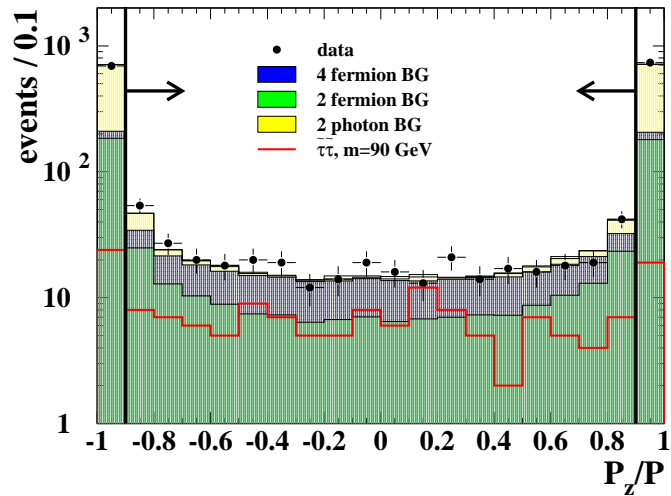


Figure 7.5: Direction of the momentum of the entire event P_z/P ($P = |\vec{P}| = |\sum \vec{p}_{\text{track}}|$) in the $r - z$ plane (for $P \geq 10 \text{ GeV}$) and cut 5: e^+e^- data and contributions of the expected background processes is shown as well as the position of the cut (thick lines). The displayed data were taken in the years 1998 – 2000 with $\sqrt{s} = 189 \text{ GeV} – 209 \text{ GeV}$. The simulated background is normalised to the integrated luminosity ($\mathcal{L} = 569.4 \text{ pb}^{-1}$). The simulated distribution of the process $e^+e^- \rightarrow \tilde{\tau}\tilde{\tau}$ is shown with $m_{\tilde{\tau}} = 90 \text{ GeV}$, generated at $\sqrt{s} = 208 \text{ GeV}$ (in arbitrary scale).

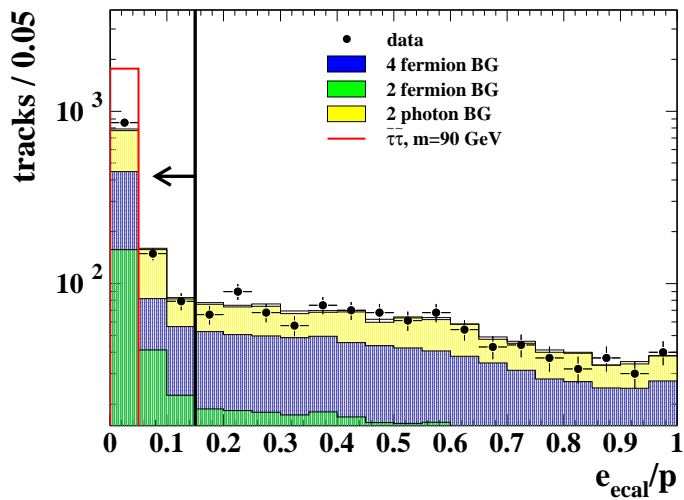


Figure 7.6: Ratio of the energy per track measured in the electromagnetic calorimeter and the track momentum and cut 6: e^+e^- data and the different contributions of the expected background is shown as well as the position of the cut (thick line). The displayed data were taken in the years 1998 – 2000 with $\sqrt{s} = 189 \text{ GeV} – 209 \text{ GeV}$. The simulated background is normalised to the integrated luminosity ($\mathcal{L} = 569.4 \text{ pb}^{-1}$). The simulated distribution is shown for the process $e^+e^- \rightarrow \tilde{\tau}\tilde{\tau}$ with $m_{\tilde{\tau}} = 90 \text{ GeV}$, generated at $\sqrt{s} = 208 \text{ GeV}$ (in arbitrary scale).

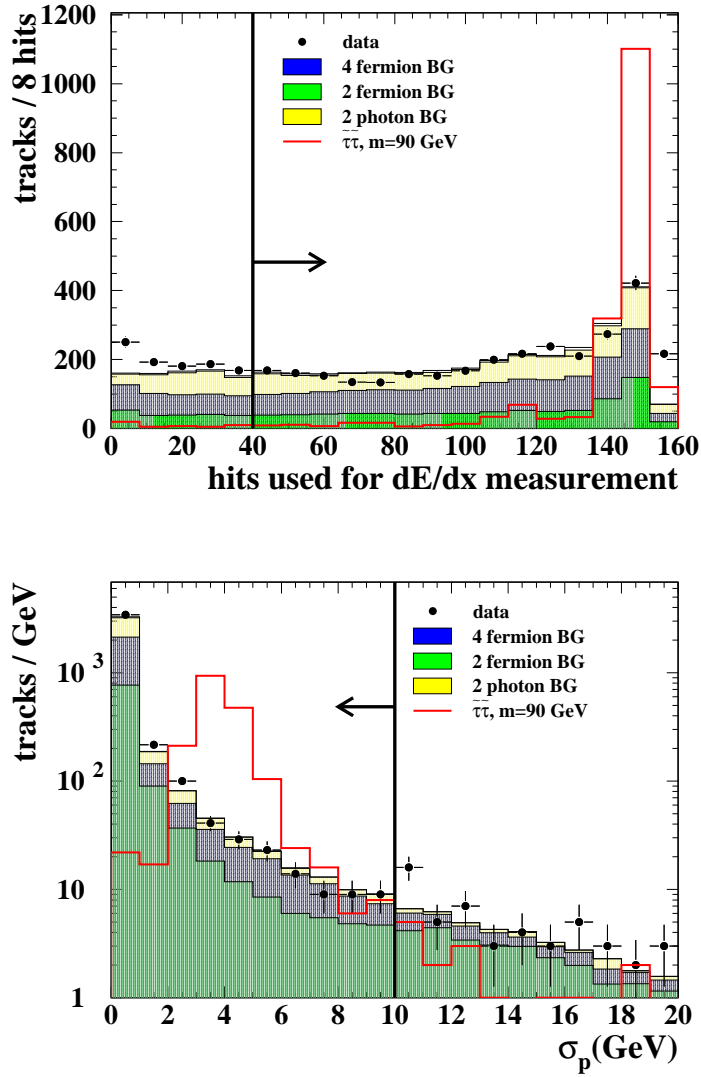


Figure 7.7: Hits used for dE/dx measurement and error in p per track and cut 8 (tightened track quality criteria); e^+e^- data and the different contributions of the expected background is shown as well as the position of the cuts (thick lines). The displayed data were taken in the years 1998 – 2000 with $\sqrt{s} = 189 \text{ GeV} – 209 \text{ GeV}$. The simulated background is normalised to the integrated luminosity ($\mathcal{L} = 569.4 \text{ pb}^{-1}$.) The simulated distribution of the process $e^+e^- \rightarrow \tilde{\tau}\tilde{\tau}$ with $m_{\tilde{\tau}} = 90 \text{ GeV}$ is shown, generated at $\sqrt{s} = 208 \text{ GeV}$ (in arbitrary scale).

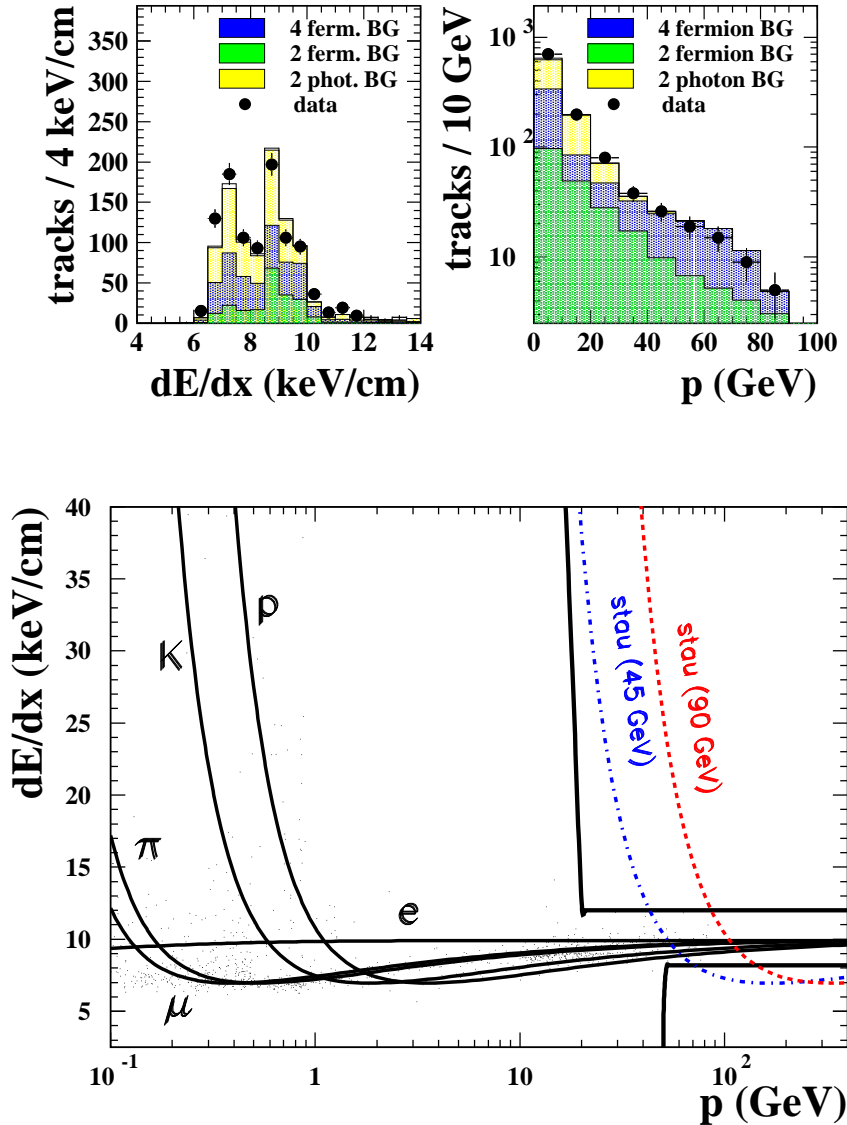


Figure 7.8: dE/dx and p distributions and cut 9: the upper two plots show e^+e^- data and different contributions of the expected background. The data displayed were taken in the years 1998 – 2000 with $\sqrt{s} = 189$ GeV – 209 GeV. The simulated background is normalised to the integrated luminosity ($\mathcal{L} = 569.4 \text{ pb}^{-1}$). The lower scatter plot shows the corresponding two dimensional data distribution in the $dE/dx - p$ plane and the applied cut for the separation of the heavy stable charged particles from Standard Model particles. The expected energy loss of electrons (e), muons (μ), protons (p), pions (π) and kaons (K) in the $dE/dx - p$ plane is indicated as well as the energy loss of two long-lived staus with $m_{\tilde{\tau}} = (45, 90)$ GeV.

7.3 Result

The total number of e^+e^- data and expected Standard Model events after each cut is shown in the Tables 7.1 and 7.2 for different centre-of-mass energy bins from 189 GeV up to 209 GeV, together with the corresponding integrated luminosities \mathcal{L} .

After the cut against non-simulated background a reasonable agreement between data events and MC simulation can be observed. No data event passes the event selection in any centre-of-mass energy bin. In addition, the last column of Table 7.2 contains the evolution of the signal selection efficiency for the pair-production of stable staus with mass $m = 90$ GeV at $\sqrt{s} = 208$ GeV with ascending cut number. The efficiency is calculated as $\epsilon = N_{\text{sel}}/N_{\text{gen}}$ with N_{gen} being the number of generated and N_{sel} the number of selected signal events. The efficiency of this specific process decreases from 99.7% after the preselection to 90.3% after the last cut. Of course, quite different efficiencies are obtained for other assumed masses or processes, which will be described later in Section 7.4.

Table 7.3 shows the number of remaining events after all cuts for the low centre-of-mass energy bins, ranging from $\sqrt{s} = 131$ GeV up to $\sqrt{s} = 183$ GeV. In this case, the expected Standard Model background is estimated from the other centre-of-mass energy bins by taking the luminosity weighted mean value.

In all centre-of-mass energy bins together 0.795 events are expected according to the Standard Model while no data event is selected.

7.4 Determination of the Selection Efficiency

In this section the determination of the selection efficiency for all signal topologies and arbitrary masses is described. In addition, the selection efficiency using the modified track reconstruction, which is used in the further analysis, is compared with the efficiency obtained with the standard OPAL track reconstruction.

In order to calculate the signal efficiency Monte Carlo samples at fixed masses of the SUSY particles are generated for all considered topologies. A list of the generated mass samples is given in Appendix B. For a parametrisation of the efficiencies for arbitrary masses of the heavy stable charged particles with a reasonable amount of signal Monte Carlo samples, an interpolation between the different mass points is carried out.

The selection efficiency turns out to be a function of the centre-of-mass energy, \sqrt{s} , the mass of the heavy stable charged particle, m , as well as of the masses of the other involved SUSY particles. To simplify the interpolation between different mass points it is convenient to introduce $\beta\gamma = |\vec{p}|/m$ of the heavy stable particle, with \vec{p} being the momentum in the laboratory frame, and to express the selection efficiency as a function of this quantity: $\epsilon = \epsilon(\beta\gamma)$ [122]. It turns out that this function is no longer dependent on \sqrt{s} and the specific mass scenario, since the selection procedure depends essentially only on the properties of the two highly ionising tracks, and the ionisation is a function of $\beta\gamma$ and not on m and p separately. In the following the determination of $\epsilon(\beta\gamma)$ is described.

\sqrt{s} bin (GeV)	189		196		200		202	
$(\sqrt{s})_{\text{mean}}$ (GeV)	188.5		195.5		199.5		201.6	
\mathcal{L} (pb $^{-1}$)	174.0		70.8		73.9		37.8	
after:	# events		# events		# events		# events	
	N_{data}	N_{bkg}	N_{data}	N_{bkg}	N_{data}	N_{bkg}	N_{data}	N_{bkg}
preselection	24216	16953.60	10535	6504.80	9036	6444.21	4750	3226.47
reduction of non-sim. Bkg.	6418	6287.99	2813	2487.52	2389	2513.52	1308	1276.97
cut 1	4173	4290.21	1831	1721.05	1535	1718.70	873	879.07
cut 2	3835	4088.83	1699	1647.81	1424	1643.04	815	845.89
cut 3	2391	2780.08	1032	1116.63	844	1116.87	490	567.59
cut 4	659	637.37	277	270.89	220	266.52	134	133.94
cut 5	196	173.43	67	75.33	72	71.26	42	37.67
cut 6	188	167.18	65	72.75	69	67.90	41	35.79
cut 7	183	166.94	65	72.65	68	67.68	41	35.68
cut 8	151	139.15	55	59.23	58	54.28	31	28.59
cut 9	0	0.11	0	0.11	0	0.36	0	0.06
cut 10	0	0.07	0	0.08	0	0.33	0	0.04

Table 7.1: Integrated luminosity \mathcal{L} and remaining number of events after each cut for data (N_{data}) and simulated background (N_{bkg}) in different centre-of-mass energy bins from $\sqrt{s} = 189$ GeV – 202 GeV.

Interpolation of the efficiency for pair-produced heavy stable charged particles
 $\beta\gamma$ of a pair-produced particle can be expressed as

$$\beta\gamma = \frac{|\vec{p}|}{m} = \sqrt{\frac{s}{4m^2} - 1}. \quad (7.1)$$

if photon emission in the initial state (initial state radiation, ISR) is neglected, which is especially justified close to the kinematic limit. The function $\epsilon = \epsilon(\beta\gamma)$ is found via a simple linear interpolation between the efficiency of the different generated MC mass points.

Selection efficiency functions for pair-produced particles are displayed in Fig. 7.9: the upper plot shows the efficiency of pair-produced spin-0 particles determined from the process $e^+e^- \rightarrow \tilde{\tau}\tilde{\tau}$ at $\sqrt{s} = 208$ GeV. The efficiency is model independent because only s-channel contributes in the production mechanism. The characteristic behaviour of the efficiency which reflects the position of cut 9 in the dE/dx - p plane: the eye-catching dip at $1.0 \lesssim \beta\gamma \lesssim 1.6$ results from the region which is cut in order to separate SM particles at momenta $p \gtrsim 50$ GeV (Fig. 7.8). Here, efficiencies $\lesssim 2\%$ are obtained. For $\beta\gamma > 1.6$ the selection efficiency becomes roughly 40%, and in the low $\beta\gamma$ region, i.e. $\beta\gamma < 0.9$, values $\gtrsim 90\%$ are reached. The efficiency resulting from the standard OPAL track reconstruction

\sqrt{s} bin (GeV)	204 – 205		206 – 207		208 – 209		208
$(\sqrt{s})_{\text{mean}}$ (GeV)	205.0		206.4		208.0		208.1
\mathcal{L} (pb $^{-1}$)	77.2		127.6		8.1		-
after:	# events		# events		# events		efficiency
	N_{data}	N_{bkg}	N_{data}	N_{bkg}	N_{data}	N_{bkg}	$e^+e^- \rightarrow \tilde{\tau}\tilde{\tau}$
preselection	10713	5231.74	19093	8716.87	1193	529.82	0.997
reduction of non-sim. Bkg.	2667	2094.03	4231	3506.40	279	219.06	0.972
cut 1	1743	1458.48	2692	2412.53	184	150.45	0.951
cut 2	1607	1395.14	2493	2306.94	166	143.75	0.950
cut 3	969	966.74	1494	1578.63	88	100.33	0.950
cut 4	264	231.44	425	395.17	20	24.06	0.950
cut 5	77	63.33	110	109.40	8	6.62	0.907
cut 6	76	61.26	101	105.23	8	6.36	0.903
cut 7	76	60.88	101	104.77	7	6.35	0.903
cut 8	61	48.74	87	84.26	5	5.08	0.903
cut 9	0	0.09	0	0.14	0	0.02	0.903
cut 10	0	0.06	0	0.11	0	0.01	0.903

Table 7.2: Integrated luminosity \mathcal{L} and remaining number of events after each cut for data (N_{data}) and simulated background (N_{bkg}) in different centre-of-mass energy bins from $\sqrt{s} = 204$ GeV – 209 GeV. The corresponding signal efficiencies for the process $e^+e^- \rightarrow \tilde{\tau}\tilde{\tau}$ with $m_{\tilde{\tau}} = 90$ GeV at $\sqrt{s} = 208$ GeV are shown in addition.

\sqrt{s} bin (GeV)	131 – 136		161		172		183
$(\sqrt{s})_{\text{mean}}$ (GeV)	133.2		161.3		172.3		182.7
\mathcal{L} (pb $^{-1}$)	5.6		8.0		9.0		40.1
after:	# events		# events		# events		# events
	N_{data}	N_{bkg}	N_{data}	N_{bkg}	N_{data}	N_{bkg}	N_{data}
cut 10	0	0.01	0	0.01	0	0.01	0
							0.05

Table 7.3: Integrated luminosity \mathcal{L} and remaining number of events after cut 10 for data (N_{data}) and simulated background (N_{bkg}) in different centre-of-mass energy bins from $\sqrt{s} = 131$ GeV – 183 GeV. The number of expected background events is given by the (luminosity) weighted mean value of MC background in all energy bins from 189 GeV to 209 GeV.

is indicated by squares while the efficiency calculated with the modified reconstruction (Section 5.3.4) is shown as dots. For $\beta\gamma < 0.2$ the modified reconstruction leads to a significantly higher selection efficiency.

The second plot of Fig. 7.9 contains the selection efficiency of the process $e^+e^- \rightarrow \tilde{e}\tilde{e}$ at $\sqrt{s} = 208$ GeV. The corresponding Monte Carlo events were generated with $\mu = -200$ GeV

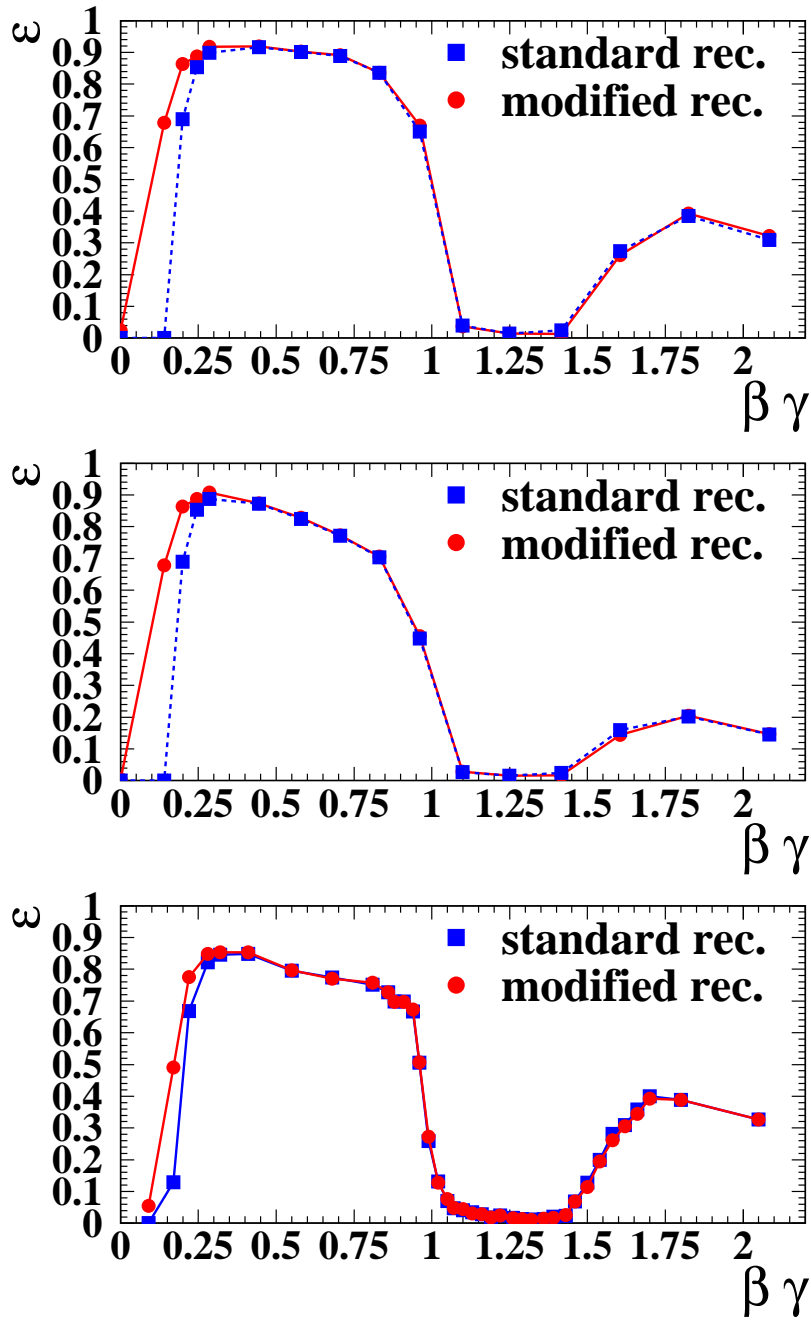


Figure 7.9: Selection efficiencies (ϵ) as a function of $\beta\gamma$ for the pair-production of heavy stable charged particles, found with linear interpolation between the generated MC points. The upper plot shows the model independent efficiency for pair-produced stable staus. The central plot shows the signal efficiency for the pair-production (s- and t- channel) of stable selectrons. Maximum t-channel contribution is assumed, see text. The lower plot contains the model independent selection efficiency for the production of spin-0 particles, e.g. heavy leptons. The striking dip of all efficiencies around $\beta\gamma \approx 1.25$ is due to the region which is cut against high energetic Standard Model particles. In each plot, the squares indicate the efficiency obtained using the standard OPAL track reconstruction, and the dots show the efficiency of the modified reconstruction.

and $\tan\beta = 1.5$. This parameter choice was found to give a conservative estimate of the selection efficiency for selectrons (i.e. maximal neutralino t-channel contribution as its polar angle distribution is more forward peaked, and thus the selection efficiency is lower) by varying the parameters over the range $100\text{ GeV} < |\mu| < 1000\text{ GeV}$ and $1 < \tan\beta < 50$ [123]. Furthermore, the neutralino mass is set to zero, which is unphysical, but yields the most conservative estimate of the efficiency. Owing to t-channel contribution a significant fraction of the stable particles are produced under small polar angles θ which leads to a smaller acceptance and hence to a smaller efficiency. This effect is especially pronounced for $\beta\gamma > 1.6$, where only values of $\epsilon \approx 20\%$ are reached, but it can be neglected for particles produced with very low $\beta\gamma$. Therefore the enhancement of the efficiency using the modified reconstruction is similar to the previous case. The efficiency dip is located also in the same region.

The model independent selection efficiency function for pair-produced spin-1/2 particles (e.g. heavy leptons) is displayed in the lower plot of the figure. It is determined with Monte Carlo events with exclusive s-channel production. The large quantity of generated mass points is used later to determine the systematic uncertainty owing to interpolation. The behaviour of the efficiency is very similar to the first case described in this paragraph.

Note that as data sets at different centre-of-mass energies are combined (Section 6.1), a reasonable selection efficiency is achieved for all masses up to very close to the kinematic limit, which is illustrated in the following example: at $\sqrt{s} = 208\text{ GeV}$ a stable stau of mass $m = 65\text{ GeV}$ is produced with $\beta\gamma \approx 1.25$ and yields a selection efficiency $\epsilon \lesssim 2\%$. At $\sqrt{s} = 161\text{ GeV}$ a stau of the same mass features $\beta\gamma \approx 0.73$, and the selection efficiency is roughly 90%.

Modelling of the efficiency in the case that the heavy stable charged particles appear as decay products of pair-produced particles

If the heavy stable charged particles are not being pair-produced but are decay products of earlier produced particles, the situation is more complicated than in the previous case, because masses of more SUSY particles become relevant: in the case, the stable particle L is the decay product of a pair-produced particle A the masses m_A and m_L have to be taken into account. If the decay chain is longer, i.e. another intermediate particle B appears according to $e^+e^- \rightarrow AA \rightarrow BB\ell\ell \rightarrow LL\ell\ell\ell\ell$ ($\ell = \text{lepton}$), the efficiency is a function of the three masses m_A , m_B and m_L .

In both cases, $\beta\gamma$ of the stable particle is no longer a fixed value for one mass point, but rather a spectrum.

In this case, the following ansatz is made for the efficiency:

$$\epsilon = \int \epsilon_0(\beta\gamma_1, \beta\gamma_2) \cdot g(\beta\gamma_1, \beta\gamma_2) \, d\beta\gamma_1 d\beta\gamma_2. \quad (7.2)$$

Here, ϵ_0 is the efficiency to select a signal event expressed as a function of the $\beta\gamma$ values of the two stable particles. It is assumed to be independent of the masses and of the centre-of-mass energy. g denotes the normalised $\beta\gamma$ spectrum of the heavy stable charged particle. ϵ_0 is determined by calculating the efficiency in 40×40 $\beta\gamma$ bins using simulated signal events. The calculation of g using kinematics is described in the following.

In the case that the heavy stable particle L is a direct decay product of the pair-produced particle A , in the rest frame of the primary particle A the energy E_L of the stable particle is

$$E_L = \frac{m_A^2 - m_B^2 + m_L^2}{2m_A}, \quad (7.3)$$

and its momentum is given by

$$|p_L| = \frac{[(m_A^2 - (m_L + m_B)^2)(m_A^2 - (m_L - m_B)^2)]^{1/2}}{2m_A}. \quad (7.4)$$

According to the Lorentz boost, the energy E_L^* of the stable particle in the laboratory frame is

$$E_L^* = \gamma_A E_L - (\beta\gamma)_A p_{\parallel L} = \gamma_A E_L - (\beta\gamma)_A |p_L| \cdot \cos\theta. \quad (7.5)$$

Here, $p_{\parallel L}$ denotes the parallel component of the momentum of the stable particle L . Thus in the laboratory frame the minimum and maximum accessible energies of the stable particle are

$$E_{\min/\max} = \gamma_A E_L \mp (\beta\gamma)_A |p_L| = \frac{E_{\text{beam}}}{m_A} \cdot E_L \mp (\beta\gamma)_A \cdot |p_L|. \quad (7.6)$$

The energy spectrum of the heavy stable particle is approximated by a flat distribution according to

$$\tilde{g}(E) = \begin{cases} 0 & : E < E_{\min} \\ C & : E_{\min} \leq E \leq E_{\max} \\ 0 & : E > E_{\max} \end{cases} \quad (7.7)$$

with the constant $C > 0$. Figure 7.10 shows some examples of energy spectra of stable staus produced in $e^+e^- \rightarrow \tilde{\chi}_1^0 \tilde{\chi}_1^0 \rightarrow \tilde{\tau}\tilde{\tau}\tau\tau$ at $\sqrt{s} = 206$ GeV. The deviation of the real spectra from a flat distribution will be taken into account in the systematic studies.

Using

$$\beta\gamma = \sqrt{\frac{E^2}{m^2} - 1}. \quad (7.8)$$

for the calculation of $\beta\gamma$, and

$$g(\beta\gamma) = \tilde{g}(E) \frac{dE}{d\beta\gamma} \quad (7.9)$$

to calculate the shape of the $\beta\gamma$ spectrum yields

$$g(\beta\gamma) = \begin{cases} 0 & : \beta\gamma < (\beta\gamma)_{\min} \\ C \frac{\beta\gamma \cdot m}{\sqrt{(\beta\gamma)^2 + 1}} & : (\beta\gamma)_{\min} \leq \beta\gamma \leq (\beta\gamma)_{\max} \\ 0 & : \beta\gamma > (\beta\gamma)_{\max}. \end{cases} \quad (7.10)$$

Figure 7.11 shows as an example four one dimensional $\beta\gamma$ spectra of a stable stau, produced according to $e^+e^- \rightarrow \tilde{\chi}_1^0 \tilde{\chi}_1^0 \rightarrow \tilde{\tau}\tilde{\tau}\tau\tau$ at $\sqrt{s} = 206$ GeV. The solid lines indicate the generated and the dashed lines the calculated spectra according to Eq. 7.10. The

reproduction of the true expected spectrum is reasonable. Apart from statistical fluctuations the differences between both calculation and generated spectrum are due to the negligence of ISR, i.e. if the production of the stable particles takes place with a reduced centre-of-mass energy $\sqrt{s'} < \sqrt{s}$: the generated distributions show a tail pointing to the direction of smaller $\beta\gamma$. This effect will be taken into account in the determination of the systematic error.

For the calculation of the efficiency according to Eq. 7.2 the spectrum must be written as a function of two arguments, i.e. of the $\beta\gamma$ of the two heavy stable charged particles:

$$g((\beta\gamma)_1, (\beta\gamma)_2) = g((\beta\gamma)_1) \cdot g((\beta\gamma)_2) \quad (7.11)$$

Finally, the factor C is determined in order to fulfil the condition

$$\int g((\beta\gamma)_1, (\beta\gamma)_2) d(\beta\gamma)_1 d(\beta\gamma)_2 = 1. \quad (7.12)$$

In the case that the heavy stable charged particle is produced in a longer decay chain, i.e. via an additional intermediate particle, the Lorentz transformation in Eq. 7.5 is done twice: first, the rest frame of the intermediate particle B is boosted into the rest frame of the pair-produced particle A . Then a second boost transforms the system into the laboratory frame. The remaining procedure is the same as described above. Finally, the efficiency $\epsilon_0 = \epsilon_0(\beta\gamma)$ is determined in 40×40 $\beta\gamma$ bins using signal MC.

In the presented analysis efficiencies are determined for pair-produced SUSY particles decaying 100% into stable NLSPs. The following GMSB signal events (Section 4.4) were simulated at $\sqrt{s} = 206$ GeV:

- (a) $e^+e^- \rightarrow \tilde{\chi}_1^0 \tilde{\chi}_1^0 \rightarrow \tilde{\tau}\tilde{\tau}\tau\tau$ (stau NLSP scenario)
- (b) $e^+e^- \rightarrow \tilde{\chi}_1^0 \tilde{\chi}_1^0 \rightarrow \tilde{\ell}\tilde{\ell}\ell\ell$ (slepton co-NLSP scenario)
- (c) $e^+e^- \rightarrow \tilde{\chi}_1^+ \tilde{\chi}_1^- \rightarrow \tilde{\tau}\tilde{\tau}\nu_\tau\nu_\tau$ (stau NLSP scenario)
- (d) $e^+e^- \rightarrow \tilde{\chi}_1^+ \tilde{\chi}_1^- \rightarrow \tilde{\ell}\tilde{\ell}\nu\nu$ (slepton co-NLSP scenario)
- (e) $e^+e^- \rightarrow \tilde{\mu}\tilde{\mu} \rightarrow \tilde{\chi}_1^0 \tilde{\chi}_1^0 \mu\mu \rightarrow \tilde{\tau}\tilde{\tau}\tau\tau\mu\mu$ (stau NLSP scenario)
- (f) $e^+e^- \rightarrow \tilde{e}\tilde{e} \rightarrow \tilde{\chi}_1^0 \tilde{\chi}_1^0 ee \rightarrow \tilde{\tau}\tilde{\tau}\tau\tau ee$ (stau NLSP scenario)

(a) and (b) are generated with $\mu = -200$ GeV and $\tan\beta = 1.5$. In (a) the mass of the selectron which is exchanged in t-channel is fixed to $m = 110$ GeV, i.e. right beyond the kinematic limit of LEP, in (b) the selectron mass is given by the slepton mass. In (c) and (d) a sneutrino is exchanged in t-channel. The contribution is destructive, and the change in the angular distribution owing to different t-channel contributions is very small leading to only marginal effects on the selection efficiency. The process (e) is model independent because of exclusive s-channel production. In (f) the mass of the neutralino exchanged in t-channel is determined by the studied mass point. The neutralino is assumed to be dominated by its gaugino component, i.e. it has maximum coupling. All generated mass points can be found in Appendix B.

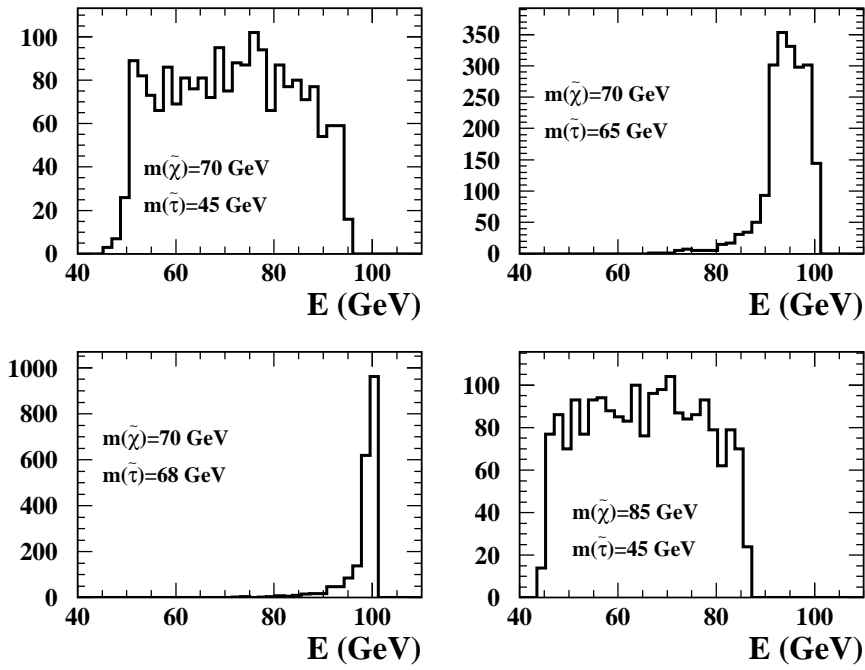


Figure 7.10: Energy spectra of stable staus (arbitrary units), produced according to $e^+e^- \rightarrow \tilde{\chi}_1^0 \tilde{\chi}_1^0 \rightarrow \tilde{\tau}\tilde{\tau}\tau\tau$ at $\sqrt{s} = 206$ GeV. Different mass scenarios are shown. For the calculation of the efficiency the energy spectra are approximated by a flat distribution between the maximum and minimum value. ISR is neglected.

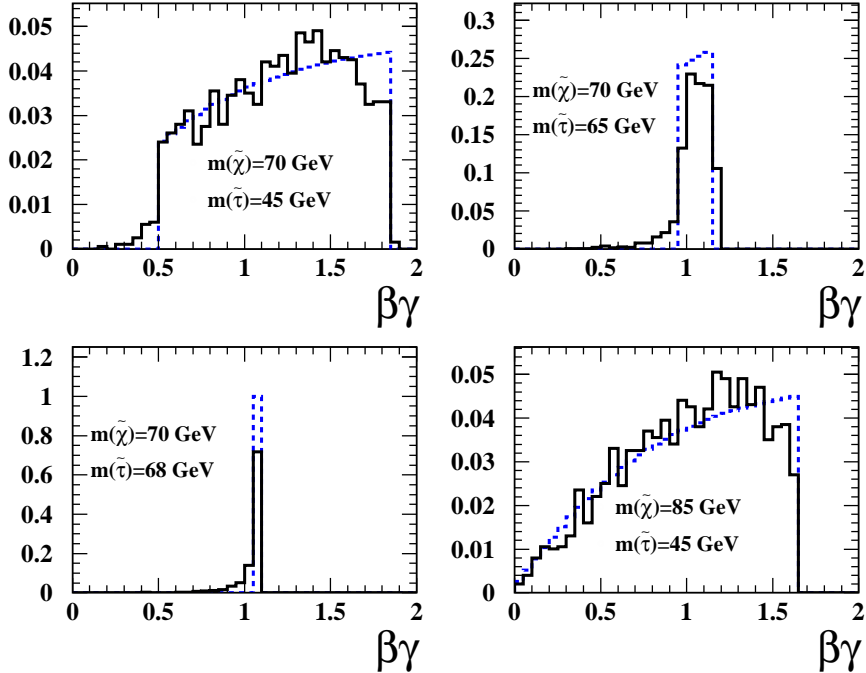


Figure 7.11: $\beta\gamma$ spectra (arbitrary units) of stable staus, produced according to $e^+e^- \rightarrow \tilde{\chi}_1^0 \tilde{\chi}_1^0 \rightarrow \tilde{\tau}\tilde{\tau}\tau\tau$ at $\sqrt{s} = 206$ GeV. Different mass scenarios are shown. The solid lines indicate the generated and the dashed lines the calculated spectra.

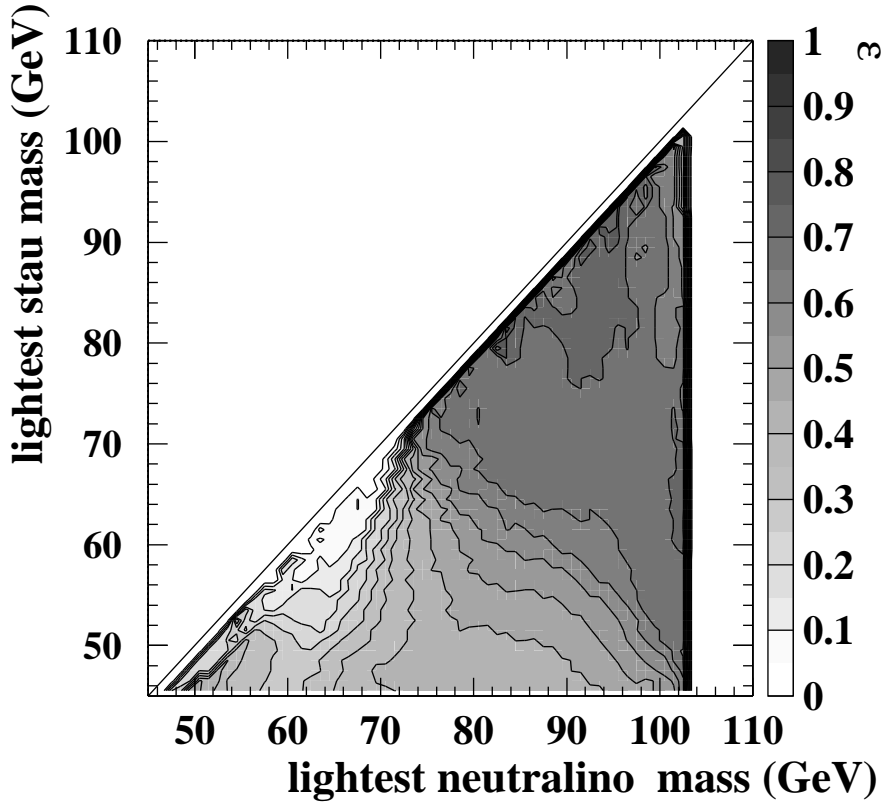


Figure 7.12: Selection efficiency ϵ of the process $e^+e^- \rightarrow \tilde{\chi}_1^0\tilde{\chi}_1^0 \rightarrow \tilde{\tau}\tilde{\tau}\tau\tau$ in the stau NLSP scenario, displayed as a function of the masses of the primary particle (neutralino) and the heavy stable charged particle (stau).

Figures 7.12 and 7.13 show the selection efficiency of the process (a) and (c), respectively, i.e. stau NLSP scenario. The corresponding efficiencies in the slepton NLSP scenario, i.e. (b) and (d) are similar. The efficiencies of (e) and (f) are shown in the Figs. 7.14 and 7.15. Here the displayed contours are the minimum values obtained by varying the mass of the intermediate particle ($\tilde{\chi}_1^0$) over the kinematically allowed region ($m_{\tilde{\tau}} + m_{\tau} \leq m_{\chi^0} \leq m_{\tilde{\ell}} - m_{\ell}$). The efficiency dips (i.e. $\epsilon \lesssim 2\%$) are located around masses of the heavy stable particle of $m \approx (60 - 65)$ GeV for small mass differences with respect to the pair-produced particle, i.e. sharp $\beta\gamma$ spectra. The same heavy stable particle mass yields efficiencies around 30% for larger mass differences, i.e. broader $\beta\gamma$ spectra. In both cases the maximum selection efficiencies are around (70 – 80)%.

7.5 Systematic Uncertainties

7.5.1 Systematic Uncertainties of the Data Selection

As main tool, this analysis uses the information of the tracks which are reconstructed using the signals of the OPAL tracking devices. Therefore the main systematic error of

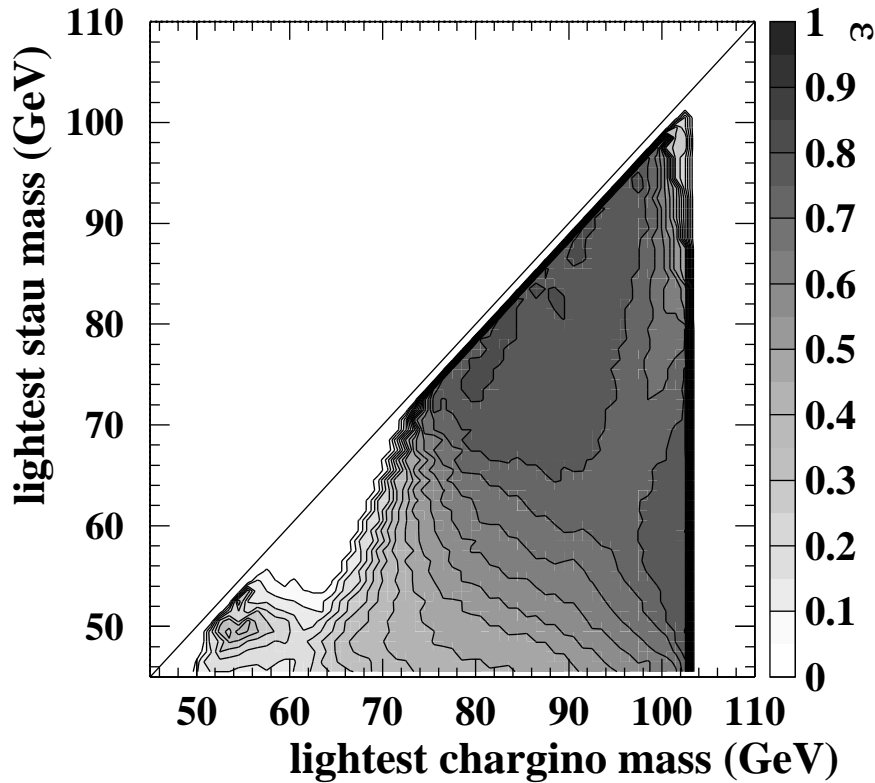


Figure 7.13: Selection efficiency ϵ of the process $e^+e^- \rightarrow \tilde{\chi}_1^+\tilde{\chi}_1^- \rightarrow \tilde{\tau}\tilde{\tau}\tau\tau$ in the stau NLSP scenario, displayed as a function of the masses of the primary particle (chargino) and the heavy stable charged particle (stau).

the event selection can arise from a too optimistic or pessimistic assumption on the track quality and the modelling of the measurement of the specific energy loss in the simulation. This may lead to uncertainties of the determination of the event selection efficiency and in the Standard Model background expectation. In the following, the determination of these systematic effects will be presented. Then the influence of using modified and standard event reconstruction for e^+e^- data events and simulated background, respectively, is discussed.

Performance of the tracking devices

The systematic error arising from the track measurement is evaluated by degrading the quality of the simulated track parameters (smearing) by a certain amount which was determined by comparing momentum and d_0 resolutions from muon pairs and Bhabhas for data and Monte Carlo simulation. A smearing of 5% for the $r-\phi$ parameters (κ, ϕ, d_0) and 20% for the z parameters (θ, z) has been found to be appropriate [124–126]. Repeating the entire analysis with smeared track parameters for simulated signal and background determines the first contribution to the systematic error arising from the central tracking system. The relative error is found to be 2.0% for the signal efficiency and 10.0% for the

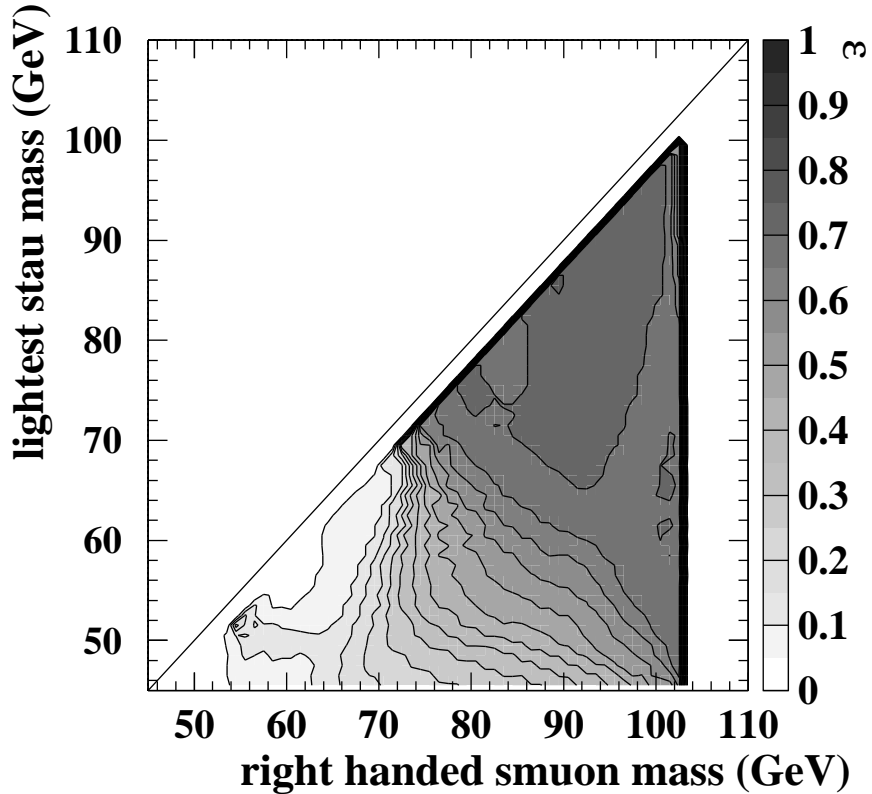


Figure 7.14: Signal efficiency ϵ of the process $e^+e^- \rightarrow \tilde{\mu}\tilde{\mu} \rightarrow \tilde{\chi}_1^0\tilde{\chi}_1^0\mu\mu \rightarrow \tilde{\tau}\tilde{\tau}\tau\tau\mu\mu$ in the stau NLSP scenario, displayed as a function of the masses of the primary particle (smuon) and the heavy stable charged particle (stau). The contours represent the minimum efficiency obtained by varying the mass of the intermediate particle ($\tilde{\chi}_1^0$) over the kinematically allowed region.

number of expected background events.

The second contribution to the systematic error is due to uncertainties of the modelling of the measured dE/dx value. These uncertainties have been quantified to be 10% of the measurement error $\sigma_{dE/dx}$ comparing muon pairs, Bhabha electrons, charged pions, and kaons in simulation and data [126]. In order to determine the contribution to the overall systematic error, the analysis is redone twice for the simulated signal and background, respectively. Each time the measured dE/dx is replaced by a value $(dE/dx)'$ before performing the preselection, which is illustrated in Fig. 7.16: first, $(dE/dx)'$ is chosen such that more events pass cut 9, second, the value is changed in the way less events are selected. This is done by adding, respectively subtracting the above explained systematic uncertainty, depending on the position of the measured specific energy loss with respect to the mean value of upper and lower limit of the cut:

$$(dE/dx)' = \begin{cases} dE/dx + 0.1 \cdot \sigma_{dE/dx} & : dE/dx < (dE/dx)_{\text{mean}} \\ dE/dx - 0.1 \cdot \sigma_{dE/dx} & : dE/dx > (dE/dx)_{\text{mean}} \end{cases} \quad (7.13)$$

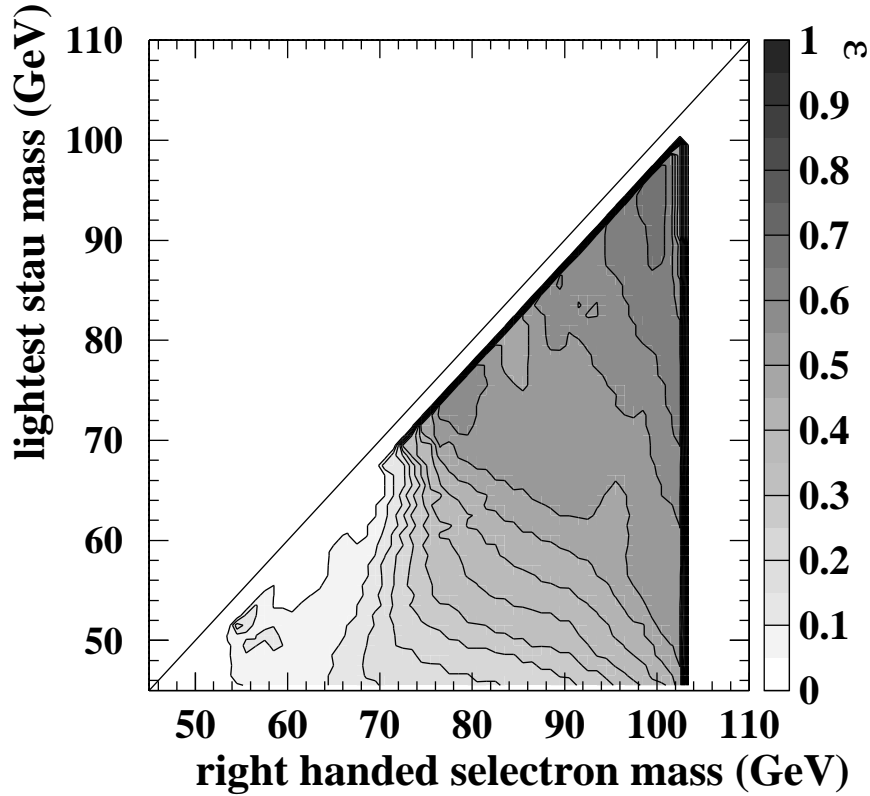


Figure 7.15: Signal efficiency ϵ of the process $e^+e^- \rightarrow \tilde{e}\tilde{e} \rightarrow \tilde{\chi}_1^0\tilde{\chi}_1^0\mu\mu \rightarrow \tilde{\tau}\tilde{\tau}\tau\tau\mu\mu$ in the stau NLSP scenario, displayed as a function of the masses of the primary particle (selectron) and the heavy stable charged particle (stau). The contours represent the minimum efficiency obtained by varying the mass of the intermediate particle ($\tilde{\chi}_1^0$) over the kinematically allowed region.

$$(dE/dx)' = \begin{cases} dE/dx - 0.1 \cdot \sigma_{dE/dx} & : dE/dx < (dE/dx)_{\text{mean}} \\ dE/dx + 0.1 \cdot \sigma_{dE/dx} & : dE/dx > (dE/dx)_{\text{mean}} \end{cases} \quad (7.14)$$

with

$$(dE/dx)_{\text{mean}} = (12.0 \text{ keV/cm} + 8.2 \text{ keV/cm})/2 = 10.1 \text{ keV/cm} \quad (7.15)$$

The studies show that the selection efficiency can change 0.5% and the number of expected background events 5% due to uncertainties of the measured dE/dx . The overall systematic uncertainty caused by the data selection is calculated by taking the squared sum of these values and the error obtained by track smearing, leading to 2.1% for the selection efficiency and 11.2% for the expected Standard Model background. All contributions are summarised in Table 7.4. Both systematic errors for the efficiency and number of expected background events are taken into account as the contribution of the selection to the overall systematic error.

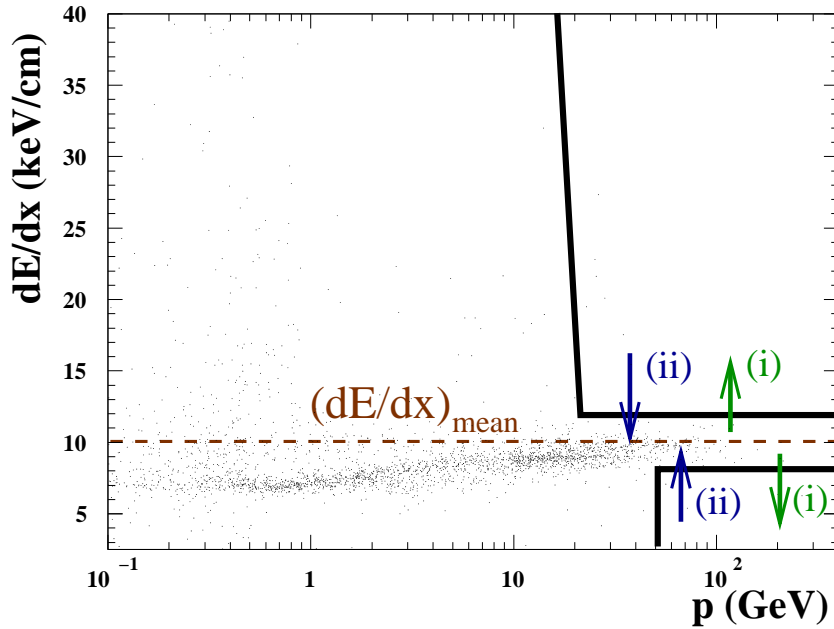


Figure 7.16: Illustration of the displacement of the measured specific energy loss for the determination of the systematic error due to uncertainties in the dE/dx modelling. The analysis is redone changing the measured specific energy loss by $\sigma_{dE/dx}$ (see text) in the way more (i) and less (ii) events pass cut 9.

contribution	ϵ_{signal}	N_{bkg}
track parameter smearing (σ_{track})	2.0%	10.0%
dE/dx modelling ($\sigma_{dE/dx}$)	0.5%	5.0%
$(\sigma_{\text{track}}^2 + \sigma_{dE/dx}^2)^{1/2}$	2.1%	11.2%

Table 7.4: Contributions to the systematic error on the signal selection efficiency ϵ_{signal} and on the number of expected background events N_{bkg} due to uncertainties in the measurement using the central tracking devices.

Influence of the reconstruction modes

As discussed in Section 6.2.5 the modified event reconstruction (Section 5.3.4) is applied in e^+e^- data and simulated signal events for $\sqrt{s} \geq 200$ GeV, while all simulated Standard Model background is reconstructed conventionally. To estimate the influence of using different reconstruction modes on the number of expected background events, the modified reconstruction is applied additionally to the SM background sample which contributes most to the overall expected background, see Tables 7.1 and 7.2: in the 200 GeV energy bin the number of remaining background events is dominated entirely by one two-photon event which survives all cuts. A submission of the corresponding background sample to the modified event reconstruction shows that the number of remaining events from cut three onwards are the same independent of the reconstruction mode. The numbers are summarised in Table 7.5. Therefore the influence of the different event reconstruction modes is neglected in the further analysis.

7.5.2 Systematic Uncertainties of the Efficiency

Limited MC statistics

The statistical uncertainty on the signal efficiency is calculated using the formula

$$\Delta\epsilon_S^{\text{stat}} = \sqrt{\epsilon_S(1 - \epsilon_S)/N} \quad (7.16)$$

with N being the number of generated events in the Monte Carlo sample. For the relative error due to limited MC statistics values of 0.9, % up to 27.6% are found. The statistical uncertainty on the number of background events, N_{bkg} , due to the limited statistics of simulated Standard Model events is

$$\Delta N_{\text{bkg}}^{\text{stat}} = \mathcal{L} \cdot \sqrt{\sum_i (\sigma_i \Delta\epsilon_i^{\text{stat}})^2}. \quad (7.17)$$

Here, $\Delta\epsilon_i^{\text{stat}}$ is calculated analogously to formula 7.16. Thus the uncertainties due to Monte Carlo statistics depend on the square root of the number of selected simulated events. The relative uncertainty on the number of expected SM background events varies between 23.7% and 64.6%.

Interpolation of the efficiency for pair-produced heavy stable charged particles

The uncertainty due to linear interpolation of the signal efficiency is estimated as the difference between the interpolated values and the efficiency obtained at a generated mass point when that specific mass point is omitted from the interpolation procedure. The relative differences are filled into histograms: a distinction is drawn between regions where the efficiency depends only slightly on $\beta\gamma$, i.e. flat efficiency regions with efficiencies of roughly 40% or (80–90)%, and regions of strong $\beta\gamma$ dependence where the efficiency drops down to values below 2%. The two corresponding histograms are shown in Fig. 7.17. 2σ of a Gaussian fitted to the distributions yields a conservative estimate for the uncertainty. In high efficiency regions a relative error of 7.7% is found, and in regions of large efficiency gradient 31.2%. The latter value is the largest contribution to the overall systematic error for pair-produced stable particles. Table 7.6 gives the definition of the different regions as well as a summary of the relative interpolation errors.

Modelling of the efficiency in the case that the heavy stable charged particles appear as decay products of pair-produced particles

For simulated mass samples the efficiency is calculated using the above described method (see Eq. 7.2) and compared with the efficiency at simulated MC points. The relative difference gives a measure for the expected error. According to the shape of the contributing $\beta\gamma$ spectrum, two cases are distinguished: the spectrum is classified to be broad if its width $\Delta(\beta\gamma) = (\beta\gamma)_{\text{max}} - (\beta\gamma)_{\text{min}}$ exceeds the extension of the efficiency dip, i.e. $\Delta(\beta\gamma) > 0.5$. For $\Delta(\beta\gamma) \leq 0.5$, the spectrum is classified as sharp. Depending on their mean $\beta\gamma$ value, sharp spectra are assigned to regions of high efficiency with a flat behaviour and regions of strong efficiency rise/drop. The definition of the regions is the same as described in the previous case (Table 7.6). For sharp spectra, the uncertainty in the calculation of the

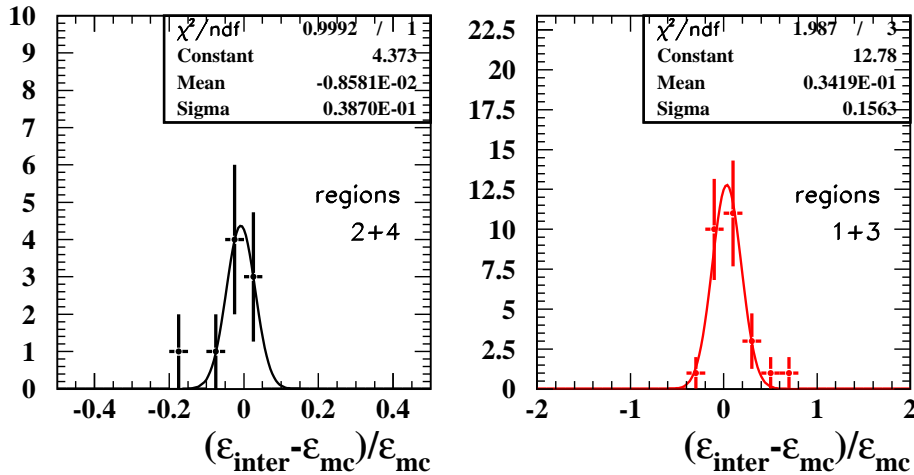


Figure 7.17: Determination of the relative systematic error due to interpolation of the efficiency. The error is estimated as the difference between interpolated values and the efficiency obtained at a generated MC mass points, when that mass point has been omitted in the interpolation procedure. The error varies strongly with the $\beta\gamma$ value of the heavy stable particle. Therefore different regions with specific $\beta\gamma$ range are considered, see Table 7.6. A Gaussian fit yields the expected error. In order to be conservative, 2σ is taken for the interpretation of the results of this analysis.

selection efficiency is large because the negligence of ISR in the modelling of the spectrum and binning have strong influence on the calculation of the integral in Eq. 7.2. The relative deviation of the calculated and simulated efficiency is filled into the right histogram of Fig. 7.18 for sharp spectra in regions with large efficiency gradient. In regions of flat efficiency behaviour the negligence of ISR as well as binning have only a small effect on the calculation. The same holds true for broad spectra regardless of their position, where the integration (Eq. 7.2) is carried out over a large $\beta\gamma$ region. The obtained relative deviations to the efficiency determined from the simulated mass point are filled into the left histogram of Fig. 7.18. Again, 2σ of a Gaussian fitted to the histograms yields a conservative estimate for contribution of the efficiency modelling to the systematic error. For sharp $\beta\gamma$ spectra in regions of large efficiency gradient the relative error is 42.8%, which gives the largest contribution to the overall systematic error, and in the case of sharp spectra in flat efficiency regions and broad spectra 10.5% are found. The errors are summarised in Table 7.6.

7.6 Summary

In the OPAL data taken during the years 1996 – 2000 from $\sqrt{s} = 131$ GeV up to 209 GeV corresponding to an overall integrated luminosity of $\mathcal{L} = 632.1 \text{ pb}^{-1}$ no event passes the selection cuts while roughly 0.795 ± 0.394 events are expected by the Standard Model.

The selection efficiency for all signal topologies is characterised by strong variations with $\beta\gamma$: in the dip region efficiencies of less than 2% are found while high efficiency regions reach values of (70 – 90)%.

\sqrt{s} bin (GeV)	200	
after:	# two-photon events	
	standard reconstr.	modified reconstr.
preselection	599.354	606.163
reduction of non-sim. Bkg.	86.16	88.08
cut 1	39.78	39.78
cut 2	36.80	36.38
cut 3	11.06	11.06
cut 4	10.63	10.63
cut 5	1.91	1.91
cut 6	1.91	1.91
cut 7	1.91	1.91
cut 8	1.91	1.91
cut 9	0.21	0.21
cut 10	0.21	0.21

Table 7.5: Comparison of the number of Standard Model events obtained with the standard OPAL reconstruction and the modified event reconstruction. The numbers shown result from simulated two-photon events which yield the largest contribution. One generated event passes the cuts and yields 0.21 after normalisation. The sample corresponds to roughly 1/4 of the total integrated luminosity in the 200 GeV centre-of-mass energy bin. From cut 3 onwards the same numbers of remaining events are obtained independently of the reconstruction mode. In the present search, simulated Standard Model events are all reconstructed conventionally.

region	$\beta\gamma$	gradient of the efficiency	uncertainty (%)		
			interpol. (stable primary particles)	modelling (stable decay products)	
				sharp spectra	broad spectra
1	< 0.15	large	31.2	42.8	10.5
2	$0.15 - 0.75$	small	7.7	10.5	10.5
3	$0.75 - 1.70$	large	31.2	42.8	10.5
4	> 1.70	small	7.7	10.5	10.5

Table 7.6: Relative systematic error on the selection efficiency due to interpolation (pair-produced stable particles) and modelling of the $\beta\gamma$ spectra (stable secondary and tertiary particles): The error varies strongly with the (mean) $\beta\gamma$ value of the heavy stable particle. Therefore different regions with specific $\beta\gamma$ range are considered. In the case of efficiency modelling, the width of the $\beta\gamma$ spectrum plays a crucial role for the precision of the calculation (see text).

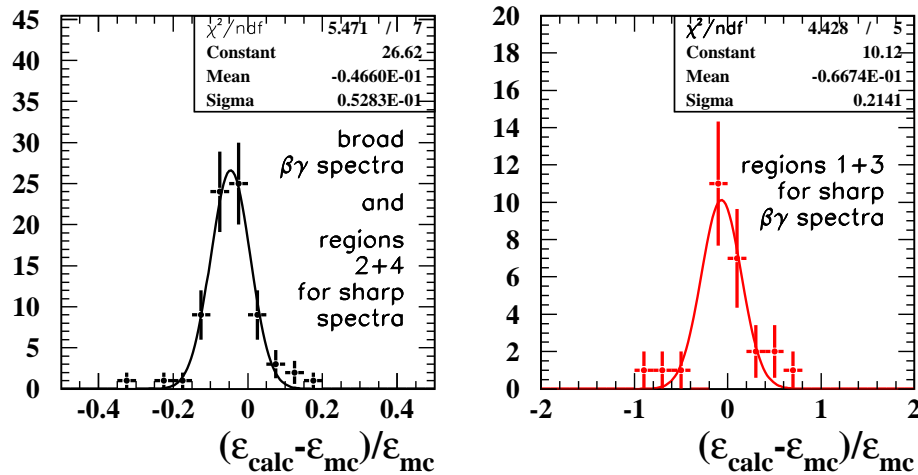


Figure 7.18: Determination of the relative systematic error due to modelling of the efficiency. The relative deviation between the efficiencies determined with MC events and using Eq. 7.2 are filled in the histograms: the right histogram contains values in case the $\beta\gamma$ spectrum is sharp and its mean value is located inside a region of large efficiency variation, i.e. regions 1 and 3, see Table 7.6. All other relative deviations are filled into the left histogram. A Gaussian fit yields the expected error for both cases. In order to be conservative, 2σ is taken for the interpretation of the results of this analysis.

The strong $\beta\gamma$ dependence of the efficiency gives rise to a large systematic uncertainty. Therefore for the determination of the systematic error it is appropriate to introduce two different regions: in flat (i.e. high) efficiency regions the relative systematic error attached to the calculated efficiency is around 10%. The relative systematic error in regions of high efficiency gradient is found to be much larger, i.e. (30–40)%. It is the largest contribution to the overall efficiency error.

A summary of all sources of systematic uncertainties is given in Table 7.7, and Table 7.8 summarises the total numbers of data and expected Standard Model events, N_{bkg} , after the entire selection.

contribution	systematic uncertainty (%)		
	ϵ_{signal}		N_{bkg}
	high eff. region	low eff. region	
monop. trigger emulation	< 1.0		-
integr. luminosity \mathcal{L}	-		$\lesssim 0.3$
selection cuts	2.1		11.2
MC statistics	0.9 – 4.6	2.2 – 27.6	23.7 – 64.6
interpol. of the efficiency (pair-produced heavy stable charged particles)	7.7	31.2	-
modelling of the eff., sharp spectra (for stable particle as decay product)	10.5	42.8	-
modelling of the eff., broad spectra (for stable particle as decay product)	10.5		-

Table 7.7: Summary of the relative systematic uncertainties for the signal efficiency (ϵ_{signal}) and the expected Standard Model background (N_{bkg}). For the determination of the signal selection efficiency using interpolation (pair-production of the stable particle) and modelling of the $\beta\gamma$ spectrum (if the stable particle is a decay product of a pair-produced particle) two cases have to be distinguished: high efficiency regions: $0.15 \leq \beta\gamma \leq 0.75$ and $\beta\gamma > 1.7$ and low efficiency regions including regions of strong rise/drop of the efficiency: $\beta\gamma < 0.15$ and $0.75 \leq \beta\gamma \leq 1.7$.

\sqrt{s} bin range (GeV)	$(\sqrt{s})_{\text{mean}}$ (GeV)	\mathcal{L} (pb^{-1})	N_{bkg}	observed
131.0 – 137.0	133.2	5.6	0.008 ± 0.002	
160.0 – 162.0	161.3	8.0	0.011 ± 0.003	
171.0 – 173.0	172.3	9.0	0.012 ± 0.003	
180.0 – 184.0	182.7	40.1	0.054 ± 0.013	
188.0 – 190.0	188.5	174.0	0.068 ± 0.053	
195.0 – 197.0	195.5	70.8	0.078 ± 0.022	0
199.0 – 201.0	199.5	73.9	0.333 ± 0.218	
201.0 – 203.5	201.6	37.8	0.044 ± 0.013	
203.5 – 205.5	205.0	77.2	0.060 ± 0.024	
205.5 – 207.5	206.4	127.6	0.114 ± 0.040	
> 207.5	208.0	8.1	0.013 ± 0.003	
131 – 209	195.8	632.1	0.795 ± 0.394	0

Table 7.8: Summary of the search results. For the examined centre-of-mass energy bins the expected Standard Model background N_{bkg} is shown as well as the systematic uncertainties. No data event is observed in any bin.

Chapter 8

Interpretation

No candidate events for stable or long-lived heavy charged particles are observed in data. This result is now used to derive upper limits on their production cross-sections, and it will be interpreted within GMSB models.

8.1 Limit Calculation

The result of a counting search experiment can be summarised in a few numbers: The number of expected background events b , the number of expected signal events s for a given signal topology and set of model parameters and the number of candidates n found in e^+e^- data.

Two hypotheses can be distinguished: the production and detection of signal events together with Standard Model background, called $s+b$, and the presence of only Standard Model background, called b .

To separate signal-like from background-like outcomes a *test statistic* or *estimator* is introduced. It is generally a function of b , s and n , monotonically increasing with n . An optimal choice for the estimator is the *likelihood ratio* [127]:

$$X = \frac{e^{-(s+b)}(s+b)^n}{n!} \Big/ \frac{e^{-b}b^n}{n!} \quad (8.1)$$

For the case of N search experiments or channels, e.g. different centre-of-mass energy bins, the estimator can be extended to

$$X = \prod_{i=1}^N X_i = \prod_{i=1}^N \frac{e^{-(s_i+b_i)}(s_i+b_i)^{n_i}}{n_i!} \Big/ \frac{e^{-b_i}b_i^{n_i}}{n_i!}. \quad (8.2)$$

Now, the *Confidence Level* (CL) for excluding the possibility of the $s+b$ hypothesis can be defined as the probability P_{s+b} that X would be less than or equal to the value X_{obs} observed in data:

$$\text{CL}_{s+b} = P_{s+b}(X \leq X_{obs}). \quad (8.3)$$

X_{obs} is the value of the estimator 8.2 computed from b , s and the observed n .

Taking into account exclusively CL_{s+b} for a statistical analysis has the disadvantage, that in the case of a statistical downward fluctuation of the background, any signal or even the b hypothesis could be excluded.

Therefore, the limit calculation includes also the confidence level for excluding the possibility of the presence of only background. It is defined similarly to 8.3:

$$\text{CL}_b = P_b(X \leq X_{obs}) . \quad (8.4)$$

Now, the quantity CL_s is defined as the ratio

$$\text{CL}_s = \text{CL}_{s+b}/\text{CL}_b , \quad (8.5)$$

and the confidence level for the exclusion of a signal is

$$\text{CL} = 1 - \text{CL}_s . \quad (8.6)$$

A point in the parameter plane studied, e.g. the $\Lambda - \tan \beta$ plane in the GMSB parameter space, is excluded at 95% CL, if $\text{CL}_s < 0.05$ for all hypotheses with these values of Λ and $\tan \beta$, while points with $\text{CL}_s > 0.05$ are allowed.

In order to obtain an upper limit on the cross-section σ for a given process, σ and therefore s is varied until $\text{CL}_s = 0.05$ for the given values of b and n .

8.2 Cross-Section Limits

In this section model-independent limits at 95% CL on the production cross-sections of different signal processes are presented. The limits are calculated in a grid of 60 masses between 45 and 105 GeV of all appearing particles, i.e. steps of 1 GeV.

In order to combine cross-section limits obtained at different centre-of-mass energies, \sqrt{s} , assumptions must be made for the cross-section dependence: for pair-produced spin-1/2 particles a β/s dependence of the cross-section, and for scalars generally a β^3/s dependence was assumed (β = velocity of the particle, s = centre-of-mass energy squared). These assumptions are strictly true only for the photon propagator [117] and are approximations, especially for processes with a dominant t-channel. A different approach is used only in the case of pair-produced stable smuons and staus: Here, predictions of the GMSB model for the \sqrt{s} dependence of the cross-sections are used to combine different centre-of-mass energy bins. This approach is based on a scan over a GMSB parameter space, which will be explained later in Section 8.3.1. However, as will be shown, the dependence is rather model independent.

8.2.1 Pair-Production of Heavy Stable Charged Particles

Pair-Production of Spin-0 Particles

The pair-production cross-section limit at $\sqrt{s} = 206$ GeV for the process $e^+e^- \rightarrow \tilde{\tau}^+\tilde{\tau}^-$ is shown in Fig. 8.1. The limit is model independent because the s-channel contributes exclusively. Therefore it is also valid for $e^+e^- \rightarrow \tilde{\mu}^+\tilde{\mu}^-$ and for any other stable scalars X^+X^- produced only in the s-channel.

Over the whole mass range up to very close to the kinematic limit cross-sections larger than 0.14 pb can be excluded; for masses $m \leq 52$ GeV and $68 \text{ GeV} \leq m \leq 101$ GeV cross-sections larger than 0.02 pb are excluded and in the mass region between 72 GeV and 88 GeV even cross-sections larger than 0.01 pb are excluded. The relatively weak limit at masses around 60 GeV is owing to the region on the $\beta\gamma$ axis where the selection efficiency drops below 2%. The right plot of the figure shows a magnification of the high mass region including results obtained using the standard OPAL event reconstruction.

Compared to the search for stable and long-lived massive charged particles described in [128], the cross-section limit is weaker in the present search for the major part of the particle masses. This is due to the fact that the present analysis a single selection is used to measure several signal topologies described in 4.4 while the above cited analysis is restricted to topologies with two pair produced stable particles opening a track angle of approximately 180° (back-to-back topology). However, as this analysis is optimised for the detection of heavy stable charged particles at the maximum kinematically accessible masses, i.e. $m_{\tilde{\ell}} \gtrsim 100$ GeV, the cross-section limit is improved in this region, see Fig. 8.1. The improvement using the modified reconstruction is comparable with the result which would have been obtained using the standard OPAL reconstruction with data taken at an increased centre-of-mass energy by approximately 2 GeV.

Fig. 8.2 shows the cross-section limit obtained for pair-production of stable selectrons. Maximum t-channel contribution is assumed, such that the presented limit is conservative (the polar angle distribution of the t-channel contribution is more forward peaked, and thus the selection efficiency is lower). The limit shows a similar behaviour as in the previous case, but it is slightly worse owing to the lower signal selection efficiency. Cross-sections larger than 0.17 pb are excluded over the mass range up to very close to the kinematic limit. In the restricted mass range, omitting the region between 52 GeV and 68 GeV pair-production cross-sections are excluded larger than 0.03 pb. Again, the right plot of the figure shows a magnification of the high mass region (only the result obtained with the modified reconstruction algorithm is shown).

Pair-Production of Spin-1/2 Particles

Model independent limits are obtained for stable spin-1/2 particles produced exclusively via s-channel, for example production of heavy leptons. The cross-section limit, displayed in the left part of Fig. C.1, shows a similar behaviour as for spin-0 particles. Over the whole mass range up to very close to the kinematic limit cross-sections larger than 0.14 pb are excluded; for masses $m \leq 52$ GeV and $68 \text{ GeV} \leq m \leq 101$ GeV cross-sections larger than 0.02 pb are excluded.

An interpretation of this limit within the MSSM can be found in Appendix C.

8.2.2 Indirect Production of Heavy Stable Charged Particles

Heavy stable secondary particles

Upper limits on the production cross-section times branching ratio squared ($[\text{BR}(\tilde{\chi} \rightarrow \tilde{\ell}\ell)]^2$, $\tilde{\chi} = \tilde{\chi}_1^0, \tilde{\chi}_1^\pm$) are obtained for pair-produced neutralinos decaying into stable sleptons according to

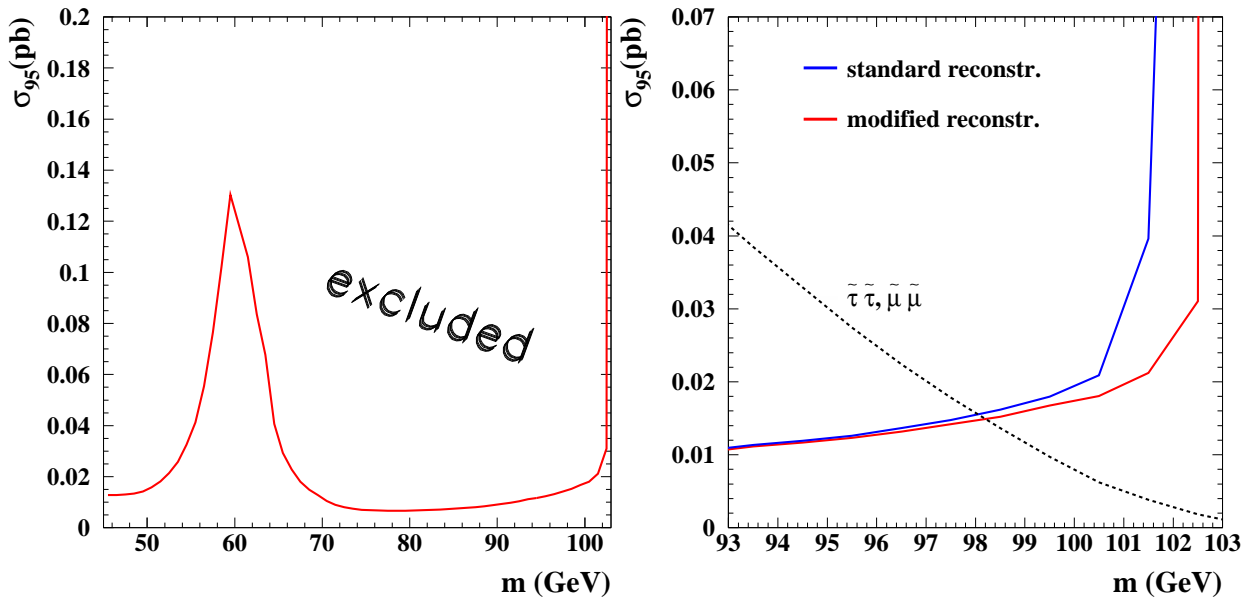


Figure 8.1: Model independent 95% CL upper limit on the pair-production cross-section for spin-0 heavy stable charged particles at $\sqrt{s} = 206$ GeV. The right plot shows a magnification of the high mass region. It shows the limit obtained with the standard OPAL track reconstruction code and the expected cross-section for the pair-production of stable staus/smuons. The exclusion of the standard reconstruction is weaker. But, as the predicted cross-sections for pair-produced heavy stable charged particles are low in the GMSB, the derived mass limit, given by the crossing point of theoretical and experimental curve, does not improve significantly with the modified reconstruction.

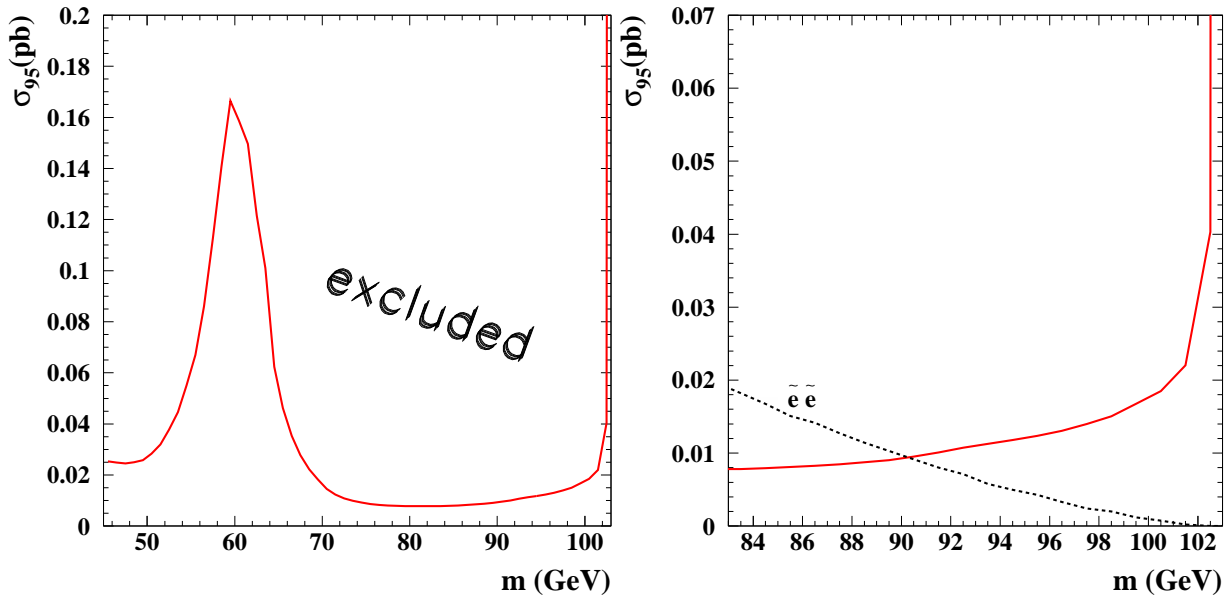


Figure 8.2: Upper limit at 95% CL on the production cross-section of stable selectron pairs at $\sqrt{s} = 206$ GeV. The right plot shows a magnification of the high mass region including the expected cross-section for pair-production of the light selectron. The crossing point of theoretical and experimental curves yields the lower mass limit for light selectrons at 95% CL. The result obtained with the modified event reconstruction is shown.

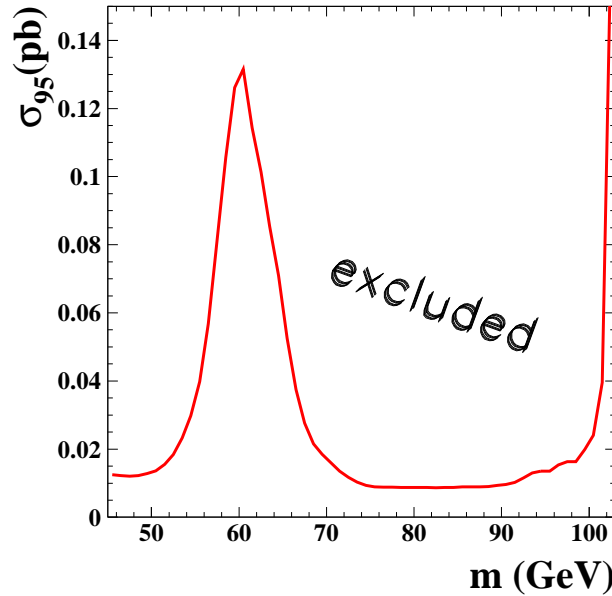


Figure 8.3: Model independent 95% CL upper limit on the (s-channel) pair-production cross-section of spin-1/2 heavy stable charged particles at $\sqrt{s} = 208$ GeV. The result obtained with the modified event reconstruction is shown.

- (a) $e^+e^- \rightarrow \tilde{\chi}_1^0 \tilde{\chi}_1^0 \rightarrow \tilde{\tau} \tilde{\tau} \tau \tau$ (stau NLSP scenario)
- (b) $e^+e^- \rightarrow \tilde{\chi}_1^0 \tilde{\chi}_1^0 \rightarrow \tilde{\ell} \tilde{\ell} \ell \ell$ (slepton co-NLSP scenario)

for $\mu = -200$ GeV and $\tan \beta = 1.5$. Both GMSB scenarios, the stau NLSP scenario with the neutralino decaying to 100% into $\tilde{\tau}_1 \tau$ and the co-NLSP scenario with equal branching fractions to all flavours are studied and lead, as expected, to a very similar result. The upper cross-section limits for $\sqrt{s} = 208$ GeV are shown in Fig. 8.4 for (a) and in Fig. 8.5 for (b). For the major part of the accessible phase space (i.e. $m_{\tilde{\chi}_1^0} > m_{\tilde{\ell}, \tilde{\tau}} + m_{\ell, \tau}$) cross-sections larger than 0.03 pb and often 0.01 pb can be excluded. The limit in the region of the efficiency dip reflects the behaviour of the selection efficiency of this topology (Section 7.4).

A similar result is obtained for pair-produced charginos decaying into stable sleptons and neutrinos according to

- (c) $e^+e^- \rightarrow \tilde{\chi}_1^+ \tilde{\chi}_1^- \rightarrow \tilde{\tau} \tilde{\tau} \nu_\tau \nu_\tau$ (stau NLSP scenario)
- (d) $e^+e^- \rightarrow \tilde{\chi}_1^+ \tilde{\chi}_1^- \rightarrow \tilde{\ell} \tilde{\ell} \nu_\ell \nu_\ell$ (slepton co-NLSP scenario).

The upper cross-section limits for $\sqrt{s} = 208$ GeV are shown in Fig. 8.6 for (c) and in Fig. 8.7 for (d).

Heavy stable tertiary particles

For stable staus produced according to

- (e) $e^+e^- \rightarrow \tilde{\mu} \tilde{\mu} \rightarrow \tilde{\chi}_1^0 \tilde{\chi}_1^0 \mu \mu \rightarrow \tilde{\tau} \tilde{\tau} \tau \tau \mu \mu$ (stau NLSP scenario)

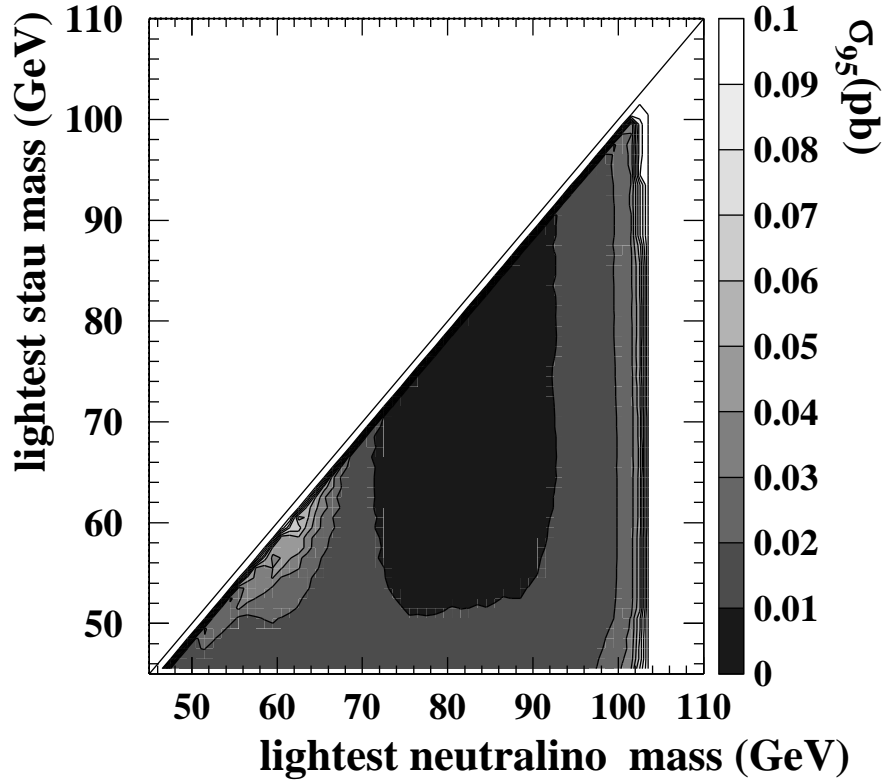


Figure 8.4: Upper limits at $\sqrt{s} = 208$ GeV and 95% CL on the production cross-section times branching ratio squared for pair-produced neutralinos decaying into stable staus in the stau NLSP scenario. The contours are shown as a function of the neutralino and the stau mass.

upper limits on the production cross-section times branching ratio squared ($[\text{BR}(\tilde{\ell} \rightarrow \tilde{\chi}_1^0 \ell) \times \text{BR}(\tilde{\chi}_1^0 \rightarrow \tilde{\tau} \tau)]^2$) are shown in Fig. 8.8 plane for $\sqrt{s} = 208$ GeV. For each point in the $m_{\tilde{\mu}} - m_{\tilde{\tau}}$ plane, a scan over $m_{\tilde{\chi}_1^-}$ is performed and the weakest exclusion is shown. For the major part of the accessible phase space (i.e. $m_{\tilde{e}} > m_{\tilde{\tau}} + m_{\ell} + m_{\tau}$) cross-sections larger than 0.04 pb and often 0.02 pb can be excluded. The limit in the region of the efficiency dip reflects the behaviour of the selection efficiency (Section 7.4).

A very similar result is obtained for pair-produced selectrons (assuming maximum t-channel contribution):

$$(f) \quad e^+ e^- \rightarrow \tilde{e} \tilde{e} \rightarrow \tilde{\chi}_1^0 \tilde{\chi}_1^0 ee \rightarrow \tilde{\tau} \tilde{\tau} \tau \tau ee \text{ (stau NLSP scenario).}$$

The upper cross-section limit is displayed in Fig. 8.9. Here $m_{\tilde{\chi}_1^\pm}$ is scanned and the weakest limit is shown.

8.3 Interpretation within the Framework of GMSB Models

Up to this point, cross-section limits have been presented. A comparison with theoretical expectations of GMSB models allows to set mass limits for stable particles. Additionally, constraints on GMSB parameters are derived.

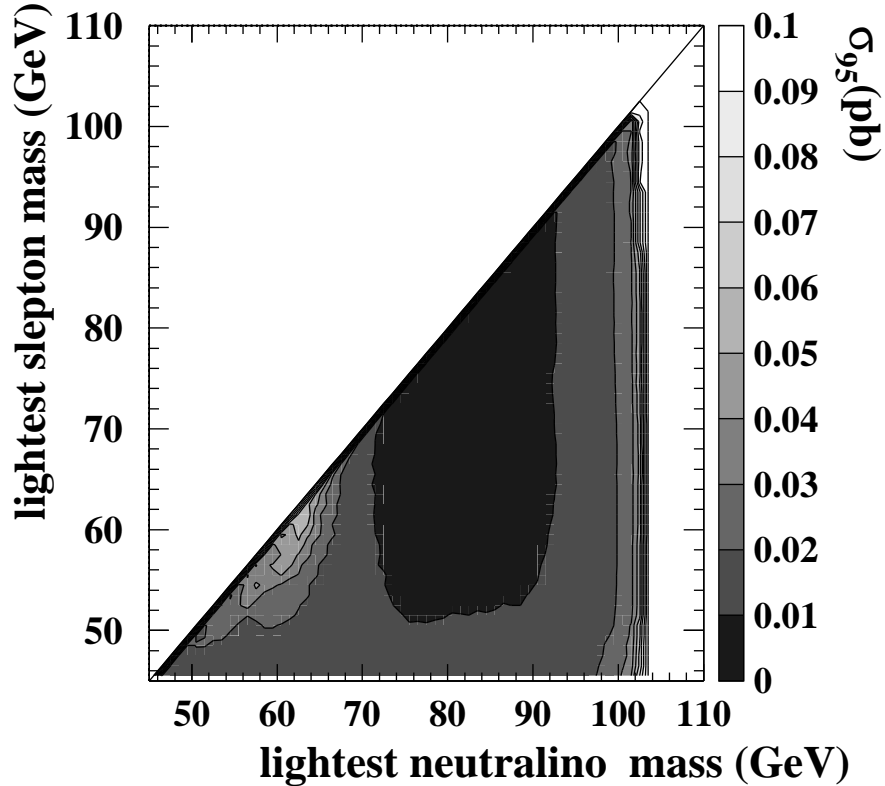


Figure 8.5: Upper limits at $\sqrt{s} = 208$ GeV and 95% CL on the production cross-section times branching ratio squared for pair-produced neutralinos decaying into stable sleptons in the slepton-co NLSP scenario. The contours are shown as a function of the neutralino and the slepton mass.

8.3.1 The GMSB Parameter Space

In order to create a database containing the theoretical expectations, a scan in the parameter space was performed to calculate the complete mass spectrum, the production cross-sections and the branching ratios for different SUSY particles at the considered points [81, 87]. This scan was performed according to the framework and formulae of [129]. The calculations were embedded in the **SUSYGEN** generator. The model parameters as well as the range and step size considered for these parameters in the scan are summarised in Table 8.1.

The messenger scale is arbitrary in the minimal model, but, as the mass m_m of the messenger bosons is given by $m_m = M\sqrt{1 \pm \Lambda/M}$, the relation $M > \Lambda$ has to be fulfilled in order to obtain a positive messenger boson mass squared. Both models with $M \approx \Lambda$ and $M \gg \Lambda$ are viable. Therefore three scenarios for the messenger scale are studied: M very close to Λ ($M = 1.01 \cdot \Lambda$), $M = 250$ TeV and M very large ($M = 10^6$ TeV). For the integer parameter N values up to five are considered. This is adequate, since perturbativity of the gauge interactions up to the GUT scale, M_X , implies [78]

$$N \lesssim \frac{150}{\ln(M_X/M)}.$$

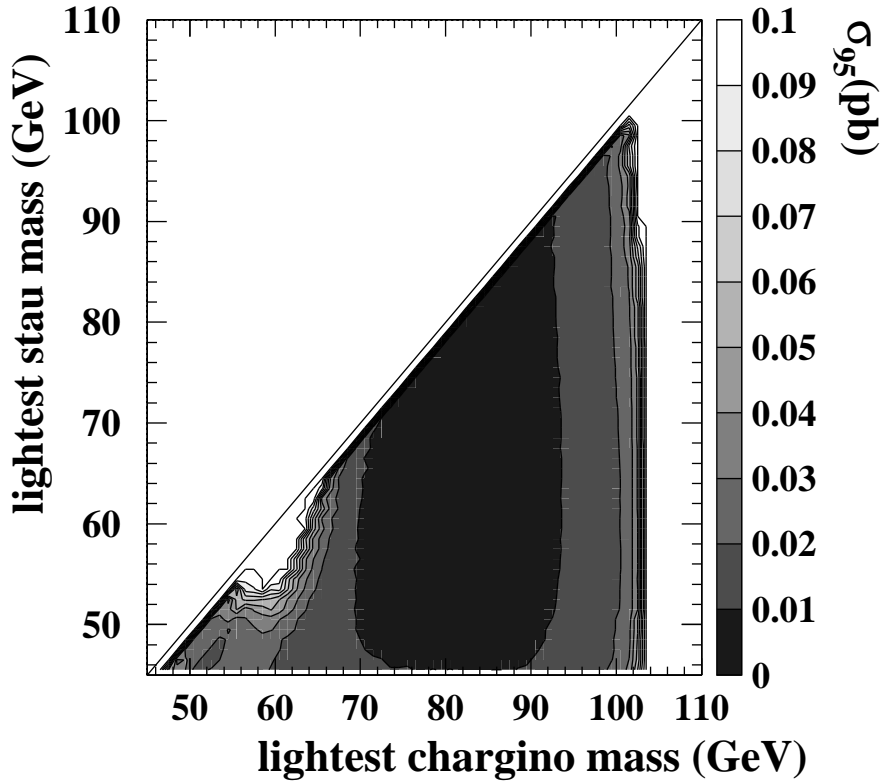


Figure 8.6: Upper limits at $\sqrt{s} = 208$ GeV and 95% CL on the production cross-section times branching ratio squared for pair-produced charginos decaying into stable staus in the stau NLSP scenario. The contours are shown as a function of the chargino and the stau mass. In the region not covered by the displayed range with $m_{\tilde{\chi}_\pm} > m_{\tilde{\tau}}$, which corresponds to the region where the efficiency drops down, cross-sections of $\sigma \gtrsim 0.2$ pb can still be excluded.

parameter	scan ramp	step size
Λ	5 – 150 TeV	1 TeV
$\tan \beta$	2.0 – 50.0	0.2
M	$1.01 \cdot \Lambda$, 250 TeV, 10^6 TeV	–
N	1 – 5	1
$\text{sign}(\mu)$	+1, -1	–

Table 8.1: Scan of the GMSB parameter space. The parameter Λ sets the overall mass scale of the SUSY particles, $\tan \beta$ is the ratio of the vacuum expectation values of the two Higgs doublets, M is the messenger scale, N the messenger index, and $\text{sign}(\mu)$ is the sign of the Higgs sector mixing parameter.

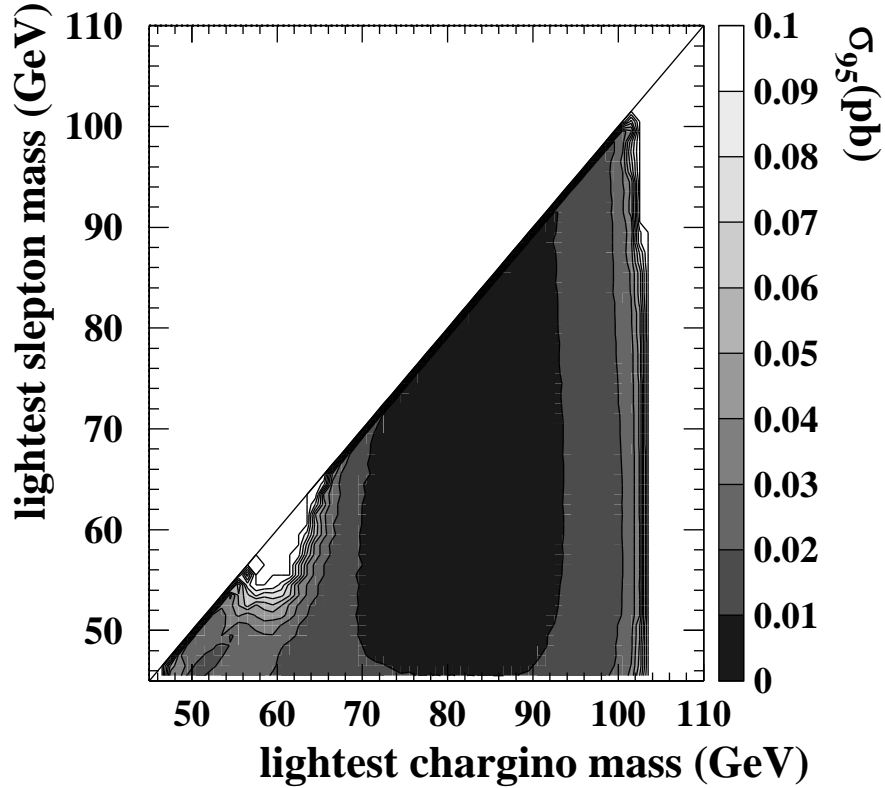


Figure 8.7: Upper limits at $\sqrt{s} = 208$ GeV and 95% CL on the production cross-section times branching ratio squared for pair-produced charginos decaying into stable sleptons in the slepton-co NLSP scenario. The contours are shown as a function of the chargino and the slepton mass. In the region not covered by the displayed range with $m_{\tilde{\chi}_\pm} > m_\ell$, which corresponds to the region where the efficiency drops down, cross-sections of $\sigma \gtrsim 0.2$ pb can still be excluded.

Thus for a messenger mass scale $M = 100$ TeV, $N \leq 5$ is required, and even for very high M of 10^{10} TeV, $N > 10$ is disfavoured from theory. For the parameter μ both signs are studied. For each of the resulting 30 combinations of N , M and $\text{sign}(\mu)$, a scan in Λ and $\tan \beta$ is performed: for each scan point the sparticle masses, branching ratios and their production cross-section at $\sqrt{s} = 208$ GeV are calculated. The upper and lower limits of the scan are chosen according to the following considerations: for $\Lambda > 150$ TeV the supersymmetric particles are already very heavy and cannot be produced at LEP energies. For $\tan \beta < 2.0$ the calculations are unstable. The regions with $\tan \beta > 50.0$ and $\Lambda < 5$ TeV are theoretically forbidden. The exact shape of the theoretically inaccessible region in the $\Lambda - \tan \beta$ plane depends on the other parameters.

For the gravitino mass a value of 2 eV, corresponding to a SUSY breaking scale of $\sqrt{F} \approx 100$ TeV, was chosen. This is motivated by the requirement that the branching ratio of the third lightest SUSY particle, the next-to-NLSP to the gravitino is small and only the NLSP decays into the gravitino. As long as this is fulfilled, the cross-sections and branching ratios do not depend on the gravitino mass.

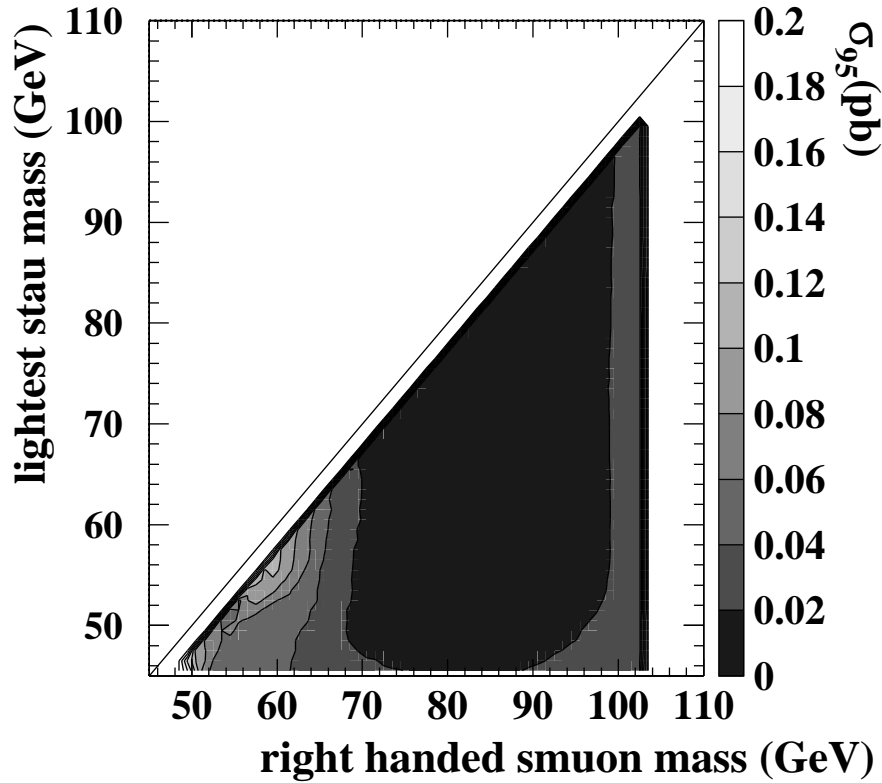


Figure 8.8: Model independent upper limits at $\sqrt{s} = 208$ GeV and 95% CL on the production cross-section times branching ratio squared for pair-produced smuons decaying into stable staus via an intermediate particle, the neutralino. The contours are shown as a function of the smuon and the stau mass. The limits are valid for all neutralino masses.

The minimal expected cross-section for pair-produced stable particles

For the combination of data with different centre-of-mass energies as well as for the calculation of NLSP mass limits, the theoretically expected cross-sections σ within the model have to be known. To obtain values which are valid for each of the parameter sets considered, the following procedure was applied.

For each of the 30 parameter combinations, a scan over the parameters Λ and $\tan\beta$ was performed to obtain for each NLSP mass the minimum cross-section within this special parameter set. The result is displayed in Fig. 8.10. For pair-produced scalar electrons (selectrons) strong variations of σ are found because of additional interfering t-channel production which contributes differently for the various parameter sets. For smuons and staus the cross-sections are much more uniform due to the fact that for these only s-channel production is allowed. Thus in these cases the cross-section is a function of the kinematics (slepton mass and \sqrt{s}) rather than of the details of the model.

8.3.2 Mass Limits

The lower limits on the masses are determined by the crossing point between the experimental cross-section limit and the theoretical expectation. The latter is given by

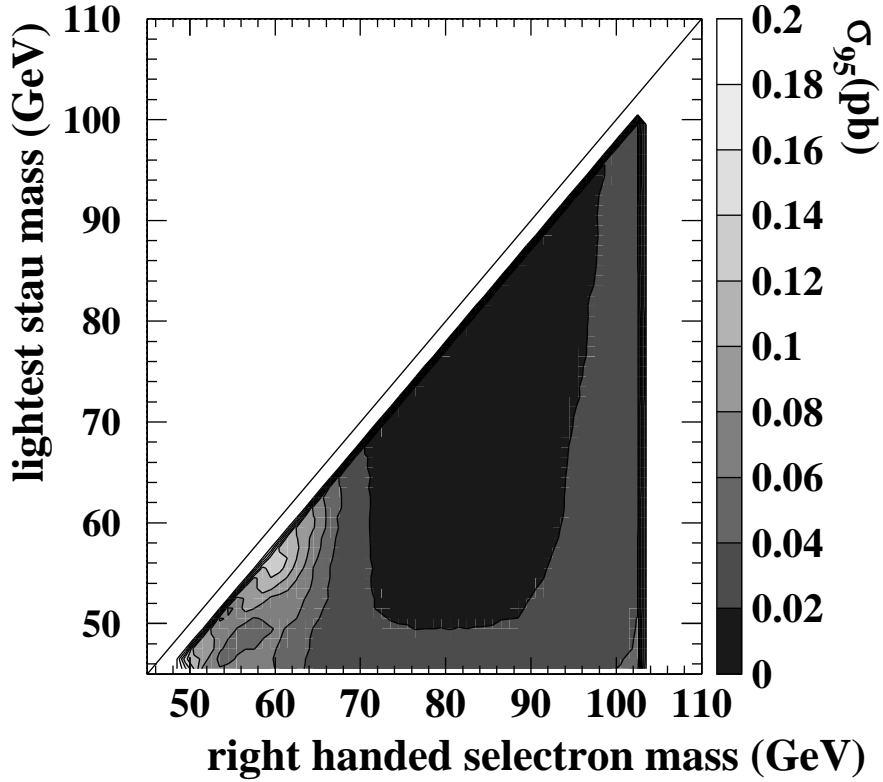


Figure 8.9: Upper limits at $\sqrt{s} = 208$ GeV and 95% CL on the production cross-section times branching ratio squared for pair-produced selectrons decaying into stable staus via an intermediate particle, the neutralino. The contours are shown as a function of the selectron and the stau mass. The limits are valid for all neutralino masses.

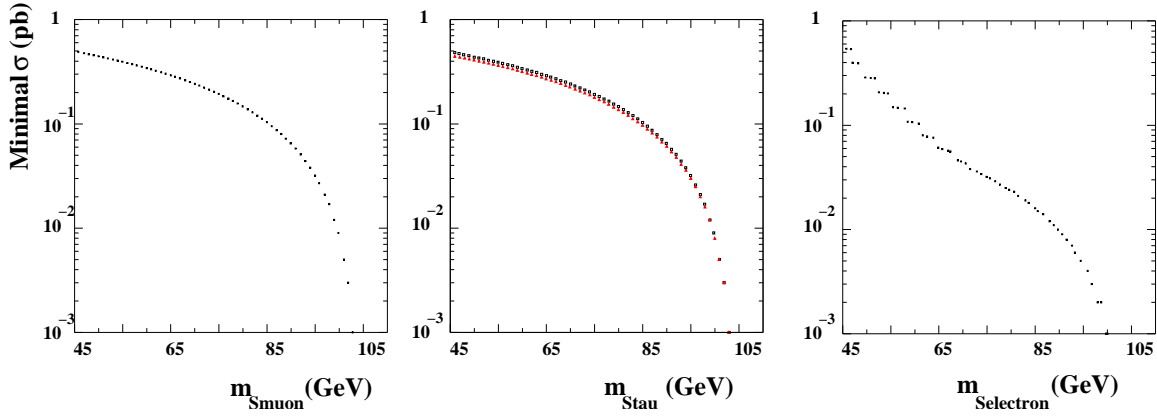


Figure 8.10: Minimal GMSB cross-section for smuon (left), stau (centre) and selectron (right) pair-production at $\sqrt{s} = 208$ GeV. In the case of stau pair-production the slepton co-NLSP scenario (black) and the stau NLSP scenario (red) are distinguished.

the minimal expected cross-section described above. It is displayed in the plots on the right hand side of the Figs. 8.1 and 8.2 for pair-produced staus/smuons and selectrons, respectively. The crossing points with the experimental curve yield at 95% CL

$$m_{\tilde{\ell}} > 98.1 \text{ GeV} \quad (\tilde{\ell} = \tilde{\tau}_1, \tilde{\mu}_R) \quad \text{and} \quad m_{\tilde{e}_R} > 90.2 \text{ GeV}. \quad (8.7)$$

As in GMSB models the right handed selectron can only be the NLSP in the case of mass degeneracy with the right handed smuon and the lightest stau, the first mass limit is valid for all sleptons.

8.3.3 Exclusions in the GMSB Parameter Space

For each of the 30 sets of the GMSB parameters N , M , and $\text{sign}(\mu)$ considered in the GMSB parameter scan (Section 8.3.1), the exclusion in the $\Lambda - \tan(\beta)$ plane is studied under the assumption that the NLSP is the lightest slepton, i.e. stau NLSP or slepton-co NLSP scenario. At each point in this plane, the mass spectrum, the cross-section for the various channels as well as their branching ratios are known. A point in the parameter space is excluded if it is kinematically accessible and the expected cross-section in at least one channel is larger than the experimental 95% CL cross-section limit in this channel taking into account the branching ratios BR. The regions where the NLSP is lighter than 45 GeV, the LEP I search region, are not considered in this analysis.

Figure 8.11 shows the excluded regions in the $\Lambda - \tan(\beta)$ plane for $N = 3$ and $N = 5$, each for three combinations of M and positive μ . The different colours correspond to different search channels, i.e. signal topologies. However, in the scanned parameter space, the regions excluded by the search for indirectly produced heavy stable charged particles are generally already covered by the search for pair-produced NLSPs. One important exception is the stable NLSP production via chargino pairs, which for $N \gtrsim 2$ often excludes a small region at low $\tan\beta$ and low Λ , which is not covered by any other search channel (e.g. $N = 5$, $M = 1.01\Lambda$, $\mu > 0$). Thus this search channel turns out to be indispensable to set general limits on Λ (next section).

In general, for low M more points can be excluded than for high M , and slightly more points can be excluded for $\mu < 0$. With increasing N , the slepton NLSP scenarios dominate more and more, and the neutralino is the NLSP only for small Λ and $\tan(\beta)$. This behaviour is particularly pronounced for low M .

In addition, all six plots contain constraints implied by lower bounds on the mass m_{h^0} of the MSSM Higgs boson h^0 . The mass constraint on the Standard Model Higgs boson ($m_H > 114.4 \text{ GeV}$) [130] is a good approximation for m_{h^0} because in GMSB scenarios the HZZ coupling is not suppressed compared to the SM coupling in almost any region of the parameter space [131]. A conservative estimate for the used database is obtained by reducing the Standard Model bound by 3 GeV [132]. The exclusion in the $\tan(\beta) - \Lambda$ plane is given by the region below the solid black line. The experimental error of $\approx 5\%$ of the top quark mass might change m_{h^0} by roughly 5%, too. The corresponding lower mass bound is represented in each plot by the region below the dashed curve.

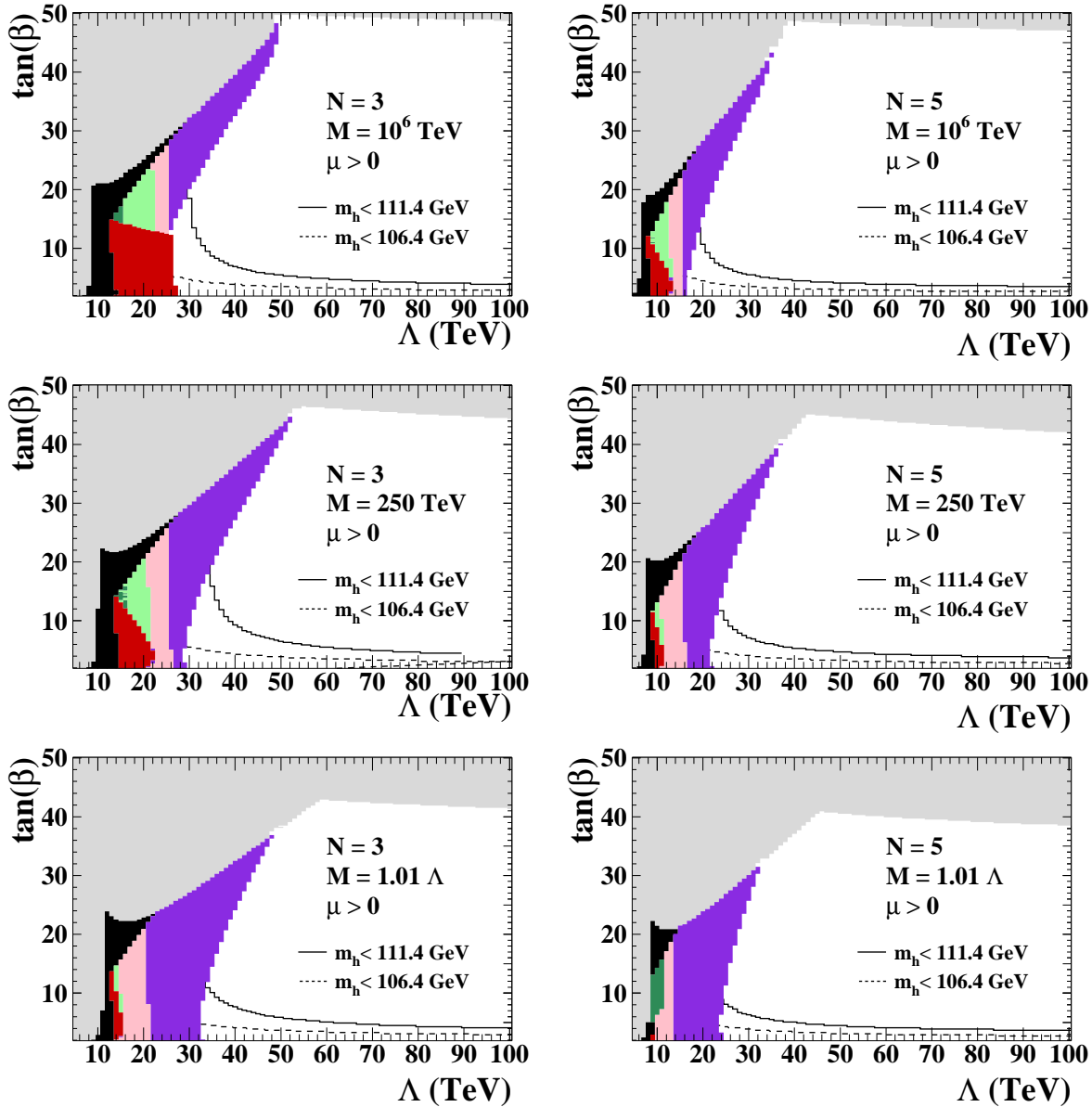


Figure 8.11: Excluded regions in the $\Lambda - \tan \beta$ plane for $N = 3$ (left) and $N = 5$ (right) for different values of M and positive μ , valid for lifetimes $\tau > 10^{-6}$ s. The gray regions are not allowed by theory. In the black regions the NLSP is lighter than 45 GeV, which is not considered in this analysis. The regions below the solid and dashed lines indicate exclusions implied by lower Higgs boson (h^0) mass bounds of 111.4 GeV and 106.4 GeV, respectively. The coloured regions are

- █ neutralino NLSP scenarios,
- █ only excluded by stable slepton pair-prod. in the stau or slepton co-NLSP scenario,
- █ excluded by smuon/selectron pair-production in the stau NLSP scenario,
- █ excluded by neutralino pair-production in the stau or slepton co-NLSP scenario,
- █ excluded by chargino pair-production in the stau or slepton co-NLSP scenario.

8.3.4 Constraints on the SUSY Particle Mass Scale Λ

From the exclusions in the $\Lambda - \tan(\beta)$ plane presented in the previous section, lower limits on the SUSY particle mass scale Λ , independent of $\tan(\beta)$, can be inferred. The parameter Λ determines, for fixed N , the GMSB particle spectrum at the messenger scale, since the gaugino masses are given by [129]

$$m_i(M) \propto N \cdot \Lambda \frac{\alpha_i(M)}{4\pi}, \quad (8.8)$$

where i denotes the gauge group and α_i the GUT normalised coupling constants of these groups. Also the scalar masses at the messenger scale are determined by Λ [129]:

$$m^2(M) \propto 2 N \cdot \Lambda^2 \sum_{i=1}^3 k_i \left(\frac{\alpha_i(M)}{4\pi} \right) \quad (8.9)$$

where the sum runs over the gauge groups $SU(3)_C \otimes SU(2)_L \otimes U(1)_Y$ with $k_1 = 3/5(Y/2)^2$, $k_2 = 3/4$ for $SU(2)_L$ doublets and 0 for singlets, and $k_3 = 4/3$ for $SU(3)_C$ triplets and 0 for singlets.

The results for the 30 parameter sets included in the scan are summarised in Table 8.2 (assuming a slepton as NLSP). As visible from this table, the constraints on Λ decrease with larger N , with lower limits of $\gtrsim 58$ TeV for $N = 1$ and $\gtrsim 16$ TeV for $N = 5$. The constraints depend on M , but are almost independent of the sign of the parameter μ .

lower limit at 95% CL on Λ [TeV]						
		$N = 1$	$N = 2$	$N = 3$	$N = 4$	$N = 5$
high M	$\mu < 0$	74	36	28	24	21
	$\mu > 0$	75	38	28	24	21
medium M	$\mu < 0$	75	37	25	19	16
	$\mu > 0$	76	38	25	19	16
low M	$\mu < 0$	58	40	32	27	23
	$\mu > 0$	58	40	32	27	24

Table 8.2: Lower limits at 95% CL on the SUSY particle mass scale Λ , for various sets of the GMSB parameters M , N and $\text{sign}(\mu)$. The numbers are valid under the assumption that the lightest slepton is the NLSP.

The constraints on Λ imply lower limits on the masses of all SUSY particles, including those which are kinematically not accessible at LEP II. Such lower limits are calculated for all N , the results are shown in Fig. 8.12.

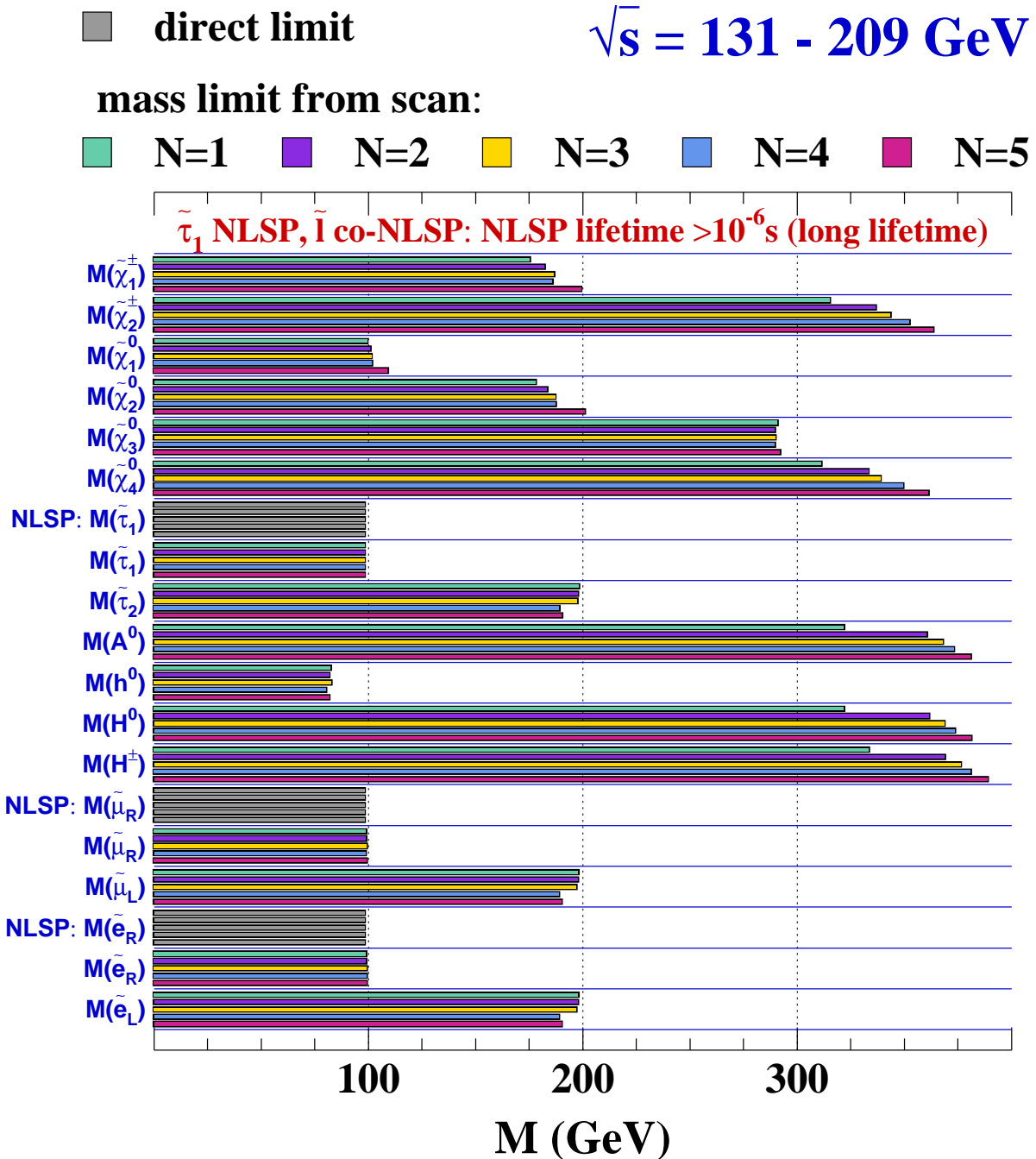


Figure 8.12: Indirect (coloured) and direct (gray) constraints on the masses of various SUSY particles, implied by the limits on the parameter Λ , for different values of the messenger index N and within the framework of the GMSB parameter scan used in this thesis. The constraints are valid in all slepton NLSP scenarios and for any values of $\tan\beta$, M and $\text{sign}(\mu)$.

Chapter 9

Summary and Conclusion

In the first part of this thesis studies for the GEM readout of a TPC for the linear collider TESLA were presented. The measurements were carried out using a TPC prototype with a field cage of 1 m length and an inner diameter of 38 cm, filled with a gas mixture of Ar-CO₂-CH₄ (93 : 2 : 5)% . No magnetic field was applied. Primary charges were produced with muons from cosmic radiation, and gas amplification was carried out using a structure of two GEMs mounted in cascade among one another. The digitisation of the electron signals was carried out with 8-bit FADCs operating at 11.4 MHz.

In GEMs, amplification of the primary electrons takes place owing to a strong electric field ($E \approx 80 \text{ kV/cm}$) inside the small GEM holes of $\mathcal{O}(100 \mu\text{m})$. Compared to conventional wire chamber readout the main advantages of GEMs (and Micromegas) are the intrinsic reduction of ion feedback and several factors which increase the intrinsic resolution capability: two dimensional symmetry (corresponding to the symmetry of the TPC endplate), small dimensions of the amplification structures which reduce $\vec{E} \times \vec{B}$ effects, low material budget in the supporting structure, which reduces multiple scattering and, finally, a narrow spread of the charge cloud after amplification. The latter aspect, however, turns out to be critical as the readout pad size cannot be arbitrary reduced. The induction signal, which is generally broader, is too small to be read out easily. Thus the narrow charge cloud may be collected on a single pad only which can lead to a worse track reconstruction quality. One approach to compensate the absence of a sizable induction signal is the use of specially shaped pads.

Basic performance studies showed that GEMs are fully operable as gas amplification structures in the TPC readout. A signal to noise ratio of approximately 48, an effective gas amplification of $\mathcal{O}(1000)$ and a signal efficiency close to 100% were achieved with a double GEM structure at GEM voltages around 400 V. The measured r.m.s. variation of the gain was $\approx 3\%$ which lies within the intrinsic tolerance of the electronic amplification system.

Further measurements with cosmic muons were carried out in order to determine the single point resolution especially focussing on different readout pad geometries (rectangles and chevrons). The track fit was performed using the charge centre of gravity method. Rectangular pads of the size $2 \times 6 \text{ mm}^2$ (as proposed for TESLA) were found to yield a resolution in x (perpendicular to the drift direction) of $\sigma_x = (200 - 380) \mu\text{m}$, depending on the drift length l_{drift} . As no magnetic field was applied, the resolution was dominated

by diffusion rather than by pad geometry. In order to measure effects of the pad shape anyhow, the pad size was scaled in x according to the ratio of the diffusion coefficients for no magnetic field and the for magnetic field planned at the TESLA detector (magnetic field $B = 4$ T). Pads were developed with an extension in x of $d = 14$ mm as well as the corresponding chevron pads with four “zigzags”. Thus the ratio of the pad dimension and the extension of the charge expected at TESLA could be maintained even without magnetic field. Rectangular pads and chevrons showed both a different behaviour favouring chevrons for short drift distances.

This behaviour was confirmed by simulations which were carried out under TESLA conditions ($B = 4$ T): using chevrons, a point resolution of $\sigma_x = 120 \mu\text{m}$ for $l_{\text{drift}} = 25$ cm and $\sigma_x = 200 \mu\text{m}$ for $l_{\text{drift}} = 225$ cm was found. For rectangular pads the resolution capability was found to decrease at $l_{\text{drift}} < 100$ cm until it reaches values of $\sigma_x = (300 - 450) \mu\text{m}$ for $l_{\text{drift}} < 25$ cm.

Simulating a geometry of the readout module designed especially to exploit the gas diffusion properties (large gap between GEM and pads) a significant charge spread for both pad geometries and all drift distances was achieved, such that nearly the same point resolution was obtained for chevrons and rectangles. For $l_{\text{drift}} = 25$ cm the point resolution was found to be $\sigma_x < 80 \mu\text{m}$ for both pad geometries.

The z resolution was determined in measurements to ≈ 0.5 mm and ≈ 1.0 mm depending on the drift distance. As the longitudinal diffusion is not influenced by a magnetic field parallel to the drift direction, the z resolution is in good approximation independent of the magnetic field and the measurements at $B = 0$ T yield universal results.

The studies are very promising for the GEM application in the TPC readout. In the future, however, more R&D is necessary to investigate if all detector requirements can be met, such that the advantages offered by GEMs can fully be exploited in the operation of a TPC at a linear collider.

In the second part of the thesis a search for heavy stable charged (mass $m \geq 45$ GeV and lifetime $\tau \geq 10^{-6}$ s) particles was performed in e^+e^- collisions of centre-of-mass energies from 131 GeV up to 209 GeV. The search was carried out using data recorded with the OPAL detector at the LEP collider.

Heavy stable charged particles produced in e^+e^- collisions are expected to yield an anomalous specific energy loss dE/dx , which was used in the present analysis to identify signal signatures. A rather general event selection was performed, requiring at least one track per event with significant dE/dx while several other tracks were allowed, such that a high selection efficiency ($\epsilon \approx (50 - 90)\%$) was achieved for many different signal signatures. A new approach for maximally ionising particles, i.e. particles with low $\beta\gamma$, was introduced, based on a change in the track reconstruction algorithm. Tracks could be reconstructed even if the dynamic range of the jet chamber FADCs was exceeded. Owing to this modification the sensitivity of the search was increased at the kinematic limit by roughly 2 GeV, and a kinematic region was explored which so far has not been analysed at LEP.

In data which correspond to an integrated luminosity of $\mathcal{L} = 632.1 \text{ pb}^{-1}$ no event was selected while (0.795 ± 0.394) events were expected from the Standard Model. This result was used to derive upper limits at 95% CL (Confidence Level) on the cross-section

for the direct and the indirect production of heavy stable charged particles. The limits are model independent in the case of exclusive s-channel production. Several limits are derived, however, which are valid in supersymmetric extensions of the Standard Model where the heavy stable charged particle is the NLSP (Next-to-Lightest Supersymmetric Particle). Apart from GMSB models, where several different signal signatures are possible, the AMSB model allows the NLSP to be stable.

For the pair-production of heavy stable charged particles via s-channel, a model independent upper cross-section limit of $\sigma = 0.14 \text{ pb}$ was derived at $\sqrt{s} = 206 \text{ GeV}$ for spin-0 particles and at $\sqrt{s} = 208 \text{ GeV}$ for spin-1/2 particles (for particle masses m between 45 GeV and 102 GeV). For $m \leq 52 \text{ GeV}$ and $68 \text{ GeV} \leq m \leq 101 \text{ GeV}$ cross-sections larger than $\sigma = 0.02 \text{ pb}$ are excluded. The weaker limit at masses around 60 GeV is owing to the $\beta\gamma$ region where the selection efficiency drops below 2%.

Slightly worse limits were obtained for the pair-production of stable selectrons where additional t-channel contribution has to be taken into account. In the analysis maximum t-channel contribution was assumed such that the derived limit is conservative. For the whole mass range a cross-section limit at $\sqrt{s} = 206 \text{ GeV}$ of $\sigma = 0.17 \text{ pb}$ was set, and omitting the region between 52 GeV and 68 GeV , cross-sections larger than $\sigma = 0.03 \text{ pb}$ are excluded.

For heavy stable charged particles produced as direct decay products of previously pair-produced particles (stable secondary particles) similar results were obtained for neutralino pair-production ($e^+e^- \rightarrow \tilde{\chi}_1^0 \tilde{\chi}_1^0 \rightarrow \tilde{\ell} \tilde{\ell} \ell \ell$, $\ell = \tilde{\tau}_1, \tilde{e}_R, \tilde{\mu}_R$) and chargino pair-production ($e^+e^- \rightarrow \tilde{\chi}_1^+ \tilde{\chi}_1^- \rightarrow \tilde{\ell} \tilde{\ell} \nu \nu$). Cross-sections larger than 0.03 pb and often 0.01 pb are excluded at $\sqrt{s} = 208 \text{ GeV}$, depending on the considered phase space region.

Finally, conservatively derived limits for heavy stable charged tertiary particles ($e^+e^- \rightarrow \tilde{\ell} \tilde{\ell} \rightarrow \tilde{\chi}_1^0 \tilde{\chi}_1^0 \ell \ell \rightarrow \tilde{\tau} \tilde{\tau} \tau \tau \mu \mu$, $\ell = \tilde{e}_R, \tilde{\mu}_R$) at $\sqrt{s} = 208 \text{ GeV}$ are $\sigma = 0.04 \text{ pb}$ and $\sigma = 0.02 \text{ pb}$ in a large fraction of the accessible phase space.

The results were interpreted within the framework of GMSB models. The universal lower limit on the mass of the lightest slepton ($m_{\tilde{\ell}}$) assuming a slepton NLSP scenario was determined to $m_{\tilde{\ell}} > 98.1 \text{ GeV}$. Implications within the GMSB parameter space were derived additionally: the constraint on the universal mass scale of the SUSY particles Λ was found to decrease with larger N , which denotes the number of generations of messenger particles, with lower limits of $\Lambda \gtrsim 58 \text{ TeV}$ for $N = 1$ and $\Lambda \gtrsim 16 \text{ TeV}$ for $N = 5$. These constraints are valid for all values of M , i.e. the mass scale of the messenger field and for both positive and negative μ , which is the mixing parameter of the Higgs doublet fields. The constraints on Λ imply lower limits on the masses of all SUSY particles, including those which were kinematically not accessible.

The presented search results will enter into the final OPAL publication on GMSB searches for all NLSP lifetimes [88].

Appendix A

Technical Sketch of Endplate 2

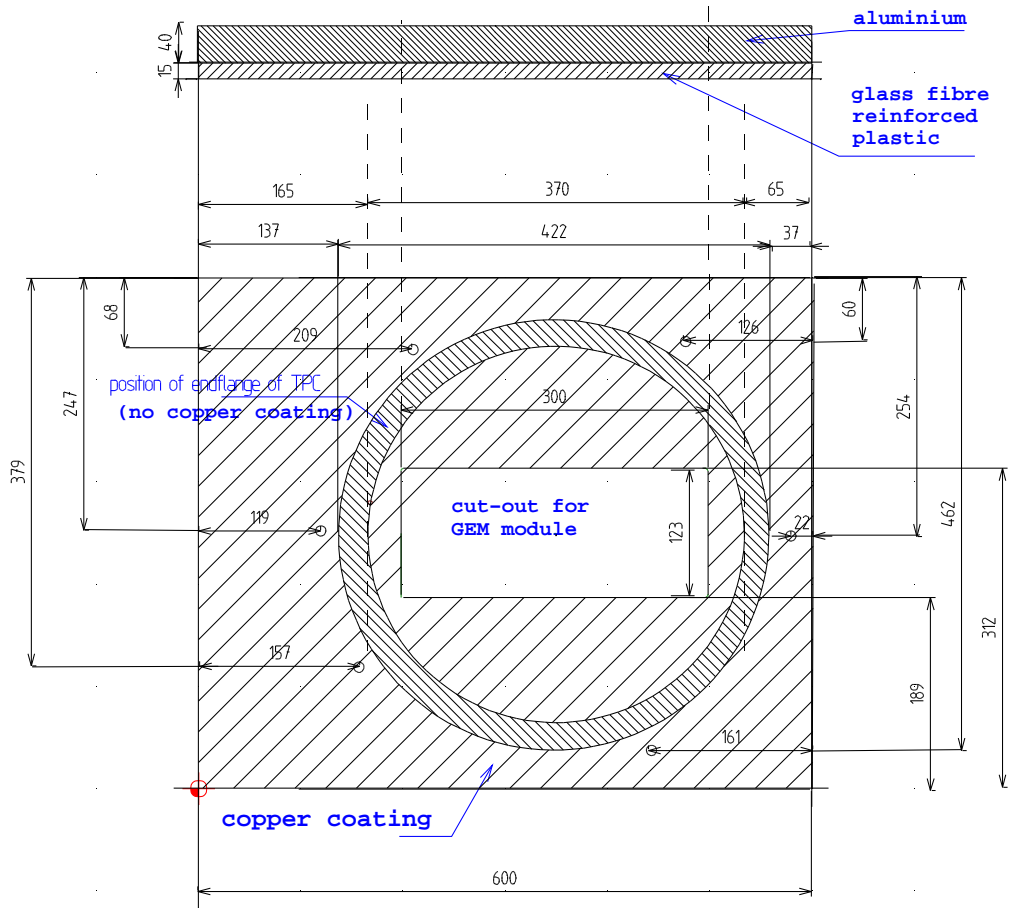


Figure A.1: Technical sketch of endplate#2. Dimensions are in mm.

Appendix B

The Signal Monte Carlo Grid used in the Search

In this appendix a complete list of the simulated signal Monte Carlo points is given (lifetime of the heavy stable charged particle = 10^{-6} s).

1. GMSB Topologies

- Selectron and smuon pair-production in the slepton co-NLSP scenario:

$$\sqrt{s} = 208.1 \text{ GeV.}$$

$$M_{\tilde{\ell}_R} = (45, 50, 55, 60, 65, 70, 75, 80, 85, 90, 95, 100, 104) \text{ GeV.}$$

- Stau pair-production: $\sqrt{s} = 208.1$ GeV.

$$M_{\tilde{\tau}_1} = (45, 50, 55, 60, 65, 70, 75, 80, 85, 90, 95, 100, 101, 102, 103, 104) \text{ GeV.}$$

- Neutralino pair-production with a slepton NLSP: $\sqrt{s} = 206.0$ GeV.

For both the stau NLSP scenario and the slepton co-NLSP scenario 17 combinations of neutralino and slepton masses have been generated:

$$M_{\tilde{\chi}_1^0} = 50 \text{ GeV: } M_{\tilde{\ell}} = (45, 48) \text{ GeV}$$

$$M_{\tilde{\chi}_1^0} = 70 \text{ GeV: } M_{\tilde{\ell}} = (45, 65, 68) \text{ GeV}$$

$$M_{\tilde{\chi}_1^0} = 85 \text{ GeV: } M_{\tilde{\ell}} = (45, 65, 83) \text{ GeV}$$

$$M_{\tilde{\chi}_1^0} = 95 \text{ GeV: } M_{\tilde{\ell}} = (45, 65, 85, 93) \text{ GeV}$$

$$M_{\tilde{\chi}_1^0} = 102 \text{ GeV: } M_{\tilde{\ell}} = (45, 65, 85, 95, 100) \text{ GeV}$$

- Chargino pair-production with a slepton NLSP: $\sqrt{s} = 206.0$ GeV.

For both the stau NLSP scenario and the slepton co-NLSP scenario 24 combinations of chargino and slepton masses have been generated:

$$M_{\tilde{\chi}_1^+} = 60 \text{ GeV: } M_{\tilde{\ell}} = (50, 57) \text{ GeV}$$

$$M_{\tilde{\chi}_1^+} = 70 \text{ GeV: } M_{\tilde{\ell}} = (50, 60, 67) \text{ GeV}$$

$$M_{\tilde{\chi}_1^+} = 80 \text{ GeV: } M_{\tilde{\ell}} = (50, 60, 70, 75) \text{ GeV}$$

$$M_{\tilde{\chi}_1^+} = 90 \text{ GeV: } M_{\tilde{\ell}} = (50, 60, 70, 80, 83) \text{ GeV}$$

$$M_{\tilde{\chi}_1^+} = 100 \text{ GeV: } M_{\tilde{\ell}} = (50, 60, 70, 80, 89) \text{ GeV}$$

$$M_{\tilde{\chi}_1^+} = 102.5 \text{ GeV: } M_{\tilde{\ell}} = (50, 60, 70, 80, 90) \text{ GeV}$$

- Slepton pair-production in the stau NLSP scenario: $\sqrt{s} = 206.0$ GeV.
61 combinations of slepton, neutralino and stau masses have been generated:

$$M_{\tilde{\ell}_R} = 60 \text{ GeV: } M_{\tilde{\tau}_1} = 50 \text{ GeV: } M_{\tilde{\chi}_1^0} = (52, 58) \text{ GeV}$$

$$M_{\tilde{\ell}_R} = 60 \text{ GeV: } M_{\tilde{\tau}_1} = 56 \text{ GeV: } M_{\tilde{\chi}_1^0} = 58 \text{ GeV}$$

$$M_{\tilde{\ell}_R} = 70 \text{ GeV: } M_{\tilde{\tau}_1} = 50 \text{ GeV: } M_{\tilde{\chi}_1^0} = (52, 60, 68) \text{ GeV}/c^2$$

$$M_{\tilde{\ell}_R} = 70 \text{ GeV: } M_{\tilde{\tau}_1} = 60 \text{ GeV: } M_{\tilde{\chi}_1^0} = (62, 68) \text{ GeV}$$

$$M_{\tilde{\ell}_R} = 70 \text{ GeV: } M_{\tilde{\tau}_1} = 66 \text{ GeV: } M_{\tilde{\chi}_1^0} = 68 \text{ GeV}$$

$$M_{\tilde{\ell}_R} = 80 \text{ GeV: } M_{\tilde{\tau}_1} = 50 \text{ GeV: } M_{\tilde{\chi}_1^0} = (52, 65, 78) \text{ GeV}/c^2$$

$$M_{\tilde{\ell}_R} = 80 \text{ GeV: } M_{\tilde{\tau}_1} = 60 \text{ GeV: } M_{\tilde{\chi}_1^0} = (62, 70, 78) \text{ GeV}$$

$$M_{\tilde{\ell}_R} = 80 \text{ GeV: } M_{\tilde{\tau}_1} = 70 \text{ GeV: } M_{\tilde{\chi}_1^0} = (72, 78) \text{ GeV}$$

$$M_{\tilde{\ell}_R} = 80 \text{ GeV: } M_{\tilde{\tau}_1} = 76 \text{ GeV: } M_{\tilde{\chi}_1^0} = 78 \text{ GeV}$$

$$M_{\tilde{\ell}_R} = 90 \text{ GeV: } M_{\tilde{\tau}_1} = 50 \text{ GeV: } M_{\tilde{\chi}_1^0} = (52, 70, 88) \text{ GeV}/c^2$$

$$M_{\tilde{\ell}_R} = 90 \text{ GeV: } M_{\tilde{\tau}_1} = 60 \text{ GeV: } M_{\tilde{\chi}_1^0} = (62, 75, 88) \text{ GeV}$$

$$M_{\tilde{\ell}_R} = 90 \text{ GeV: } M_{\tilde{\tau}_1} = 70 \text{ GeV: } M_{\tilde{\chi}_1^0} = (72, 80, 88) \text{ GeV}$$

$$M_{\tilde{\ell}_R} = 90 \text{ GeV: } M_{\tilde{\tau}_1} = 80 \text{ GeV: } M_{\tilde{\chi}_1^0} = (82, 88) \text{ GeV}$$

$$M_{\tilde{\ell}_R} = 90 \text{ GeV: } M_{\tilde{\tau}_1} = 86 \text{ GeV: } M_{\tilde{\chi}_1^0} = 88 \text{ GeV}$$

$$M_{\tilde{\ell}_R} = 100 \text{ GeV: } M_{\tilde{\tau}_1} = 50 \text{ GeV: } M_{\tilde{\chi}_1^0} = (52, 75, 98) \text{ GeV}$$

$$M_{\tilde{\ell}_R} = 100 \text{ GeV: } M_{\tilde{\tau}_1} = 60 \text{ GeV: } M_{\tilde{\chi}_1^0} = (62, 80, 98) \text{ GeV}$$

$$M_{\tilde{\ell}_R} = 100 \text{ GeV: } M_{\tilde{\tau}_1} = 70 \text{ GeV: } M_{\tilde{\chi}_1^0} = (72, 85, 98) \text{ GeV}$$

$$M_{\tilde{\ell}_R} = 100 \text{ GeV: } M_{\tilde{\tau}_1} = 80 \text{ GeV: } M_{\tilde{\chi}_1^0} = (82, 90, 98) \text{ GeV}$$

$$M_{\tilde{\ell}_R} = 100 \text{ GeV: } M_{\tilde{\tau}_1} = 90 \text{ GeV: } M_{\tilde{\chi}_1^0} = (92, 98) \text{ GeV}$$

$$M_{\tilde{\ell}_R} = 100 \text{ GeV: } M_{\tilde{\tau}_1} = 96 \text{ GeV: } M_{\tilde{\chi}_1^0} = 98 \text{ GeV}$$

$$M_{\tilde{\ell}_R} = 102.5 \text{ GeV: } M_{\tilde{\tau}_1} = 50 \text{ GeV: } M_{\tilde{\chi}_1^0} = (52, 76.2, 99.9) \text{ GeV}$$

$$M_{\tilde{\ell}_R} = 102.5 \text{ GeV: } M_{\tilde{\tau}_1} = 60 \text{ GeV: } M_{\tilde{\chi}_1^0} = (62, 81.3, 99.9) \text{ GeV}$$

$$M_{\tilde{\ell}_R} = 102.5 \text{ GeV: } M_{\tilde{\tau}_1} = 70 \text{ GeV: } M_{\tilde{\chi}_1^0} = (72, 86.2, 99.9) \text{ GeV}$$

$$M_{\tilde{\ell}_R} = 102.5 \text{ GeV: } M_{\tilde{\tau}_1} = 80 \text{ GeV: } M_{\tilde{\chi}_1^0} = (82, 91.2, 99.9) \text{ GeV}$$

$$M_{\tilde{\ell}_R} = 102.5 \text{ GeV: } M_{\tilde{\tau}_1} = 90 \text{ GeV: } M_{\tilde{\chi}_1^0} = (92, 96.2, 99.9) \text{ GeV}$$

$$M_{\tilde{\ell}_R} = 102.5 \text{ GeV: } M_{\tilde{\tau}_1} = 98 \text{ GeV: } M_{\tilde{\chi}_1^0} = 99.9 \text{ GeV}$$

2. Other

- Heavy lepton production:
 $\sqrt{s} = 208.1$ GeV.
 $m = (45, 50, 52, 53, \dots, 76, 77, 78, 80, 85, 90, 95, 98, 99, 100.5, 101.5, 102.59) \text{ GeV}$

In all cases 1000 events have been generated for each point of the mass grid.

Appendix C

Interpretation of the Search Result in the MSSM with small $\Delta m_{\tilde{\chi}_1}$

This part of the appendix is dedicated to an interpretation of the search result in the MSSM with $\Delta m_{\tilde{\chi}_1} = m_{\tilde{\chi}_1^\pm} - m_{\tilde{\chi}_1^0} \lesssim 0.1 \text{ GeV}$. The cross-section limit is compared to the limit obtained by the combination of the results of the four LEP experiments.

s-channel pair-production of stable spin-0 particles can be interpreted as chargino pair-production in the MSSM with very low Δm_{χ_1} for sneutrino masses larger than $\mathcal{O}(100 \text{ GeV})$ (Fig. 8.3). However, very close to the kinematic limit, i.e. $m_{\tilde{\chi}_1} \gtrsim 100 \text{ GeV}$, t-channel contribution is negligible and the efficiency is equal to the efficiency obtained for exclusive s-channel production (Fig. 7.9). Therefore the obtained experimental upper limit on the production cross-section is valid for all possible sneutrino masses close to the kinematic limit.

Fig. C.1 shows the cross-section limit at the highest accessible masses and the theoretically expected cross-sections for chargino pair-production at $\sqrt{s} = 208 \text{ GeV}$, marked at each scan point by a dot. Blue dots indicate parameter combinations for which the sneutrino mass is above 500 GeV, for green points it is below 500 GeV but above 41 GeV. The cross-sections are calculated using **SUSYGEN**. The yellow region indicates the experimentally excluded cross-section region at $\sqrt{s} = 208 \text{ GeV}$ and 95% CL, combining all available data of the four LEP experiments, between 131 and 208 GeV. The cross-section limit set by the present analysis, represented by the dashed line, can be used to exclude a larger set of parameter combinations than the LEP combination owing to the introduced modification of the event reconstruction.

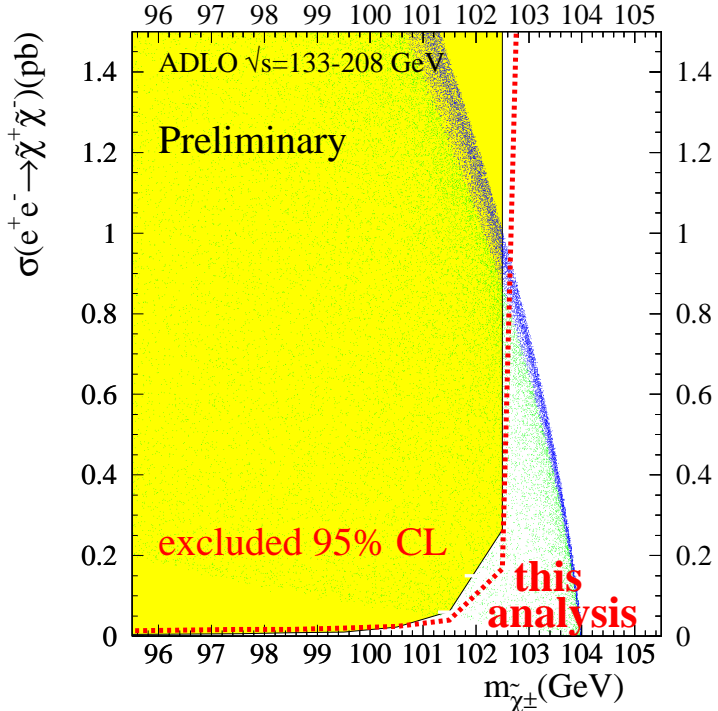


Figure C.1: Model independent 95% CL upper limit on the (s-channel) pair-production cross-section of spin-1/2 heavy stable charged particles at $\sqrt{s} = 208$ GeV (see also Fig. 8.3). The limit can be interpreted as a limit on the chargino pair-production in the MSSM with very low mass difference between lightest chargino and neutralino, given a sneutrino mass larger than $\mathcal{O}(100)$ GeV. The plot shows a magnification of the region close to the kinematic limit including a scan over the MSSM parameter space. The cross-sections for chargino pair-production at $\sqrt{s} = 208$ GeV is marked at each scan point by a dot. Blue dots indicate parameter combinations for which the sneutrino mass is above 500 GeV, for green points it is below 500 GeV but above 41 GeV. The cross-sections are calculated using **SUSYGEN**. The yellow region indicates the experimentally excluded cross-section region at 95 % CL, combining all available data of the four LEP experiments, between 131 and 208 GeV. The cross-section limit set by the present analysis (dashed line), is lower in the region very close to the kinematic limit, which can be used to set better MSSM mass limits.

Bibliography

- [1] G. Charpak and F. Sauli: *An Interesting Fallout of High Energy Physics Techniques: the Imaging of X-rays at various Energies for Biomedical Applications*. Presented at the Conference on Computer Assisted Scanning, Padua, Italy, Apr 21-24, 1976 and at Topical Meeting on Intermediate Energy Physics, Zuoz, Switzerland, Apr 1-10, 1976.
- [2] H. J. Besch, C. Grupen, N. Pavel, and A. H. Walenta: *Applications of Particle Detectors in Medicine, Biology and Astrophysics. Proceedings, 1st International Symposium, SAMBA '99, Siegen, Germany, October 6-8, 1999*. Prepared for the Symposium of Applications of Particle Detectors in Medicine, Biology and Astrophysics (SAMBA 99), Siegen, Germany, 6-8 Oct 1999.
- [3] W. Blum and L. Rolandi: *Particle Detection with Drift Chambers*. Berlin, Germany; Springer (1993).
- [4] R. K. Bock and A. Vasilescu: *The Particle Detector Briefbook*. Berlin, Germany; Springer (1998).
- [5] T. Lohse and W. Witzeling: *The Time Projection Chamber*. Adv. Ser. Direct. High Energy Phys. **9**(1992) 81.
- [6] F. Sauli: *Principles of Operation of Multiwire Proportional and Drift Chambers*. CERN-77-09.
- [7] M. Huk, P. Igo-Kemenes, and A. Wagner: *Electron Attachment to Oxygen, Water, and Methanol, in various Drift Chamber Gas Mixtures*. Nucl. Instrum. Meth. **A267**(1988) 107.
- [8] M. Hohlmann, C. Padilla, N. Tesch, and M. Titov: *Aging Phenomena in Gaseous Detectors: Perspectives from the 2001 Workshop*. Nucl. Instrum. Meth. **A494**(2002) 179.
- [9] G. Charpak and B. Southworth: *New Particle Detectors: the Multiwire Proportional Chamber and the Drift Chamber*. CERN-SIS-PU-77-08.
- [10] A. Walenta, J. Heintze, and B. Schürlein: *The Multiwire Drift Chamber, a new type of Multiwire Proportional Chamber*. Nucl. Instrum. Meth. **92**(1971) 373.
- [11] D. R. Nygren: *A Time Projection Chamber*. Presented at the 1975 PEP Summer Study. Included in Proceedings.

- [12] F. Sauli: *The Time Projection Chamber for Heavy Ion Collisions: Trends and Perspectives*. Z. Phys. **C38**(1988) 339.
- [13] A. Breskin *et al.*: *High flux Operation of the Gated Multistep Avalanche Chamber*. Nucl. Instr. Meth. **178**(1980) 11.
- [14] D. Buskulic *et al.* (ALEPH): *Performance of the ALEPH Detector at LEP*. Nucl. Instrum. Meth. **A360**(1995) 481.
- [15] P. S. Marrocchesi *et al.*: *The Spatial Resolution of the ALEPH TPC*. Nucl. Instrum. Meth. **A283**(1989) 573.
- [16] W. B. Atwood *et al.*: *Performance of the ALEPH Time Projection Chamber*. Nucl. Instrum. Meth. **A306**(1991) 446.
- [17] E. Aker *et al.* (Crystal Barrel): *The Crystal Barrel Spectrometer at LEAR*. Nucl. Instrum. Meth. **A321**(1992) 69.
- [18] O. Biebel *et al.*: *Performance of the OPAL Jet Chamber*. Nucl. Instrum. Meth. **A323**(1992) 169.
- [19] K. Hagiwara *et al.* (Particle Data Group): *Review of Particle Physics*. Phys. Rev. **D66**(2002) 010001.
- [20] M. Hauschild: *Progress in dE/dx Techniques used for Particle Identification*. Nucl. Instrum. Meth. **A379**(1996) 436.
- [21] M. Hauschild: *Frequently Asked Questions about Tracking and dE/dx* (1998). <http://opalinfo.cern.ch/opal/group/cj/cj.html>.
- [22] W. W. M. Allison: *Relativistic Particle Identification by dE/dx : the Fruits of Experience with ISIS*. Invited paper given at Int. Conf. on Instrumentation for Colliding Beam Physics, Stanford, Calif., Feb 17-23, 1982.
- [23] A. H. Walenta, J. Fischer, H. Okuno, and C. L. Wang: *Measurement of the Ionization Loss in the region of Relativistic Rise for Noble and Molecular Gases*. Nucl. Instrum. Meth. **161**(1979) 45.
- [24] F. Richard, J. R. Schneider, D. Trines, and A. Wagner: *TESLA Technical Design Report Part I: Executive Summary* (2001). DESY-01-011, [hep-ph/0106314](http://arxiv.org/abs/hep-ph/0106314).
- [25] R. Brinkmann *et al.*: *TESLA: The Superconducting Electron Positron Linear Collider with an integrated X-ray Laser Laboratory Technical Design Report. Pt. 2: The Accelerator*. DESY-01-011.
- [26] J. A. Aguilar-Saavedra *et al.*: *TESLA Technical Design Report Part III: Physics at an e^+e^- Linear Collider* (2001). DESY-01-011, [hep-ph/0106315](http://arxiv.org/abs/hep-ph/0106315).
- [27] T. Behnke, S. Bertolucci, R. D. Heuer, and R. Settles: *TESLA: The Superconducting Electron Positron Linear Collider with an integrated X-ray Laser Laboratory. Technical Design Report. Pt. 4: A Detector for TESLA*. DESY-01-011.

[28] T. Abe *et al.* (American Linear Collider Working Group): *Linear Collider Physics Resource Book for Snowmass 2001. 1: Introduction* (2001). [hep-ex/0106055](#).
 T. Abe *et al.* (American Linear Collider Working Group): *Linear Collider Physics Resource Book for Snowmass 2001. 2: Higgs and supersymmetry studies* (2001). [hep-ex/0106056](#).
 T. Abe *et al.* (American Linear Collider Working Group): *Linear Collider Physics Resource Book for Snowmass 2001. 3: Studies of exotic and standard model physics* (2001). [hep-ex/0106057](#).
 T. Abe *et al.* (American Linear Collider Working Group): *Linear Collider Physics Resource Book for Snowmass 2001. 4: Theoretical, accelerator, and experimental options* (2001). [hep-ex/0106058](#).

[29] N. Akasaka *et al.*: *JLC Design Study*. KEK-REPORT-97-1.
 K. Abe *et al.* (ACFA Linear Collider Working Group): *Particle Physics Experiments at JLC* (2001). [hep-ph/0109166](#).

[30] G. Wagner: *Neutron Background Studies at the TESLA Collider*. Linear Collider Note LC-DET-2001-048.

[31] T. Behnke: *BRAHMS - A Detector Simulation Program for TESLA*. Prepared for the 5th International Linear Collider Workshop (LCWS 2000), Fermilab, Batavia, Illinois, 24-28 Oct 2000.

[32] T. Behnke and G. A. Blair: *BRAHMS - Version 102: A Monte Carlo for a Detector at a 500 GeV to 800 GeV Linear Collider*. Linear Collider Note LC-PHSM-2001-005.

[33] R. Brun, R. Hagelberg, M. Hansroul, and J. C. Lassalle: *GEANT: Simulation Program for Particle Physics Experiments. user guide and reference manual*. CERN- DD-78-2-REV.

[34] F. Sauli: *GEM: A new Concept for Electron Amplification in Gas Detectors*. Nucl. Instrum. Meth. **A386**(1997) 531.

[35] S. Bachmann *et al.*: *Charge Amplification and Transfer Processes in the Gas Electron Multiplier*. Nucl. Instrum. Meth. **A438**(1999) 376.

[36] Gas Detectors Development Group, <http://gdd.web.cern.ch/GDD/>.

[37] F. Sauli and A. Sharma: *Micropattern Gaseous Detectors*. Ann. Rev. Nucl. Part. Sci. **49**(1999) 341.

[38] A. Bondar, A. Buzulutskov, L. Shekhtman, and A. Vasiljev: *Study of Ion Feedback in Multi-GEM Structures*. Nucl. Instrum. Meth. **A496**(2003) 325.
 F. Sauli, S. Kappler, and L. Ropelewski: *Electron Collection and Ion Feedback in GEM-based Detectors*. IEEE Trans. Nucl. Sci. **50**(2003) 803.
 M. Killenberg *et al.*: *Modelling and Measurement of Charge Transfer in Multiple GEM structures*. Nucl. Instrum. Meth. **A498**(2003) 369.

M. Hamann: *R&D on the GEM Readout of the TESLA TPC*. Proceedings of the International Workshop on Linear Colliders, Jeju, Korea, 2002 (2003).

T. Lux: *Bau und Test einer Mini-TPC mit GEM-Auslese zur Messung des Ionen-Rückflusses* (2003). Diploma thesis.

[39] Y. Giomataris, P. Rebougeard, J. P. Robert, and G. Charpak: *Micromegas: A High-Granularity Position-Sensitive Gaseous Detector for High Particle-Flux Environments*. Nucl. Instrum. Meth. **A376**(1996) 29.

[40] M. Schumacher: *Pad Readout Geometries for a TPC with GEM Readout for the TESLA Linear Collider*. Linear Collider Note LC-DET-2001-014.

[41] S. F. Biagi: *A Multiterm Boltzmann Analysis of Drift Velocity, Diffusion, Gain and Magnetic Field Effects in Argon Methane Water Vapor Mixtures*. Nucl. Instrum. Meth. **A283**(1989) 716.

[42] C. Bowdery: *ALEPH Handbook 1995, Volume 1, Chapter V*. ISBN 92-9083-072-7.

[43] A. Kaoukher: (2003). Personal communication.

[44] M. Gruwe: *Gas Studies for the TPC of a Detector for the Future Linear Collider TESLA*. Linear Collider Note LC-DET-1999-003-TESLA.

[45] S. Bachmann *et al.*: *Optimisation of the Gas Electron Multiplier for High Rate Application*. Nucl. Instrum. Meth. **A461**(2001) 42.

[46] A. Sharma: *3D simulation of Charge Transfer in a Gas Electron Multiplier (GEM) and Comparison to Experiment*. Nucl. Instrum. Meth. **A454**(2000) 267.

[47] I. Smirnov: *HEED Simulation Programme for Energy Loss*.

[48] D. Karlen: *Pad Geometry Study for a Linear Collider TPC*. Proceedings of the International Workshop on Linear Colliders, Jeju, Korea, 2002 (2003).

[49] K. Sachs *et al.*: *GEM TPC R&D in Canada*. Proceedings of the International Workshop on Linear Colliders, Jeju, Korea, 2002 (2003).

[50] A. Kaoukher: (2003). PhD thesis in preparation, University of Rostock, Germany.

[51] H. v/d Graaf: *TPC R&D Report from NIKHEF* (2003). <http://www.nikhef.nl/ecfa-desy/ECspecific/Program/programoverview.htm>.

[52] K. Miuchi *et al.*: *Performance of the TPC with Micro Pixel Chamber Readout: Micro-TPC*. IEEE Trans. Nucl. Sci. **50**(2003) 825. [hep-ex/0301012](https://arxiv.org/abs/hep-ex/0301012).

[53] M. Killenberg *et al.* (LC TPC Group): *LC TPC R&D: A Proposal to the DESY PRC*. DESY-PRC-RD-01-03.

[54] M. Gruwe: *Studies of dE/dx Capabilities of a TPC for the Future Linear Collider TESLA*. Linear Collider Note LC-DET-2001-043.

M. Hauschild: *Particle ID with dE/dx at the TESLA TPC*. Prepared for the 5th International Linear Collider Workshop (LCWS 2000), Fermilab, Batavia, Illinois, 24-28 Oct 2000.

M. Hauschild: *2D and 3D Cluster Counting with GEMs and small Pads: the digital TPC ?* Proceedings of the International Workshop on Linear Colliders, Jeju, Korea, 2002 (2003).

[55] S. L. Glashow: *Partial Symmetries of Weak Interactions*. Nucl. Phys. **22**(1961) 579.

[56] S. Weinberg: *A Model of Leptons*. Phys. Rev. Lett. **19**(1967) 1264.

[57] A. Salam: *Weak and Electromagnetic Interactions*. Originally printed in Svartholm: Elementary Particle Theory, Proceedings Of The Nobel Symposium Held 1968 at Lerum, Sweden, Stockholm 1968, 367-377.

[58] D. J. Griffiths: *Introduction to Elementary Particles*. New York, USA: Wiley (1987).

[59] B. R. Martin and G. Shaw: *Particle Physics*. Chichester, UK: Wiley (1997).

[60] C. Berger: *Elementarteilchenphysik*. Berlin, Heidelberg, New York: Springer (2001).

[61] P. Schmüser: *Feynman-Graphen und Eichtheorien für Experimentalphysiker*. Berlin, Heidelberg, New York: Springer (1995).

[62] M. Drees: *An Introduction to Supersymmetry* (1996). [hep-ph/9611409](#).

[63] H. P. Nilles: *Supersymmetry, Supergravity and Particle Physics*. Phys. Rept. **110**(1984) 1.

[64] J. R. Ellis: *Beyond the Standard Model for Hillwalkers* (1998). [hep-ph/9812235](#).

[65] S. P. Martin: *A Supersymmetry Primer* (1997). [hep-ph/9709356](#).

[66] N. Polonsky: *Supersymmetry: Structure and Phenomena. Extensions of the Standard Model*. Lect. Notes Phys. **M68**(2001) 1. [hep-ph/0108236](#).

[67] H. Spiesberger, M. Spira, and P. M. Zerwas: *The Standard Model: Physical Basis and Scattering Experiments* (2000). [hep-ph/0011255](#).

[68] K. Riesselmann: *Limitations of a Standard Model Higgs Boson* (1997). [hep-ph/9711456](#).

[69] J. Wess and B. Zumino: *A Lagrangian Model Invariant Under Supergauge Transformations*. Phys. Lett. **B49**(1974) 52.

[70] J. Wess and B. Zumino: *Supergauge Transformations in Four Dimensions*. Nucl. Phys. **B70**(1974) 39.

[71] D. V. Volkov and V. P. Akulov: *Possible Universal Neutrino Interaction.* JETP Lett. **16**(1972) 438.

[72] H. E. Haber and G. L. Kane: *The Search for Supersymmetry: Probing Physics Beyond the Standard Model.* Phys. Rept. **117**(1985) 75.

[73] A. H. Chamseddine, R. Arnowitt, and P. Nath: *Locally Supersymmetric Grand Unification.* Phys. Rev. Lett. **49**(1982) 970.

[74] V. Trimble: *Existence and Nature of Dark Matter in the Universe.* Ann. Rev. Astron. Astrophys. **25**(1987) 425.

B. Sadoulet: *Deciphering the Nature of Dark Matter.* Rev. Mod. Phys. **71**(1999) S197.

M. S. Turner and J. A. Tyson: *Cosmology at the Millennium.* Rev. Mod. Phys. **71**(1999) S145. <http://arXiv.org/abs/astro-ph/9901113>.

N. A. Bahcall, J. P. Ostriker, S. Perlmutter, and P. J. Steinhardt: *The Cosmic Triangle: Revealing the State of the Universe.* Science **284**(1999) 1481. [astro-ph/9906463](http://arXiv.org/abs/astro-ph/9906463).

[75] S. Dimopoulos and D. W. Sutter: *The Supersymmetric Flavor Problem.* Nucl. Phys. **B452**(1995) 496.

[76] J. F. Gunion and H. E. Haber: *Higgs Bosons in Supersymmetric Models. 2. Implications for Phenomenology.* Nucl. Phys. **B278**(1986) 449.

[77] J. Rosiek: *Complete set of Feynman Rules for the Minimal Supersymmetric Extension of the Standard Model.* Phys. Rev. **D41**(1990) 3464.

[78] G. F. Giudice and R. Rattazzi: *Theories with Gauge Mediated Supersymmetry Breaking.* Phys. Rept. **322**(1999) 419. [hep-ph/9801271](http://arXiv.org/abs/hep-ph/9801271).

[79] S. Deser and B. Zumino: *Broken Supersymmetry and Supergravity.* Phys. Rev. Lett. **38**(1977) 1433.

[80] S. Ambrosanio, G. D. Kribs, and S. P. Martin: *Signals for Gauge Mediated Supersymmetry Breaking Models at the CERN LEP II Collider.* Phys. Rev. **D56**(1997) 1761. [hep-ph/9703211](http://arXiv.org/abs/hep-ph/9703211).

[81] K. Klein: *A Search for Sleptons with Intermediate Lifetimes in e^+e^- Collisions at $\sqrt{s} = 183 - 209$ GeV.* Ph.D. thesis, Ruperto-Carola University of Heidelberg, Germany (2002).

[82] J. F. Gunion and S. Mrenna: *Probing Models with Near Degeneracy of the Chargino and LSP at a Linear e^+e^- Collider.* Phys. Rev. **D64**(2001) 075002. [hep-ph/0103167](http://arXiv.org/abs/hep-ph/0103167).

[83] C. H. Chen, M. Drees, and J. F. Gunion: *Addendum/Erratum for 'Searching for Invisible and Almost Invisible Particles at e^+e^- Colliders' and 'A Non-standard String/SUSY Scenario and its Phenomenological Implications'* (1999). [hep-ph/9902309](#).

[84] A. Brignole, L. E. Ibanez, and C. Munoz: *Soft Supersymmetry-breaking terms from Supergravity and Superstring Models* (1997). [hep-ph/9707209](#).

[85] C. H. Chen, M. Drees, and J. F. Gunion: *A Non-standard String/SUSY Scenario and its Phenomenological Implications.* Phys. Rev. **D55**(1997) 330. [hep-ph/9607421](#).

[86] G. Anderson *et al.*: *Motivations for and Implications of Non-universal GUT-scale Boundary Conditions for soft SUSY-breaking parameters* (1996). [hep-ph/9609457](#).

[87] *Searches for Gauge Mediated SUSY Breaking Topologies in e^+e^- Collisions at $\sqrt{s} = 189 - 209$ GeV* (2002). OPAL Physics Note 504.

[88] *Searches for Gauge Mediated SUSY Breaking Topologies in e^+e^- Collisions at $\sqrt{s} = 189 - 209$ GeV* (2003). OPAL paper in preparation.

[89] K. Ahmet *et al.* (OPAL): *The OPAL Detector at LEP.* Nucl. Instrum. Meth. **A305**(1991) 275.

[90] *ROPE Users' Guide* (last update: March, 2002).

[91] T. Omori, S. Asai, I. Nakamura, and I. Yamashita: *A Matching Algorithm: MT Package.* OPAL Technical Note 381.

[92] T. Omori, S. Asai, and I. Nakamura: *Attempt to Compensate Energy in OPAL Calorimeter Complex Based on MT Package.* OPAL Technical Note 447.

[93] S. Mihara and S. Yamashita: *MT 3.00: a new Algorithm to Calculate Energy Flow Based on MT Package.* OPAL Technical Note 574.

[94] M. Hauschild *et al.*: *Particle Identification with the OPAL Jet Chamber.* Nucl. Instrum. Meth. **A314**(1992) 74.

[95] M. Arignon *et al.* (OPAL): *The Trigger System of the OPAL Experiment at LEP.* Nucl. Instrum. Meth. **A313**(1992) 103.

[96] J. L. Pinfold *et al.*: *Detector for Magnetic Monopoles at OPAL.* Nucl. Instrum. Meth. **A302**(1991) 434.

[97] C. Hawkes: *Luminosity Counting in ROPE.* Technical Report TN003, OPAL (1990).

[98] R. Nisius: *The Photon Structure from Deep Inelastic Electron Photon Scattering.* Phys. Rept. **332**(2000) 165. [hep-ex/9912049](#).

[99] G. A. et al. (OPAL): *Tests of the Standard Model and Constraints on New Physics from Measurements of Fermion-Pair Production at 189 – 209 GeV at LEP*. CERN-EP-2003-053, Submitted to Eur. Phys. J.C (2003).

[100] F. A. Berends, P. Daverveldt, and R. Kleiss: *Radiative Corrections to the Process $e^+e^- \rightarrow e^+e^-\mu^+\mu^-$* . Nucl. Phys. **B253**(1985) 421.

[101] F. A. Berends, P. H. Daverveldt, and R. Kleiss: *Monte Carlo Simulation of Two-Photon Processes. 1. Radiative Corrections to Multiperipheral $e^+e^-\mu^+\mu^-$ Production*. Comput. Phys. Commun. **40**(1986) 271.

[102] F. A. Berends, P. H. Daverveldt, and R. Kleiss: *Monte Carlo simulation of two photon processes. 2. complete lowest order calculations for four lepton production processes in electron positron collisions*. Comput. Phys. Commun. **40**(1986) 285.

[103] F. A. Berends, P. H. Daverveldt, and R. Kleiss: *Monte Carlo Simulation of Two-Photon Processes. 3. Complete Lowest Order Calculations for $e^+e^- \rightarrow e^+e^-\mu^+\mu^-$ with Large Angle Tagging Conditions*. Comput. Phys. Commun. **40**(1986) 309.

[104] J. A. M. Vermaseren: *Two-Photon Processes at Very High Energies*. Nucl. Phys. **B229**(1983) 347.

[105] L. Lonnblad *et al.*: *$\gamma\gamma$ Event Generators* (1995). [hep-ph/9512371](#).

[106] G. Marchesini *et al.*: *HERWIG: A Monte Carlo Event Generator for Simulating Hadron Emission Reactions with Interfering Gluons. Version 5.1*. Comput. Phys. Commun. **67**(1992) 465.

[107] S. Jadach, W. Placzek, and B. F. L. Ward: *BHWIDE 1.00: $\mathcal{O}(\alpha)$ YFS exponentiated Monte Carlo for Bhabha Scattering at Wide Angles for LEP I/SLC and LEP II*. Phys. Lett. **B390**(1997) 298. [hep-ph/9608412](#).

[108] D. Karlen: *Radiative Bhabha Scattering for Singly Tagged and Untagged Configurations*. Nucl. Phys. **B289**(1987) 23.

[109] S. Jadach, B. F. L. Ward, and Z. Was: *The Precision Monte Carlo Event Generator KK for Two-Fermion Final States in e^+e^- Collisions*. Comput. Phys. Commun. **130**(2000) 260. [hep-ph/9912214](#).

[110] G. Montagna, O. Nicrosini, and F. Piccinini: *NUNUGPV: A Monte Carlo Event Generator for $e^+e^- \rightarrow \nu\bar{\nu}\gamma(\gamma)$ Events at LEP*. Comput. Phys. Commun. **98**(1996) 206.

[111] S. Jadach, W. Placzek, M. Skrzypek, B. F. L. Ward, and Z. Was: *Monte Carlo Program KoralW 1.42 for all Four-Fermion Final States in e^+e^- Collisions*. Comput. Phys. Commun. **119**(1999) 272. [hep-ph/9906277](#).

[112] J. Fujimoto *et al.*: *grc4f v1.1: a Four-Fermion Event Generator for e^+e^- Collisions*. Comput. Phys. Commun. **100**(1997) 128. [hep-ph/9605312](#).

- [113] F. A. Berends and R. Kleiss: *Distributions for Electron-Positron Annihilation into two and three Photons*. Nucl. Phys. **B186**(1981) 22.
- [114] T. Sjostrand: *High Energy Physics Event Generation with PYTHIA 5.7 and JETSET 7.4*. Comput. Phys. Commun. **82**(1994) 74.
- [115] S. Jadach, J. H. Kuhn, and Z. Was: *TAUOLA: A library of Monte Carlo programs to simulate decays of polarized τ leptons*. Comput. Phys. Commun. **64**(1990) 275.
- [116] M. Jezabek, Z. Was, S. Jadach, and J. H. Kuhn: *The τ decay Library TAUOLA, update with exact $\mathcal{O}(\alpha)$ QED Corrections in $\tau \rightarrow \mu(e)\nu\bar{\nu}$ decay modes*. Comput. Phys. Commun. **70**(1992) 69.
- [117] S. Katsanevas and P. Morawitz: *SUSYGEN2.2: A Monte Carlo Event Generator for MSSM Sparticle Production at e^+e^- Colliders*. Comput. Phys. Commun. **112**(1998) 227. [hep-ph/9711417](#).
- [118] N. Ghodbane: *SUSYGEN3: An Event Generator for Linear Colliders* (1999). [hep-ph/9909499](#).
- [119] R. Tafirout and G. Azuelos: *EXOTIC: A heavy fermion and excited fermion Monte Carlo generator for e^+e^- physics*. Comput. Phys. Commun. **126**(2000) 244.
- [120] J. Allison *et al.*: *An Application of the GEANT3 Geometry Package to the Description of the OPAL Detector*. Comput. Phys. Commun. **47**(1987) 55.
- [121] J. Allison *et al.* (OPAL): *The Detector Simulation Program for the OPAL Experiment at LEP*. Nucl. Instrum. Meth. **A317**(1992) 47.
- [122] C. Rembser and B. List: *Description of Selection Efficiencies in Searches for Heavy Particles with Finite Lifetime*. Technical Report TN643, OPAL (2000).
- [123] G. Abbiendi *et al.* (OPAL): *Search for Anomalous Production of Acoplanar Di-Lepton Events in e^+e^- Collisions at $\sqrt{s} = 183$ GeV and 189 GeV*. Eur. Phys. J. **C14**(2000) 51. [hep-ex/9909052](#).
- [124] T. Junk: *Tracking Performance in 1999*. Technical Report TN651, OPAL (2000).
- [125] R. Batley *et al.*: *DST-Level Tracking Adjustments and Refit with Silicon Hits*. Technical Report TN520, OPAL (last update: 2000).
- [126] M. Hauschild: (2002). Personal communication.
- [127] T. Junk: *Confidence Level Computation for Combining Searches with small Statistics*. Nucl. Instrum. Meth. **A434**(1999) 435. [hep-ex/9902006](#).
- [128] G. Abbiendi *et al.* (OPAL): *Search for Stable and Long-Lived Massive Charged Particles in e^+e^- Collisions at $\sqrt{s} = 130$ GeV to 209 GeV* (2003). [hep-ex/0305031](#).

- [129] S. Dimopoulos, S. Thomas, and J. D. Wells: *Sparticle Spectroscopy and Electroweak Symmetry Breaking with Gauge Mediated Supersymmetry Breaking*. Nucl. Phys. **B488**(1997) 39. hep-ph/9609434.
- [130] *Search for the Standard Model Higgs Boson at LEP*. Phys. Lett. **B565**(2003) 61.
- [131] S. Ambrosanio, A. Dedes, S. Heinemeyer, S. Su, and G. Weiglein: *Implications of the Higgs Boson Searches on different Soft SUSY-Breaking Scenarios*. Nucl. Phys. **B624**(2002) 3.
- [132] C. Rembser and G. Weiglein: (2003). Personal communication.

Danksagung

Mein besonderer Dank gilt Prof. Dr. Rolf-Dieter Heuer und Dr. Ties Behnke für die Förderung und Unterstützung während der gesamten Arbeit.

Prof. Dr. Beate Naroska, Prof. Dr. Peter Schleper und Prof. Dr. Götz Heinzelmann danke ich für die Erstellung der Gutachten beziehungsweise für die Leitung der Disputation.

Dr. Christoph Rembser danke ich für die intensive und geduldige Betreuung der OPAL-Analyse und Dr. Klaus Desch für viele gute Tipps und sein reges Interesse an meiner Arbeit.

Bei Dr. Michael Hauschild möchte ich mich für die fundierte und ausführliche Beantwortung meiner Fragen bedanken.

Dr. Felix Sefkow danke ich für sein Engagement bei TPC-Angelegenheiten sowie Prof. Dr. Alexander Bondar, Dr. Madhu Dixit, Prof. Dr. Dean Karlen, Dr. Ron Settles und der Aachener TPC-Gruppe für fruchtbare Gespräche.

Für die technische Unterstützung der TPC-Gruppe möchte ich speziell Karsten Gadow, Helmut Krause, Hans-Jürgen Seidel und der Werkstatt der Uni Hamburg danken. Vielen Dank auch an die CERN GDD-Gruppe und an Rui de Oliveira für die Wiederherstellung zahlreicher GEMs.

Für das Korrekturlesen der Dissertation ein Dankeschön an Bernhard, Markus S., Thorsten K., Thorsten L. und vor allem an Dr. Ties Behnke, Dr. Klaus Desch und Dr. Ron Settles.

Desweiteren habe ich allen ehemaligen und aktuellen FLC-Kollegen eine sehr angenehme Arbeitsatmosphäre zu verdanken. Ein herzliches Dankeschön auch an Bernhard, Marius, Markus S., Mathieu, Thorsten L. und Wolfgang für das ein oder andere gemeinsame Bier und speziell an Carsten und Petra.

Zum Schluss möchte ich meinen Dank für den moralischen Beistand an Andreas, Dagmar, Frauke, Gaby, Hubertus, Jan und Nora aussprechen sowie an meinen Vater Rainer für die Unterstützung während meiner gesamten Ausbildung.